

THE EFFECT OF SELECTED FLUID PARAMETERS
ON SPATIAL DROP SIZE DISTRIBUTION

by

Edward Junior Rice

A thesis submitted in partial fulfillment of the
requirements for the degree of

DOCTOR OF PHILOSOPHY

(Mechanical Engineer)

at the

UNIVERSITY OF WISCONSIN

FACILITY FORM 602

N 68-11610

(ACCESSION NUMBER)

270

(PAGES)

TMX # 52381

(NASA CR OR TMX OR AD NUMBER)

(THRU)

(CODE)

(CATEGORY)

1966

ACKNOWLEDGEMENTS

The author wishes to express his gratitude to his faculty advisors Professors P. S. Myers and O. A. Uyehara and to Professor M. M. El-Wakil who are credited with the conception of the fluorescent technique for obtaining spray photographs. Gratitude is due Dr. G. M. Benson who performed the original work on this project and to J. F. Groeneweg who as co-worker with the author contributed greatly to the refinement of the technique.

The generous financial grants of the National Science Foundation, Cummins Engine Company, and the Wisconsin Alumni Research Foundation have made the continued work on this project possible.

Gratitude is due the Continental Can Company for the loan of the particle counter without which the data reduction would have been formidable.

The National Aeronautics and Space Administration, Lewis Research Center is thanked for the preparation of this manuscript, the granting of the necessary computer time, and the cooperation of its personnel which have all made the completion of this work possible.

ABSTRACT

This thesis covers the continuation of work done on a project using a fluorescent technique for the study of the microscopic properties of a fluid spray.

This technique enables the examination of the spray properties to be made with extremely fine spatial resolution. A cross section of the spray virtually perpendicular to the spray axis and having a volume of $4 \times 4 \times 0.2$ mm. can be studied. By movement of the nozzle holding apparatus the cross section of an entire quadrant of the spray can be studied. The distance from the nozzle to this quadrant can also be varied.

The extreme spatial resolution is obtained by the use of a high intensity sheet of radiation which intersects the spray at 75 degrees and which has a virtually uniform thickness of 0.2 mm. for the 4 mm. length of sheet covered in the sampling volume. The droplets in this sampling volume absorb radiation from the radiation sheet and emit fluorescent radiation due to the fluorescent dye dissolved in the fluid and thus act as primary radiators. A high resolution camera of 25 magnification and capable of resolving a 10 micron drop with less than 10 percent error is used to photograph the droplets.

In addition this technique provides a minimum of out-of-focus drops due to the coincidence of the camera depth of field and the radiation sheet.

A DuMont Iconumerator flying spot counter modified with an added sizing circuit is used to size the drops on the photographs. A discussion of the sizer and its calibration is included.

The apparatus used in this technique as well as its alignment and calibration are discussed. A discussion of a new light source of extremely high intensity and low duration with a long, narrow, guided spark gap is included.

The data taken using this technique is presented. A traverse of the spray at six adjacent radial positions was made using a Monarch F-80, 0.75 gph, 30 degree solid cone nozzle. Three fluids of varying properties were used at three pressures for each of these six locations. Thus 54 data conditions were analyzed.

Statistical considerations of sample size and also data analysis are given. The data was correlated using the upper limit log normal distribution. It was found that each drop size distribution could be described by the use of just one parameter, the maximum drop size. The maximum drop size was correlated with the fluid properties, nozzle pressure, and position in the spray by means of an empirical equation involving the Weber and Reynolds Numbers and the angle from the nozzle axis.

A discussion of possible modifying improvements and extensions of the technique is included.

TABLE OF CONTENTS

	Page
ACKNOWLEDGEMENTS	ii
ABSTRACT	iii
LIST OF TABLES	ix
LIST OF FIGURES	x
INTRODUCTION	1
TECHNIQUE	5
APPARATUS	12
Excitation Optical System	12
Condensing Lens	13
Spherical Mirror	19
Camera	22
Camera Curvature of Field	27
Light Source	30
General Requirements	30
Former Light Source	31
Tests of Light Sources	33
Light Sources Tested	34
Test Procedure and Equipment	36
Test Results	40
Present Light Source	48
Test of Present Light Source	54
Power Supply	57
Particle Counter and Sizer	60
Du Mont Iconumerator	60
Particle Size Discriminator	67

	Page
Iconumerator Modifications	75
Optical System Modification	76
Electrical Modification	78
Calibration Procedure	80
Iconumerator Adjustments	82
Size Discriminator Adjustment	83
Calibration of Combined System	84
Calibration Check with Drop Pictures	87
Possible Errors in Sizing Particles	88
Nozzle Carriage	99
CONSIDERATIONS FOR IMPROVEMENT OF LIGHT SOURCE	100
Discharge Circuit Parameters	101
Temperature Saturation	103
Summary	110
OPTICAL ALIGNMENT PROCEDURE	114
Camera Focus	114
Condensing Lens Alignment	118
Spherical Mirror Alignment	121
PHOTOGRAPHIC PROCEDURE	123
Development and Intensification	126
High Sensitivity Light Meter	131
Possible Methods of Increasing Film Speed	134
FLUORESCENCE	136
Concentration Quenching	137
Cause of Concentration Quenching in Uranin Solutions	143

	page
Temperature Effect on Quenching in Uranin Solutions	144
Effect of Solution pH on Fluorescence	147
STATISTICAL CONSIDERATIONS	151
Possible Error Due to Edge Effects on The Film	152
A Priori Confidence Interval Estimate	156
Confidence Interval Using the t-Distribution	162
Comparison of A Priori and t-Distribution	
Confidence Intervals	165
CENTRIFUGAL PRESSURE-ATOMIZING NOZZLE	168
Flow of Liquid Through a Centrifugal Nozzle	168
A Model for Sheet Break-up	178
DATA PRESENTATION	181
DATA REDUCTION AND ANALYSIS	185
The Drop Size Distribution	185
Spray Parameters in Dimensionless Groups	190
Correlation of Drop Size Volume Distribution	192
Comparison of Results to Other Data	205
Spatial Mass Distribution	214
A Possible Explanation for the Observed Mass	
Distribution and Variation of Maximum Drop	
Size with Angle in the Spray	217
Conclusions Drawn from Data Analysis	219
FORTRAN IV PROGRAM FOR WEIGHTED LEAST-SQUARES CURVE FIT	221
The Least-Squares Weighting Function	222
A Weighting Function for Frequency Distributions	223

	page
The Method of Weighted Least-Squares with Nonlinear Parameters	225
APPENDIX I MEASURED PROPERTIES OF GLYCEROL-ETHANOL SOLUTIONS AT 20° C	231
APPENDIX II 95 PERCENT CONFIDENCE INTERVALS USING THE t-DISTRIBUTION	232
APPENDIX III DROP COUNT TABULATIONS	235
APPENDIX IV NONLINEAR PARAMETER WEIGHTED LEAST-SQUARES FITTING PROGRAM	244
BIBLIOGRAPHY	253

LIST OF TABLES

Table		Page
I	SPARK DISCHARGE TEMPERATURE VRS. RATE OF CURRENT INCREASE	103
II	RELATIVE QUANTUM YIELD Q_r OF THE FLUORESCENCE OF FLUORESCEIN AS A FUNCTION OF THE DYE CONCENTRATION c (IN GRAMS/LITER) IN VARIOUS SOLVENTS	138
III	FLUID PROPERTIES AND FLOW PARAMETERS FOR THE DATA	192
IV	GLYCEROL-ETHANOL SOLUTION PROPERTIES VRS. PERCENT GLYCEROL	231
V	CONFIDENCE INTERVALS FOR SIX SAMPLE DATA GROUPS	233
VI	NUMBER OF DROPS COUNTED AND MEAN DROP SIZES	235

LIST OF FIGURES

Figure	Page
1. Apparatus Layout	6
2. Dilute Aqueous Uranin Solution Characteristics	8
3. Photograph of Fluorescing Spray in Horizontal Plane	9
4. Voltage versus Knife Edge Movement for Intensity Measurement	14
5. Radiation Sheet Cross Sections Photographed Through Microscope Using Different Lens Stops	16
6. Lens Stop Test Setup	18
7. Screen Image of Figure 6	20
8. Lens Stop Configurations	21
9. Excitation Optical System	23
10. Camera Curvature of Field	29
11. Spark Intensity and Time Measurement Circuit	37
12. Response of S-4 Surface with Wratten 75 Filter	38
13. Intensity versus Time Recordings of Guided Spark Discharge	41
14. Relative Peak Intensity versus Capacitor Voltage for Various Light Sources as Measured by a 929 Vacuum Phototube with Wratten 75 Filter	42
15. Half Peak Duration versus Capacitor Voltage for Various Light Sources as Measured by a 929 Vacuum Phototube with Wratten 75 Filter	43

Figure		page
16.	Relative Radiant Energy versus Capacitor Charging Energy for Various Light Sources as Measured by a 929 Vacuum Phototube with Wratten 75 Filter	44
17.	Breakdown Voltage versus Pressure Times Gap Length for Atmospheric Pressure	49
18.	Cut-away View of Bottom Half of Light Source	51
19.	Front and Side View of Light Source and Condenser	55
20.	Power Supply 50 KV DC Circuit Diagram	58
21.	Front Panel of Power Supply	61
22.	Apparatus as Currently Used	62
23.	Block Diagram of Iconumerators with Sizer Included	64
24.	Particle Size Discriminator	68
25.	Sizer Signals for Various Points in Circuit	69
26.	Iconumerators Optical System Modifications	77
27.	Video Cathode Follower Modification	79
28.	Effect of High Frequency Compensation on Small Particles	81
29.	Calibration Slide for Final Sizer Calibration	85
30.	Microdensitometer Profiles of Drop Photographs	89
31.	Variation of Apparent Drop Diameter with Different Image Intensity and Development Conditions	91
32.	Block Diagram of Suggested Circuit for Removing Blurred Drops	95
33.	Maximum Channel Temperature as Calculated from Maximum Radiation Intensity at Various Wavelengths For Several Gases	105

Figure		page
34.	Variation of the Maximum Spectral Density of the Brightness of the Channel of the Spark Discharge in Argon and Xenon as a Function of Circuit Inductors	109
35.	Diagrammatic Illustration of Complete and Partial Brightness Saturation	111
36.	Diagram of Focusing Setup	115
37.	Radiation Sheet Cross-Section Photographs	120
38.	Kodak Royal-X Pan Density-Log E Curves	124
39.	Spectral Sensitivity of Kodak Royal-X Pan and Green Sensitive Photofluore Film	125
40.	Kodak Green Sensitive Photofluore Density-Log E Curves	127
41.	Effect of Intensification on Density of Kodak Royal-X Pan	130
42.	High Sensitivity Light Meter	132
43.	Relative Fluorescent Strength of Fluorescein as a Function of Dye Concentration in Various Solvents as Calculated by $F = c Qr$	139
44.	Relative Fluorescent Strength of Fluorescein as a Function of Dye Concentration in Various Solvents as Determined Experimentally	141
45.	Effect of Temperature on Aqueous and Glycerol Uranin Solutions	146
46.	Effect of Solution pH on the Fluorescent Spectrum of Uranin	148

Figure		Page
47.	Diagram of Edge Effect Model	153
48.	Apriori Confidence Interval (95 percent) versus Fraction of Drops in Size Category for Various Sample Sizes	160
49.	Apriori Confidence Interval (95 percent) for Small Fraction of Drops in a Size Category	161
50.	Comparison of Apriori and t-Distribution Confidence Intervals	166
51.	Centrifugal Pressure-Atomizing Nozzle	169
52.	Discharge Coefficient and Fraction of Orifice Filled versus A	176
53.	Discharge Coefficient for Some Real Fluids	177
54.	Location of Data Sampling Stations	182
55.	Sample Photographs of an Ethanol Spray	184
56.	Cumulative Volume Distribution for a Typical ' Set of Data	187
57.	Sauter Mean Diameter versus Position in the Ethanol Sprays	195
58.	Pressure Effect on Bimodal Property of x_m for Ethanol Sprays	197
59.	Viscosity Effect on Bimodal Property of x_m	199
60.	Calculated Maximum Drop Size Compared to Largest Observed Drop Size	201
61.	Comparison of Sauter Mean Diameters Calculated from Correlation to that of Raw Data	202

Figure	Page
62. Volume Distribution versus Percent Maximum Drop Size for Ethanol Sprays	203
63. Volume Distribution versus Percent Maximum Drop Size for Ethanol Sprays	204
64. Number Distribution versus Percent Maximum Drop Size for Ethanol Sprays	206
65. Number Distribution versus Percent Maximum Drop Size for Glycerol Sprays	207
66. Comparison of Data on Upper-Limit Function Cumulative Volume Basis	208
67. Mass Median Diameter versus Sauter Mean Diameter for Data of Other Observers	212
68. Spatial Mass Distributions for Ethanol Sprays	216
69. Percent Error versus Percent of Total Sample	234

INTRODUCTION

"Atomization is the first and possibly the most important step involved in the combustion of liquid fuels in propulsion devices" (30). The function of the atomization process is to increase the surface area of the fuel to accelerate vaporization and to distribute the fuel droplets throughout the combustion chamber. A nonuniform spatial distribution of the fuel spray may cause local overheating and consequent burnout of parts (31). Combustion efficiency (32,33) and flame stability (34) are related to fuel drop size.

As important as the atomization process is, it is little understood. No fundamental theory is available from which the drop size distribution and spatial distribution can be predicted for even the simplest atomization devices. Many workers have studied the atomization process with various techniques and a qualitative understanding of spray breakup has resulted.

A problem with most sampling techniques is that in one way or another the results are a function of the apparatus used. A common method of spray sampling is the collection of droplets on greased slides or in fluids which are immiscible with the fuel. This method results in missing most of the small drops since they will follow the gas flow streamlines around the slide. The spattering and flattening of the droplets upon impact with the slide is another disad-

vantage. The slide will certainly disturb the spray and intrained gas flow pattern.

Frozen drop and wax methods have also been used. The sprayed fluid is solidified and then sieved to determine the drop size distribution. Disadvantages of this technique are the unavailability of very fine sieves, the jamming of the sieve by waxy particles, and the dependence of size distribution on the sieving technique.

Optical methods have been used which depend upon transmission or scattering of a light beam passed through the spray. This technique provides rapid and easily obtained measurements, and the spray is not disturbed. The greatest disadvantage is that information is obtained only on an average drop size, and drop size distribution data cannot be obtained.

The cascade impactor method utilizes the principle that the large drops will strike a slide plate, but small drops will be carried around the slide following the air flow. Several slides are placed in cascade with the air velocity increasing at each stage. With increasing velocity the small drops will follow the air flow less closely and more will hit the slide. This method is fast and easy, but must provide an extreme disturbance to the spray.

The most promising method (and most difficult) of spray sampling appears to be the direct photographic technique. If properly designed, this technique can provide accurate drop size distribution data without disturbing the spray or gas flow. One of the problems with this method is that if nonparallel light is used such as in a shadowgraph

technique a large number of out-of-focus drops will appear on the photograph. If parallel light is used, all spatial resolution of spray distribution along the light beam is lost. This method is also very laborious since it involves the sizing of a large number of drops on the photographs to obtain a reasonable sample size.

The direct photographic technique provides only a spatial drop size distribution (the size distribution found in a given volume at a given time) rather than the temporal drop size distribution (the size distribution of drops passing a given area per unit time). To obtain the temporal distribution the drop velocities might be obtained by use of a two flash exposure photograph (35), a rotating mirror camera (36), or by some separate independent method. A more complete discussion of the above techniques can be found in Reference (37).

A modification of the direct photographic method which uses the fluorescent light emitted by the drops in an exciting radiation sheet is described here. Many of the disadvantages of the above methods have been overcome with this technique. A camera of long working distance with a magnification of 25 is used which does not interfere with the spray as would a slide or a short working distance microscope. A minimum of out-of-focus drops is obtained due to the thin radiation sheet. The sample volume is located almost perpendicular to the nozzle axis so that by movement of the nozzle the drop size distribution can be studied over a quadrant of a cross section of the spray. Spatial resolution of drop size distribution is thus quite easily obtained with this technique.

The work reported in this paper represents a continuation of work on this technique conducted at the University of Wisconsin and first reported by Benson (1). Drop size distribution data was taken with several fluids at several locations in a cross section of the spray formed by a centrifugal nozzle. The data is presented and analyzed in this paper.

It is hoped that this technique in its present form will be a contribution to the further study of atomization and as part of a more complete system will provide a useful tool for study of vaporization and combustion.

TECHNIQUE

This method of spray analysis uses the fluorescent radiation emitted by a fluorescent dye dissolved in the sprayed fluid to make a photographic image of the individual drops in a small portion of the spray. Figure 1 shows the apparatus layout used in this technique.

The spray cone formed by the pressure nozzle is intersected at nearly a right angle by an intense extremely thin sheet of radiation. The camera located normal to the radiation sheet will then see a very small and well defined volume of the spray determined by the field of view of the camera and the radiation sheet thickness. In this study a $4 \times 4 \times 0.2$ mm. volume was used.

The radiation sheet is formed by the light source, condensing lens, and spherical mirror system. The light source is a high intensity, vertical, line spark discharge. This is discharged and the sheet of radiation formed is focused by the quartz condensing lens system into the sampling volume. Due to axial spherical aberration of the condensing lens, the light source image is spread along the optical axis for a sufficient distance to provide a very uniform thickness radiation sheet in the sampling volume. The spherical mirror is located with its optical center at the position of best source image, and this doubles the incident solid angle as well as helping to reduce nonuniformities in the radiation distribution of the sheet.

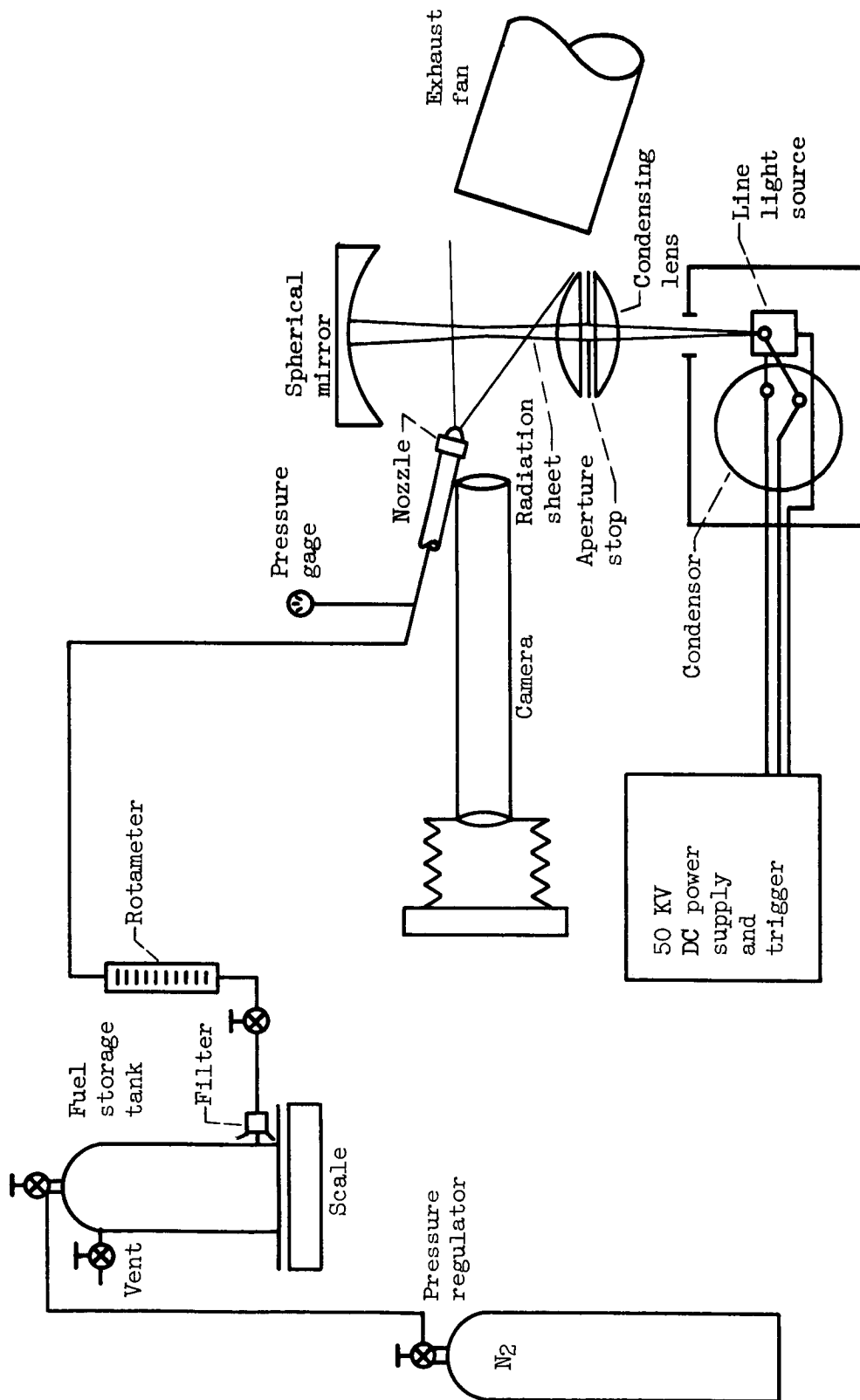


Figure 1. - Apparatus layout.

The camera, with a depth of field slightly greater than the radiation sheet, is focused upon this sheet. Thus it can be seen that when the light source is pulsed any drops within the radiation sheet will absorb radiation falling within the fluorescent dye's absorption spectrum and reradiate radiation in the wavelengths of its fluorescent spectrum. This enables the camera to form a photographic image of these drops only. Figure 2 (2)* gives the relative absorption and fluorescent spectrum for a dilute aqueous uranium solution. The drops to the front or rear of the radiation sheet will not be irradiated and thus will not be visible to the camera. The light source is of sufficiently short duration to effectively stop the drops with little motion blur. Figure 3 (1) illustrates the spray and radiation sheet intersection.

This technique provides the spatial resolution necessary to observe the change in drop size distribution with position in the spray. This variation with position is quite apparent from the data taken and analyzed in this paper. Other techniques such as shadowgraph photography suffer from a complete loss of spatial resolution since the photograph will have drops from all portions of the spray through the section studied. Thus all positional variations will be averaged out. A complete survey of one quadrant of the spray can be made by moving the nozzle by means of a three-dimensional movement.

Another advantage of this technique is the minimum number of out of focus drops on the photographs, since drops outside of the radiation sheet and thus outside of the camera's depth of field will not

*Numbers in parenthesis refer to bibliography at end of report.

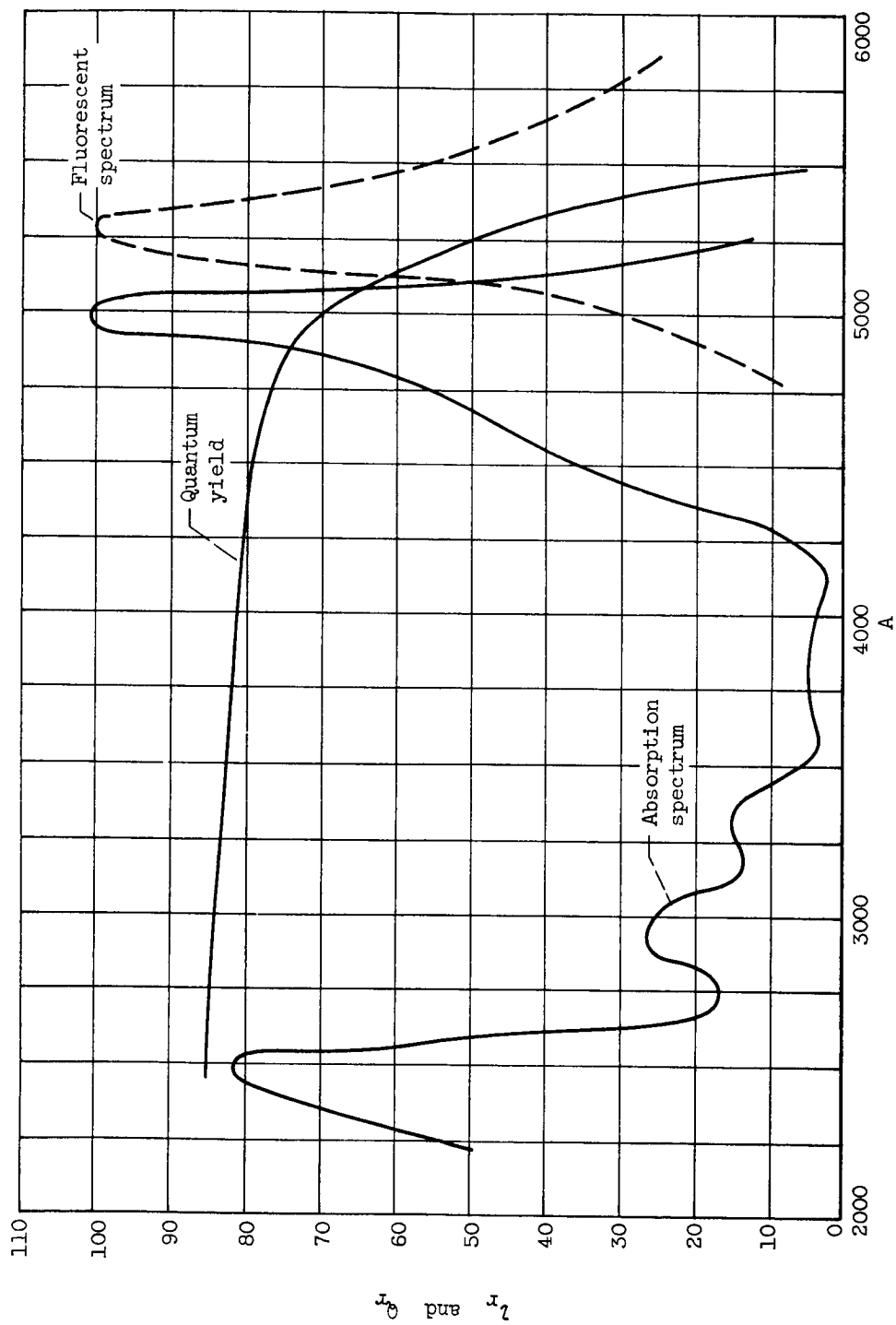


Figure 2. - Dilute aqueous-uranin solution characteristics.

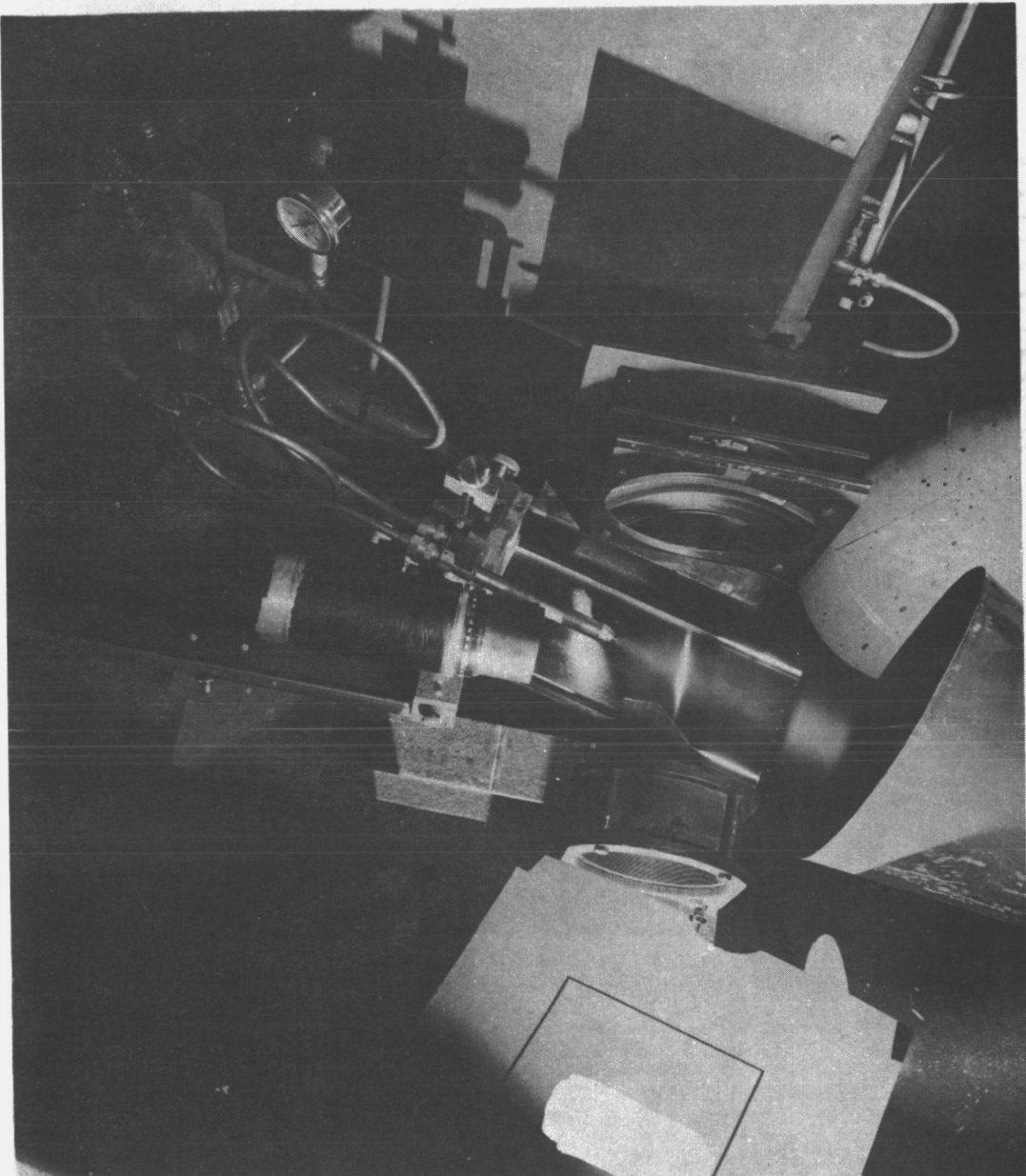


Figure 3. - Photograph of fluorescing spray in horizontal plane.

be recorded. In reality, however, there will be some drops on the edge of the light sheet, but these will be only partially irradiated and also less sharply defined. The resulting lower density image can then be eliminated during counting by proper density discrimination level setting.

The drop photographs are analyzed on a DuMont Iconumerators with an added sizing circuit. The Iconumerators is a flying spot scanning particle analyzer of high resolution. This counter and sizing circuit addition will be discussed in detail in the apparatus section.

The fluid flow system used is as follows. The fluid with the fluorescent dye in solution is kept in the fuel storage tank. The necessary pressure is applied to this tank by a high pressure nitrogen bottle through a pressure regulator valve. The fluid is thus forced through the rotameter and the pressure nozzle forming the spray cone in the test section. An exhaust fan then gathers the spray and removes it from the test area. The exhaust fan has a duct with a honeycombed array of flow straightening tubes which remove the swirling component of air velocity which would otherwise be present. This duct is also located far enough downstream from the spray so that the spray is gathered only after the majority of its kinetic energy has been expired. It is therefore a good assumption that this fan has a negligible effect on the spray formation at least for a considerable distance from the nozzle.

Precise flow measurements are determined by the change in weight of the storage tank during a run by means of the scale on which this tank rests.

Due to the low level of fluorescent radiation a very fast film and extensive development and intensification procedures must be used.

The essential components and procedures used in this technique will be discussed in more detail in later sections.

APPARATUS

The components of the system as originally assembled by G. M. Benson (1) showed that the technique was feasible and that data could be taken. Reference 1 gives a thorough literature survey on most of the components in the system and therefore will not be repeated here. Some of the components such as the camera were so excellent that no attempt was made to improve upon the equipment itself. Reference 1 outlines the elaborate testing program involving many expensive lens systems which proved to be inadequate for this technique. The operation of the camera was changed some, however, in an effort to minimize curvature of field effects.

The light source was completely changed and a new higher voltage DC power supply as well as trigger power supply was built.

The aperture stop configuration in the excitation optical system was modified to increase the sharpness of the radiation sheet, and the focusing and alignment procedure was improved.

The component parts of the apparatus will now be discussed with the modifications to each component included.

Excitation Optical System

The original excitation optical system was composed of two components: the condensing lens and a spherical mirror.

Condensing lens. - The condensing lens was a compound lens consisting of two plano-parabolic fused quartz lens elements of condenser quality ground by Bausch and Lomb to have a 6-inch focal length and a 1.2 f-number. These lenses were placed with their plane sides together and a vertical rectangular aperture stop placed between them. This configuration provided the axial spherical aberration necessary for the required axial image smear in the sampling volume (1).

During the focusing procedure in which the radiation sheet cross section was observed in a microscope, a large amount of radiation was found to be falling outside the well defined 200 micron source image. The presence of this undesirable radiation produced a radiation sheet with effective width greater than the camera's depth of field. Although this radiation was less intense than the image proper, there was a possibility that out of focus drops were being sufficiently irradiated to be recorded on the film.

When a piece of film was placed normal to the radiation sheet and the light source pulsed, the resulting photographs confirmed the presence of this stray radiation. To get a relative quantitative measure of the intensities in this band and radiation sheet proper, a vertical knife edge was moved in increments of 0.001 inch through the radiation sheet perpendicular to the sheet axis. An RCA 5581 gas phototube was placed on the radiation sheet axis so that when the knife edge was removed the entire radiation sheet fell on the cathode. A Millivac voltmeter was used to obtain relative intensity values for radiation reaching the phototube for each movement of the knife edge. A plot of voltage versus knife edge movement is shown in Figure 4.

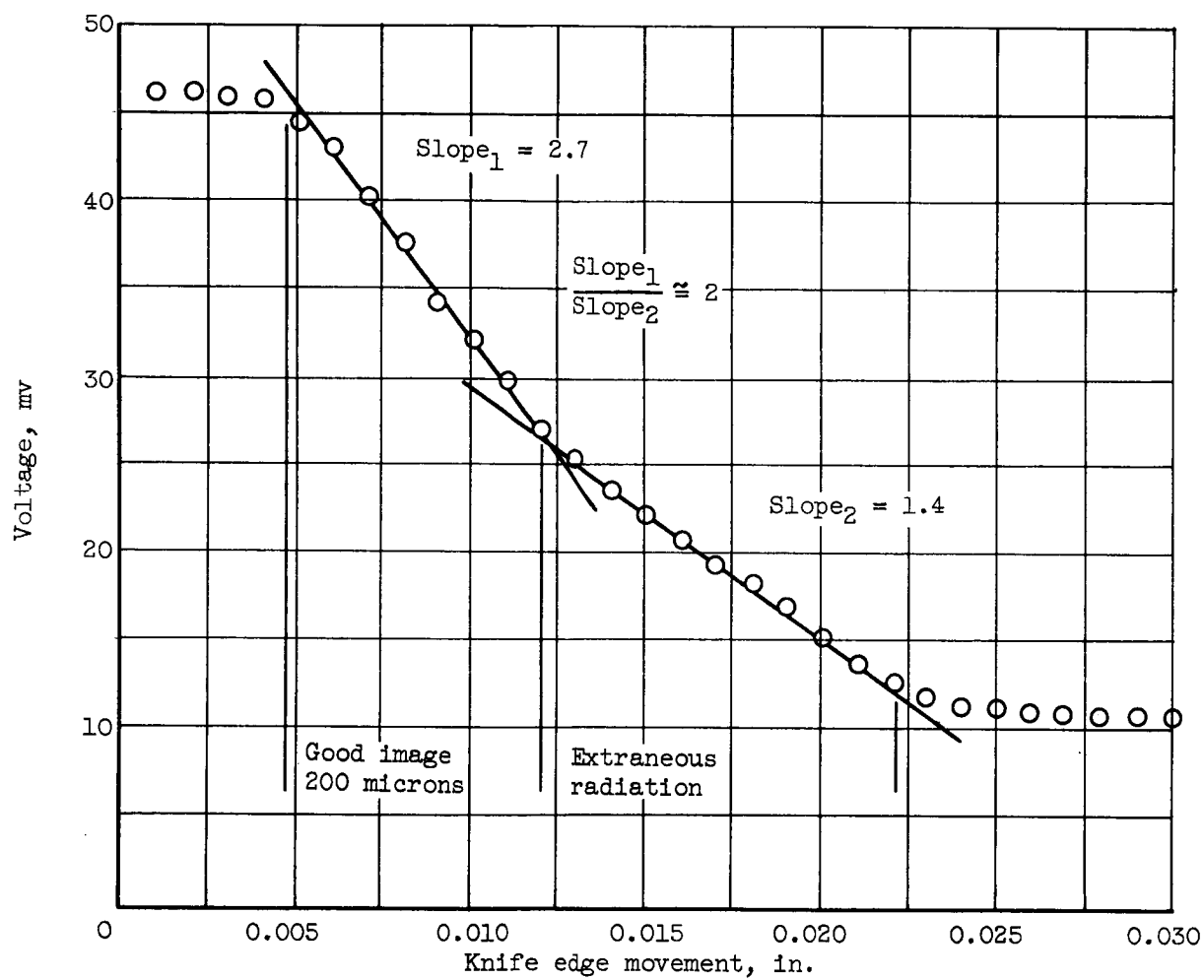


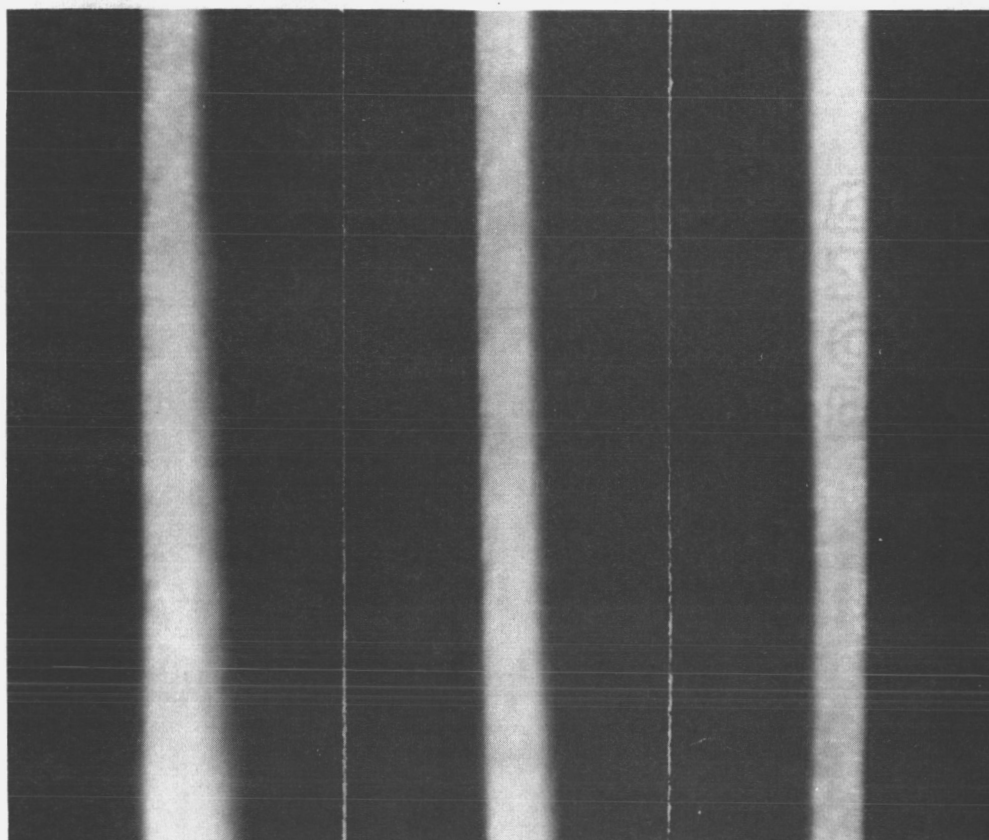
Figure 4. - Voltage versus knife edge movement for intensity measurement.

The slope of this curve at any point is a measure of the intensity at a given position in the radiation sheet cross section. As can be seen from Figure 4, the undesirable radiation is approximately one half the intensity of the radiation sheet proper.

A stop was then inserted in front of the condensing lens to increase the effective f-number. With the stop in various positions, the procedure for intensity determination outlined above was repeated until the intensity for the radiation sheet proper was approximately $1/2$ of its original value, i.e., equal to the original intensity of the undesirable band. Spray photographs were taken under usual conditions except for the stop on the condensing lens. Faint drop images appeared on the film indicating that this intensity level was sufficient to record out of focus drops during normal operations. In view of these results, efforts were made to eliminate the extraneous radiation.

The plano-parabolic condensing lenses were mounted on an optical bench. Lens stops of varying configurations were placed between the condensing lenses, and the corresponding radiation sheet cross sections were viewed in a microscope. Rotation of the lenses with respect to each other and with respect to the lens holder also affected the image quality. Photographs of the sheet cross section were taken through the microscope using a low-gamma film. Figure 5(a) shows the original cross section.

In order to quickly check the intensity magnitudes in the radiation sheet for the more promising lens-stop configurations, an automatic version of the moving knife edge method was used. A light



(a) Original 8mm
stop.

(b) Stop c of
Fig. 8.

(c) Stop d of
Fig. 8.

Figure 5. - Radiation sheet cross sections photographed
through microscope using different lens stops.

chopper consisting of a revolving knife edge driven at constant speed was placed to cut the radiation sheet cross section at known positions along the sheet axis. An RCA 929 vacuum phototube, cathode follower, and differentiating circuit continuously traced the intensity versus knife edge movement on an oscilloscope.

The clue to the final shape of the aperture was found in the following manner. As shown in Figure 6 an illuminated piece of frosted glass with a set of knife edges separated 0.8 mm. was used to simulate the light source. The condensor lens was positioned as usual except that instead of having a lens stop between the lenses only a small target for focusing lens 2 was inserted. Thus the condensor lens was wide open and all parts of it passed light. A second set of knife edges separated 0.2 mm. was placed at the position of the best image of the source. Lens 2 was inserted and with the aid of the target between the condensor lenses it was focused so that the plane of the condensor lenses was imaged upon the screen. The image on the screen now represents that portion of the condensor lens which contributes light to the 0.2 mm. light sheet while any portion not contributing will strike the knife edges and will not pass on to the screen. The image on the screen will then appear bright in areas where the condensor lens should be used and dark everywhere else. If a lens stop were then made with this shape it would block off all radiation that would otherwise fall outside of the desired radiation sheet. This configuration was very irregularly shaped and changed somewhat with rotation of one of the condensor lenses. Therefore, more conventional easily made shapes of lens stops resembling that of the screen image were

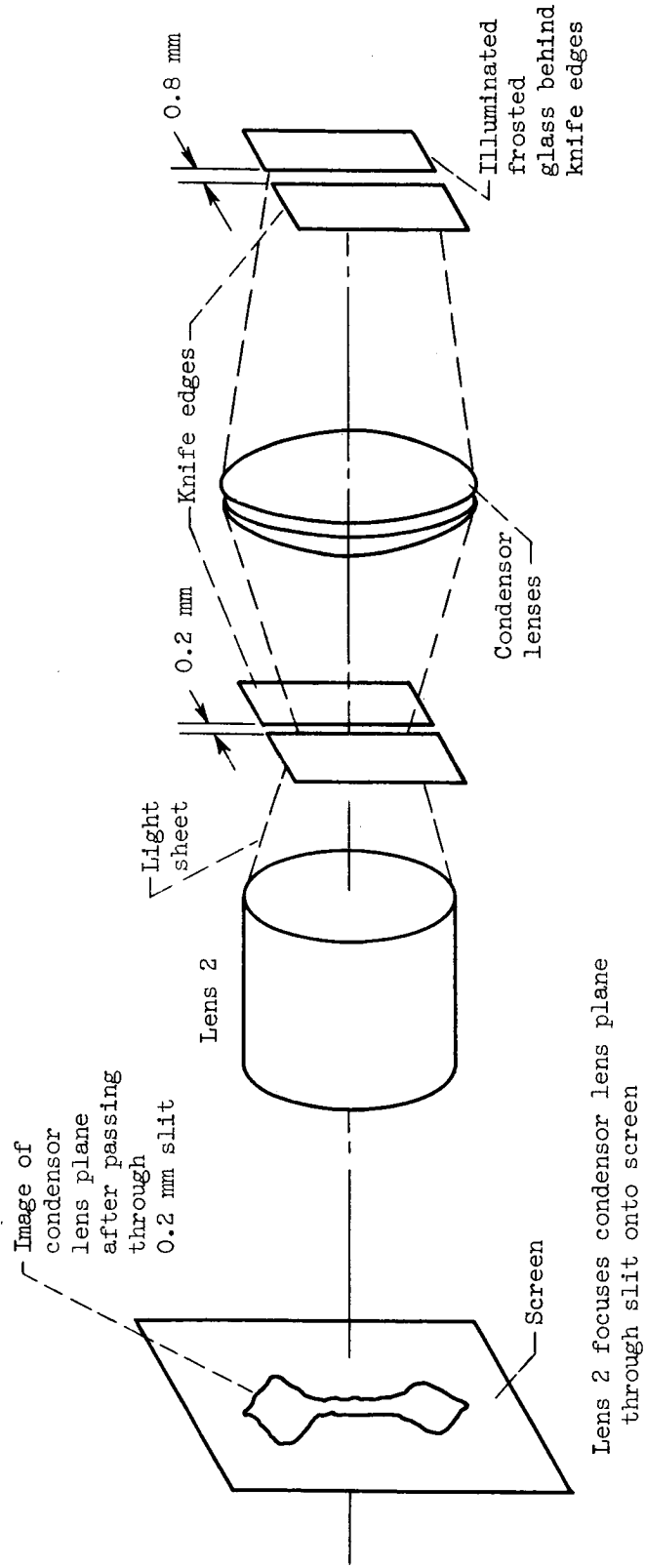


Figure 6. - Lens stop test setup.

made for trial. Figure 7 shows the screen image obtained.

Optimization of the radiation sheet quality requires that a compromise be made between the high intensity necessary for dense photographic images and sharp intensity cut-off at the edges necessary to prevent the recording of out of focus drops. Over thirty lens-stop shapes were tested. Figure 8 shows some of the more promising configurations. The use of stops 8(c) and (d) resulted in the greatest image quality. Figure 5(b) and (c) are corresponding photographs of the radiation sheet cross sections produced. The lens stop of Figure 8(d) produced the highest image quality consistent with intensity requirements. In this case the intensity was approximately 95% of the intensity in the original unsatisfactory image. The relative intensities were determined from the differentiated chopped phototube signal.

Spherical mirror. - This mirror is a first surface concave spherical mirror of condensor quality having an 8-inch-diameter and an 8-inch radius of curvature which was ground from a pyrex blank and surfaced with aluminum silicate (high reflectivity in a spectral range from 2400 to 5500 A) by Evaporated Metal Films Co., Ithica, New York (1).

The spherical mirror is placed opposite to the condensing lens with its center of curvature located on the condensor lens optical axis and at the point of best focus of the light source image. This will cause the light sheet to be returned upon itself. This can be seen to be true if one considers the following. A light ray passing through the center of curvature, whatever the direction so long as it

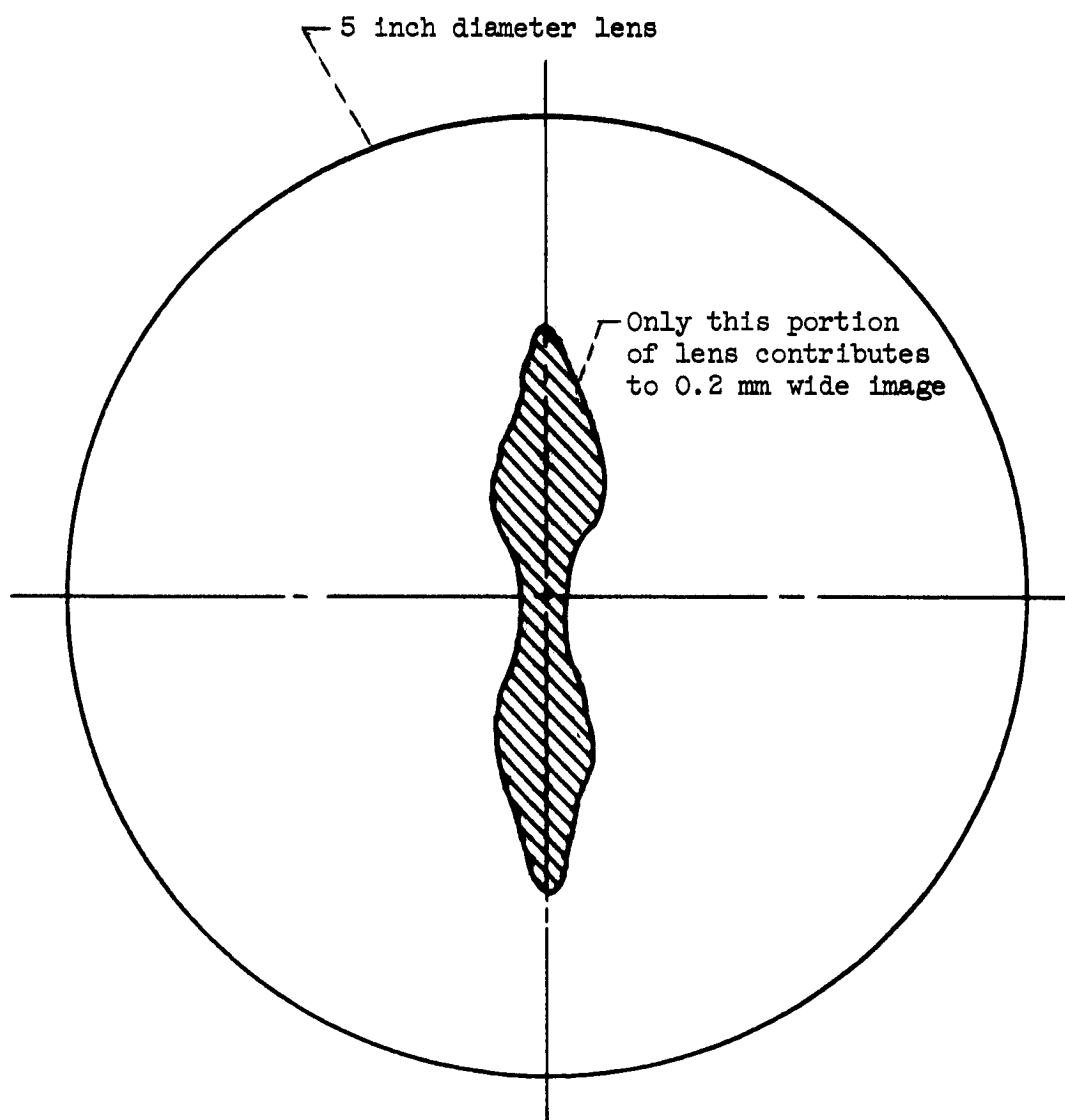
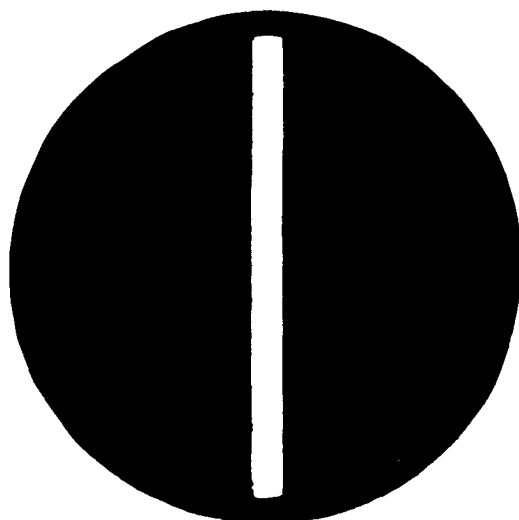
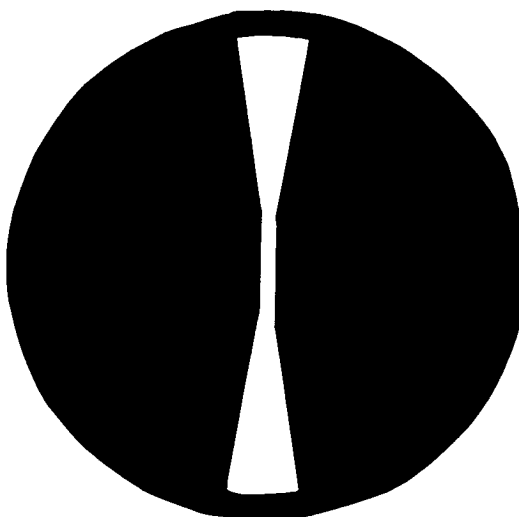


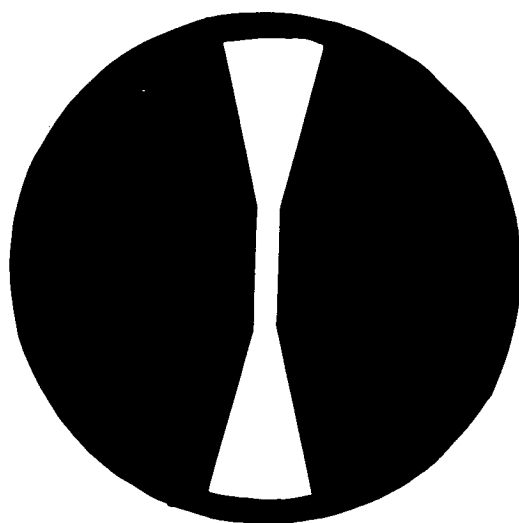
Figure 7. - Screen image of figure 6.



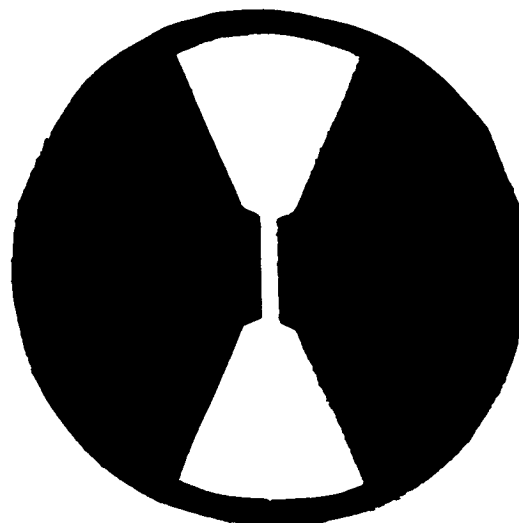
(a) 8mm.



(b) 4mm.



(c) 6mm.



(d) 4mm.

Figure 8. - Lens-stop configurations.

intercepts the mirror, will strike the mirror normally and will retrace its path back to the center of curvature. A ray which passes below the center of curvature and having an incident angle α will return above the center of curvature at an angle α also (α being measured between the ray and the line between the center of curvature and the point of incidence on the mirror which is of course the normal to the mirror at that point). This is true, of course, in the horizontal plane as well. Thus, the sample volume illumination is inverted, horizontally reversed, and axially reversed by the spherical mirror. The caustic envelope on the condensor lens side will be reproduced on the mirror side of the sample volume. This property of the mirror will tend to average out local variations in the illumination. All drops will be irradiated from both sides unless two drops happen to be diametrically opposite each other in the sample volume which is very unlikely. The mirror will not, however, balance out any intensity gradients which are symmetrical with the axis.

The quality of this mirror is apparent during the mirror focusing procedure when a small hole in the light source is back lighted, the image is transmitted through the condensor lens, and returned by the mirror and condensor lens with very little spread of the image back on the light source.

The excitation optical system and its position with respect to the spray and the camera can be seen in Figure 9.

Camera

The camera used in this system consists of a special Wollensak

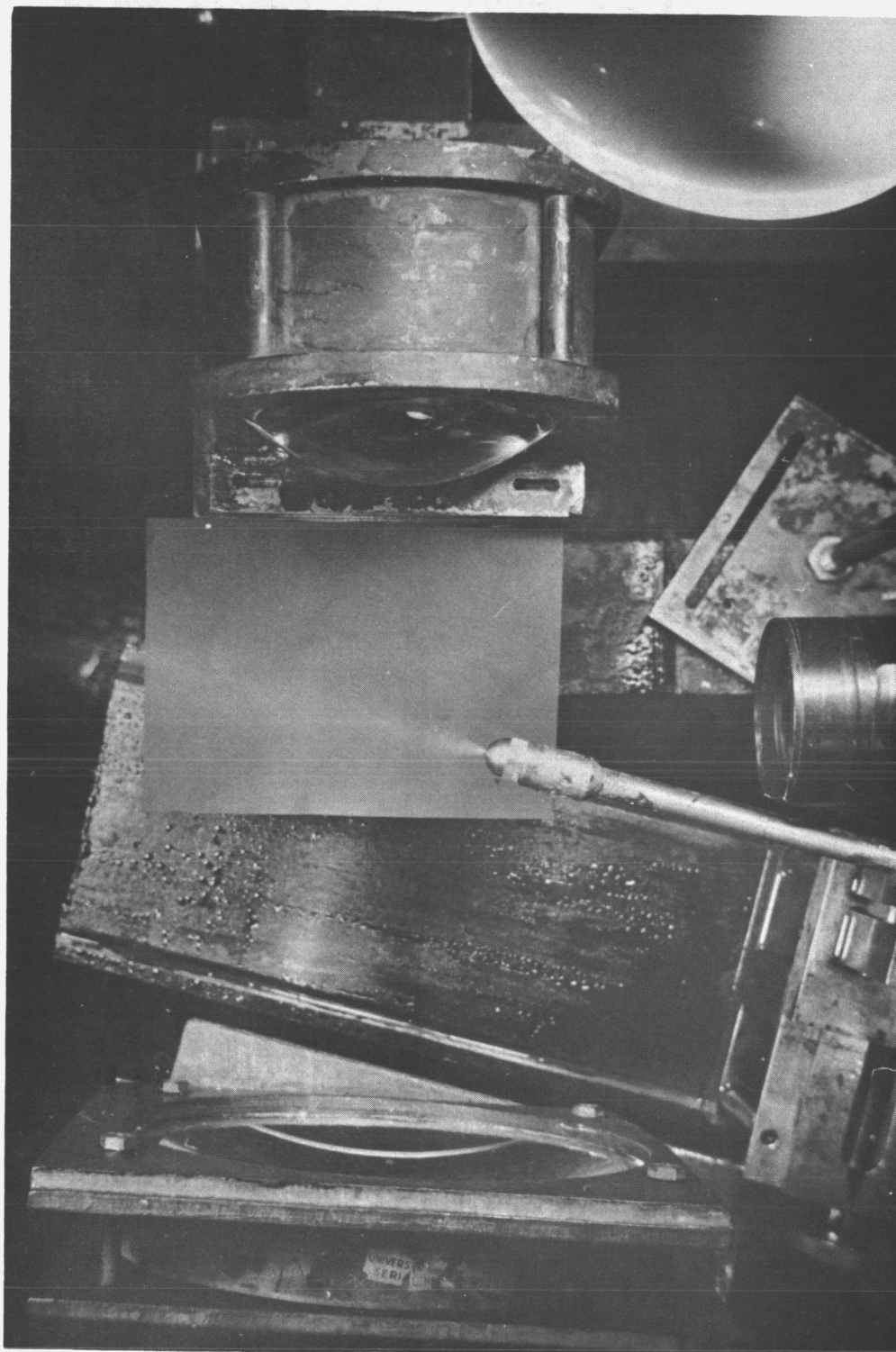


Figure 9. - Excitation optical system.

6-inch $f/3.5$ (T3.7) Raptar lens in iris diaphragm barrel as the objective lens, and a Carl Zeiss Jena 58-mm. $f/2.0$ Biotar lens as the secondary (re-imaging) lens of the system (1).

In order for the camera to work well in this technique it must be capable of resolving the small droplets found in high pressure sprays. There are seven basic aberrations, or image errors, which detract from the ability of a lens to form a perfect image. These aberrations require that photographic lenses consist of several elements if they are to produce high quality results. The seven basic aberrations are: spherical aberration, coma, astigmatism, field curvature, distortion, longitudinal chromatic aberration, and lateral chromatic aberration (3).

The Raptar lens is a symmetrical anastigmat. An anastigmat is a lens which has been corrected for astigmatism. It is symmetrical in that the part of the lens behind the diaphragm is a mirror image of the part ahead of the diaphragm. The lateral aberrations such as coma, distortion, and lateral color of each half of the lens will be of opposite sign and will then cancel each other (3). This is true at a one to one ratio of image to object distance and the canceling will decrease as this ratio changes from one.

In spite of this aberration correction in compound lenses, it is apparent from reference 1 that no single lens commercially available was sufficiently corrected to be of satisfactory quality for operation in this system. G. M. Benson therefore underwent an extensive trial and error testing procedure to find a pair of lenses to be used in a relay system which would effectively cancel each other's aberrations.

tions to a sufficient degree such that the final image was acceptable. Many expensive lenses were tested among them the Taylor-Hobson-Cooke f/1.5 and the Ross X-Press f/4.0. The lenses finally used were as described in paragraph one and produced an excellent image over the field angle used in this technique.

In addition to the limiting of resolution by the aberrations listed above there is another limit due to the wave nature of light. Even if the lens system were perfect, a point source would not appear as a point image but would instead appear as a small circle called the Airy disc. This is due to the diffraction patterns caused by any limiting diaphragms in the optical system. The size of the Airy disc is determined by the diameter of the first minimums in the diffraction pattern and is given by (3):

$$s = 1.22 \lambda \frac{f}{d}$$

For $\lambda = 5200 \text{ \AA}$ and $f/d = 5.6$, $s = 3.55 \text{ microns}$. Thus, a 10 micron drop would appear to be approximately 13.55 microns. The film will not, however, respond to this spread image all the way out to the zero illumination diameter on the gradient at the edge of the drop. The diameter of 13.55 microns is thus pessimistic and the actual image on the film will be closer to 10 microns than the above indicates if only diffraction limitations are considered.

The actual image spread will be a combination of the aberration effects, the diffraction effects, and the film processing used. The system must therefore be calibrated under identical conditions used when taking data.

The calibration technique can be summarized by the following (1). An annular reticle with concentric decreasing sized rings is placed in the various positions covering the field of view of the camera. This reticle is backlighted using a condensing lens and filter such that the radiation falling on the film is of similar intensity, duration and spectral characteristics as that from a fluorescent drop. The film is then processed using the same procedure as that for actual data. The apparent size versus actual size can be determined and plotted as in reference 1. It was determined that for the system used in this technique the indeterminacy of a 10 micron drop is approximately 10 percent with this percentage decreasing rapidly with increasing drop size.

Due to the low intensity of the fluorescent radiation from the irradiated drops, the camera must gather as much light as possible in order to provide a suitable density image on the film. The light gathering power of the camera is inversely proportional to the f-number and thus a low f-number is desirable from this standpoint. A low f-number, however, increases the effects the lens aberrations due to the transmission of the more oblique rays striking the spherical surface of the lens further off axis. Thus a compromise must be made to balance the need for high light gathering power and low distortion. The camera used in this system is operated at $f/5.6$ to obtain this balance.

A long working distance, which is the distance from the front of the lens mount to the object plane, is required of the camera used in this system. This is necessary so that the camera can be maintained

at a considerable distance from the spray so as not to interfere with the production of the spray. Another consideration is that the spray should not fall upon the lens elements and thus further degrade the image quality.

Other techniques have been devised in which a camera of short working distance has been placed directly in the spray but this would fail on both of the above mentioned accounts. The camera would undoubtedly interfere with the intrained air flow in the spray even if the ambient gas velocity were zero and much more so if an ambient velocity were superimposed. Also a complicated shutter system must be employed to leave the lens elements exposed to the spray for a minimum duration during the time of the exposure.

For these reasons a long working distance and thus long focal length objective lens were required in the original selection of lenses for this system.

Camera curvature of field. - During the procedure of alignment and focusing, a considerable curvature of field was found to be present when the camera was operated at 20X as originally intended. The depth of field and curvature were determined by placing a reticle at a 45° angle of the axis of the camera. The reticle was placed in various positions in the field of view of the camera with a known portion of the reticle in the radiation sheet. The reticle was then photographed and the lines on the reticle which were in focus determined. The curvature can then be determined by the shift between those lines in the light sheet and those in focus.

The resolution of the reticle is quite demanding upon the camera. The reticle consists of lines 10 microns apart, and each line is about 2 microns in thickness. Thus when placed at 45° to the camera axis the reticle appeared as about 6 micron transparent spaces separated by 1.5 micron opaque lines.

The curvature of field as first measured was not acceptable over the 5 millimeter field of view. A procedure was therefore followed in which the operation of the two lenses in the relay system were changed slightly in an effort to decrease this curvature. The curvature with each change was noted visually with a microscope. It was found that at 25X the curvature was minimized. The camera was then operated at this condition for the remainder of the tests and for the taking of the data. For a constant usable film size of 4×4 inches the above condition reduced the field of view from 5×5 mm. to 4×4 mm. This was probably the major cause for the curvature reduction. This increase in magnification decreases the illumination on the film somewhat, but with an increase in the brightness of the light source this was compensated for adequately.

Figure 10 shows the curvature as measured from the photographs at 25X. It is noted that a 4 mm. field can just be obtained with proper focusing and alignment. It must be remembered that the resolution requirement used in obtaining Figure 10 was more stringent than that for a 10 micron drop which is the minimum size measured. In addition a narrow segment of each film is masked by the film holder during counting so that the film is not used to the extremity of the field of view.

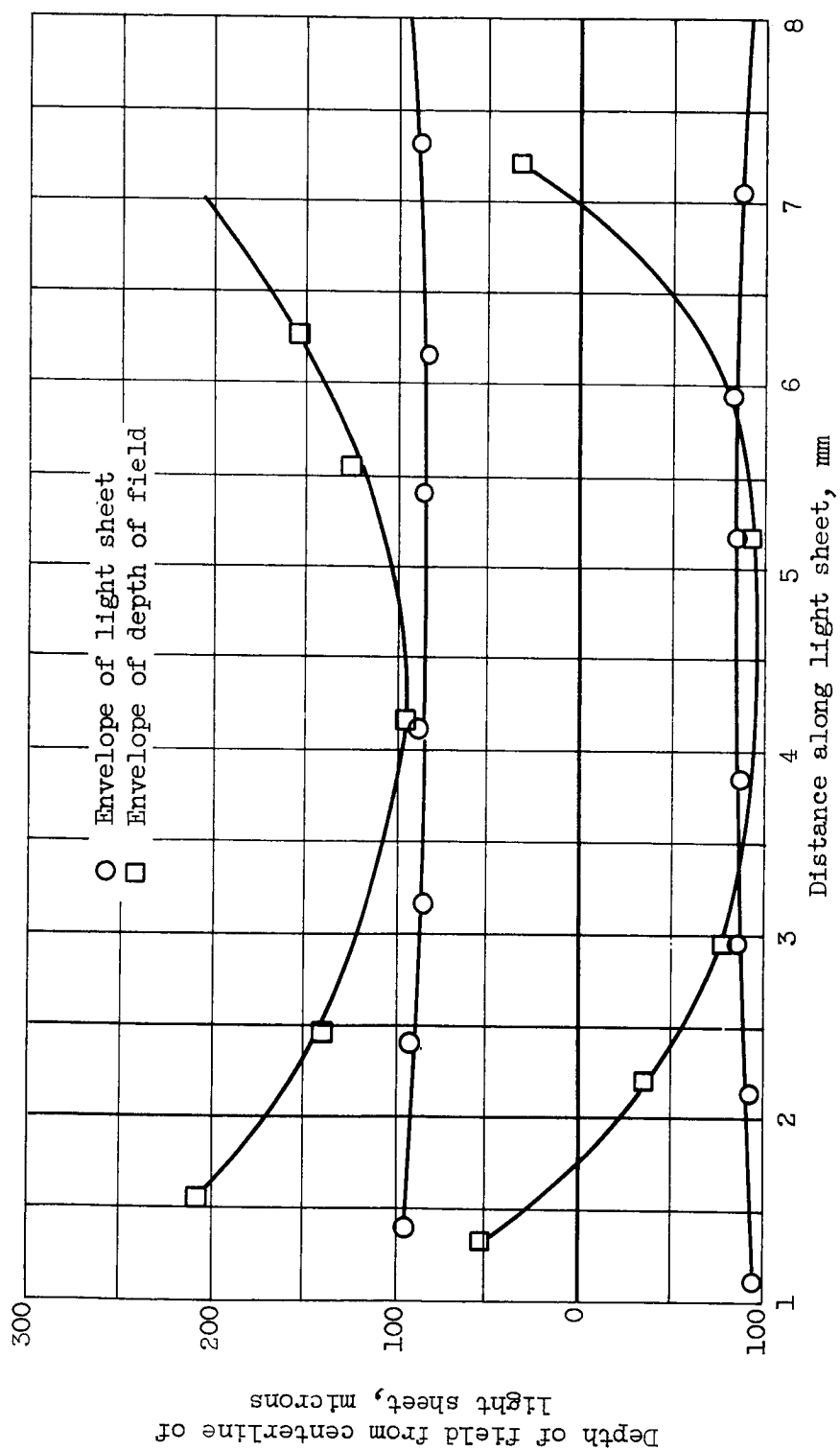


Figure 10. - Camera curvature of field.

It should be noted that in Figure 10 the abscissa is 100 times the scale of the ordinate and thus the curvature is exaggerated 100 times.

Light Source

General requirements. - The requirement of a light source for use in this technique are as follows:

(1) The light source must be a line source. This requirement stems from the fact that a very thin but long source is required for the production of the light sheet in the sample volume. The size of the light sheet is fixed by the depth of field and field of view of the camera. It is recalled that the sheet must be over 4 mm. high and have a thickness of 0.2 mm. for at least 4 mm. of sheet length. There is some latitude in the operation of the condensor lens to match this sheet size with the source size, but this latitude is quite small. For instance, if too long a source were used then the minification of the condensor lens must be increased. This will, however, increase the convergence of the light rays into the sample volume and reduce the length of sheet that has a 0.2 mm. thickness. This would also move the condensor lens closer to the spray and increase the chances of lens wetting by the spray. If the source were too short then the knife edges in front of the source would have to be moved closer to preserve the height to width ratio of at least twenty thus possibly removing a good share of the available radiating area of the source. The ideal size of the source height should be somewhat over 16 mm. and the width somewhat over 0.8 mm.

(2) The light source must be of high intensity in the spectral range where the fluorescent dye has high absorptivity. Figure 2 shows this to be in the region of 2500 Å and 5000 Å for fluorescein which was used for this study. Since the fluorescent radiation is very weak the higher the source brightness in these spectral regions the better. G. M. Benson (1) estimates the degree of saturation of the fluorescence to be less than 10^{-3} percent for aqueous uranium so too much brightness could never be attained.

(3) The light source must be of very low time duration so that fast moving droplets can be effectively stopped. A submicrosecond light source would be beneficial, but unfortunately ultrashort durations go with ultralow intensities. This can be seen in that for low durations low values of inductance and capacitance must be used. With low inductance goes small size and in turn low capacitance and low voltage. Thus the energy storage of the capacitor is reduced since $E = \frac{1}{2} CV^2$.

(4) The light source should be reliable and easily maintained. The intensity and duration of the source cannot vary from flash to flash if reliable data are to be taken. With the large volume of data necessary for spray studies it is desirable that the source be capable of providing many flashes, and when replacement is necessary it must be easily accomplished so that extended interruptions in data collection is not necessary.

Former light source. - The light source as assembled by G. M. Benson (1) for the initial development of this technique con-

sisted of a General Electric BH-6 lamp in series with an air gap trigger using a 0.15 ufd. capacitor bank.

The General Electric BH-6 is a quartz enveloped capillary tube. It is filled with 1/15 atmosphere of argon and has mercury pools surrounding a tungsten electrode at each end. The light emitting portion of the tube is approximately 25 mm. in length.

The BH-6 is ideal for this technique as far as its shape is concerned. The central portion of the tube was utilized by placing a pair of knife edges separated by 0.8 mm. in front of the BH-6.

General Electric does not recommend that the BH-6 be pulsed, and that it should be used steady state in a horizontal position. No data is therefore given for pulsed service. However, for steady state operation at 25, 50, and 100 atmospheres Hg. pressure the spectral brightness is given in Reference 1. It was observed from these curves that only at $p = 25$ atmospheres was there an appreciable amount of radiation which is useful to excite the fluorescence of fluorescein. The minimum brightness at all three pressures occurs in the neighborhood of 5000 Å. At $p = 25$ atmospheres there is appreciable radiation at 2500 Å. This ultra-violet band disappears at the higher pressures. This is due to the mean free path of the electrons decreasing at higher pressures and thus being unable to attain the energy necessary to excite the higher energy ultra-violet radiation levels.

It would thus appear that a more efficient source could be obtained to place more radiant energy in the 2500 and 5000 Å region.

G. M. Benson (1) reported half peak duration of the BH-6 with 0.15 ufd. to be 5 microseconds. The author confirmed this if all radiation were measured but if only the green and ultraviolet are considered the duration is 1.6 and 1.8 microseconds, respectively.

The BH-6 was loaded to its maximum for use in this technique. Frequent shattering of the quartz envelopes occurred. Even when actual rupture did not occur there was always a build-up of a contaminant on the inner surface of the capillary tube. This might occur on the first flash or the 15th flash, thus the only reliable way to use this tube was to inspect it after each flash. The contaminant could often be removed by running the tube in its recommended horizontal position and steady state with air cooling for about 5 minutes. Often this did not help due to a permanent etching of the quartz in the capillary.

It can be seen that the BH-6 when pulsed at these necessary high loadings does not provide a reliable and easily maintained source. A great amount of time must be spent cleaning the tubes as above, and considerable expense is involved in keeping a sufficient supply of tubes on hand for any extensive data production.

Due to the above-mentioned disadvantages of the BH-6 it was considered advisable to search for a better light source.

Tests of light sources. - The purpose of these tests was to determine the characteristics of various light sources as they would apply to the requirements of this technique. The important characteristics are the intensity and duration of the flash in the spectral region of the fluorescent absorption peaks. Thus the light sources were

tested for their characteristics in the ultra-violet and green spectral regions. It was also of interest to see how far the light sources could be pushed as far as their energy loading was concerned. From these tests the direction for design of a better light source was hoped for.

Light sources tested. - The following four light sources were tested:

(1) General Electric BH-6. It was known that this light source would function in this technique since it was the source used up to this time, but its characteristics were desired in relation to the other light sources. The tests of the other sources could then be compared to the BH-6 to see if an improvement could be obtained. The description of the BH-6 has already been given in the Former Light Source discussion and will not be repeated here.

(2) E. G. and G., FX-3. This is a large quartz flash tube filled with 4.5 cm. Hg of Xenon and 1.5 cm. Hg of hydrogen. It is composed of two concentric tubes the center one of course containing the radiating capillary. The overall length is $8\frac{1}{16}$ inches and the O. D. is $13/16$ inch. The inner radiating capillary is 1 mm. I. D. and has a length of $3\frac{5}{8}$ inches. At each end of the capillary there is a tungsten electrode and lead-in wire. Around the outside of the tube a spiral trigger wire is wound.

(3) E. G. and G., FX-12. The FX-12 has only one quartz envelope and differs in size from the FX-3. The overall length is $2\frac{5}{8}$ inches and the O. D. is $9/32$. The radiating capillary has a length of $1/4$ inch and an I. D. of 1 mm. Tungsten electrodes are again used at each

end of the capillary.

The FX-12 is more similar in construction to the BH-6 than is the FX-3. With a shortening of the electrodes thus resulting in a longer capillary, the FX-12 could replace the BH-6 without any modification of the system. Such a tube could be obtained on special order.

Both the FX-3 and FX-12 are manufactured by Edgerton, Germeshausen and Grier, Inc., Boston, Massachusetts.

(4) Guided air spark. A guided air spark was investigated in the hope that a more refined model of this prototype could be used in this system. There are mechanical advantages of such an air spark. Almost unlimited energies could be put into the spark channel without fear of the light source shattering if the proper materials are used and escape of the high pressure gas is provided. The three above mentioned tubes will shatter their quartz envelopes if their small maximum loading were exceeded. Even if the air spark does not provide the radiant efficiency of xenon or mercury, this could more than be compensated for by the extremely high energy loading which could be used. This is certainly possible since power consumption and portability are not even considered in this technique.

The spark must be guided to provide a uniform line light source that does not wander about in space as an ordinary air spark would. Mechanical guiding was used due to its simple, straightforward approach over that of magnetic guiding. It was felt that with the immense currents involved in the spark and thus the large magnetic fields, it would be difficult to provide positive guiding with a magnetic technique.

A simple guided spark gap was constructed of teflon. This contained a 1 inch long, $1/8$ inch deep, and $1/32$ inch wide slot milled in the teflon block. Brass electrodes with rounded and polished ends were used. A third trigger electrode with a pointed end was inserted into the side of the block so that the trigger and ground electrode were visible to each other, but the trigger and high voltage electrodes had no easy path between them.

Test procedure and equipment. - Figure 11 shows the circuit used for the measurement of the intensity and duration of the flash. The right half of this figure is devoted to the measurement of the visible spectrum near 5000 A. A cathode follower output was used to minimize high frequency losses in the output lines.

In order to study this portion of the visible spectrum an RCA 929 vacuum phototube with an S-4 surface and a Kodak Wratten 75 filter were used. The response of the S-4 surface with and without the filter are shown in Figure 12. It can be seen that a very narrow spectral region centered near 4900 A is thus obtained.

The left half of Figure 11 is used to give an indication of the ultra-violet output of the flash tubes. This is identical to the visible measuring circuit except for the phototube and filter. Here an RCA 935 vacuum phototube with an S-5 surface, an ultra-violet lamp filter, and a 0.6 neutral density filter were used. The S-5 surface responds well into the ultra-violet below 2500 A. The exact response of the ultra-violet lamp filter was not precisely known, however, and these measurements were used only as a rough analysis of the ultra-

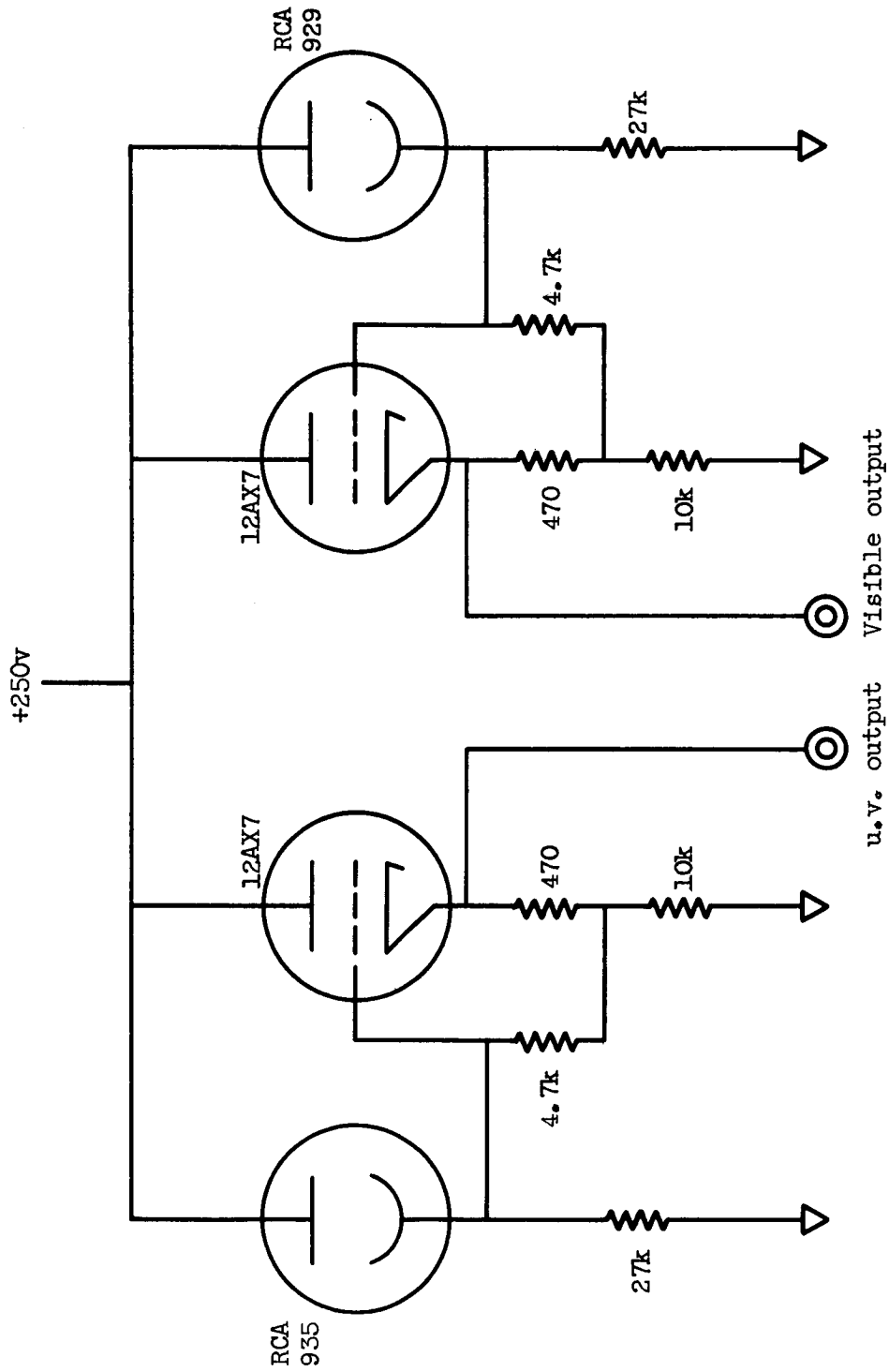


Figure 11. - Spark intensity and time measurement circuit.

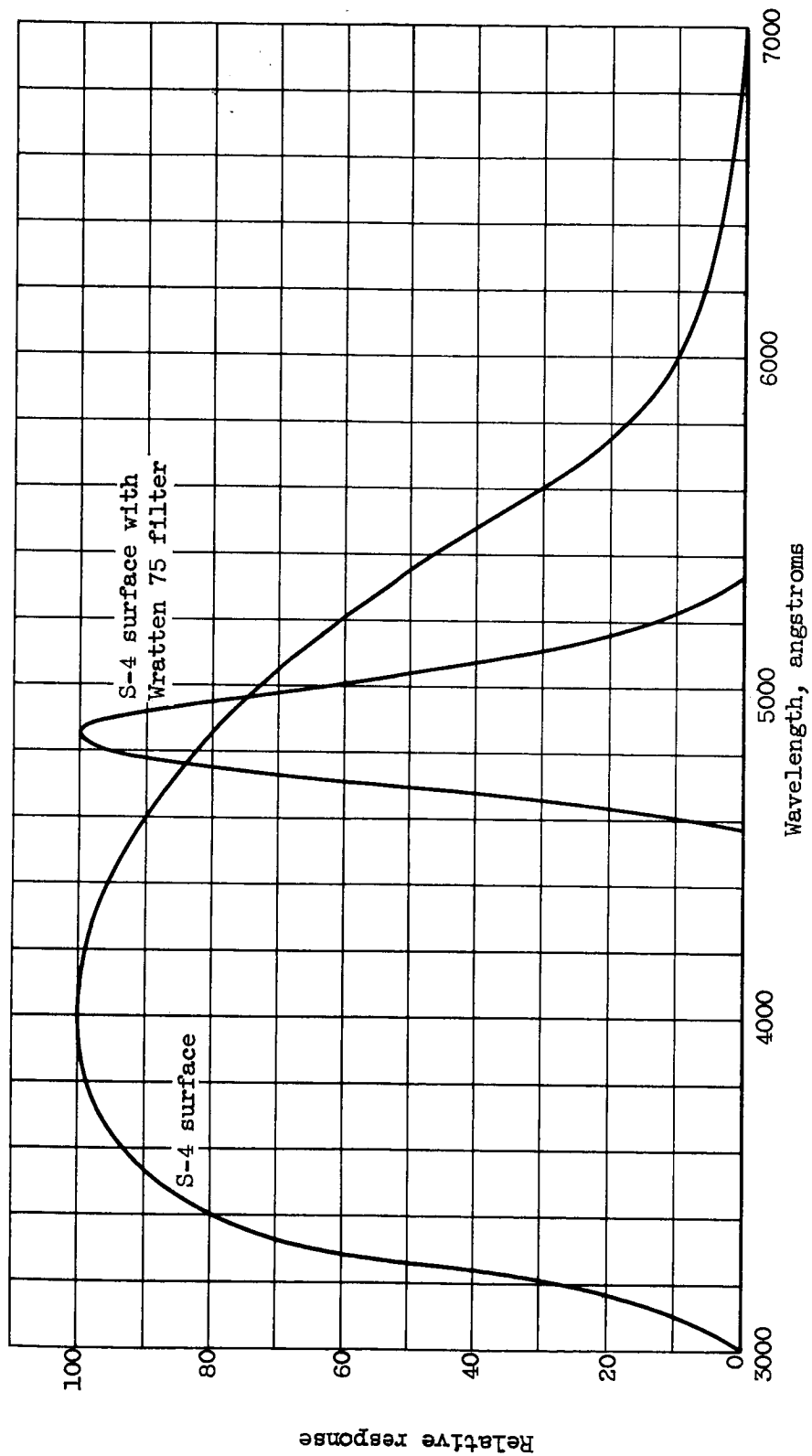


Figure 12. - Response of S-4 surface with Wratten 75 filter.

violet radiation. The circuit of Figure 11 was mounted on a chassis with a meter stick rigidly fastened to this chassis. The light source under test was always placed at the end of this meter stick to insure that the distance from the light source to the phototubes as well as the solid angle as seen by the phototubes remained constant for each test.

As originally designed, the circuit also contained an amplifier so that the phototubes could be used at their low rated maximum currents and still provide a reasonable amplitude output to the oscilloscope. This worked fine during the initial testing with a light chopper, but it was a different matter when used in an actual test with a light source. Due to the immense size of the electric fields used and their rapid change during the spark discharge, a large induced noise resulted at the cathode follower output. It was hard to determine the light output signal from this noise. Exhaustive shielding attempts were made with large grounding cables used. This was to no avail, however, and the use of the amplifier had to be abandoned.

The phototubes were thus of necessity operated far beyond their rated maximum current. The reader will no doubt consider these tests to be affected by phototube space charge effects and saturation. This was considered a possibility and thus the following tests were conducted.

The radiant flux from a light source decreases in proportion to the inverse of the radius squared. Thus a test was conducted such that the distance from the light source to the phototube was varied for several flashes of each light source. The phototube output

voltage was measured for each distance and over the entire range of voltages used for the following tests. A plot of output voltage versus $1/r^2$ was made. Except for some experimental scatter, all of this data fell along a straight line. It can be then concluded that even with substantial overload the phototube output was linear with light input.

Each light source was then tested using the above apparatus. The capacitance was varied from 0.06 to 0.15 ufd. in 0.03 ufd. steps, and the voltage varied from 6 to 8.6 KV for the BH-6, FX-3, and FX-12. A constant capacitance of 0.2 ufd. and varying voltage from 15 to 25 KV was used with the guided air spark.

The phototube output was measured and recorded using a Tektronic 555 oscilloscope with a Polaroid camera attachment. A typical recording is shown in Figure 13. The vertical scale is 20 v/cm and the time scale is 0.5 microseconds per cm. The upper trace in each case is the visible and the lower trace the ultra-violet output. The capacitance was 0.2 ufd. and the voltage 19.5, 20, and 22 KV, respectively.

Test results. - The results of the light source tests are seen in Figures 14, 15, and 16. These curves show the results for only the 5000 A spectral region. The trends for the ultra-violet radiation are very similar, and the slight difference doesn't warrant a repeat of these curves. Any differences will be mentioned in the text.

Figure 14 shows the peak voltage as read from the polaroid traces versus the capacitor charging voltage. It can be seen that the slope of a line if drawn through the data points of each light source would

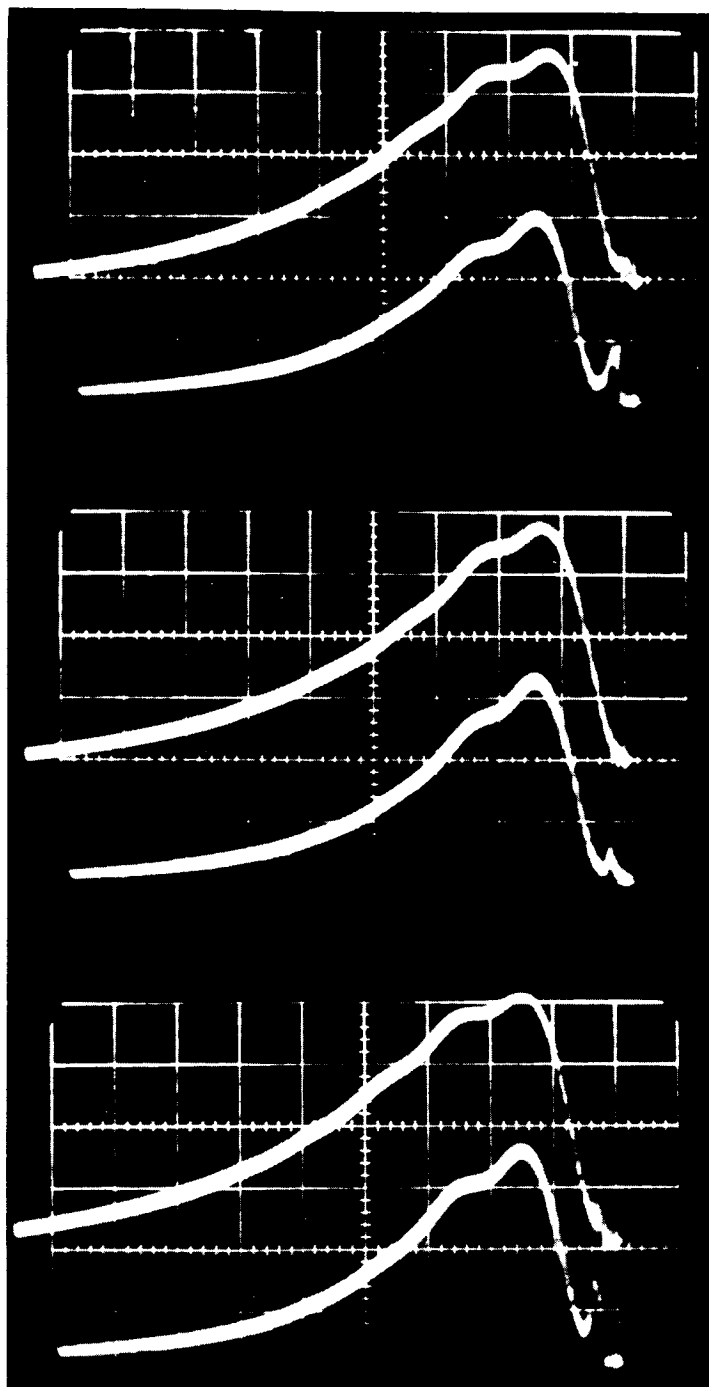


Figure 13. - Intensity versus time recordings of guided spark discharge (0.5μ sec/cm).

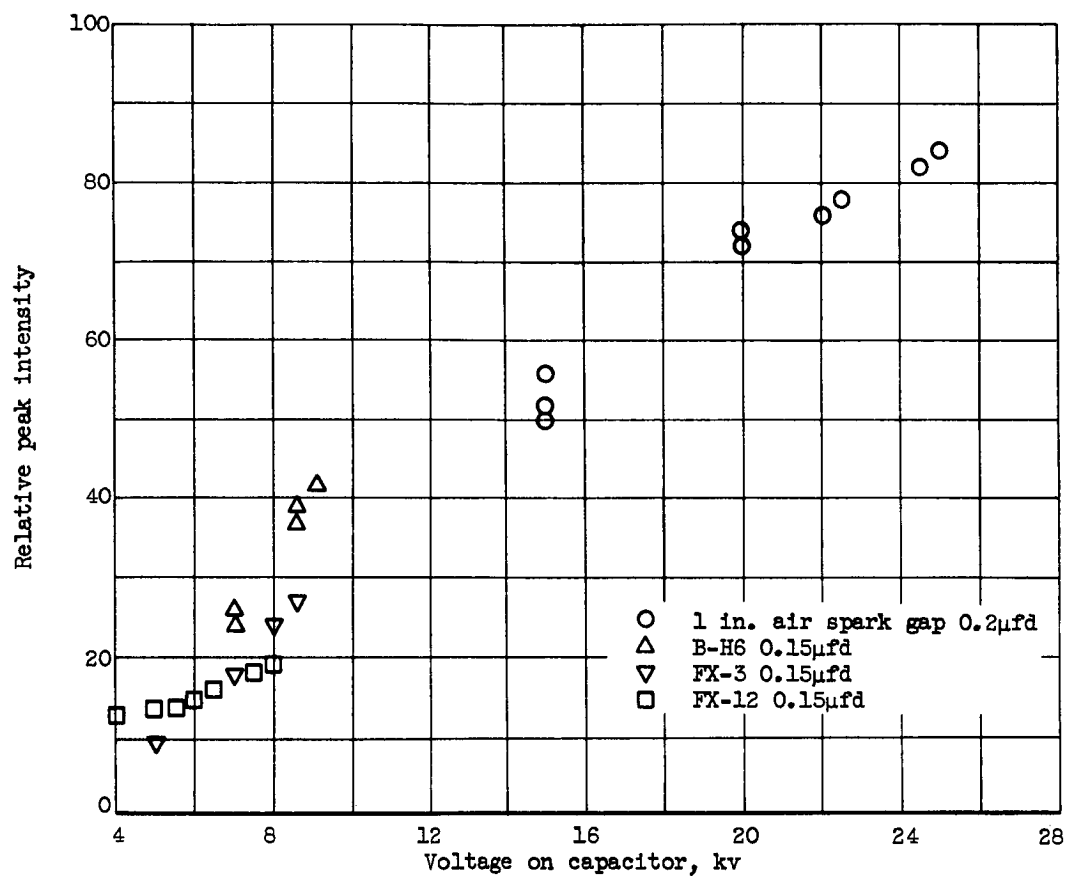


Figure 14. - Relative peak intensity versus capacitor voltage for various light sources as measured by a 929 vacuum phototube with Wratten #75 filter.

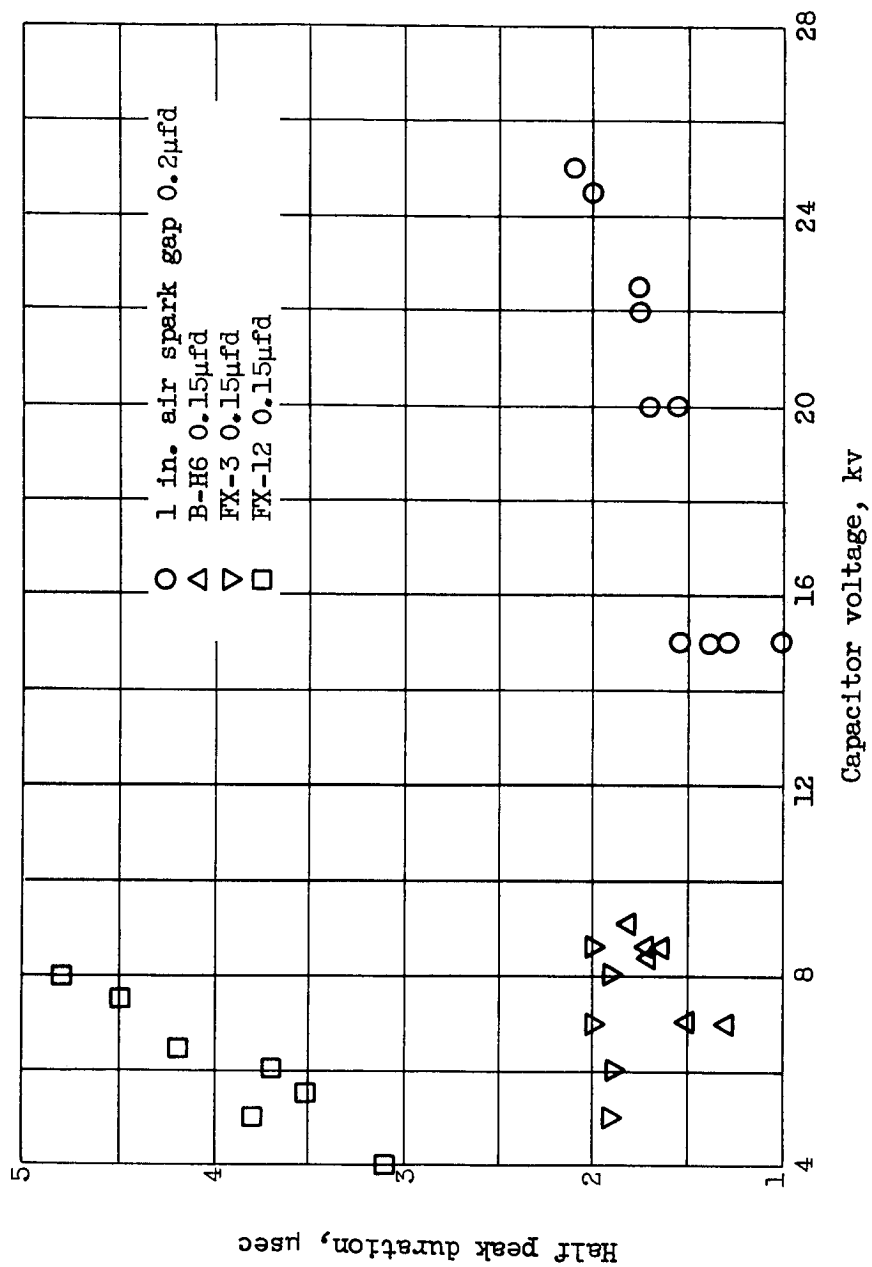


Figure 15. - Half peak duration versus capacitor voltage for various light sources as measured by a 929 vacuum phototube with Wratten #75 filter.

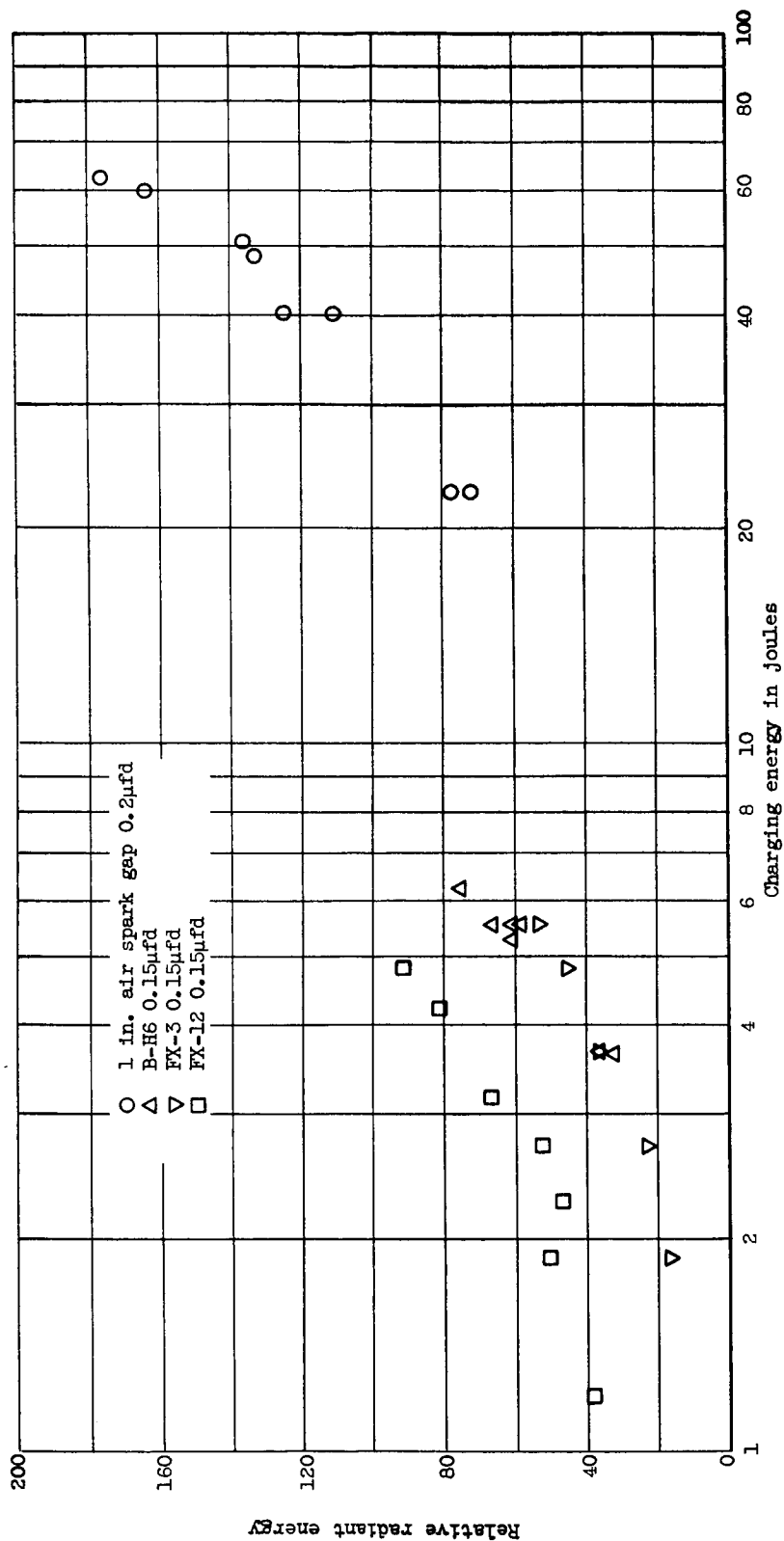


Figure 16. - Relative radiant energy versus capacitor charging energy for various light sources as measured by a 929 vacuum phototube with Wratten #75 filter.

vary considerably. The increase in radiant energy with voltage for the BH-6 is substantially higher than that of any of the other three light sources. The FX-12 produces very little additional radiation with additional voltage. Apparently this tube is saturated and has reached its maximum blackbody temperature at least for the 5000 Å radiation. The maximum temperature exists for every gas and will be discussed in more detail in the section on considerations for improved light sources.

In interpreting these results the difference in the tube dimensions must be recalled. The FX-12 had only a 1/4-inch length of radiating capillary. Thus a high energy concentration resulted in this tube. If this were increased to 1 inch as ultimately required the tube would not saturate at quite so low a loading. The converse is true for the FX-3. If the capillary were only 1 inch long it might saturate also or at least approach saturation.

Figure 14 also shows that the guided air spark can produce a much larger peak intensity than any of the other light sources. This is at the expense of a considerably higher voltage, but as mentioned previously, this voltage disadvantage is of no consequence in this work.

Unfortunately, the voltage on the BH-6, FX-3, and FX-12 cannot be increased much above the 9 KV used or the tubes will shatter. Many BH-6 tubes have shattered at 8 KV. Only one each of the FX-3 and FX-12 were on hand for testing so they were not pushed to their absolute maximum voltage.

Figure 15 shows the half peak duration (time between 1/2 peak

intensity on the rising portion and the falling portion of the time intensity trace) for various capacitor voltages for each light source. Again the FX-12 appears saturated. The current through the tube can increase very little, and thus the increasing energy in the capacitor must be consumed over an increasing period of time. The duration of from 3 to 5 microseconds is getting prohibitively long for use in this technique. The time-intensity curves for the FX-12 are unusually broad and flat-topped with a considerable afterglow.

The FX-3 is seen to have virtually a constant duration of 2 microseconds and apparently has not reached its maximum temperature at this loading.

The BH-6 and the guided air spark are seen to have about the same duration but do increase slightly with voltage. Apparently, these are both approaching their maximum temperature in the 5000 A region. Both have a range of from 1 to 2 microseconds.

If the duration of the BH-6 is measured without the Wratten 75 filter its duration is 5 microseconds for a voltage of 8 KV and a capacitance of 0.15 ufd. Thus it is important to know what spectral range will be of use before a duration can be specified. This can be expected from a gas discharge since the radiation from the various species in the gas reach their peaks at different times during the discharge (4). This is due to the different temperatures during the course of the discharge. Reference 4 gives an example for air at atmospheric pressure. In the earliest stages of the discharge the lines of the doubly ionized atoms prevail, later the continuous background reaches a peak, next the singly ionized atom, and finally the

arc spectrum (neutral atoms).

With the use of a smaller capacitance the duration of the guided spark could be reduced further if the inductance were not substantially increased.

Figure 16 shows the variation of relative radiant energy (as measured by peak voltage times $1/2$ peak duration) with energy input stored in the capacitor.

It can be seen that the guided spark source is indeed very promising. The light output is well over double that of the other light sources in the 5000 Å region. The FX-3 and the BH-6 have substantially the same output for the same input energy. It must be remembered, however, that due to its size the full length of the FX-3 could not be used. If the capillary of the FX-3 were reduced in length its operation would be closer to that of the FX-12.

The FX-12 is seen to have a higher light output than the BH-6 or FX-3 but only at the expense of substantial increase in its duration as previously discussed.

The only difference between the above discussion for the 5000 Å radiation and that for the ultra-violet radiation is that the intensity increases a little less and the duration increases a little more rapidly with loading.

On the basis of the above tests it was decided that a guided air spark would certainly provide an improvement over that of the BH-6. Increased intensity could be obtained while maintaining a duration of about 1.5 microseconds. The xenon flash tubes did not indicate they would provide improved intensity and furthermore the increased dura-

tion of the flash would be detrimental. A working model of the prototype guided spark source tested here was constructed which would satisfy all of the requirements of a light source for this technique as set forth previously. The next section will describe this new light source in greater detail.

Present light source. - In consideration of the previous tests it was decided to build a guided spark light source similar to that tested but with higher energy and a shorter duration.

Several capacitor manufacturers were consulted for information on the type of capacitor needed for this type of duty. The required capacitor must be a high voltage low inductance type of about 0.1 ufd. A larger capacitance would increase the energy but would also increase the flash duration. Thus the direction to go for higher energy is to use a higher voltage. Of the manufacturers consulted, only Cornell-Dubilier was able to provide this type of capacitor.

The capacitor selected was the Cornell-Dubilier NRG-341. This is a cylindrical shaped capacitor of $15\frac{1}{2}$ inches diameter and $11\frac{5}{8}$ inches long. It is rated at 40 KV peak D. C., 0.1 ufd., 80 watt-seconds, and has a self inductance of 0.010 microhenries. This capacitor can be seen in Figure 19.

With the voltage determined the next consideration is the length of the spark gap which can withstand the 40 KV without breakdown. Figure 17 gives the breakdown voltage (V) versus pressure times gap length (Pδ) for atmospheric pressure. Although these curves are for atmospheric pressure they are very general in that for lower pressures the curves will depart slightly from these curves only for high

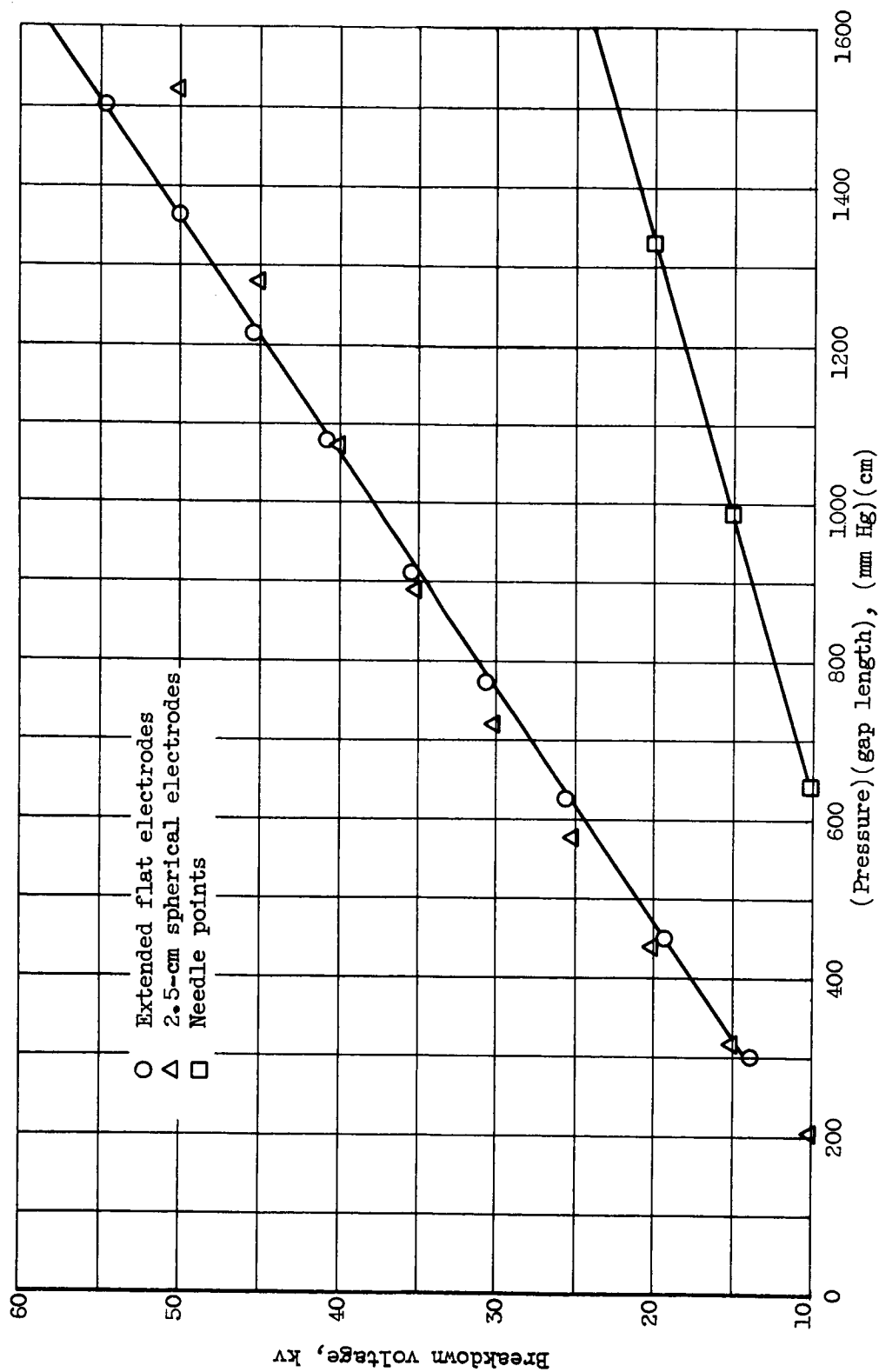


Figure 17. - Breakdown voltage versus pressure times gap length for atmospheric pressure.

voltages (5).

The curve for extended flat plates (5) is seen to show that V is linear with $P\delta$. For 2.5 cm. spherical electrodes (6) it is seen that V falls off somewhat at high $P\delta$. For pointed electrodes (6) the breakdown voltage is decreased considerably. The decreasing breakdown voltage is due to the warping and concentrating of the electric field into a very small area near the needle point.

Thus for reasonably sized rounded and polished electrodes a value of $P\delta$ in the vicinity of 1100 mm. Hg-cm. might suffice. For $P = 760$ mm. Hg, $\delta = 1.45$ cm. A higher value of gap length must be used, however, since the minimum spark channel must be 16 mm. in length for this technique. In addition there will be irregularities in the channel near the cathode and thus an even longer spark gap is required for even illumination over 16 mm. In the present light source a channel of 20 mm. is used and can be made longer by screwing out the electrodes. An additional pointed trigger electrode is provided to breakdown this longer spark gap.

Figure 18 shows a cut-away drawing of the final design of the guided spark light source. The entire structure is mounted on a bakelite base with a bakelite block mounted at the rear. This provides the rigidity and electrical insulation necessary. Next, a 3/4-inch thick teflon block is mounted with the spark guide slot milled in the front. Three focusing holes (only center hole shown) are drilled through the bakelite and teflon just up to the back of the spark guide slot. These holes are each 8 mm. apart and, after minification of 4 to 1 by the condensor lens, defines the extremities

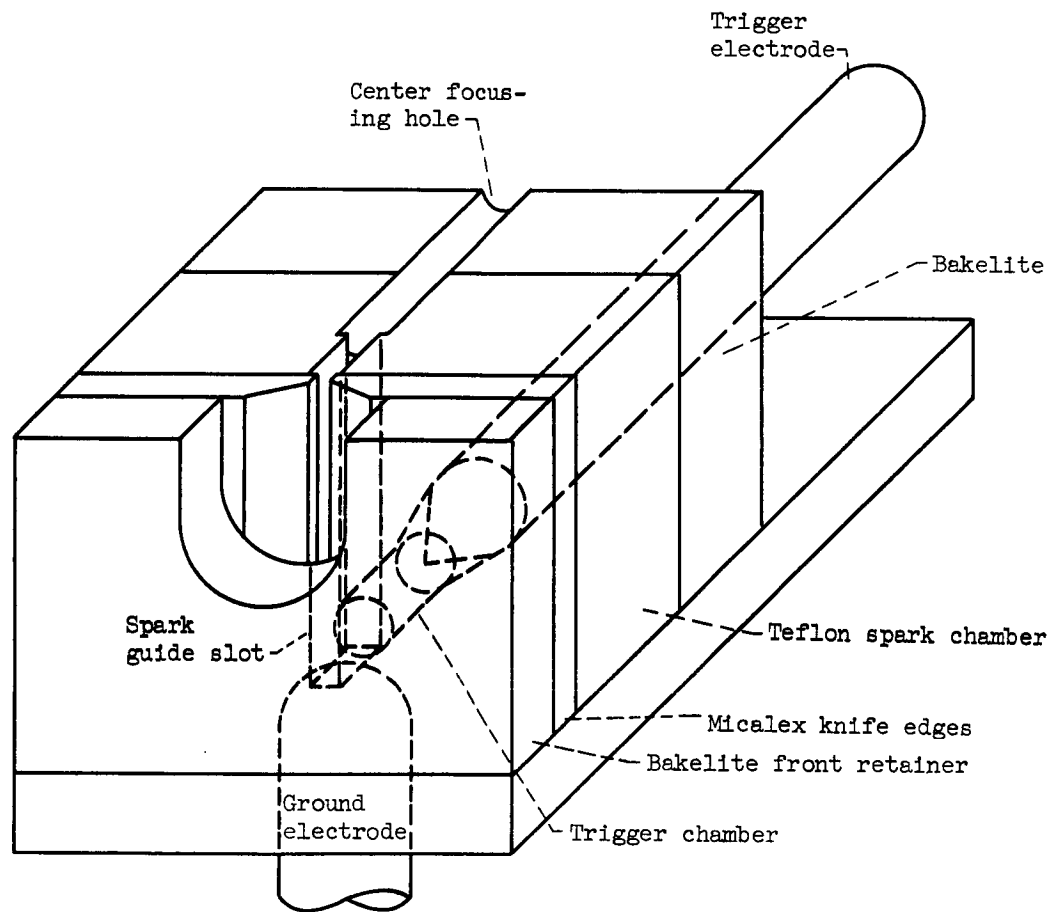


Figure 18. - Cut-away view of bottom half of light source.

of the spray sample volume. The use of these focusing holes will be described in the focusing and alignment section.

In order to have sharply defined sides on the light source, two Micalex knife edges, 0.8 mm. separated, are secured on the front of the teflon block. Finally a bakelite front retainer is located to hold the entire assembly together. Machine screws running from the front retainer to the bakelite back are used.

From the rear of the assembly the pointed trigger electrode is inserted. This trigger electrode is exposed to the ground electrode through a small hole here called the trigger chamber, but it is not exposed to the high voltage electrode. This is done so that a spark can be formed between the trigger and the ground electrode, but leakage cannot occur between the trigger and the high voltage electrode. This leakage proved to be quite a problem and will definitely occur unless the above precautions are observed. Leakage can result in the breakdown of the main spark channel at times when it is not wanted and also makes it impossible to build the capacitor voltage up to 40 KV.

Triggering is accomplished in the following manner. A negative 40 KV is applied to the high voltage electrode. A negative 500 volt pulse is produced by the trigger power supply. This pulse is then transformed into a positive 15 KV pulse by a UNILECTRON Pulse Transformer (PT-108). The 15 KV pulse breaks down the gap from the trigger electrode to the ground electrode and the main spark channel then conducts.

The 15 KV pulse causes breakdown of the main channel by two mechanisms. First, the additional 15 KV distorts the 40 KV electric field and effectively increases this field since the 40 KV is negative and the 15 KV is positive. Secondly, the breakdown between the trigger and ground electrodes causes ionization and provides the electrons necessary for the electron avalanche which ultimately causes the main spark channel to become conductive (7).

Several of the design features of this light source should be discussed at this point so that any future builder will not duplicate the unsuccessful attempts of the author.

The spark guide slot must be cut in an insulating material of high impact strength such as teflon. Teflon is advantageous also in that it will withstand high temperatures. The disadvantage of teflon is that it will not maintain its dimensions when the pressure builds up in the guide slot, i.e., the slot will widen and thus the light sheet formed by the image of this slot will widen. It might be tempting to form the guide slot in a rigid material such as Micallex which will not deform appreciably. This was tried but no construction precautions were sufficient to keep the guide slot from shattering during the spark discharge.

Thus the laminated construction finally used was the best of those tried. The teflon provides the impact strength and is allowed to deform somewhat, the Micallex knife edges provide the dimensional stability, and the bakelite front retainer distributes the load evenly upon the Micallex around the holes for the machine screws.

There are possibly better materials to provide the above effects, but as constructed the light source performs very well. After 4000 flashes which were necessary for the work reported in this paper, the light source still worked well with only some deterioration of the teflon slot occurring.

Another precaution necessary is that the machine screws which hold the light source together must be located properly to prevent leakage. They must be located at the extreme top and bottom and as far removed from the electrodes laterally as is consistent with mechanical strength. If this is not done an easy leakage path will be provided and it will be impossible to maintain full capacitor voltage. A small amount of corona dope around the screws at the joining of each laminate will also help in this regard.

Figure 19 shows the front and side views of the light source and capacitor mounted in its shielding box. This box is made of plastic and is lined on the outside with lead sheet. The lead sheet is to protect the operator from the remote chance of X-ray production. The mechanism mounted on top of the capacitor is a fail-safe capacitor discharger which automatically shorts the capacitor and shuts down the power supply if any of the access doors are inadvertently opened to a point of high voltage.

Test of present light source. - The tests as previously described were performed on the new light source. In addition a measurement of rate of change of current was made by wrapping a single loop of wire around the capacitor ground lead and connecting the ends of the wire to the oscilloscope.

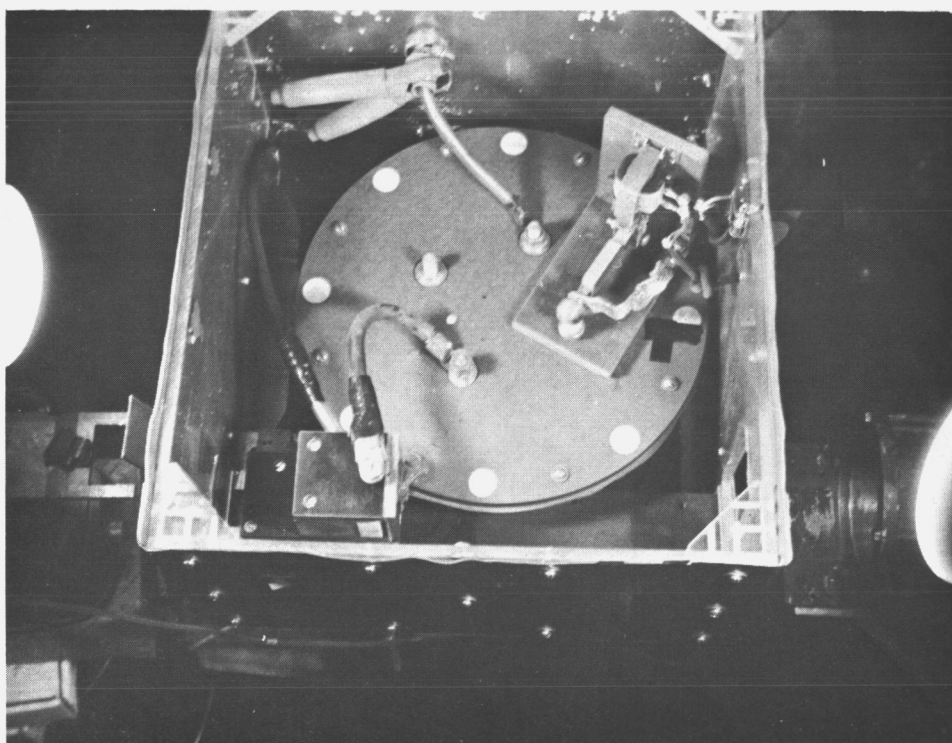
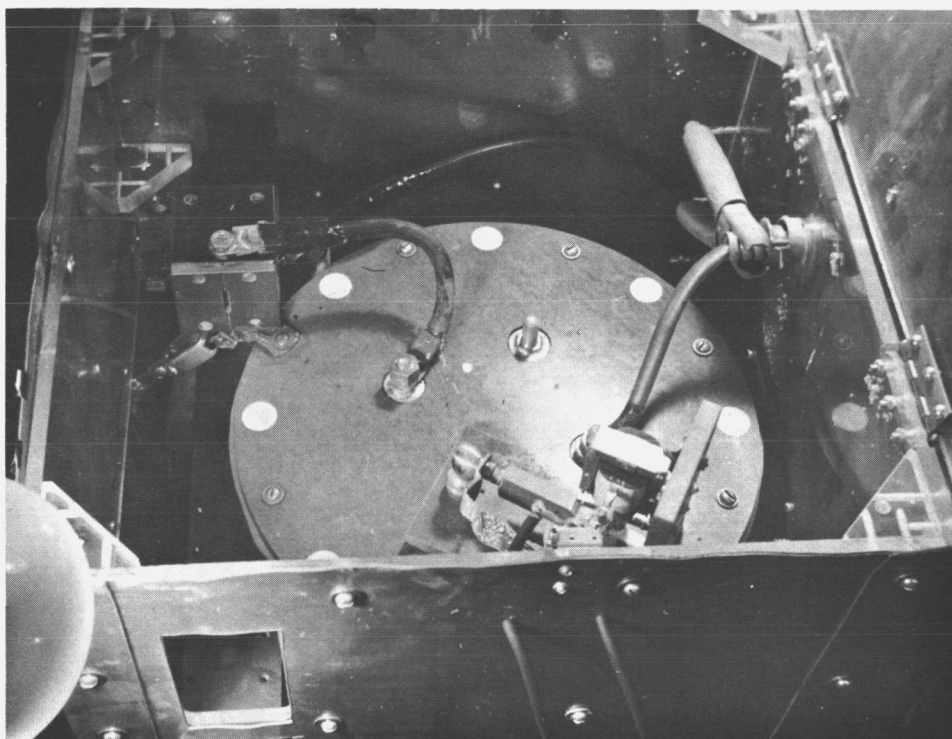


Figure 19. - Front and side views of light source and condensor.

At first appearance the tests do not seem encouraging. In the 5000 Å region the peak intensity of the new light source using 80 joules is identical with that of the 64 joule prototype but the spark duration has been cut from 2 microseconds (see Figs. 15 and 16) to 1.5 microseconds. This does mean that in this spectral region the maximum temperature has been attained and the source radiates as a black body at the maximum temperature for air ($30,000^{\circ}$ K). Since more energy has been dissipated in a shorter time than in the prototype there is a greater chance for temperature saturation for the shorter wavelength radiation which is the last to saturate (see considerations for improvement of light source). It will be recalled that fluorescein has an absorption peak also at 2500 Å (Fig. 2). With this increase in energy concentration lighter gases such as pure nitrogen or helium which have higher maximum temperatures might be used to achieve higher intensities.

Further indication of saturation was found when the electrode spacing was changed from 1 to $7/8$ inch while viewing only the central $5/8$ inch of the spark discharge. No increase in radiation was found with the shorter electrode spacing although the energy concentration increases. Thus the maximum temperature must have been established and a further brightness increase was impossible in air.

From the rate of change of current measurements the system ringing frequency was determined to be 1.25 megacycles per second. The inductance can then be determined from:

$$f = \frac{1}{2\pi} \frac{1}{\sqrt{LC}}$$

where

f = ringing frequency, mc/sec

L = inductance, microhenries

C = capacitance, microfarads

The inductance for this light source was calculated to be $L = 0.162$ microhenries.

The maximum current can be obtained from:

$$I_m = \frac{E}{\sqrt{R^2 + \frac{L}{C}}}$$

where

E = Peak D-C changing voltage, volts

R = resistance, ohms; L and C as above.

If the system is underdamped and oscillatory:

$$I_m = E \sqrt{\frac{C}{L}}$$

The light source is underdamped and thus the peak current = 31, 400 amps.

Power Supply

The high voltage necessary for the guided spark light source necessitated the building of a new high voltage D. C. power supply. The following is a brief discussion of this equipment.

Figure 20 shows the circuit diagram for the 50 KV D. C. power supply. The transformer is a Standard X-Ray Co. Model L No. 475 which was removed from a surplus X-ray machine. The half wave rectifier tube is a Westinghouse WL 5859 vacuum rectifier tube. The

filament control and range switch are also former parts of the X-ray machine.

This power supply is conservatively rated at 50 KV. Without leakage in the light source it should be able to provide around 70 KV.

The 7 megohm resistance is provided to limit the maximum current to within 10 ma. when the power supply is working into the uncharged capacitor after the light source has been fired.

The 500 megohm resistor provides a full scale reading of 50 microamps at a capacitor voltage of 25 KV. When S-4 is closed and with the 10 K potentiometer properly adjusted, a full scale reading is obtained for 50 KV.

The one megohm resistor shunting the meter prevents the possibility of 50 KV appearing at the meter in case the meter should burn out.

The range switch provides a rapid but not great change of range for the D. C. output. If a greater change in range is desired the input tap to the transformer must be changed. These are marked 100, 110, 120, and 130 volts on the circuit diagram.

The fail safe protection circuit is also shown in Figure 20. It can be seen that if any access door is opened at which a high voltage might be present, the high voltage portion of the power supply is shut down and the capacitor discharged. Provision has also been made for discharging the capacitor at any time by a switch on the front panel. This is necessary during light source development work since the capacitor discharges very slowly and can even build up a voltage over a period of time after being shorted. This is due to the residual stress in the dielectric after shorting.

The vacuum rectifier must be shielded with lead sheet since in a vacuum at 50 KV the electrons can attain sufficient kinetic energy to produce X-rays upon impact with the anode.

Figure 21 is a photograph of the front panel of the power supply.

Figure 22 shows the power supply and the light source shielding box in perspective with the rest of the apparatus as it is presently used. One man located to the rear of the camera can operate the entire apparatus with this arrangement.

Particle Counter and Sizer

The particle counter used to count the data reported in this paper was the DuMont Iconumerator built by Allen B. DuMont Laboratories, Inc., Clifton, New Jersey. Reference 8 provides a discussion of this machine.

The Iconumerator was provided on loan to the University of Wisconsin by the Continental Can Co., Equipment Development Dept., Chicago, Illinois. Without this machine the drop counting reported in this paper would have been an insurmountable and unreliable task.

This discussion will include the general operation of the Iconumerator, the detailed operation of the sizing discriminator, and the modifications made on the Iconumerator.

DuMont Iconumerator. - The Iconumerator is a flying spot scanning particle counter with a line to line memory which enables the precise count of particles in its field of scan. It was built to count bacteria colonies cultered in a Petri disk (8). It should be noted that the Iconumerator is strictly a particle counter. Modification of the

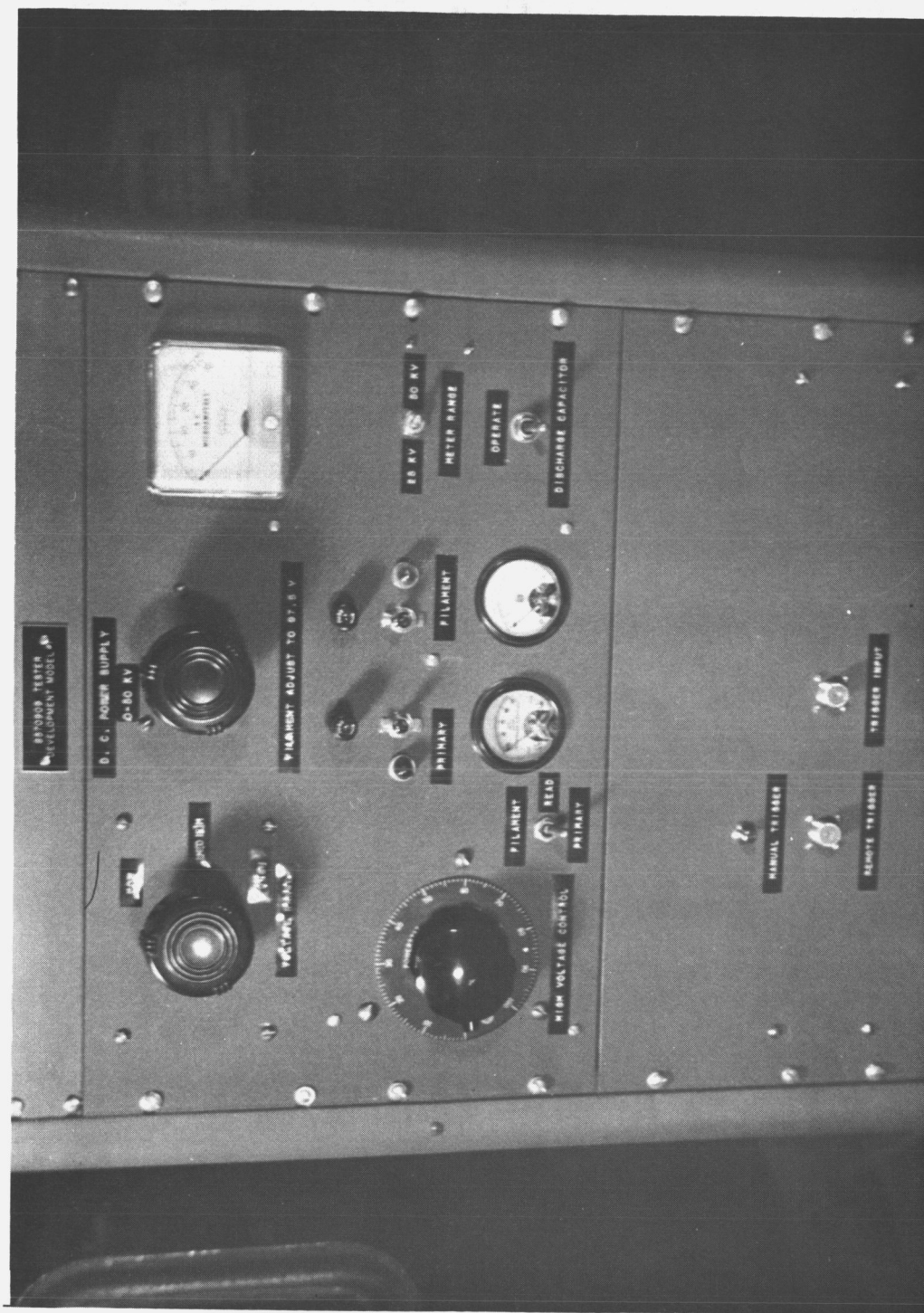


Figure 21. - Front panel of power supply.

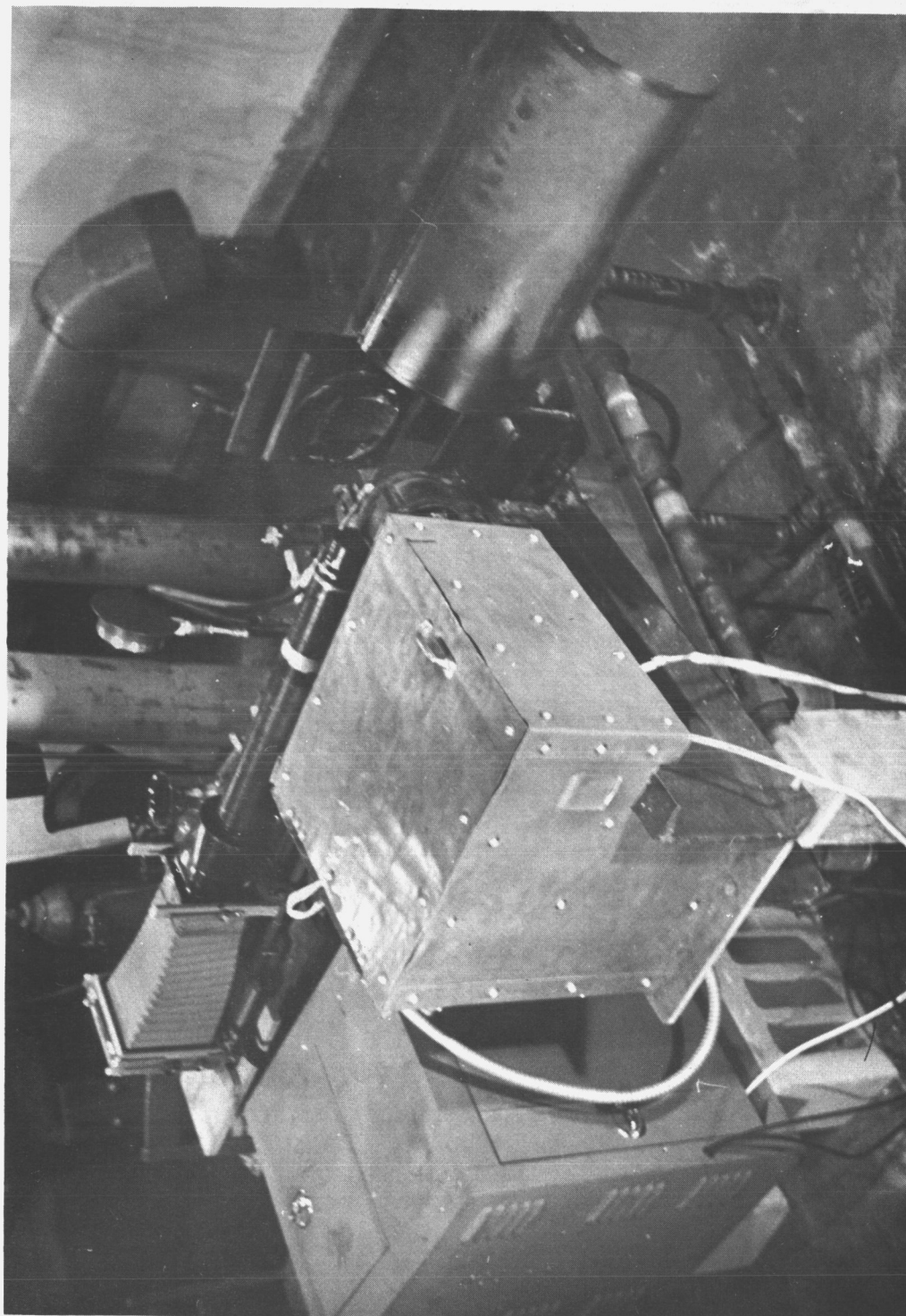


Figure 22. - Apparatus as currently used.

circuit is necessary if sizing is required.

Figure 23 shows the block diagram of the Iconumerator with the sizer included. This figure is essentially that as found in Reference 8 except for the sizing circuit. The formation of an electrical signal due to a particle and the passage of this signal through the various component circuits will now be discussed.

The scanning tube provides a 1000 line raster recurring each second. This tube is a type K1429P15 short persistence cathode ray tube especially fabricated to avoid optical defects (8). The spot size is approximately 100 microns on the tube. This raster is focused on the Petri dish (drop photograph in this case) by the optical system (see Fig. 26) at a 1:1 magnification. As the spot image passes over the transparent portion of the subject, light is passed through to the multiplier phototube. When the spot strikes an opaque particle the light reaching the phototube of course ceases. A condensing lens system (see Fig. 26) focuses the aperture of the optical system onto the multiplier phototube so that the light sensitive portion of the phototube is completely illuminated and local sensitivity differences will not produce a spurious signal.

The multiplier phototube (6292) thus produces a negative signal when the transparent area is scanned and returns the signal to the black level when a particle is encountered. The particle signal departs from a square wave due to the density gradient of the particle, phosphor persistence, and the finite time required for the spot to enter and emerge from the particle. The multiplier phototube then sends its signal via its cathode follower to the video compensation

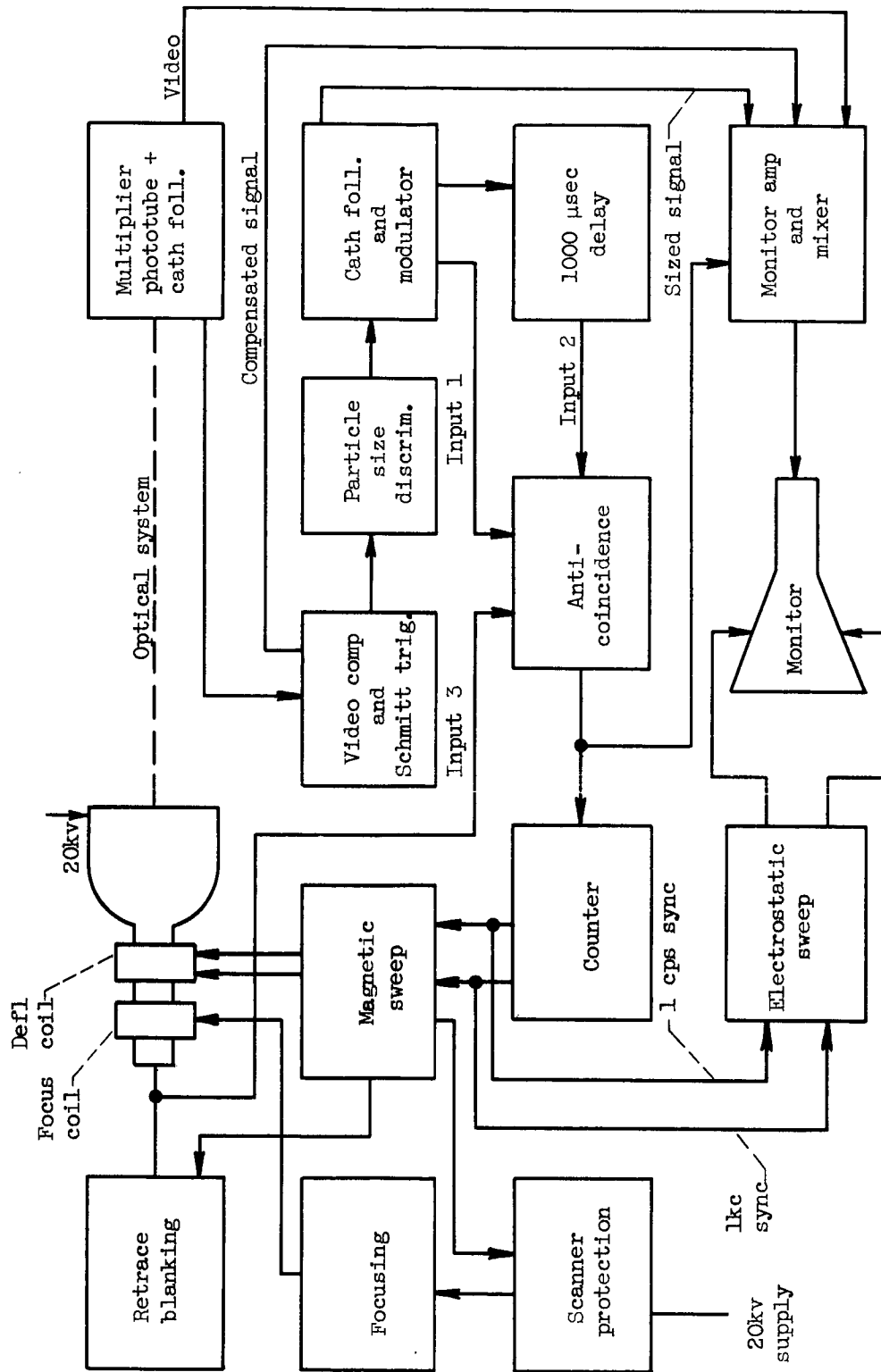


Figure 23. - Block diagram of iconnumerator with sizer included.

and Schmitt trigger.

The video compensation circuit senses the density of the background on which the particles are found and rapidly changes the base level of the pulse depending upon the opacity of the background. This is essentially a fast acting D. C. restorer (8). This circuit elevates the signal to or beyond the black level. The Schmitt Trigger Discriminator takes these signals of various amplitudes and rise and fall times and converts them to uniform amplitude signals with uniform rise and fall times. For counting, the discrimination level is set just below the black level. For sizing, however, the discrimination level must be just above the background noise so that a square wave of maximum length is produced.

In the unmodified system the discriminator square wave is sent to channel one of the anti-coincidence circuit and also is modulated and sent to the delay line.

When sizing is performed the discriminator square wave is fed to the size discriminator and operated on as discussed in detail in the next section. The sizer removes those signals of duration less than one of twelve preset times and injects those remaining signals back into the Iconumerators. These remaining signals are as above sent to channel one of the anti-coincidence circuit and to the delay line.

The delay line is a fused quartz acoustic delay system (8). This provides a 1000 microsecond delay which is precisely the time for one line of scan which enables the line to line memory mentioned above. The delayed signal is demodulated and sent to channel two of the anti-coincidence circuit.

The anti-coincidence circuit ensures that a particle is counted only once. If a signal is provided into channel one and none is present from the delay line into channel two, a count pulse is provided to and recorded by the counter. If a signal appears in channel two before the end of the signal occurs in channel one, then the circuit is clamped and no count pulse occurs. It can thus be seen that only the first intercept of a particle is counted since then and only then will a channel one pulse occur without the occurrence of a channel two pulse. Channel 3 provides anti-coincidence clamping during retrace blanking.

The counter, as well as recording the count pulses, provides the 1 KC and 1 cps synchronization pulses necessary for starting each line and each raster, respectively.

The scanner protection circuit provides defocusing of the scanning spot in case of sweep failure thus preventing phosphor burn-out.

The monitor system provides a visual display of events to the operator. The signal waveform or the raster display can be observed from the phototube, Schmitt Discriminator, or the video compensation outputs. When the sizer is used the Schmitt Discriminator mode provides a display of the particle residuals. A composite mode is also provided in which each particle counted is tagged with a bright spot on its first intercept.

The rest of the block diagram is self explanatory, and if more detail is desired on the above components Reference 8 can be consulted.

Particle size discriminator. - A particle size discriminator was designed and built so that when it is inserted into the normal Iconumerator circuit a complete sizing of the particles in the sample can be obtained. This sizer provides twelve size categories of logarithmically increasing sizes starting at 0.25 mm. on the film. Thus with a camera magnification of 25, 10 micron drops in the spray can be counted.

The circuit diagram for the particle size discriminator is shown in Figure 24. Figure 25 shows the waveforms of a square wave pulse as it passes through the circuit. The waveforms on the left are for a particle larger than a preset size and those on the right for a particle smaller than this preset size. The actual preset size is immaterial in this discussion since the same phenomena occurs for any category with a drop slightly larger and slightly smaller than the category size. The only difference which would occur is that for large residuals the pulse duration added in the signal lengthener would be a smaller percent of the total pulse width. These two figures will be discussed together to give a clear picture of the sizing operation. The point numbers on Figure 25 refer to the points in the circuit of Figure 24 shown as circled numbers.

Point A in Figure 24 is connected to the Schmitt Trigger Discriminator of the Iconumerator and the discriminator is uncoupled from its following components in the normal counting circuit. This is a D-C coupling as is all coupling back to the multiflier phototube and forward through the sizer. This is done since the restoration distortion due to capacitor coupling would cause base level shifts de-

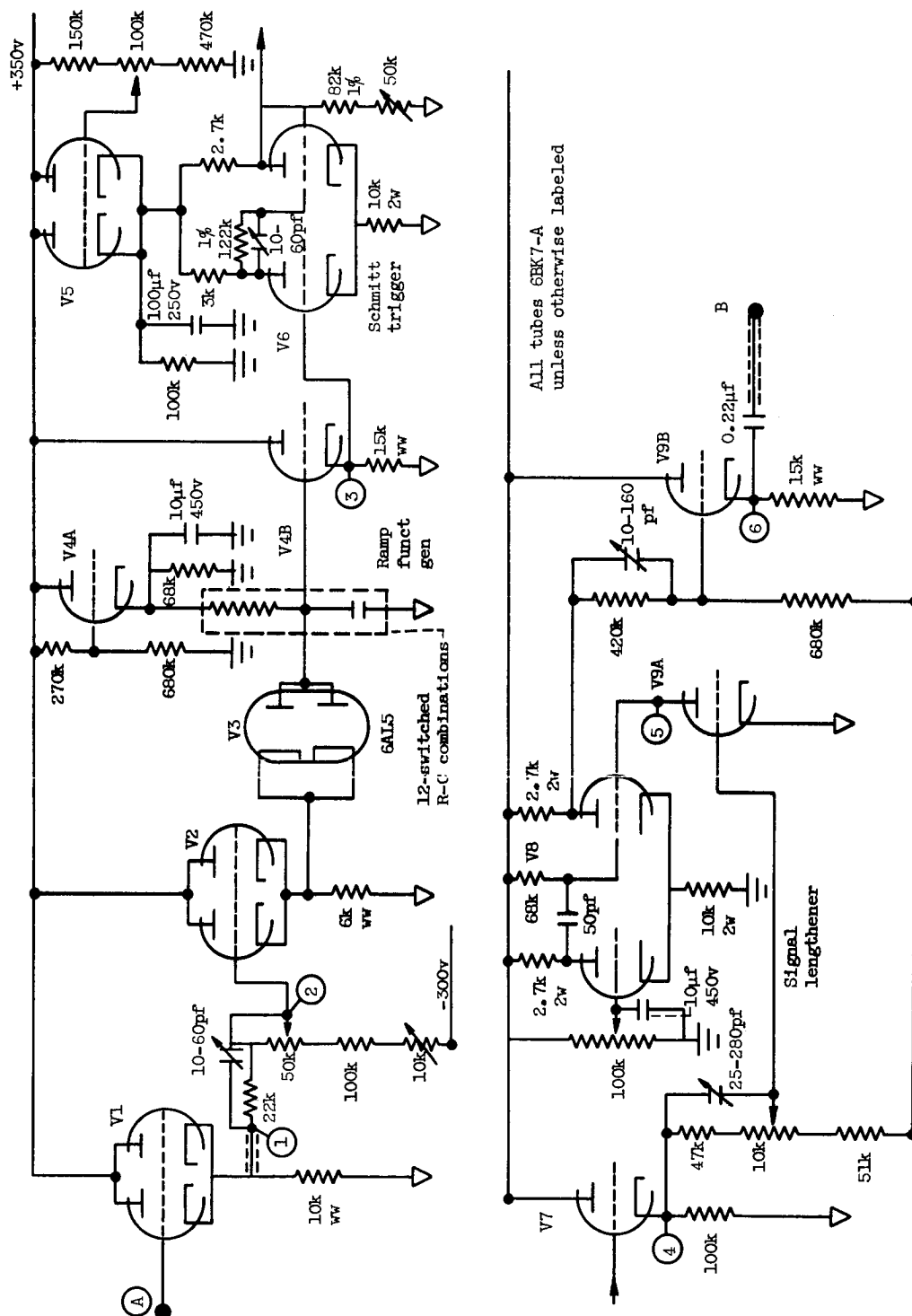


Figure 24. - Particle size discriminator.

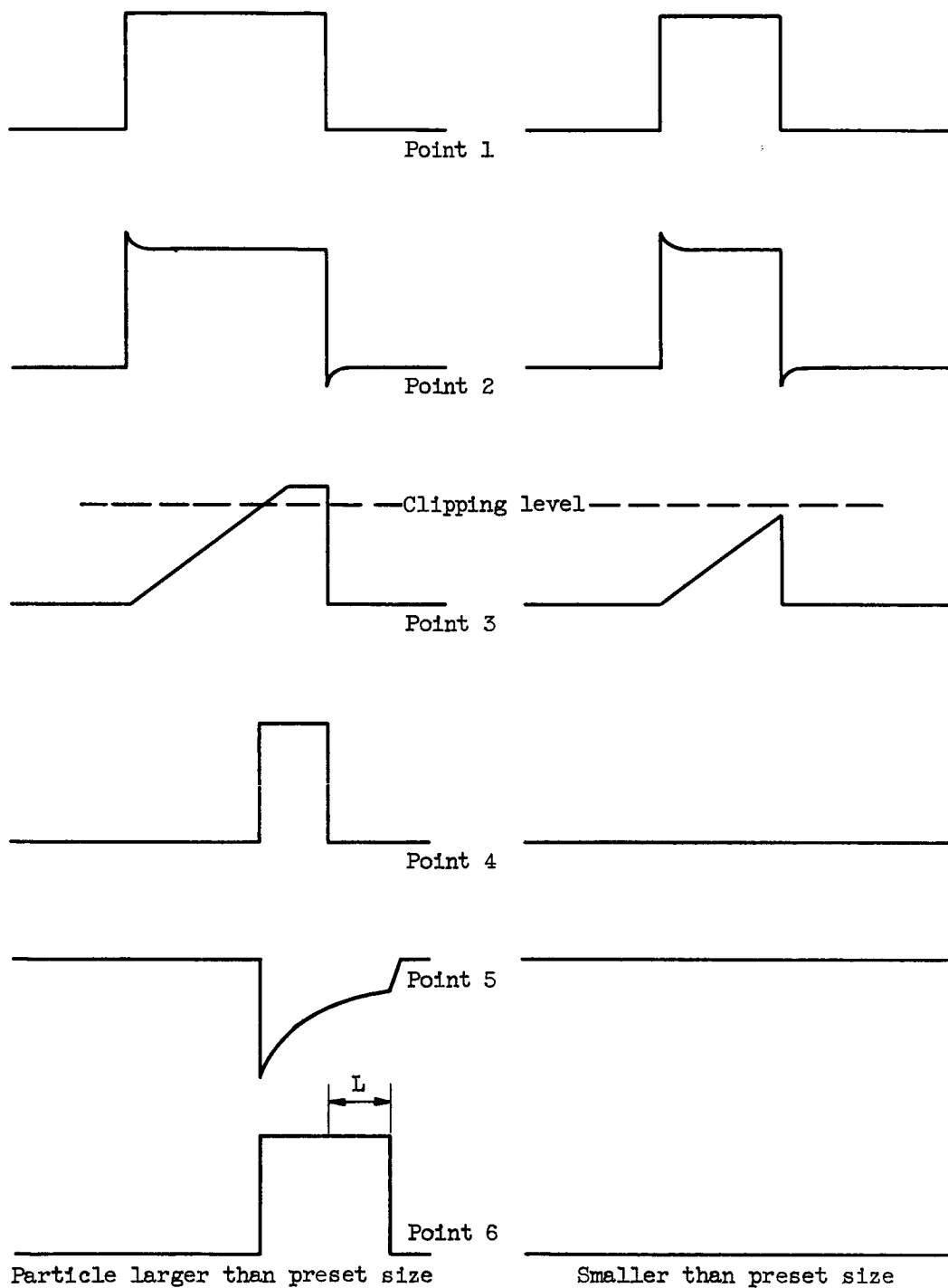


Figure 25. - Sizer signals for various points in circuit.

pending upon the number and size of particles in the sample. Base levels would also shift during flyback. Proper functioning of this circuit demands precise setting of all base levels and insurance against their drift.

Tube V-1 is a double tube cathode follower performing two tasks. First, its high input impedance eliminates loading of the Schmitt Trigger. Secondly, its low output impedance reduces high frequency losses in the voltage dividing network that follows. The signal at point 1 is essentially that of the input signal at B.

The voltage dividing network following V-1 reduces the 230 volt base level at the input to approximately 90 volts at point 3 which properly biases the sizer Schmitt Trigger. The 50 K pot is for course and the 10 K pot for fine level adjustment. The 10-60 pfd. capacitor is adjusted for a slight overshoot as shown by the signal at point 2 to compensate high frequency loss and provide an abrupt start and stop of the ramp function generator.

V-2 is another twin tube cathode follower which provides the extremely low output impedance necessary to drive the ramp function generator.

The ramp function generator consists of the twin diode V-3, an R-C combination and tube V-4-A. The cathode voltage of V-4-A determines the maximum voltage to which the capacitor can charge to and thus, for any R-C combination, the rate of increase of the capacitor voltage. The ramp function generator operates as follows. Without a positive pulse at the input point A, the voltage on the capacitor is that of the cathode of V-2. This is insured since the capacitor

tends to charge through the cathode resistor of V-4-A, but this current is bled off through the slightly forward biased diode into the low impedance of V-2. When an input pulse arrives the cathode of V-2 immediately increases and cuts off the diode by reverse biasing it. There is now no alternate path for the current from V-4-A and the capacitor starts charging positively with a time constant determined by the particular R-C combination used. If the pulse duration is sufficiently long, the capacitor will charge to the voltage of the V-2 cathode and again forward bias the diode. This will result in the ramp and then flat-topped appearance of the signal shown on the left of Figure 25, point 3. If the pulse duration is too short the ramp will be terminated abruptly when the V-2 cathode voltage again drops causing forward bias of the diode. Due to the small impedance of the V-2 cathode, the ramp will drop almost immediately to its original base level. This is shown on the right side of Figure 25, point 3.

Tube V-4-B is a cathode follower which transfers the ramp function generator signal to the Schmitt Trigger without loading the former. The signal at point 3 is thus essentially that of the ramp function.

V-5 is merely used to provide a low impedance bias of 250 volts to V-6.

V-6 is the heart of the size discrimination circuit. This is a Schmitt Trigger which normally has the left hand tube cut off and the right hand tube conducting. The output is thus normally 230 volts. If an input signal at point A has sufficient duration to cause the ramp function to build up to the clipping level of V-6, the Schmitt

Trigger will rapidly reverse its operation to that of input tube conducting and output tube cut off. The output will thus go to 250 volts. This is illustrated in Figure 25, point 4. This figure also illustrates the case in which the input signal is not of long enough duration so that the ramp function builds up to the clipping level. The voltages are shown at point 4, but this is essentially the Schmitt Trigger output since V-7 is a cathode follower.

It can thus be seen that the ramp function generator and Schmitt Trigger have subtracted a fixed duration from the leading edge of every pulse. If the pulse was of sufficient duration, a residual was obtained. If the duration was too short, the pulse was completely eliminated. It is in this manner that sizing is performed. The R-C combination can be changed to twelve different values of increasing time constant. This eliminates more and more particle pulses as the time constant is increased. A count can thus be obtained of those particles which have intercept signals greater than any one of the twelve present sizes. When the preset size exceeds the particle diameter, the particle is eliminated from the count.

There is a problem arising from the previously discussed operation. If a ~~signal~~ ^{signal} is only a very small amount longer in duration than the sizer will pass, an extremely short duration residual will result. The Iconumerators are designed to handle a minimum pulse duration of a limited time. If the residual is shorter in duration than this limit it will be lost due to a high frequency attenuation. The overlap cancelling criteria of the anti-coincidence circuit will not function properly either if the pulse is shorter in

duration than the error in the delay line.

The rest of the sizing circuit is thus provided to correct these problems. The pulse lengthener adds 3 microseconds to these very short pulses and thus they are fed back into the Iconumerator with at least a duration of 3 microseconds. The Iconumerator can easily handle this duration since its circuit will pass this pulse and the delay line error is large if it approaches 1 microsecond.

The ~~signal~~ lengthener consists of V-8 and V-9-A. V-7 is merely a cathode follower which reduces loading on the Schmitt Trigger and high frequency losses through the voltage divider which follows it.

The voltage divider provides negative bias to V-9-A to insure its cut-off. The 10 K pot is used to adjust this bias, and the 25-280 pfd. capacitor allows high frequency passage.

With V-9-A cut-off the grid of V-8-B is clamped to the cathode. This means there is grid current flowing through the 68 K resistor and very little drop between the grid and the cathode. Clamped as well as cut-off operation are the two most stable and reliable operation points of a tube.

With V-8-B clamped and conducting heavily the cathode voltage is high and the bias on the grid of V-8-A is adjusted so that V-8-A is cutoff. The plate of V-8-A is therefore at 350 volts and V-8-B is approximately 300 volts.

The residual pulse from the Schmitt Trigger is then applied to the grid of V-9-A. V-9-A comes out of cut-off and conducts thus dropping the V-8-B grid voltage. V-8-B rapidly heads toward cut-off thus reducing its plate current and decreasing its cathode voltage.

With the cathode voltage decreasing V-8-A comes out of cut-off and its plate voltage drops. Thus both sides of the capacitor have falling voltage and no capacitor discharge is necessary. The plate of V-8-A and the grid of V-8-B can thus decrease very rapidly together bringing on the complete cutoff of V-8-B. Its plate is thus at 350 volts.

This condition remains until the residual pulse at the grid of V-9-A ceases. At this point V-9-A is again cut-off. There is now, however, no low impedance path through which the 50 pfd. capacitor can charge. It must charge through the 68 K resistor. The grid of V-8-B thus increases exponentially as shown in Figure 25 point 5. After about 3 microseconds the grid voltage has increased to a point where V-8-B again starts to conduct. The cathode voltage increases and V-8-A again starts toward cut-off. Both sides of the capacitor can now increase in voltage without any capacitor current, and the more rapid rise of voltage at point 5 as shown in Figure 25 is possible.

The voltage divider to the grid of V-9-A reduces the bias to V-9-B since it could not operate with both a plate and grid voltage in the vicinity of 350 volts or else the tube drop would be near zero, the tube conducting heavily, and large grid currents flowing which would load the plate of V-8-B.

V-9-B provides a low impedance capacitor coupled output back into the Iconumerator at the point where the Schmitt Trigger Discriminator was normally connected during the simple counting operation.

It can be seen that the above circuit performs the sizing function without any disturbance to the Iconumerator. The circuit does not load the Iconumerator and it properly inserts the lengthened residual signal back into the counting circuit. If anything, the sizer has increased the ease of the counting circuit since it increased the minimum duration of the signals to be handled by the logic circuit.

Another important advantage of the sizing circuit is that it removes all of the short duration noise due to film grain, dust, and blemishes less than 0.25 mm. in diameter. The discriminator level can thus be moved down into the noise level with a minimum of problems from this noise.

Sizing of the particles in the sample is now easily accomplished. When the sizer is set for category one, all particles larger than 0.25 mm. on the film or in the Petri dish are counted. There are twelve size categories each increasing in size by a multiple of $\sqrt{2}$ larger than the previous category. The largest category thus determines the number of particles larger than 11.31 mm. A greater range of size could, of course, be obtained by simply inserting more R-C combinations.

The particle size distribution is determined by subtracting the number counted greater than a particular size from that of the number greater than the preceding category size for all size categories.

Iconumerator modifications. - The Iconumerator was modified in a few minor respects to make its operation more adaptable to the analysis of the data reported in this paper. These modifications are reported here to acquaint the future user with their effects and to

permit the restoration of the Iconumerator to its original condition upon return to the Continental Can Co., its owner, if they do not wish to use these changes.

Optical system modification. - The Iconumerator was originally designed to scan a 100 mm. Petri dish with a 1:1 magnification of the scanning crt. Since the films obtained from this fluorescent technique are 4 x 4 inches, only the center portion could be scanned. As an alternate procedure, the films were cut into 2 x 2 inch pieces and thus the entire film was used.

Since this smaller 2 x 2 inch area was to be scanned, it was decided to change the magnification of the optical system to $2/3$ so that the raster size of the scanning tube image would be reduced upon the film. To accomplish this a new lens holder was built so that the lens could be moved closer to the sample as shown in Figure 26. Final focusing was accomplished by movement of the scanning tube.

This demagnification provides several advantages. The image of the scanning spot is reduced in size, and the number of scan lines in the 2 x 2 inch film area is increased. Both of the above result in improved resolution. The scanning spot image on the film moves slower, and thus a longer duration pulse is produced for a given particle size. This enables the smallest particle to be analyzed to be reduced to $2/3$ that of the original system as far as band width of the amplifiers is concerned. Finally, since the scanning tube persistence remains the same while the pulse width is increased by $1\frac{1}{2}$, the pulse leading edge will become steeper due to reduction of this persistence effect.

The movement of the scanning lens also changes the operation of

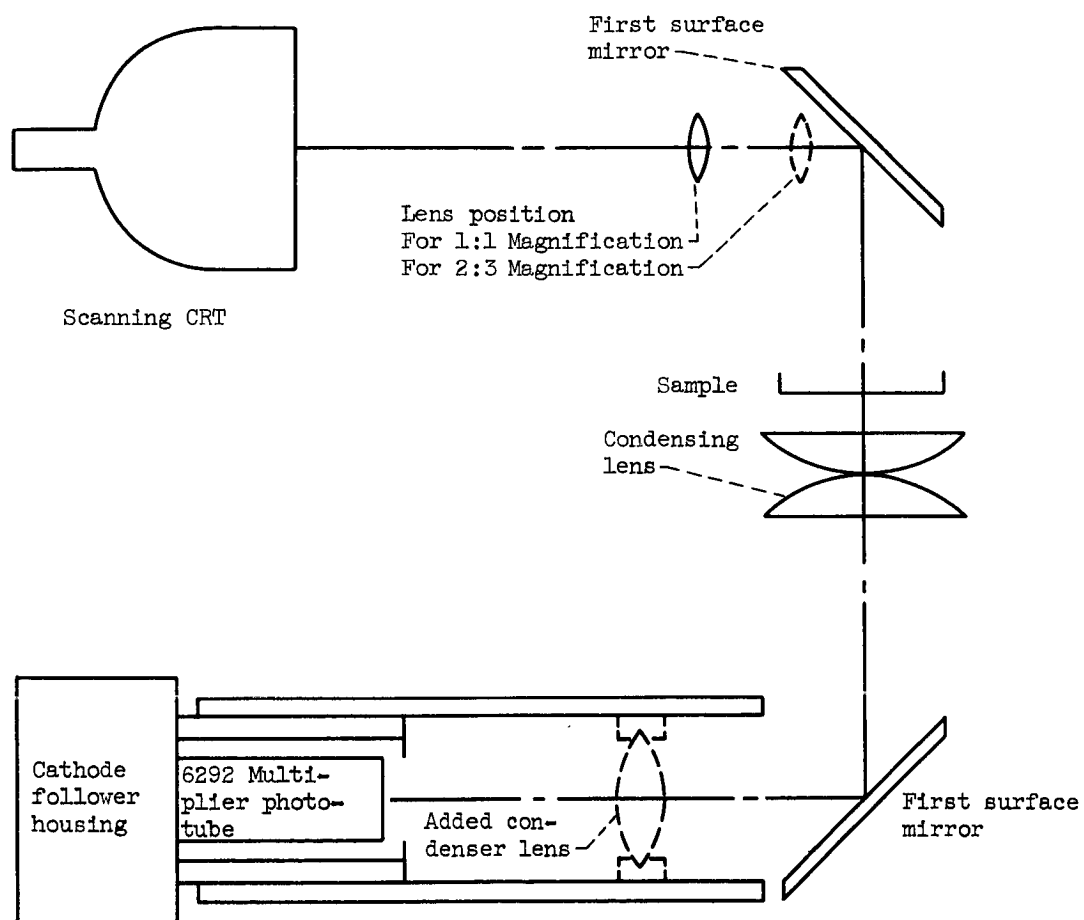


Figure 26. - Inconumerator optical system modifications.

the condensing lens system. As previously noted, the scanning lens aperture is focused by the condensing lens onto the photocathode of the multiplier phototube. With the scanning lens moved defocusing of this aperture occurs and much light escapes the photocathode. An additional condensing lens in a cylindrical mount was thus inserted into the multiplier phototube housing tube. This lens converges all of the light back onto the photocathode.

Electrical modification. - The circuit of the Iconumerator was broken into with the insertion of the size discriminator previously described. The Iconumerator circuit diagram will be referred to but not reproduced here. The output of the Schmitt Trigger V304-B is normally capacitor coupled to the phase inverter V305-B by a 0.22 ufd. capacitor. This capacitor is merely removed from the circuit and the size discriminator input connected to the plate of V304-B. The size discriminator output is then returned via a 0.22 ufd. capacitor to the grid of V305-B. These tubes are referred to as V-4-B and V-5-A, respectively, in the circuit diagram of Reference 8.

The modification to the multiplier phototube cathode follower is shown in Figure 27. The normal circuit contained only the 1 K resistor in the grid circuit. The 2 mh. coil and the 1 K potentiometer were added to increase the leading edge slope of the particle intercept signal.

An investigation of oscilloscope traces, formed when the abrupt sharp edge of a razor blade was scanned, indicated the rise time to $3/4$ of maximum signal was about 3 microseonds. The rise is at first fairly steep as the scanning spot enters the opaque edge but then de-

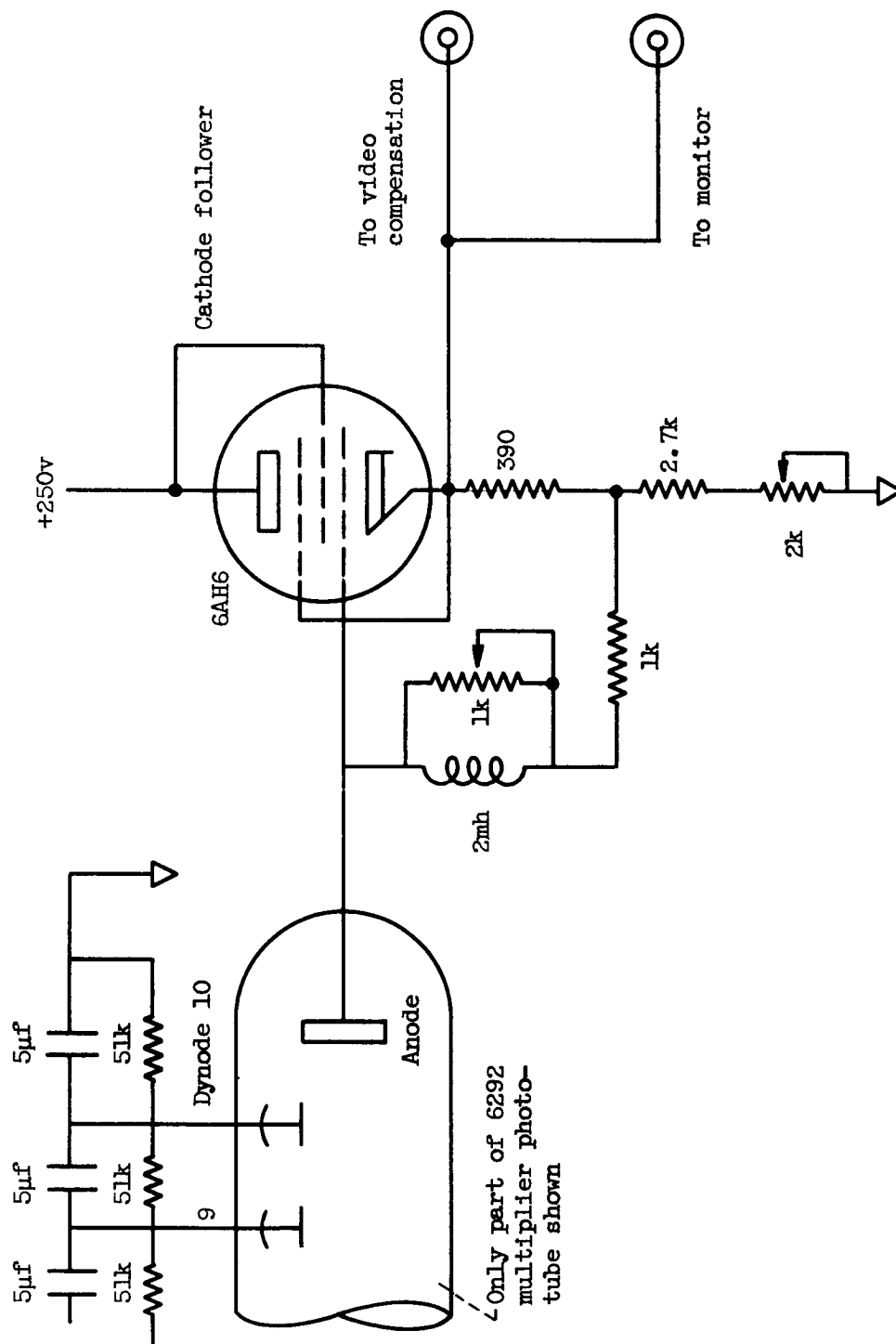


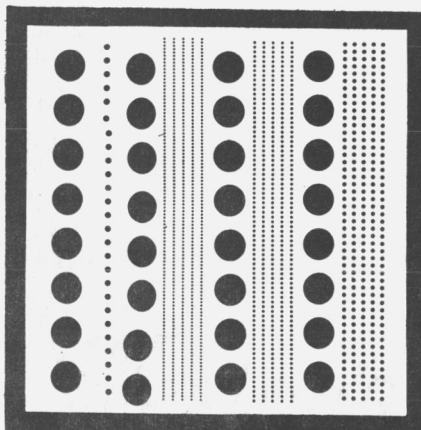
Figure 27. - Video cathode follower modification.

creases and the afterglow tail gradually dies out. With this occurring the 0.25 mm. particle signals reach barely half way up to the black level. The video compensation circuit could not be adjusted to compensate for this.

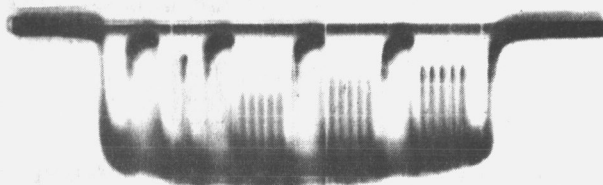
The added resistance and inductance in the cathode follower grid circuit doubles the multiplier phototube load at high frequency while not effecting operation at all at low frequency. This elevates the steep initial portion of the leading edge up to the black level. As the overshoot recovers, the slower rising original signal has increased enough so that a reasonably square leading edge is obtained. The 1 K potentiometer can be adjusted to change the compensation from zero at $R = 0$ ~~to~~ overshoot at $R = 1$ K.

Figure 28(a) shows the calibration slide scanned to perform the above adjustment. Figure 28(b) shows the signal obtained with no compensation. In Figure 28(c) the compensation has been increased to almost bring the smallest particle signals up to the black level. The smallest particles are 0.25 mm. on the calibration slide. It can be seen that the noise from the film granularity is also increased by this compensation. A compromise in this adjustment is thus made by increasing the small particle signal as much as possible but not enough to create excessive noise.

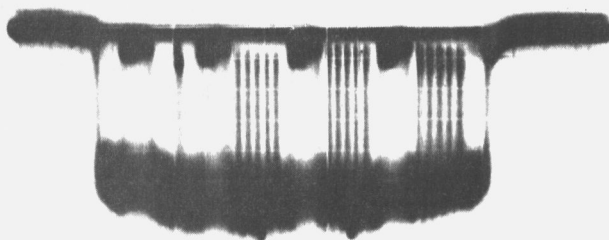
Calibration procedure. - There are several circuit adjustments which must be performed on the Iconumerators and the size discriminator before proper operation of the entire system can be obtained. The Iconumerators adjustments are in general independent of the size discriminator, but the Iconumerators must be well adjusted before the size



(a)



(b)



(c)

Figure 28 . - Effect of high frequency compensation
on small particles.

discriminator can be adjusted and calibrated precisely. These will be covered in the order in which they are performed before a sizing of data is made.

Iconumerator adjustments. - The delay line must be checked frequently to confirm the 1000 microsecond delay, but adjustment is seldom necessary. Delay line testing is done by recirculating a noise pulse from a switch through the delay line and observing this on the monitor. If delay is precisely 1000 microseconds a verticle bar will be observed on the monitor. An error of 1 microsecond causes the bar on the monitor to slant across the screen at a 45° angle. Thus very sensitive adjustment can be made and is accomplished by changing the temperature of the thermostatically controlled oven in which the delay line is located.

If a radical change in the delay seems to have occurred in the above test, it is likely that the counter is out of adjustment rather than the delay line. The counter provides the sweep sync pulses, and if this is out of adjustment the delay line test will show this as a slanting pattern on the monitor.

The next step is to focus the scanning spot. The calibration slide of Figure 28 can be used for this test. The scanning spot is focused so that the small particles give the maximum deflection possible. The focus can change with a change in scanning tube brightness, therefore, once the spot is focused brightness should not be changed. If brightness is changed appreciably the focus must be rechecked.

The optical system is then focused by moving the scanning cathode ray tube. The same calibration slide as above is used and the small

particle signal amplitudes are peaked.

There are numerous other adjustments which must be made to insure the proper voltages at various points in the circuit. Once made these will not change over a long period of time and are too numerous to discuss here.

Size discriminator adjustment. - Most of the sizer adjustments were made before the sizer was inserted into the Iconumerators circuit. The input to the sizer is obtained from a separate Schmitt Trigger identical to that in the Iconumerators which is driven by a sine wave generator. Adjustment was provided so the symmetry of the square wave could be varied. The square wave frequency can be varied by the sine wave generator.

The initial adjustments are made with the above Schmitt Trigger connected to point A but with the sine wave generator inoperative. There is thus 230 volts at point A. The 50 K potentiometer at point 2 is adjusted so that the voltage at point 3 is 100 volts. The 50 K potentiometer in the grid of V-6 is then adjusted so that the Schmitt Trigger fires at this 100 volt bias. The potentiometer at point 2 is then readjusted so that point 3 is at 90 volts. The above has insured that a 10 volt increase at point 3 will fire the Schmitt Trigger.

The external Schmitt Trigger is then caused to fire by the sine wave generator producing a square wave input. A slight overshoot is obtained by adjusting the bypass capacitor at point 2.

The input frequency is increased so that a very short residual (about 1 microsecond) is obtained at point 3. The 10-60 pfd. capacitor in the circuit of V-6 is adjusted so that the Schmitt Trigger output

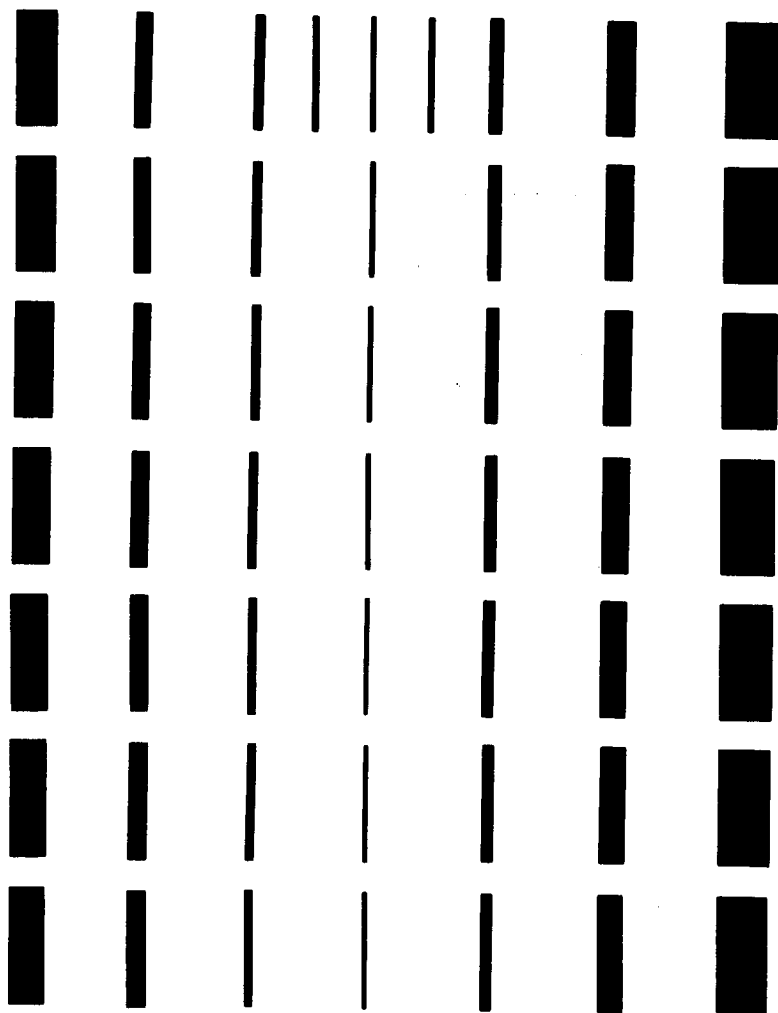


Figure 29. - Calibration slide for final sizer calibration.

The center column of seven and the two extra bars at the top provide calibration for category one. The third bar from the top is exactly 0.25 mm. The bars above the third increase in size and those below decrease in size so that the extremes are 0.266 and 0.232 mm. Each bar width changes less than 2 percent from the previous bar. The same is true for the other columns for categories two through seven. For these, however, the bar of width exactly equal to the category border is centered in the column. This calibration slide is made on film with a background density about equal to that of the actual drop pictures (about 0.5 density).

The calibration slide is then scanned by the Iconumerator. The Iconumerator Schmitt Trigger is adjusted to fire just above the background noise level.

With the Iconumerator monitor operated in the composite mode, a bright spot can be seen on the bars of the calibration slide which pass through the sizer and are counted. With the sizer set on category one the lower four bars of the center column should not be tagged while the top three and the two extra bars should be tagged. The fine level adjustment (10 K potentiometer at point 2 of Fig. 24) of the sizer is varied until the above condition is obtained. When the adjustment is exactly correct the 0.25 mm. bar should be erradically and multiply tagged. This results from the fact that the bar is not exactly 0.25 mm. over its entire length (which would be impossible to obtain). The bar may be slightly narrower at some points and slightly larger at others. It will then effectively be cut into multiple bars vertically when ever an intercept fails to pass through the

has minimum rise time.

The 10 K potentiometer is adjusted at point 4 so that V-9-A is cut off when no signal is present and conducts with a positive pulse at point 4. The bypass capacitor at point 4 is adjusted for high frequency response to V-9-A.

The 100 K potentiometer in the grid of V-8 is adjusted so that the left side of V-8 is cut-off with no signal present but conducting for a positive pulse at point 4. This is a very sensitive adjustment since if improperly done the output of V-8 will oscillate. This will provide a square wave oscillating output whenever a signal is present. This will obviously cause erratic counts.

The bypass capacitor at the grid of V-9-B is then adjusted for good high frequency output at point B.

With the above procedure the sizer should now operate properly with only the sizing category R-C combinations needing final adjustment.

The input frequency is set so that a symmetrical square wave with a positive pulse duration of 3 microseconds is obtained. The sizer is set on category one, and the resistor in the category one R-C network is adjusted until an output at point B is obtained.

The frequency is then increased by multiplies of $\sqrt{2}$ and the above repeated for each of the twelve categories. The sizer is then ready for insertion into the Iconumerator circuit for final calibration.

Calibration of combined system. - For use in the final calibration, the calibration slide shown enlarged in Figure 29 was made.

counter.

Category one is now set at least within 2 percent of 0.25 and more likely closer.

The above is repeated for categories two to seven except that any necessary adjustments are made in their respectively sized R-C circuit resistors.

Calibration of categories eight to twelve are accomplished in a slightly different manner. A sine wave generator is capacitor coupled to the Iconumerators input. The frequency at which counts are first observed in categories one to seven are determined. These frequencies can be plotted against category size and easily and safely extrapolated to larger category sizes. Using these extrapolated frequencies, categories eight to twelve can easily be calibrated.

Calibration check with drop pictures. - When drop pictures are counted the following procedure is used. A 2 x 2 inch film from each batch of 12 films (4 x 4 inch) which are developed and processed together is hand counted very carefully. This film is then analyzed on the Iconumerators. With a 10 volt signal from the multiplier phototube, the Schmitt Trigger Discriminator level is adjusted very near the noise level. A close but not exact correspondence between the hand count and the machine count can be obtained. This hand counted film is observed in between every other film analyzed to insure against any drift in the circuits. The maximum intercept signals are maintained at 10 volts by slight changes in the scanning tube brightness while the discriminator level is held constant.

While the count from the hand-counted-film by machine and by hand

counting is not exact it is felt that the machine count is most reliable. If the film were hand counted by several observers or even by the same observer several times, the count might vary radically. The machine count is consistent and more easily calibrated and is preferred where differences occur between it and the hand count.

Possible errors in sizing particles. - Figure 30(a) shows the microdensitometer profile of a large, dense, well defined drop on a drop photograph. Figure 30(b) is that of a well defined small drop and Figure 30(c) that of a fairly poor image of a small drop. Each division on the abscissa is 0.25 mm. on the film or 10 microns in the sample volume. These traces were taken on a Jarrell-Ash Microdensitometer with a slit of 25 microns by 100 microns. The edge gradients of the small drops are probably slightly better than shown since the slit length is almost half their diameter. The large drop, however, should show a very realistic picture of the true gradient.

It can be seen from the large 85 micron drop that unless the clipping level is very close to the noise caused by the film granularity, this drop could be sized smaller than it really is. If the clipping level were up near the black level the drop could be sized at 75 microns or about 12 percent undersized.

The 17 micron drop could be sized at 10 microns or a 41 percent error. The fairly poor 12 micron drop could be sized at 5 microns if the sizing went that low, but, of course, it would just not be counted at all.

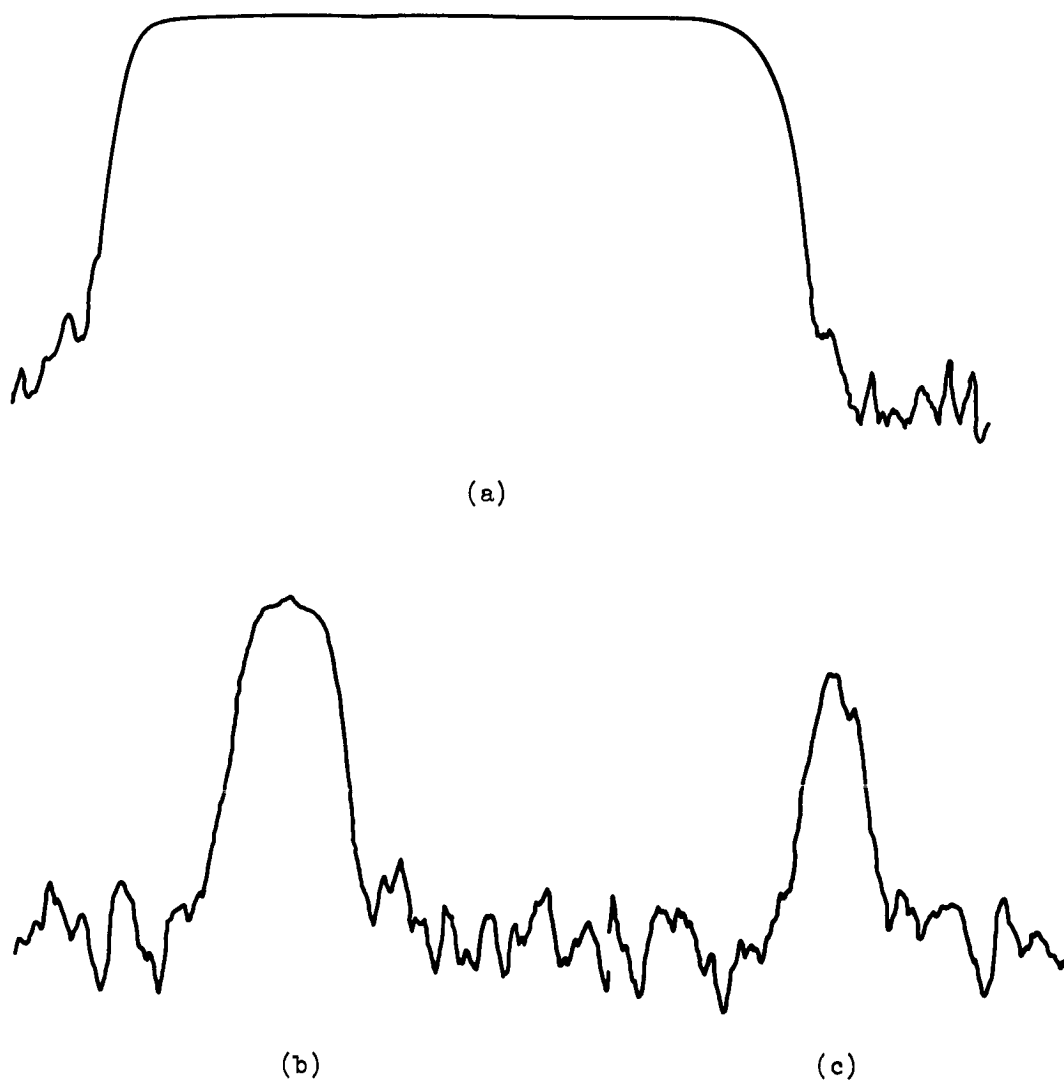


Figure 30. - Microdensitometer profiles of drop photographs.

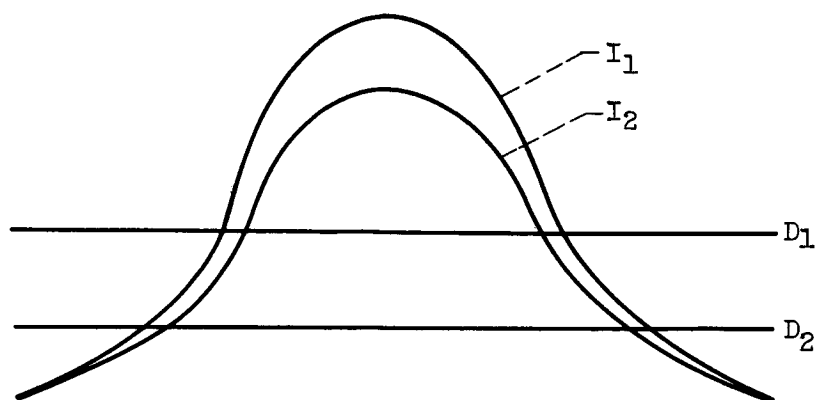
If the clipping level were high, both the 17 and 10 micron drops would be missed. It can be seen that their peak signal is lower which means their transmission is higher than for the large drop. This was a general condition noted on all of the smallest drops measured. Their density is not as great as for the larger drops.

This condition of the non-abrupt edge gradient will be found in any optical system. The image is spread out due to diffraction at any limiting aperture and by the aberrations of the lenses. The question is at what point in this intensity gradient of the image does the film start recording this image?

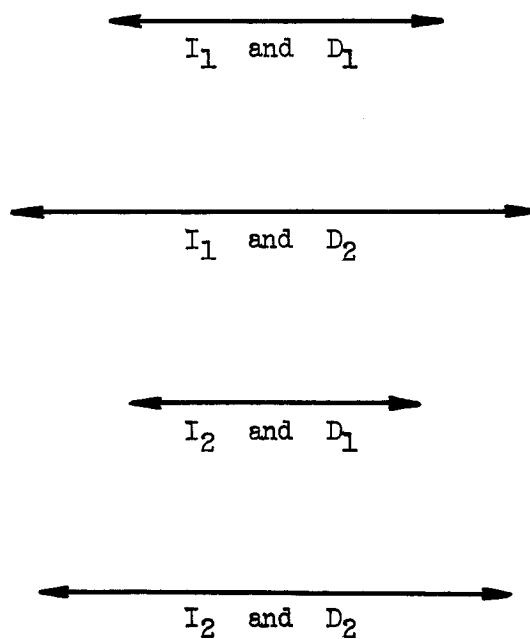
If a high contrast film is used so that the edge gradients on the film are steep no more precision has been gained. The image gradient is still there, but the question still remains where does the film start recording this image? This will depend upon the actual image intensity and the development conditions of the film.

Figure 31 illustrates the above with a hypothetical case. In Figure 31(a) two different image intensities and two film development conditions are illustrated. $I_2 = 0.8I_1$, and D_2 would indicate longer development than D_1 so that the film threshold has been decreased. Figure 31(b) shows the different apparent drop diameters possible with the above conditions.

Development conditions can, of course, be standardized so that at least this effect can be made consistent. The question still remains, however, at what conditions of development should the conditions be fixed?



(a) Two image intensities and development conditions.



(b) Apparent drop diameters for conditions in (a).

Figure 31. - Variation of apparent drop diameter with different image intensity and development conditions.

Intensity variation on the other hand is hard to control. The intensity of a light source might vary from flash to flash and also spatially over the field of view of the camera.

This error will, of course, be greatest for the small drops. For large drops the edge gradient length can be a small part of the total drop diameter, but for small drops the intensity profile can be completely made up of the edge gradients with no constant intensity portion at the drop center as seen in Figure 30.

The sign of the error cannot be definitely stated either. In this technique where the drops actually radiate, the image of the drops is increased at least by that of the Airy disc and no doubt more by the lens aberrations. If the threshold of the film is low the drops will appear larger than actual. If the threshold is high they will appear smaller. In a shadowgraph technique, however, where the drops are opaque, there is no question but that the drops will appear smaller than actual size. The image is actually smaller and development can only make it still smaller.

The above is compounded by turbidity in the film emulsion which is the diffusion of light away from the actual image on the film. This will also contribute to the edge gradient of the image. In this case a high gamma film will reduce the edge gradient due to turbidity.

A possible solution to the above problem would be to make up a calibration slide with transparent circles on an opaque background such that the circles were equal in diameter to the size category boundaries. This slide could then be backlighted with radiation similar to that of the fluorescent radiation and such that the slide

photographs were of comparable density with that of actual drop photographs. The resultant photograph could then be processed exactly as the drop photographs and sized on the Iconumerators. The size categories could then be adjusted to give a more realistic count of the data.

As previously mentioned the above has been performed with an annular ring reticle and a calibration made for a hand counting procedure, but this reticle is not adaptable to machine counting.

The question will still remain as to how close the radiation distribution in the transparent circles of the calibration reticle is to that actually coming from a fluorescing drop. The above reticle will, however, at least give an approximation to proper calibration.

Another error, although small, is the multiple exposures used on a single film. This is done since the spray population is so low in the sample volume. If multiple exposure were not used an enormous amount of film would have to be processed and analyzed to obtain a reasonable number of drops in a sample. Thus ten exposures are used on each film. Multiple exposure can cause the overlapping and masking of one drop by another. This can be observed on the films, but their occurrence is very rare, again, due to the low population density.

If two drops overlap two cases must be considered. If they are orientated with their longer dimension perpendicular to the dimension of scan, only the larger drop will be sized and counted. If they have their longer dimension parallel to the direction of scan the two drops will be sized as one larger drop.

If a large drop is at the edge of the light sheet it will be

only partially illuminated and usually is out of focus on the film. The edge gradient on such a drop is very low, but its center can easily be of sufficient density to be counted by the Iconumerator. This will result in the blurred image being sized as a smaller drop than it actually is. Fortunately, the great majority of the drops are not of this nature, but a small shift in the distribution towards smaller sizes should be expected from this error.

The above error could be minimized by an appropriate circuit addition to the Iconumerator. Figure 32 shows a block diagram of a possible circuit that could be used. The circuit would operate as follows.

The drop intercept signal is formed by the multiplier phototube. This is fed to a 3 microsecond delay circuit and to a differentiator. The differentiated leading edge is passed to a circuit which determines the amplitude of the leading edge gradient. If this gradient exceeds a certain value, the gate is opened and the intercept signal is sent to the Iconumerator for sizing and counting. The 3 microsecond delay for the intercept signal before the gate is necessary to insure that the gate is opened before the intercept arrives. Otherwise, the leading edge of the intercept might be chopped off.

The trailing edge gradient is delayed 3 microseconds and possibly amplified to close the gate and make it ready for the next intercept signal. The delay is necessary to prevent chopping of the intercept signal trailing edge.

The allowable leading edge gradient would have to be determined by careful analysis of microdensitometer profiles of both good and

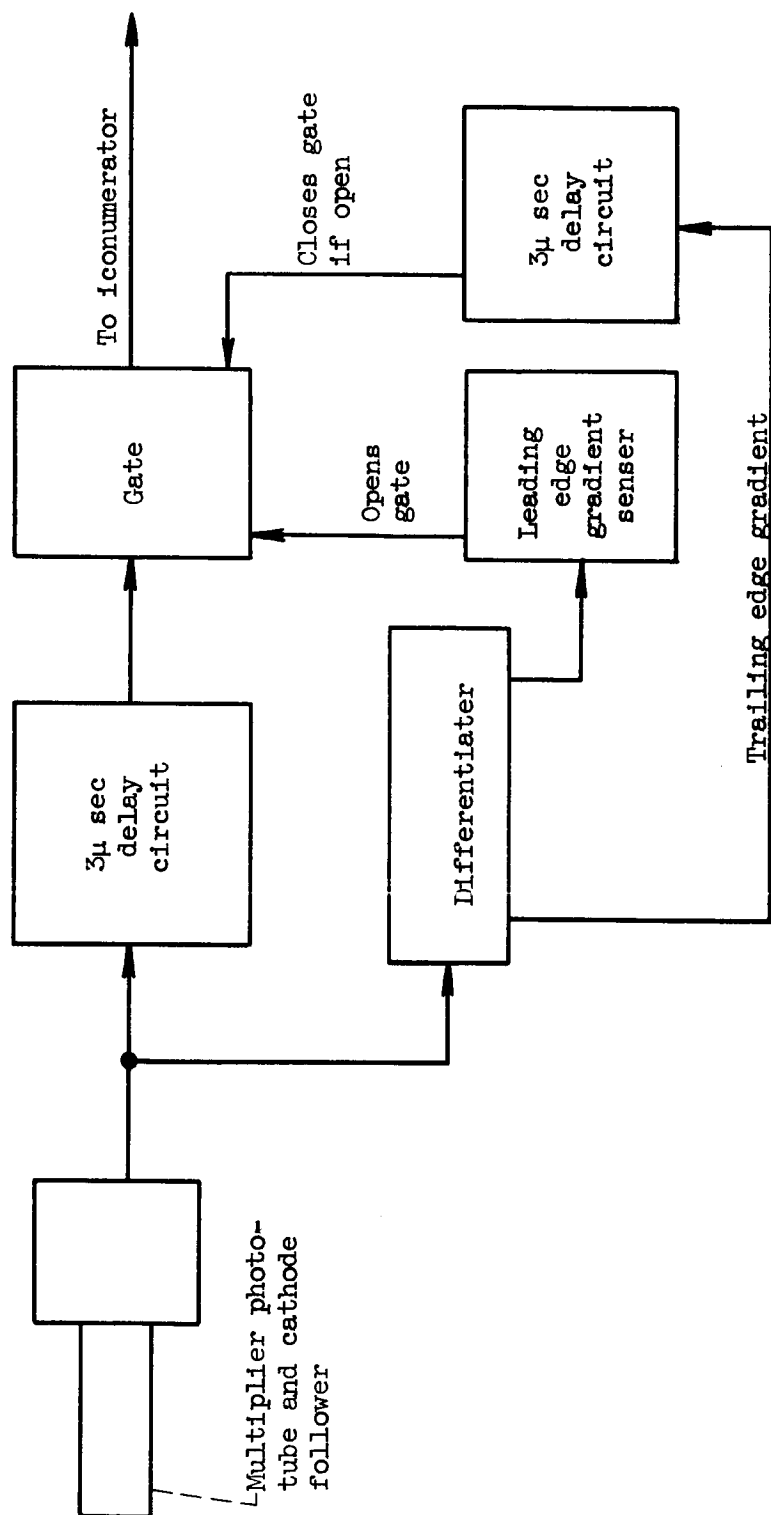


Figure 32. - Block diagram of suggested circuit for removing blurred drops.

out of focus drops.

Another possible error occurs since only two or three scan lines intercept the smallest 0.25 mm. drops on the film. It is possible that the maximum chord (the diameter) is thus not intercepted and the drop appears smaller than actual size. The resolution would have to be increased to reduce this error, or else the small size category clipping levels reduced to compensate for this error.

No correction for drops on the edge of the scanning field has been made. In the later section on Statistical Considerations it is shown that the distribution has been altered due to edge effects by the following factor.

$$E = \frac{3d}{2W}$$

where

E = fraction of drops altered in a particular category due to edge effects

d = drop size in this category (on film)

W = width of square field scanned

In this paper $W = 1\frac{3}{4}$ inches and for one of the larger drops observed $d = 5$ mm., then $E = 16.8\%$. Thus even for the largest drop only 16.8 percent will be altered due to edge effects. In view of the probable error in these large size categories due to just statistical errors in sampling, this 16.8 percent correction is not justified. This error decreases rapidly for smaller sized drops and is considered negligible.

If the largest observed drops approach the size of the scanning square this error will, of course, be large and correction must be made.

In view of the previous discussion it must be realized that some shift in the drop size distribution toward smaller sizes is to be expected. This shift should not be excessive at least for drops above 20 to 30 microns. It is admitted that in the 10 to 20 micron range more error will result.

The alternate procedure of hand counting will certainly result in a more excessive error than with the Iconumerator. With hand counting the operator must make a judgement as to whether a drop is of sufficiently good focus to be counted. Invariably the smallest drops, due to resolution, and the largest drops, due to edge effects in the light sheet, will have the poorer focus. More of these will be expelled from the count and the distribution biased toward moderate sized drops.

Hand counting also results in very poor reproducibility as was observed upon recounting of the data. The Iconumerator reproduces the count very well and is at least consistent if not perfectly accurate.

It is hoped that future workers on this project will be able to determine the errors involved more precisely and make the necessary corrections to their data. This might be accomplished by the previously mentioned calibration slide or perhaps it will necessitate a completely different approach. This can be accomplished if sufficient time is allotted.

In a letter from H. P. Mansberg (9), one of the designers of the Iconumerator, Mr. Mansberg suggested that better regulation of the CRT heater supply, high voltage phototube supply, and anode supplies

would be desirable. He also suggested redesign of the scan deflection circuits to achieve more linearity in the scan.

Redesign of the circuits was not attempted but better overall voltage regulation was obtained by the use of a constant voltage transformer. This made a definite improvement in the stability of the circuits. Without this transformer definite count differences could be obtained from changes in the line voltage.

Scanning nonlinearity was very apparent when a field of large drops on a calibration slide was scanned. A difference in the residual sizes after sizing was apparent between the left and right sides of the monitor screen. The scanning linearity controls were adjusted to reduce this nonlinearity. The nonlinearity cannot be completely removed, but its effect is considered small. A test slide with various sized particles could be scanned with various orientations without appreciably changing the sizing.

In summary, no appreciable error will occur due to the Iconumer-ator and the size discriminator themselves. This system can be accurately calibrated. The errors that do arise are from the nature of the film image itself. For very small drops in the region of 10 to 20 microns error will occur due to edge gradients. This can be minimized by setting the Iconumer-ator Schmitt Discriminator clipping level just above the background noise level. This error will decrease rapidly as the edge gradients become a smaller percentage of the total diameter which is the case for increasing drop sizes.

A consideration of errors due to the sample size will be included in the Statistical Consideration section and the discussion of the data.

Nozzle Carriage

The nozzle carriage can be seen in Figure 3. This consists of a three-dimensional movement on which is mounted the nozzle holding tube.

The carriage movement is mounted on ways machined in an I-beam. The entire carriage can be moved along this I-beam by means of a 40 threads per inch micrometer screw. This provides the axial movement of the carriage.

Lateral and vertical movement is also accomplished by two sets of 40 threads per inch micrometer screws. The range of this movement is such that one quadrant of the spray can be completely sampled.

The axis of the nozzle holding tube is parallel to the machined ways and is at a 15° angle to the camera axis.

CONSIDERATIONS FOR IMPROVEMENT OF THE LIGHT SOURCE

The radiation intensity of the present light source was shown to have attained its saturation brightness in the 5000 Å spectral region. This was indicated by the fact that a change from 65 to 80 joules resulted in no additional increase in brightness. Another indication was that shortening the gap length with constant capacitor loading resulted in no brightness increase when viewing a fixed portion of the discharge length. This should have increased the energy concentration yet no brightness increase resulted.

This section is included to show how the brightness of the guided spark can be increased by the use of a gas such as nitrogen, helium, or hydrogen rather than air. Generally the indication is that the heavier inert gases prove to provide the highest light intensity (10,15) but this is true only for very small energy loading and low gas pressure. The opposite is true for high loadings with low circuit inductance, and xenon is found to have lower intensity than even that of nitrogen. The phenomena involved here is that of a maximum plasma temperature which will be discussed.

A short discussion of the circuit parameters involved in the discharge circuit will be included since these are necessary in following sections.

Discharge Circuit Parameters

The discharge circuit is generally denoted by its equivalent circuit (11) which is a series combination of L , R , and a switch connected across a capacitor of capacitance C where:

L = inductance of capacitor and leads (Henries)

R = resistance of capacitor (internal), leads, and spark gap during conduction

C = capacitance (Farads)

The switch is used to indicate that an open circuit exists before breakdown of the spark gap.

Upon closing the switch (spark gap conducting) the differential equation for the voltage around the loop can be written and solved. This leads to three different solutions depending on the quantity:

$$w^2 = \frac{1}{LC} - \frac{R^2}{4L^2}$$

When $w^2 < 0$ the condition of an overdamped discharge occurs. If $w^2 = 0$ the circuit is critically damped. The usual case of an underdamped oscillatory discharge occurs when $w^2 > 0$ and will be considered here.

Thus for $w^2 > 0$ the solution is:

$$I = \frac{U}{wL} e^{-\mu t} \sin wt$$

where

U = initial capacitor voltage

t = time

$$\mu = \frac{R}{2L}$$

w and L as above.

For low resistance such that:

$$\frac{1}{LC} \gg \frac{R^2}{4L^2}$$

then $\omega^2 = \frac{1}{LC}$

With the above approximation:

$$I = U \frac{C}{L} e^{-\mu t} \sin \omega t$$

and $I_{\max} = U \frac{C}{L} e^{-\mu t}$.

For small t , i.e. during the early stage of discharge:

$$I = U \frac{C}{L} \sin \omega t$$

$$I_{\max} = U \frac{C}{L}$$

and

$$\left(\frac{dI}{dt} \right)_{t=0} = \frac{U}{L}$$

$\left(\frac{dI}{dt} \right)_{t=0}$ determines in first approximation the rate of power intake

by the spark gap (12) and will later be used to characterize the circuit when discussing maximum temperature in the spark discharge.

From the above it can be seen that to increase the maximum current one must increase the capacitor voltage or the capacitance itself, or decrease the inductance. Generally an increase in capacitor voltage rating or in capacitance will lead to an increase in inductance due to increased capacitor size. Specially designed coaxial capacitors such as used by Fischer (13) can be used to give maximum capacitance and voltage rating with a minimum inductance. The current path must be made as short as possible to cut down the inductance.

Reference 11 is recommended for those who wish more information on the determination of circuit parameters from experimental observations.

Temperature Saturation

Many investigators have observed the phenomena of temperature saturation in a spark discharge. In the following some of the results of these observations will be discussed.

Since the present light source used in this technique is a guided spark in air at atmospheric pressure, the work of Mak (14) is of immediate interest. This work involved a study of variation of channel temperature with rate of increase of current for a spark discharge in air. The circuit parameters were as follows: $C = 0.05$ ufd, $U = 3$ to 8 KV, $L = 4 \times 10^{-9}$ to 5.4×10^{-5} henries, spark gap 5 mm. for $L = 4 \times 10^{-9}$ and 1.5 mm for $L = 4 \times 10^{-9}$ h. The results of this work are listed below with U = capacitor voltage, L = circuit inductance.

TABLE I - SPARK DISCHARGE TEMPERATURE VRS. RATE OF CURRENT INCREASE

$\frac{U}{L} \frac{\text{amp}}{\text{sec}}$	1.3×10^8	3.2×10^8	6.8×10^8	2×10^9	7.5×10^{11}	9×10^{11}
T °K	29,000	29,000	30,000	26,000	31,000	33,000

The author stated that the scatter of the data was within the error of measurement (~30-35%). In the larger rate of current increase points, the author studied the brightness of the N II 5001A line which was quite broad and flat during the high temperature portion of the spark. This indicated black body radiation in this spectral region even at $U/L = 10^{11}$ amp/sec.

The conclusion in the above was that channel temperature varies very little with rate of increase of current when the latter is high.

The value of U/L for the present light source discussed in this paper was about 2.4×10^{11} amp/sec. This would indicate temperature saturation at least in the vicinity of 5000A.

Mak (14) states that at $U/L = 9 \times 10^{11}$ studies of the background radiation showed that under his discharge conditions the channel radiated as a black body at 33,000° K. The author also stated that the temperature in air (~30,000° K) is lower than that in nitrogen (~43,000° K) apparently due to the cooling effect of oxygen which has lower ionization and dissociation energies than that of nitrogen.

Vanyukov and Mak (16) measured the temperature of the spark-discharge channel in argon, xenon, and nitrogen as a function of the spectral density of the brightness of the channel for wavelengths corresponding to the centers of several emission bands. The rate of admission of energy U/L was varied in this study.

The radiation bands were as follows: argon, $\lambda = 4806A, 4368A,$ and $3588A$, xenon, $\lambda = 2900A, 2600A,$ and nitrogen, $\lambda = 4097A, 5001A,$ and $5045A$.

For argon and xenon the circuit parameters were: $c = 0.05$ ufd, $U = 12$ KV, and $L = 0.086$ to 1.28 microhenries. The pressures were 4 and 5 atmospheres, respectively.

The tests with nitrogen were conducted with: $C = 0.05$ ufd, $U = 15$ KV, $L = 0.086$ to 0.78 microhenries, and $p = 2$ atm.

The results of these tests are shown as curves 1, 2, and 4 of Figure 33. The temperatures were calculated by Planck's formula for

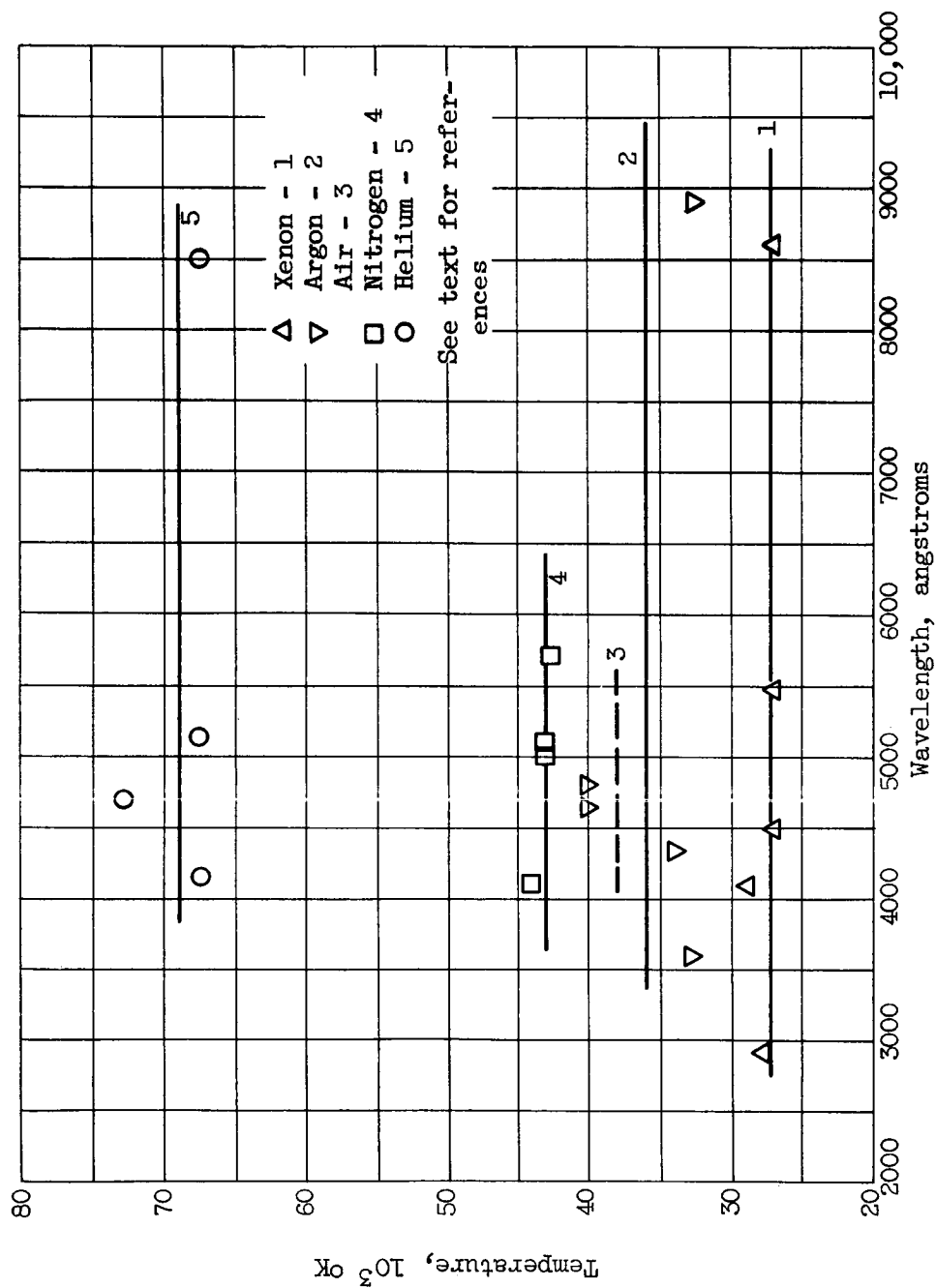


Figure 33. - Maximum channel temperature as calculated from maximum radiation intensity at various wavelengths for several gases.

black body radiation with the spectral density of the brightness for those wavelengths of the band spectra and of the continuous spectrum for which saturation of brightness is observed. The author gave no reason for the scatter in the argon but noted that the scatter of temperature calculated for different wavelengths is small for xenon and nitrogen.

Curves 3 and 5 of Figure 33 for helium and air were obtained from Reference 17 with the original reference being reference 18. Curve 5 for air shows a temperature of 38,000 K somewhat higher than the 33,000° K temperature determined in Reference 14 as previously discussed although both papers are by the same author (A. A. Mak).

Curve 3 for helium shows a temperature of near 70,000° K which is substantially higher than that of the other gases. It is, however, much lower than that of helium reported by Fischer (13).

Fischer reports a temperature obtained in a helium spark discharge of over 250,000° K. The conditions for this discharge were $C = 2.8$ ufd, $L = 0.035$ uhy, $U = 7$ KV, and $p = 35$ atmospheres. The brightness of this discharge was over 150 million candles per cm^2 as compared to an air discharge with the same equipment but 3.1 KV resulting in 45 million candles per cm^2 . In reference 12 Vanyukov and Mak are of the opinion that this temperature of 250,000° K is somewhat high but admit that it is apparently the highest temperature registered in a spark discharge channel.

Reference 17 gives an excellent discussion of the temperature saturation phenomena and reports the following conclusions. For an unbounded discharge at constant energy input the brightness increases

with pressure up to a certain limit and then no longer depends upon pressure. At a given pressure the brightness increases with energy input up to a certain limit and thereafter no longer depends upon energy input increases. For gases of smaller atomic weights the brightness is lower at small pressures and energy concentrations than for heavy gases. As the pressure and/or energy concentration is increased the brightness in the lighter gases overtakes that of the heavier gases and the upper limit of brightness is greater for the lighter gases than for the heavier gases. The absolute discharge brightness limit increases with decreasing atomic weight A of the gas approximately as $A^{-1/3}$. Reference 12 suggests that upper brightness limits depend actually upon increased ionization potential and dissociation energy and not really upon atomic weight.

The reason for an upper limit on temperature is not definitely known but the following has been suggested. For each gas the "effective specific heat" of the plasma, which accounts for the energy consumed in ionization, channel expansion, and radiation suddenly begins to increase, at a certain temperature, at such a high rate that an increase in temperature would require an impractically large increase in energy input (17). Vanyukov and Mak (12) add to this the counterbalancing phenomenon of increased energy intake due to increased ionization and radiation to that of decreasing energy intake due to lower plasma resistance from increased ionization. Thus the temperature cannot increase indefinitely.

The above discussion has been for unbounded spark discharges. Reference 12 states that even higher temperatures can be obtained in

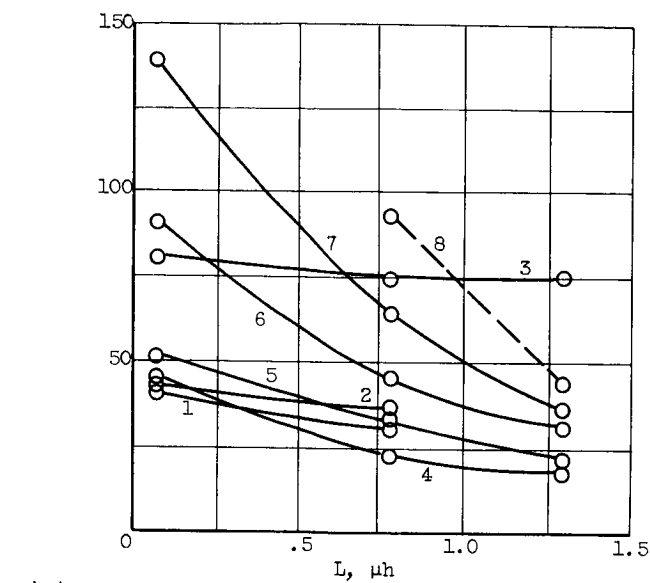
capillary discharges for any given gas. It is noted, however, that there is an optimum capillary diameter above or below which the temperature will be less than at the optimum diameter. This is shown by the following data. For an air discharge at atmospheric pressure, 12 KV, 0.011 ufd, and capillary diameters of 1.3, 0.4, and 0.25 mm. the temperatures were $29,000^{\circ}$ K, $48,000^{\circ}$ K, and $36,000^{\circ}$ K respectively.

Temperature Saturation Dependence Upon Wavelength

In the preceding section the work of Vanyukov and Mak (16) were discussed with regard to curves 1, 2, and 4 of Figure 33. The following is a further aspect of the same data and reference to this preceding discussion should be made for circuit parameters and pressures.

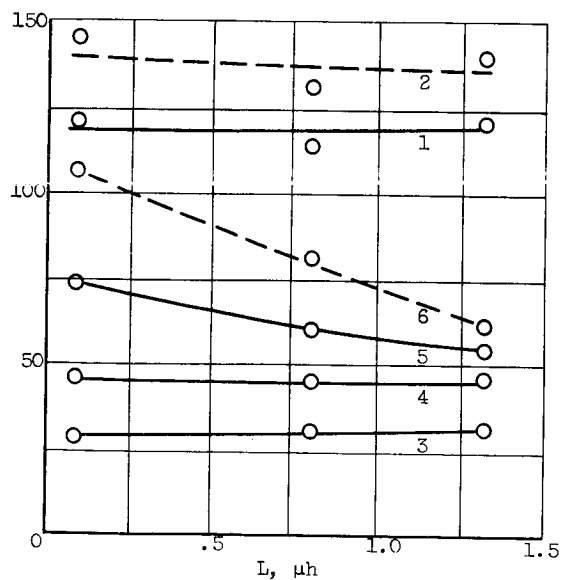
Figure 34 shows the variation of maximum spectral density of the brightness of the spark discharge with varying circuit inductance. For a fixed capacitor voltage, a lower inductance indicates a higher value of U/L which is a measure of the rate of power intake by the channel. Figure 34a is for argon and Figure 34b for xenon. It should be recalled that the band emission for argon was at 4806, 4348, and 3588 A while for xenon the band emission was at 2900 and 2600 A.

Figures 34a and 34b show that within the range of variables used, the band spectrum show brightness saturation or at least near brightness saturation while the continuous emission below 4000 A was still far from saturation. The longer wavelength continuous emission for xenon showed saturation over the entire range of inductance while



(a) Argon - Band emission: (1) 4806 Å; (2) 4348 Å; (3) 3588 Å. Continuous emission: (4) 4680 Å; (5) 3990 Å; (6) 3400 Å; (7) 2900 Å; (8) 2600 Å. Curve 8 is drawn on a relative scale.

$V_{\lambda}, \frac{W}{cm^2-ster-A}$



(b) Xenon - Band emission: (1) 2900 Å; (2) 2600 Å. Continuous emission: (3) 4490 Å; (4) 4080 Å; (5) 3400 Å; (6) 2300 Å. Curves 5 and 6 are drawn on a relative scale.

Figure 34. - Variation of the maximum spectral density of the brightness of the channel of the spark discharge in argon and xenon as a function of circuit inductance.

that for argon was near saturation but not complete. The authors also state that for nitrogen, saturation of the continuous emission (with λ greater than 5500 Å) and for the band spectra was observed.

Figure 35 shows diagrammatically the phenomenon observed above (17). Curve 1 represents the black body radiation for the maximum temperature for the particular mode of discharge. Curve 2 shows the case where insufficient energy has been discharged to saturate the entire spectrum. The band spectrum will reach the maximum brightness first while the continuum remains unsaturated except at long wavelengths. As the rate of energy input increases by either higher voltage or lower inductance, curve 2 will be raised and will ultimately coincide with curve 1.

The temperature along the cross section of the spark discharge channel can be assumed to be homogeneous. If this were not true one would expect the appearance of absorption lines since the absorption coefficient of the plasma is very dependent on the temperature (17). The absorption lines do not occur so the temperature must be constant across the channel.

Summary

From the above discussion the following conclusions can be drawn.

(1) For each gas in an unbounded spark discharge there exists an upper limit to the temperature and brightness that can be attained. This upper limit can be attained by increased rate of energy input U/L and higher pressures.

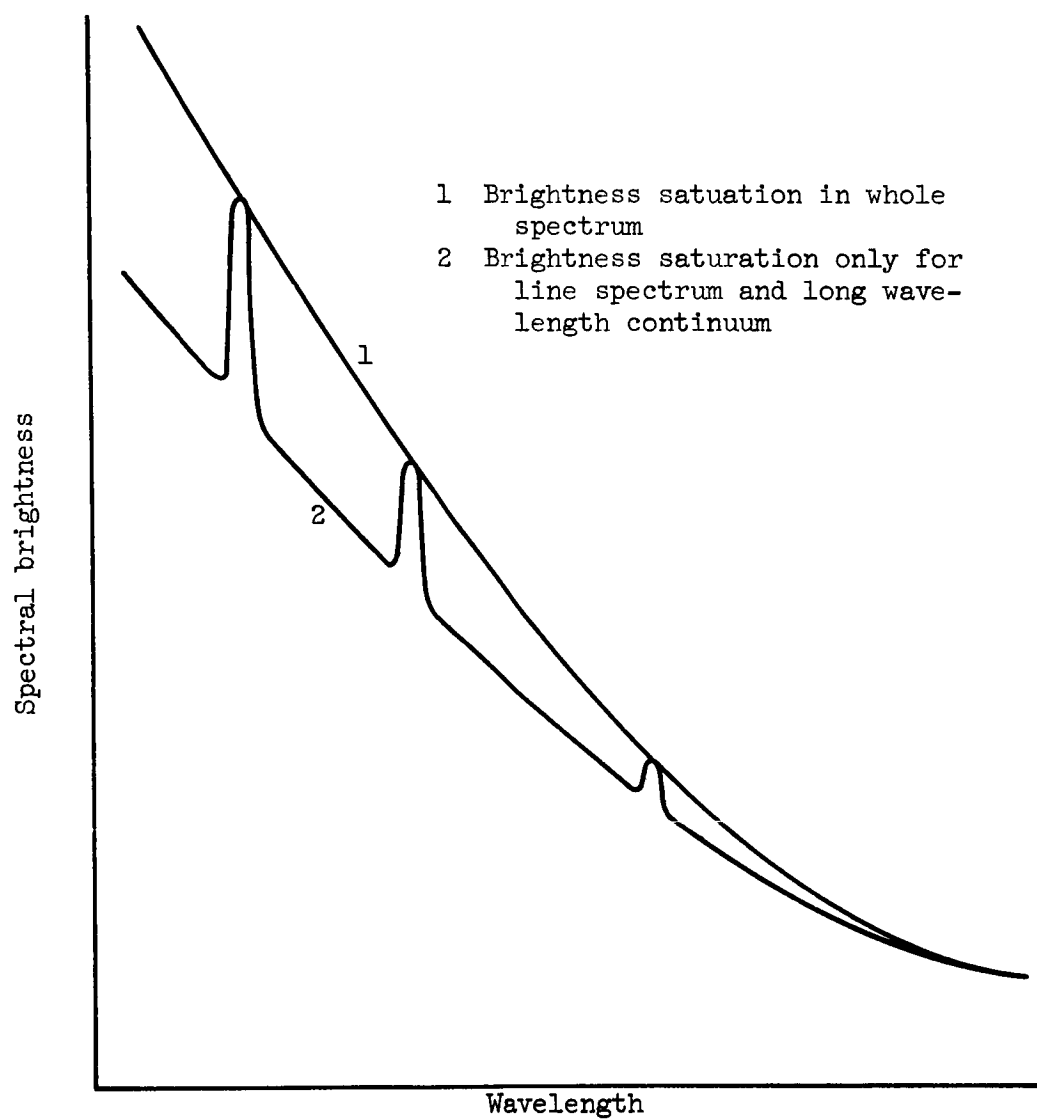


Figure 35. - Diagrammatic illustration of complete and partial brightness saturation.

(2) The lighter gases have a higher limiting brightness than the heavier gases.

(3) The higher the limiting brightness the harder this limit is to attain. The limit in xenon is obtained with low U/L while that of helium requires great rates of energy input.

(4) Brightness saturation occurs first for the line spectra and long wavelength continuous emission.

(5) Higher limiting brightness may be attained in a constricted channel than in an unbounded channel.

It is therefore suggested that future efforts to increase the brightness of the present guided spark discharge in air include the following:

(1) A discharge medium of nitrogen or preferably helium could be tried.

(2) A pressure tight envelope could be built around the light source with the condensing lens comprising one end of this enclosure or tube. This would allow pressurizing the nitrogen or helium and might make the use of hydrogen practical.

(3) Further efforts to reduce the circuit inductance and increase the supply voltage could be made. This would increase the rate of power input U/L and make the approach to brightness saturation more complete. This would be especially important if saturation near 2500 A is desired.

Increase in pressure would be necessary if helium were used since the breakdown voltage for a given pressure and gap length is

considerably lower than that of air (19).

Helium could be an improvement even if complete saturation were not attained. The He II 4686 A line is very strong even at fairly low temperatures (20). This line is well within the absorption spectrum of fluorescein and can be expected to broaden considerably as saturation is approached. A strong continuum is also observed near 2600 A (20) which would contribute to the fluorescent emission of fluorescein.

OPTICAL ALIGNMENT PROCEDURE

Precise optical alignment is an absolute necessity with this fluorescent technique. The depth of field of the camera, as determined by the resolution criterion discussed below, is 220 microns while the radiation sheet thickness is 200 microns. It can thus be seen that the precise superposition of the depth of field and the radiation sheet must be made if out of focus drops are to be minimized.

In addition, the reflected radiation sheet from the spherical mirror must be precisely superimposed upon the original light sheet if its thickness is to remain at 200 microns and within the depth of field of the camera.

The focusing of the camera, condensor lens alignment, and spherical mirror alignment will be discussed in this order since they are performed in this order to insure overall optical alignment.

Camera Focus

Figure 36 shows a top view of the focusing apparatus set-up. The components are not drawn to scale and are shown only for illustrative purposes.

A stage micrometer reticle made by the American Optical Company ruled in 10 micron divisions over a length of 2 mm. was placed in the radiation sheet at a 45° angle to the radiation sheet axis and in the center of the field of view of the camera. The ruled side faces the

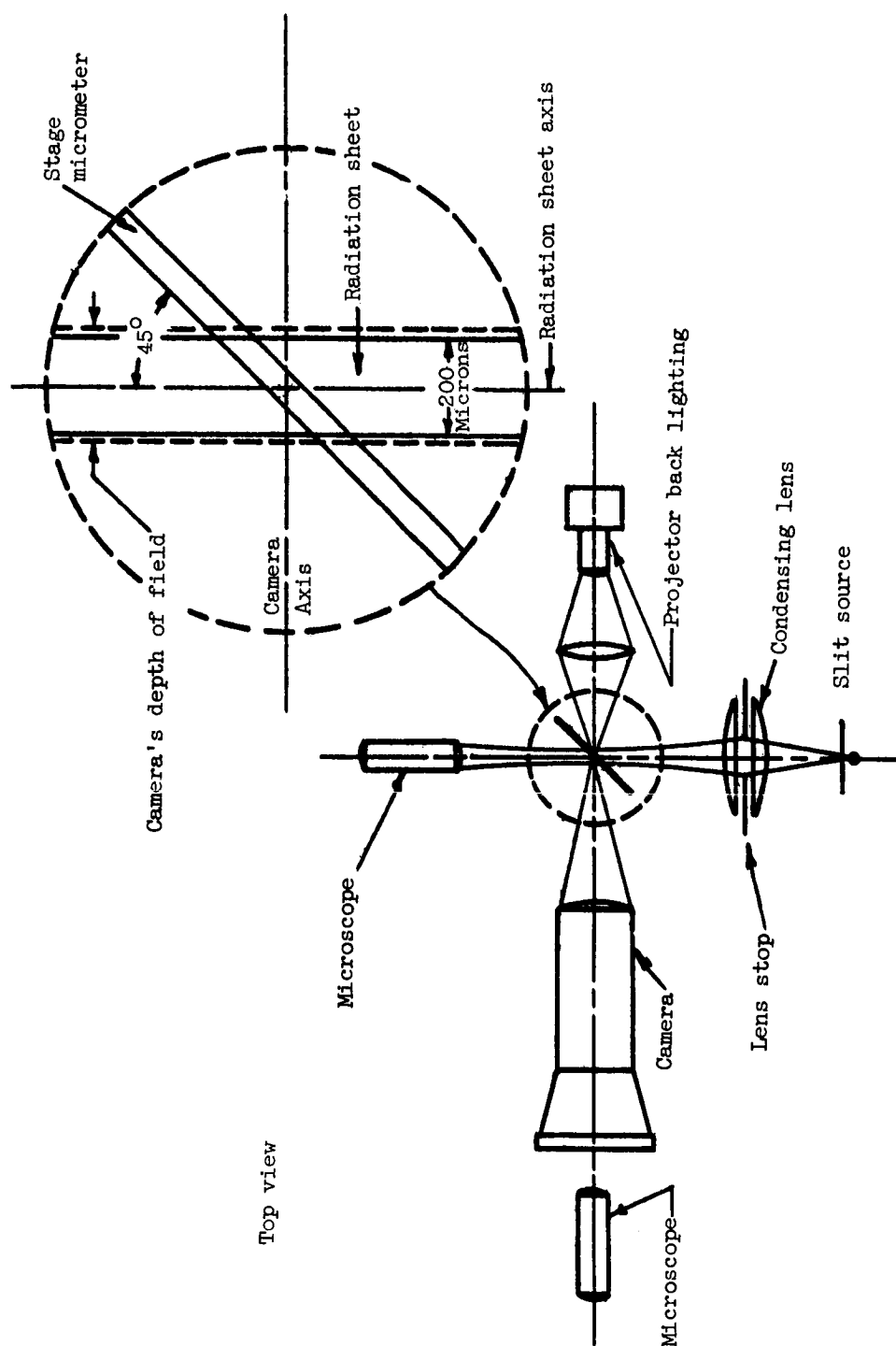


Figure 36. - Diagram of focusing apparatus set up.

camera, and the reticle cover plate was removed to eliminate refraction errors between the reticle and the camera.

The radiation sheet is viewed end-on in a microscope, and the position of the edges of the radiation sheet is noted before the reticle is put in place. This is done since the reticle will shift the apparent location of the radiation sheet due to refraction, and this shift must be considered to enable precise reticle location.

The reticle was backlighted by a projector and the radiation focused upon the reticle by a Taylor-Hobson Anastigmat $f/1.5$ lens. The f -number of the backlighting system must be less than that of the camera so that the camera will be used at its actual f -number. If a high f -number condensing lens were used, the camera would be effectively working at this high f -number, and the depth of field would appear greater than it actually is at the $f/5.6$ setting at which the camera operates.

A Kodak Wratten 74 filter was used with the backlighting system to simulate the spectrum of the fluorescent radiation.

A second microscope is used at the film plane of the camera to observe the reticle image. This microscope is focused on the film plane by inserting a piece of exposed and developed film into a special cut-away film holder. Reticle backlighting cannot be used during the focusing of this microscope since the microscope can then be moved a substantial distance with the film surface still appearing in focus. Direct lighting of the film by a lamp will provide the proper microscope focus.

To verify that the focus obtained when viewing the reticle image with the microscope is correct, the following test was made.

A pool of fluorescein-ethanol solution was irradiated by a pulsed BH-6 lamp located just above the pool. The fluorescent radiation from the pool surface was directed through the backlighting lens system by a second lens and mirrors. The resulting reticle image is recorded on Kodak Royal X-pan film. Thus conditions are duplicated as closely as possible to those under actual data taking conditions.

Upon examining the reticle photograph it was seen that viewing the image with a microscope as described above will give the proper image evaluation. If white light is used from the projector without a green filter, however, a shift of about 14 microns in the depth of field can be observed.

With the aid of the first microscope viewing the reticle directly, a known group of lines can be placed within the radiation sheet. The camera is then focused so that these lines can be clearly seen in the second microscope. Since the reticle is at 45° to the camera axis, the reticle lines will extend both in front of and beyond the camera's depth of field. By counting the number of lines in focus, a measure of the depth of field can be obtained. This was the procedure used for the measurement of the field curvature discussed in the camera section.

The above resolution criterion is indeed a stringent test of the camera. The lines on the reticle are about 2 microns in width and separated by an 8 micron transparent space. When viewed at a 45° angle it will appear as 1.4 micron lines separated by 5.6 microns.

The above procedure has shown the method of focusing used but has insured coincidence of the depth of field and the radiation sheet only at the camera axis. The condensing lens of the excitation optical system must be properly aligned to insure coincidence over the entire field of view of the camera and will be discussed next.

Condensing Lens Alignment

The above focusing procedure is repeated with the reticle placed in the extreme right and left sides of the camera field of view. A discrepancy will be noted between the group of reticle lines which are in the radiation sheet and those which are in good focus on the camera film plane. The inherent discrepancy is due to the curvature of field of the camera (see Fig. 10). The difference should be symmetrical about the camera axis. If this is not true then the radiation sheet axis is not perpendicular to the camera axis. The condenser lens then must be moved parallel to the camera axis, and the camera must be moved along its axis to maintain focus within the radiation sheet. The above is repeated until the camera axis and the condenser lens axis are perpendicular.

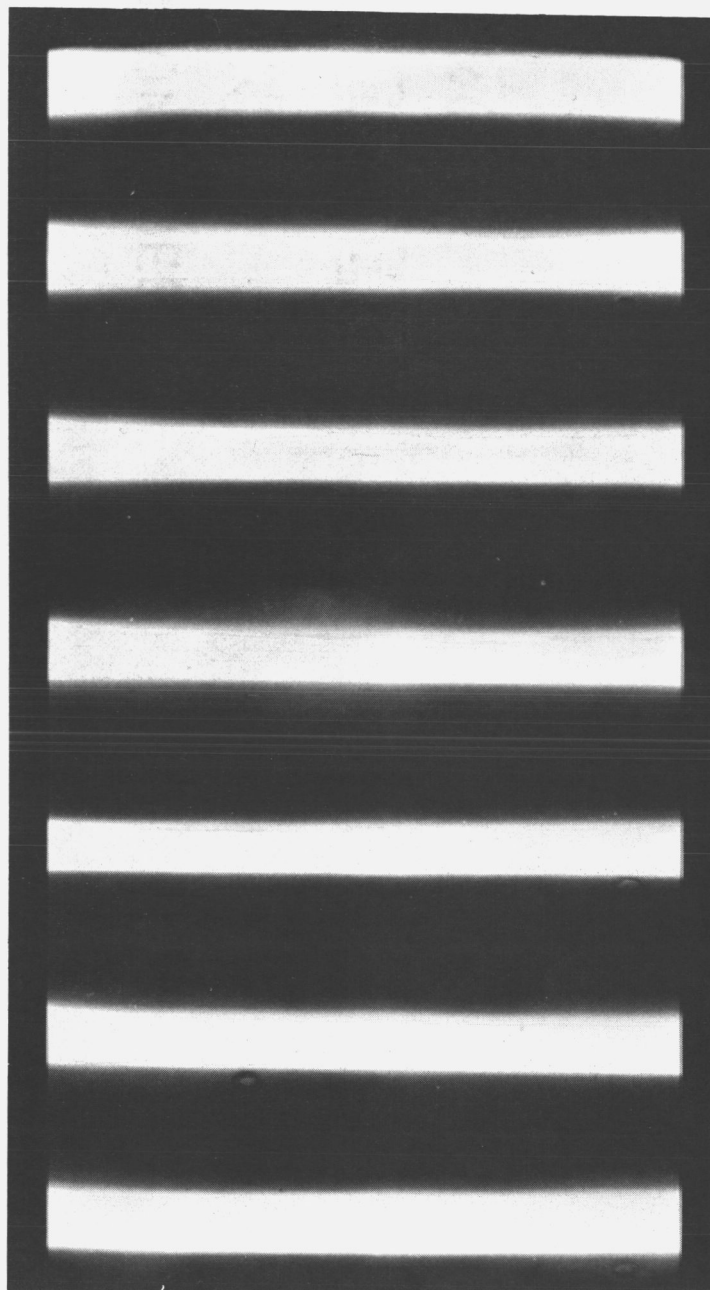
The reticle is then viewed as above but at the extreme top and bottom of the camera field of view. If an unsymmetrical discrepancy is again noted between those reticle lines in the radiation sheet and those in good focus on the camera film plane, then the camera axis is not perpendicular to the plane of the radiation sheet. The camera axis must then be rotated in a vertical plane and the above repeated until the perpendicularity is achieved.

It should be recalled that the image of the light source is spread along the axis of the condenser lens due to axial spherical aberration. This provides a radiation sheet of nearly constant thickness for about 5 mm. along the condenser lens axis. The field of view of the camera (4 mm.) must coincide with this sharpest light source image region since beyond this region the radiation sheet diverges quite rapidly.

The coincidence of the above is ascertained in the following manner. A first surface flat mirror is placed at a 45° angle to the camera and condenser lens axis. This mirror is located in the same position but perpendicular to the reticle in Figure 36. The radiation sheet is thus reflected directly into the camera. By moving the mirror along the condenser lens axis various radiation sheet cross-sections will be focused on the film plane. At each location the light source is pulsed and a complete survey of the radiation sheet profiles found in the camera field of view is recorded on a slow film.

Figure 37 shows such a survey of the radiation sheet cross-sections. It can be seen that the radiation sheet is very sharp toward the center of the film but is already beginning to diverge slightly towards the extreme left and right of the film.

If it is found that the radiation sheet is diverging rapidly and is unsymmetric about the camera field of view, the condenser lens must be moved along its axis without disturbing the light source image laterally. The above cross-section survey must then be repeated and corrections repeated until the camera field of view coincides with the best portion of the radiation sheet.



Scale: 1 inch on fig. is 1 mm in radiation sheet.

Figure 37. - Radiation sheet cross-section photographs.

Spherical Mirror Alignment

As previously mentioned the reflected radiation sheet must precisely coincide with the incident radiation sheet so that the resulting thickness of the two will not exceed 200 microns and thus exceed the camera depth of field. The test of this condition must be rapid and simple for it must be performed before each data taking run. This is necessary since slight vibrations tend to alter the mirror alignment and thus change the radiation sheet effective thickness.

Three holes were drilled into the light source from the rear and just touch the back side of the spark guide slot. The center hole can be seen in Figure 18 and the other two are located 8 mm. above and below this center hole. This spacing results in the image of the two outer holes being precisely at the top and bottom of the camera field of view in the radiation sheet. These alignment holes are back-lighted with a projector lamp.

The light passing through the alignment holes backlight the knife edges defining the light source boundaries. These rays then pass through the condenser lens and form an image in the sample volume of the radiation sheet. The spherical mirror then returns this image inverted, and the condenser lens refocuses this back upon the light source.

A piece of partially opaque paper is placed over the top alignment hole of the light sources such that a spot of light from the top hole can be faintly seen. The light from the bottom hole traverses the optical system as described above and returns in the vicinity of

the top hole. The spherical mirror is then adjusted so that the returning light spot is of minimum area and coincides precisely with the top alignment hole. This assures precise vertical, horizontal, and axial mirror alignment.

This alignment procedure is very sensitive since any error in image alignment in the radiation sheet will appear magnified four times back on the light source front face.

The light from these alignment holes is also used for reticle placement in the radiation sheet during the focusing procedure.

To insure that the best image portion of the reflected radiation sheet was being used, a procedure similar to that discussed in connection with the condenser lens was used. A first surface flat mirror was placed at 45° to the camera axis and such that the top half of the radiation sheet passes over the mirror. The spherical mirror then inverts the image such that it strikes the flat mirror and then passes into the camera. A photograph of the bottom half of the reflected radiation sheet can then be made at various locations in the camera field of view. The results of these photographs show that the above alignment procedures do indeed result in the best image region of the reflected radiation sheet being used.

The optical system is now in precise alignment. Very fine retouching of the camera focus may be necessary to insure that the curved field of the camera (see Fig. 10) covers the radiation sheet for a 4 mm. field of view.

PHOTOGRAPHIC PROCEDURE

Due to the low level of the fluorescent radiation from the irradiated drops, the recording device used in this technique must have extremely high sensitivity in the spectral region of 5200 Å. The recording device used thus far has been photographic film of which Kodak Royal X-Pan is the fastest available at this time.

Royal X-Pan is a fast, coarse grained, panchromatic film which is capable of improved speed with forced development and intensification. With an object brightness ratio of 1000 and using a low-reflectance lens of 328 lines per mm. resolution, the resolving power of Royal X-Pan is 90 lines per mm. (1). The current ASA number is 1250.

Figure 38 shows the Density-Log E characteristics and Figure 39 the spectral sensitivity of Royal X-Pan film.

According to a recent survey (21) of the films used currently in high speed photography Kodak's Royal X-Pan is still the fastest film available. This survey included forced development with various developers but did not include any intensification procedure.

Reference 21 also discussed Kodak Photofluore green sensitive film. This has a lower ASA value (1180) than Royal X-Pan (3000) when using forced development and exposure to white light. Mr. Pressman (21) did comment, however, that Photofluore was more sensitive to green light than Royal X-Pan.

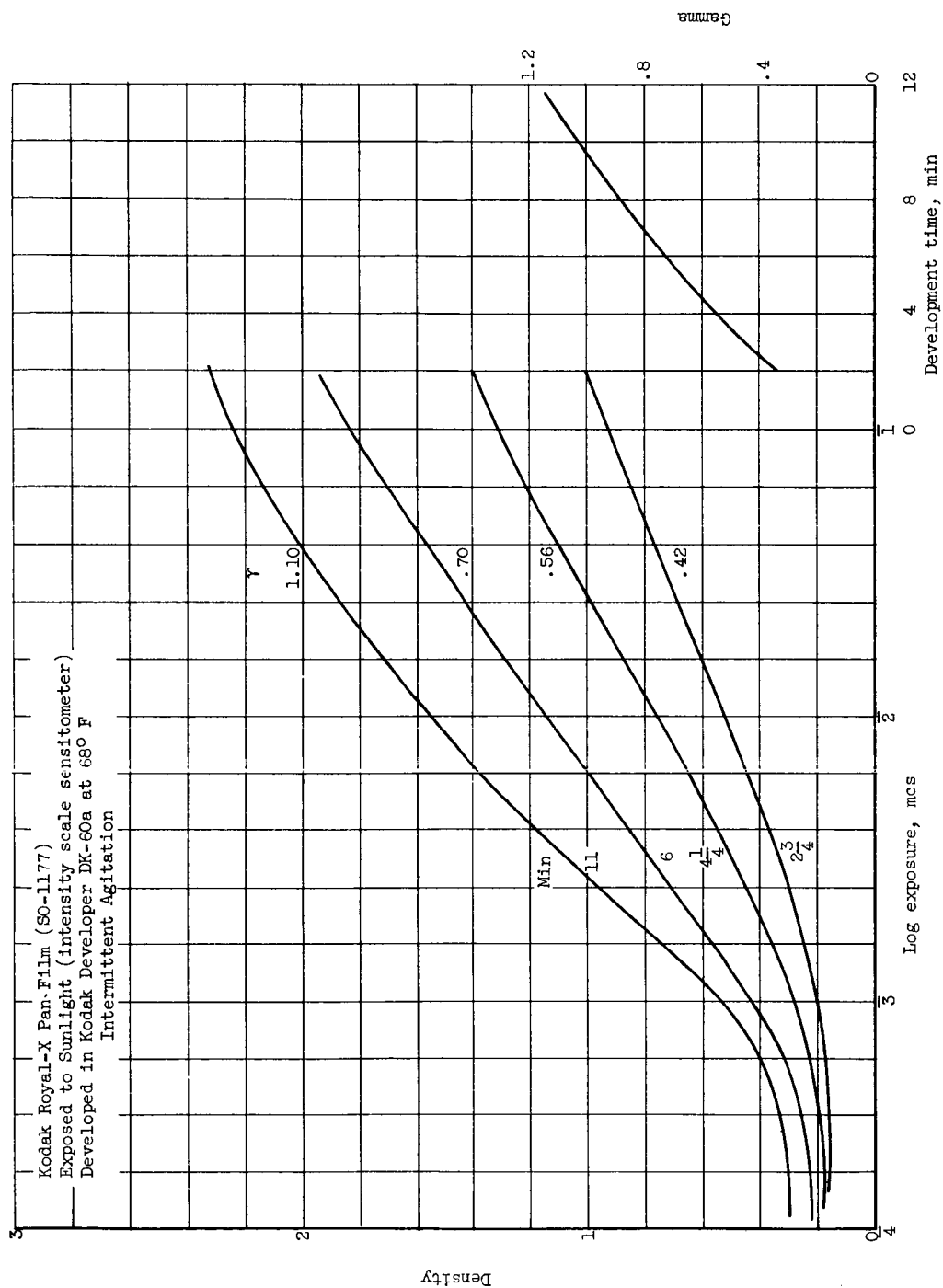


Figure 38. - Kodak Royal-X pan density - log E curves.

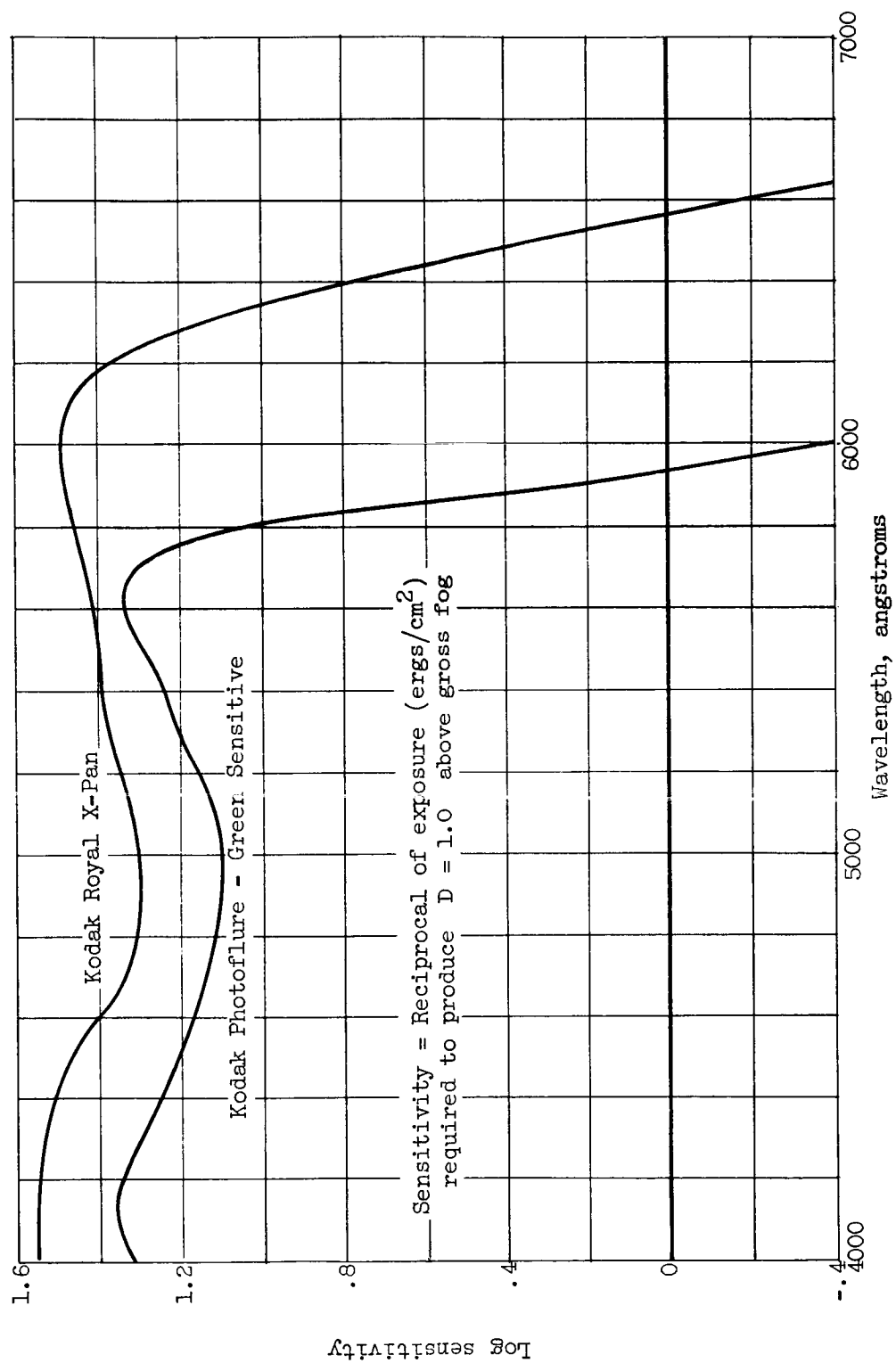


Figure 39. - Spectral sensitivity of Kodak Royal-X pan and Green Sensitive photofluore film.

Thus Photoflure was tried and drop photographs were taken. The film was developed for 7 minutes in Kodak Liquid X-ray developer. No improvement over the unintensified Royal X-Pan drop images were noted. The grain of the Photoflure appeared similar to that of Royal X-Pan.

The spectral sensitivity curve of Photoflure is also shown in Figure 39. It can be seen to be less sensitive than Royal X-Pan but approaches the latter near 5600A. It is possible that if time permitted a thorough examination of Photoflure with varying development and intensification procedures, conditions might be found such that Photoflure would outperform Royal X-Pan in the 5200A region. In Reference 21 it is stated that with the exception of Royal X-Pan improved speed will result by using high energy developers so more work should be done along this line.

The Density-Log E curves for Photoflure are given in Figure 40. Figures 38, 39, and 40 are from data published by the Eastman Kodak Company and are available upon request.

Development and Intensification

The drop photographs on Kodak Royal X-Pan are developed for 12 minutes in Kodak DK-60a at 70 F. The 4x5 inch sheet films are loaded in racks which each hold six films and are developed six racks at a time. The film racks are suspended vertically in a tank containing the developer and continuously agitated by moving them up and down with an electric motor and eccentric mechanism. Continuous agitation is necessary since otherwise a boundary layer will form on the film surface with a concentration profile ranging from development

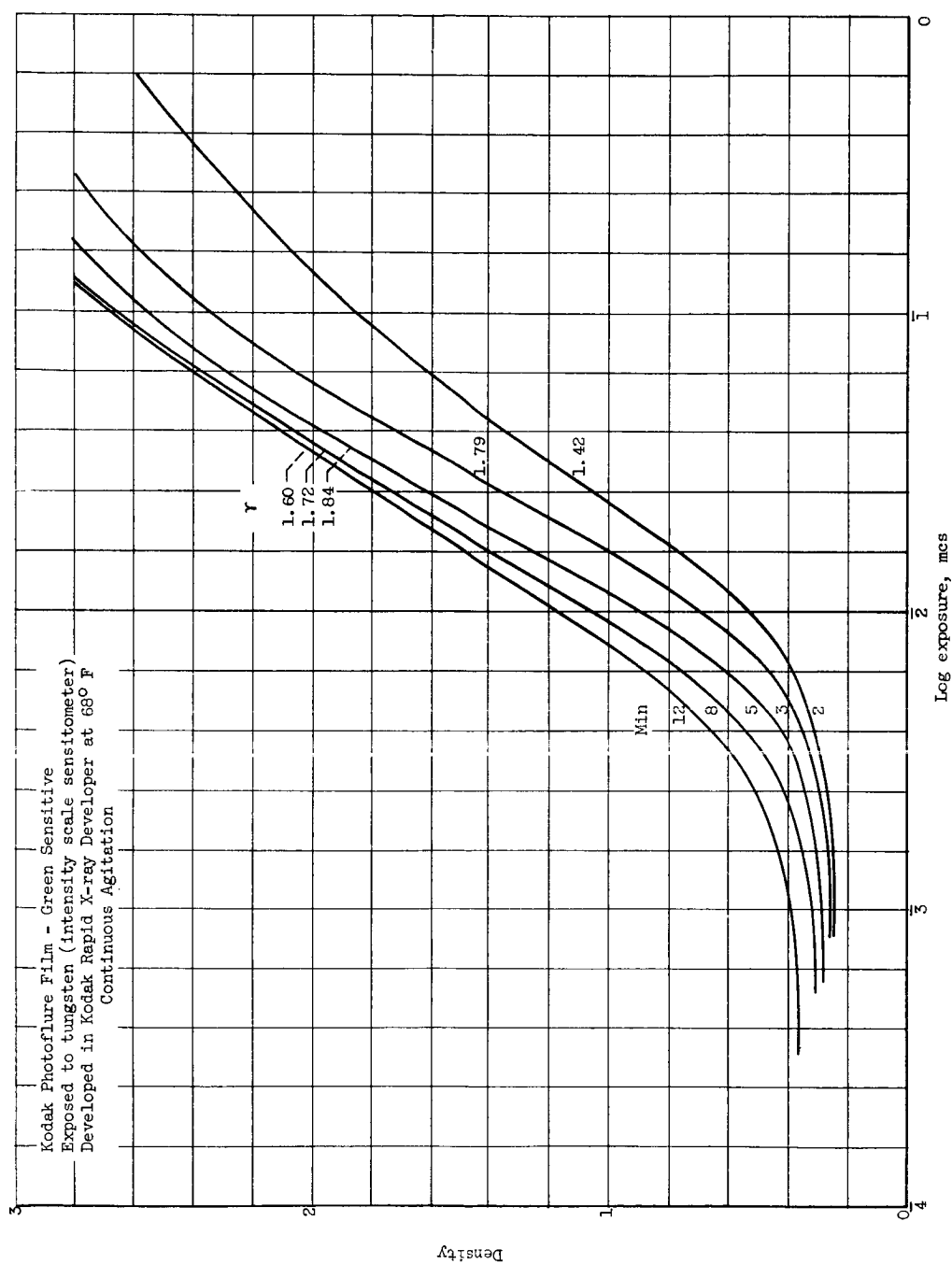


Figure 40. - Kodak green sensitive photofluor density - log E curves.

reaction products at the film surface to pure developer far from the film (55). This boundary layer must be broken up to provide fresh developer to the film. In addition without continuous agitation a stratification will occur with reaction products at the bottom of the tank and a high concentration of developer at the top (55). Thus density gradients would occur on the film with higher densities on the top.

After development the films are washed, fixed, and washed again all in their racks. A minimum of actual contact with the film by the operator is obtained in this manner. The intensification procedure is started immediately after the final wash. It was found that results were not as good and discoloring occurred if the films were allowed to dry before intensification.

The original intensification procedure consisted of bleaching the film in a chromium bleach as the first step. After washing the negatives were redeveloped in Ansco-47 Developer. The redevelopment should be done under diffuse light. The films are again thoroughly washed in preparation for the second intensification.

In the second step of intensification the films are first thoroughly bleached in a mercuric chloride bleach until white. The films are again thoroughly washed. The final step is redevelopment in Monckhoven's Intensifier. This contains potassium cyanide and great care must be taken when working with this deadly poison.

Controlled tests were run on Royal X-Pan film with the above intensification methods. The film was exposed with a tungsten filament light with a calibrated grey scale in contact with the film. All of the film was developed in Kodak DK-60a for 12 minutes at 70 F. One

group of films were then put through the entire intensification process while a second group was processed using only the second stage intensification (Mercuric chloride and Monckhoven's Intensifier). The results are shown in Figure 41.

It can be seen that either method of intensification (both stages or just second stage) double the gamma of Royal X-Pan. The gamma for 12 minute development in DK-60a is 1.12 (good comparison with Figure 38), and with either intensification method the gamma is about 2.25. The complete intensification procedure does provide a small speed increase in the toe region of the curve but also increases the fog level considerably. The second stage intensification, however, gives high gamma and some increase in speed in the toe region without much increase in fog level.

Since the useful density increase must be considered as that increase in density above the base fog, it can be seen that both stages of intensification offer very little advantage over that of only the second stage. In addition, an increase of base fog from density 0.38 to 0.5 will require an increase of spot brightness of the Iconumerator during film readout of 33%. This will increase the spot size and reduce resolution.

It was thus felt that due to the minute advantages and possible disadvantages during film readout, that the first stage of intensification be discontinued. Thus at present only the mercury and Monckhoven's Intensifiers are used.

It can be seen from Figure 41 that the results in Reference 1 were not confirmed. In Reference 1 Figure 65 it was claimed that

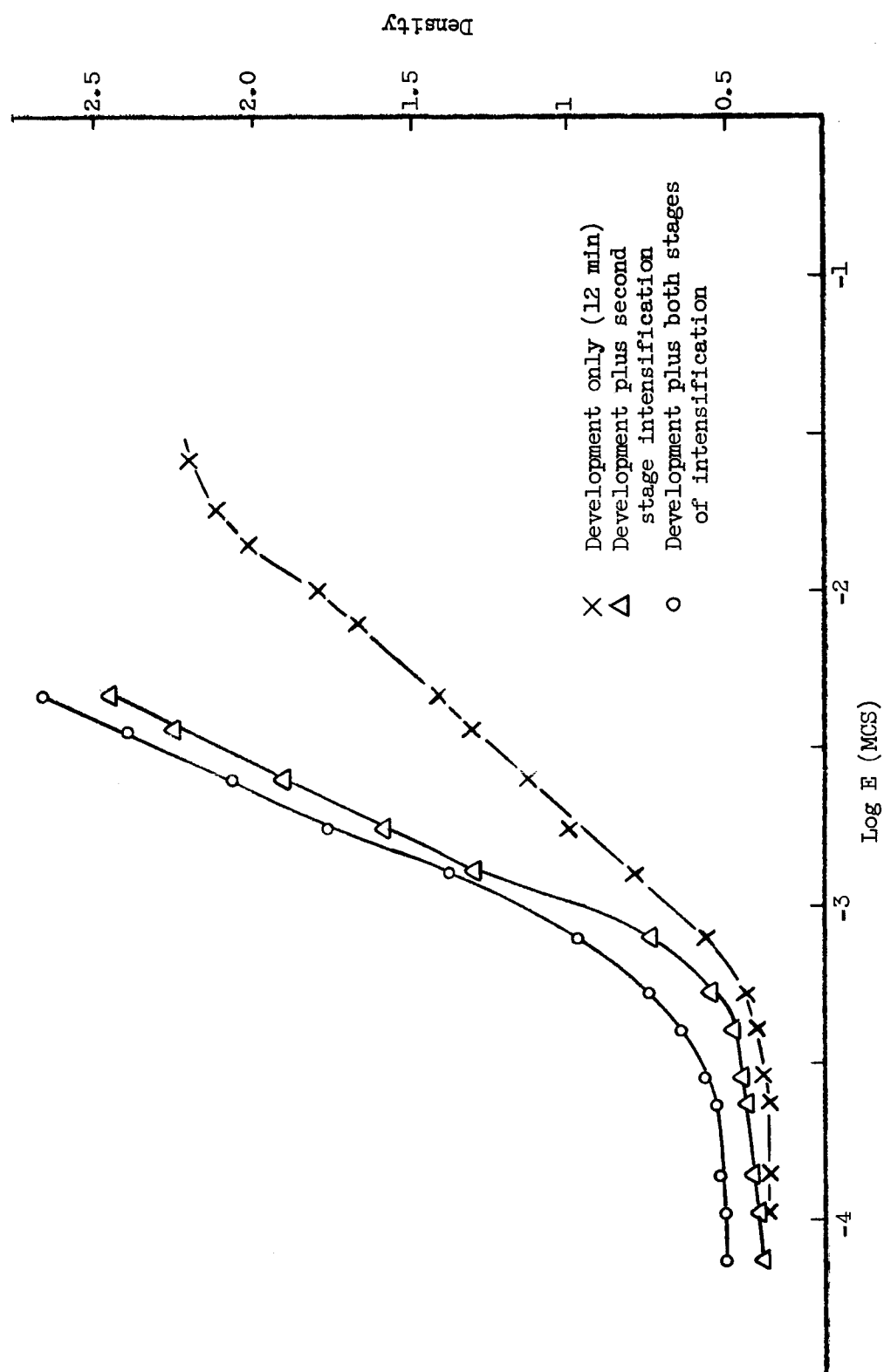


Figure 41. - Effect of intensification on density of Kodak Royal-X pan.

chromium, mercuric chloride, and Monckhoven's Intensifiers moved the toe of the Royal X-Pan Density-Log E curve from $\text{Log } E = -3$ to $\text{Log } E = -5$. It seems that the effect of this intensification was overestimated quite a bit.

High Sensitivity Light Meter

The light meter used to set the exposure in the above tests and to measure the film density is shown in Figure 42. Since very low light levels were necessary to provide low exposure with reasonable time accuracy a light meter of high sensitivity was needed. No such light meter was available so it had to be built.

The light sensitive element used was a Clairex CL 505L photoconductive cell. This has a peak spectral response at 5500A.

The light meter consists essentially of a d.c. bridge with the photoconductive cell in one leg. The bridge unbalance is amplified by a difference amplifier and measured by a 100 μ amp meter in series with the resistance shown.

The ranges available are 0.002 to 0.01, 0.01 to 0.02, 0.02 to 0.1, 0.1 to 0.2, and 0.2 to 1 foot-candles. The range covered in each step was kept small so that increased accuracy could be obtained, and so that the bridge unbalance was proportional to resistance change.

A set of reference resistors, whose values were obtained from the published curves available from Clairex Corporation, can be switched into the circuit to provide zero and full scale adjustment of the light meter. The diode is to provide meter protection when

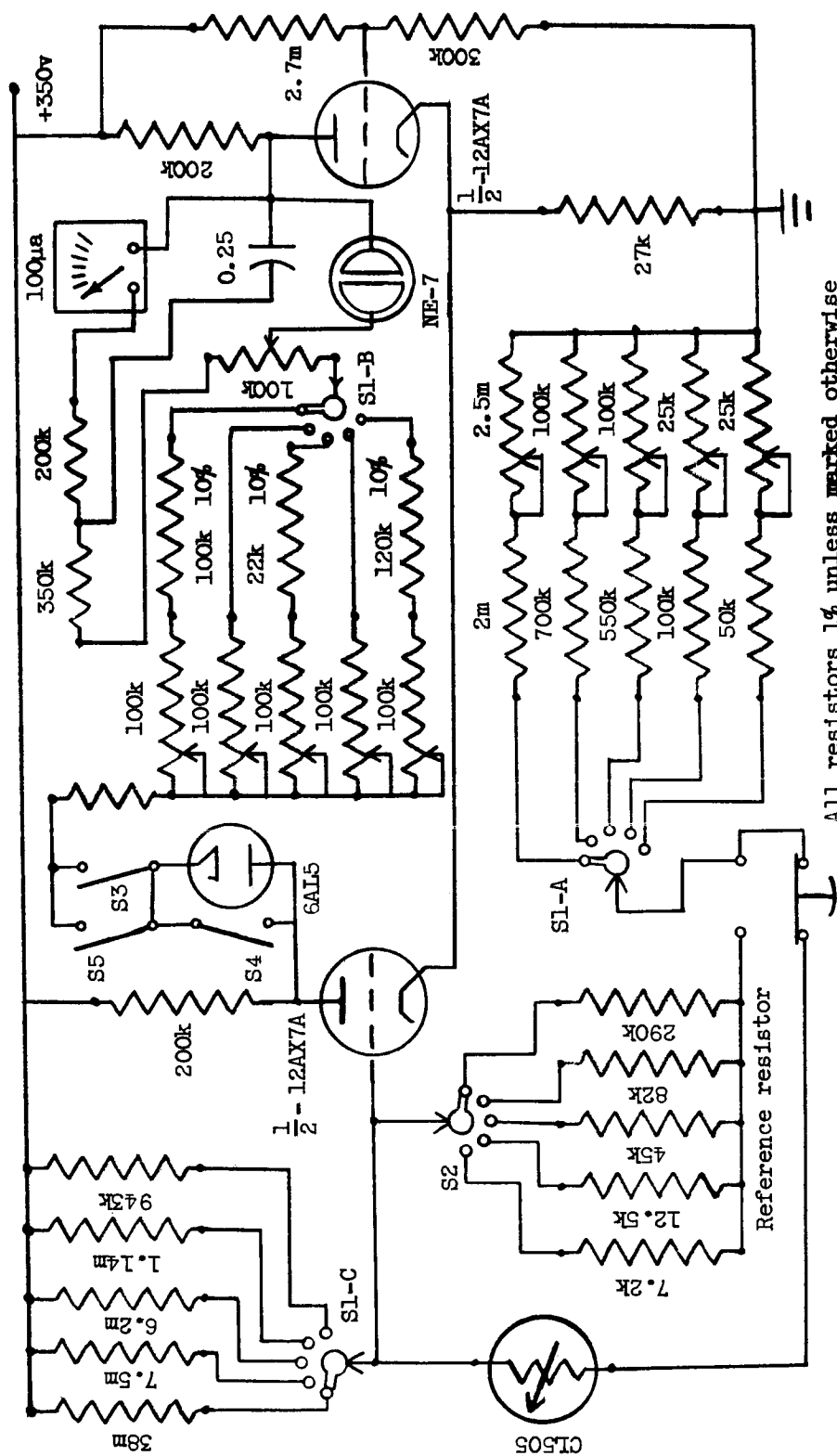


Figure 42. - High sensitive light meter.

no light is present. The neon bulb provides meter protection when too much light is present. If the allowed voltage across the meter and series resistors is exceeded, the NE-7 will break down and draw the current.

Independent zero and full scale adjustment is provided on each scale. Switch S-4 provides diode shorting when zeroing the instrument.

The photoconductive cell is mounted in a small metal box and connected to the chassis by a long cable. In this way the cell and remote switch S-5 can be used in the darkroom while the meter can be placed outside in the light for easy viewing through a small, long hole in the wall. This will admit negligible light into the darkroom.

The light meter was built to provide relative readings so comparative measurements could be made. The relative accuracy was checked by using neutral density filters with readings on several scales. This gave the expected results for several neutral density filters. A high quality but low sensitivity commercial meter was used to compare light readings on the less sensitive scales. The agreement was excellent, and thus the light meter most likely can be used for absolute measurements also. The close agreement between the experimental curve of Figure 41 for 12 minute development and the published curves of Figure 38 for 11 minute development (the 12 minute curve should and does lie slightly above the 11 minute curve), and also the close agreement between measured gamma and published gamma for 12 minute development confirm the accuracy of

this light meter.

Possible Methods of Increasing Film Speed

Reference 22 contains a useful discussion of methods for increasing film speed. Some of the information in this reference will be discussed here.

The simplest method of increasing film speed is with the use of high energy developers such as Kodak SD-19a. The formula for this developer is given in Reference 22. The authors state that the speed increases resulting from this method are at least as great as with any other known method. It should be recalled that according to Pressman (21) Kodak Royal X-Pan was the exception to this rule. However, for other films such as Kodak Photoflure the high energy developers might prove useful.

Reference 22 reports a doubling of the speed of Kodak Tri-X Sheet Film when Kodak SD-19a rather than DK-60a is used. The fog level is raised some, however, and optimum speeds are usually obtained with most films at a fog density of around 0.4. The gamma is usually higher under optimum speed conditions.

Another method of increasing film speed is by hypersensitizing before exposure. This may be accomplished by bathing the film in a dilute alkali solution such as borax or ammonia, or in a soluble silver salt (22). Exposure of the film to mercury vapor for several hours in a sealed container may also increase the speed (22). The time of mercury vapor exposure must be determined by trial.

If the film is exposed over the entire surface with just enough

light to produce a uniform latent image which if developed would produce a density just above the fog density, the speed of the film can be considerably increased. This pre-fogging activates the sensitivity centers in the film and upon subsequent exposure an image may be obtained at a lower light level than without pre-fogging. This may produce similar increases in speed to that of forced development but without the resulting grain growth (22).

A method similar to pre-fogging but which is performed after exposure is known as latensification by light. After the exposure the film is again exposed uniformly to a low intensity light. The low intensity light will cause increase in the growth of the latent-image centers but it is less effective than bright light in forming new latent-image centers. Thus an increase in film speed can be obtained without appreciable increase in base fog (22).

Reference 22 reports an increase of 100% in speed with Kodak Super Panchro-Press Film by using latensification. It is also suggested that latensification is one of the most suitable procedures for increasing speed. Increased speed can be obtained with only a moderate change in curve shape, contrast, or fog. Graininess and resolving power apparently are not affected.

For additional details on the above, Reference 22 is recommended.

FLUORESCENCE

Since the radiation used to record the droplet image on the film is the fluorescent radiation emitted by the irradiated droplet, the characteristics of the fluorescence of the fluorescent dye in various solvents is of prime importance to this technique. Various solvents must be used to obtain variation in fuel parameters so that the effect of these fuel parameters upon spray formation can be observed. Ultimately for vaporization studies the effect of elevated temperature upon the fluorescent dye in various solvents must be thoroughly studied.

A general characteristic of fluorescent dyes is that there is an optimum dye concentration in each solvent above or below which the fluorescent radiation output is less than at this optimum. Since the fluorescent intensity is low under any conditions, it is imperative that this optimum be determined so that maximum fluorescent radiation can be obtained.

Since the main purpose of this work is not the study of fluorescence per se, it is considered unnecessary and inappropriate to present a complete discussion of fluorescence here. Only those ramifications of fluorescence which directly concern this technique will be considered. A complete discussion of the theory of fluorescence may be found in Reference 2.

Uranin (Na-Fluorescein) was used in this work since it provides relatively strong fluorescence in comparison to most other fluorescent dyes (2). Uranin is soluble in ethanol, glycerol, water, and any combination of these, and thus a wide latitude of fluid properties may be obtained. The data reported in this paper was obtained using uranin and the above solvents and the discussion will thus be limited to the above.

Concentration Quenching

"The fluorescent strength F in a solution is determined by the number of photons emitted by a unit volume when light of unit intensity enters the volume through one of its surfaces. If Beer's law is assumed to be valid, it follows that:

$$F = (1 - e^{-\epsilon c})Q$$

ϵ being the molar absorption coefficient, c the concentration in moles per liter, and Q the quantum yield" (2). Since

$$e^{-\epsilon c} = 1 - \epsilon c + \frac{(\epsilon c)^2}{2!} - \frac{(\epsilon c)^3}{3!} + \dots$$

for small c :

$$F \sim \epsilon c Q$$

That is at low concentrations the fluorescent strength is proportional to concentration provided that ϵ and Q are not functions of concentration. ϵ does, however, change somewhat with concentration with an aqueous solution but very slightly with a glycerol solution. ϵ_λ varies with concentration, i.e., the dependence of absorption on wavelength varies somewhat with concentration, and thus the change

in ϵ with concentration will depend somewhat on the spectrum of the light source used to excite the fluorescence.

At high concentrations $e^{-\epsilon c} \rightarrow 0$ and therefore

$$F \rightarrow Q.$$

This would mean that as concentration is increased the fluorescent strength would asymptotically approach an upper limit with the depth of the fluorescing layer ever contracting into a surface layer of increasing brightness (2). This is not the observed result however, since Q itself is a function of concentration. The fluorescent strength increases to an optimum and then decreases with increasing dye concentration. The dependence of Q on concentration differs for different solvents. Table II gives the values of Q for various concentrations and solvents.

Table II (2)

RELATIVE QUANTUM YIELD Q_r OF THE
FLUORESCENCE OF FLUORESCCEIN AS A
FUNCTION OF THE DYE CONCENTRATION
 c (IN GRAMS/LITER) IN VARIOUS SOLVENTS

Solvent					
Water		Ethanol		Glycerol	
c	Q_r	c	Q_r	c	Q_r
0.175	1.00	2.1	1.00	0.12	0.98
.66	.96	7.0	.67	.36	1.00
1.57	.69	11.0	.45	4.60	.66
2.00	.57	16.0	.21	6.9	.52
2.82	.39	23.0	.11	9.0	.40
4.6	.18	---	---	12.4	.26

Figure 43 shows the relative fluorescent strength of fluorescence as calculated by:

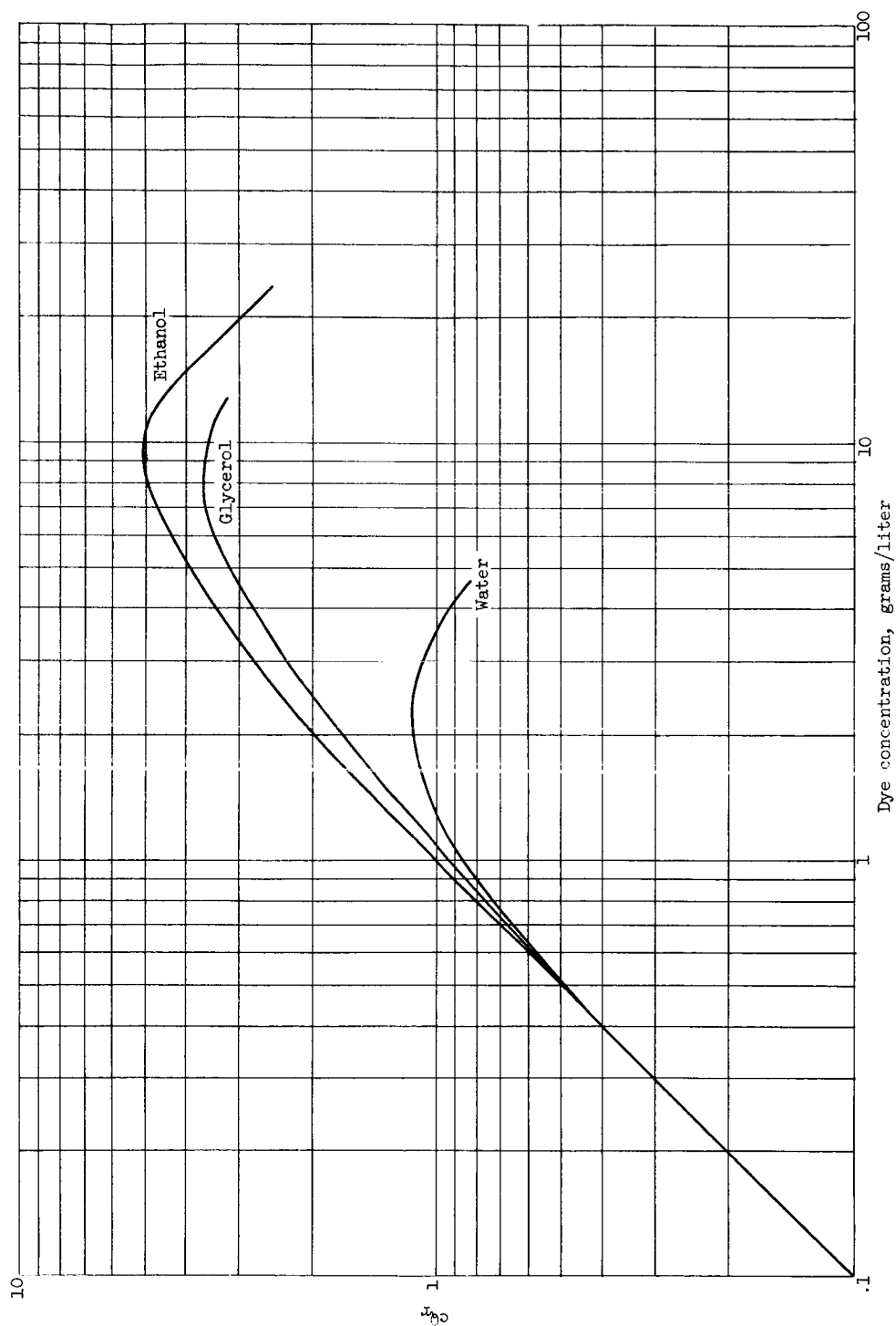


Figure 43. - Relative fluorescent strength of fluorescein as a function of dye concentration in various solvents as calculated by $F = cQ_r$.

$$F = c Q_r$$

using the values of Table II. This calculation neglects any effect of concentration or solvent on the molar absorption coefficient ϵ , and also neglects second order and higher terms of the series expansion of $e^{-\epsilon c}$.

Figure 44 shows the effect of concentration on fluorescent strength of fluorescein for various solvents as determined experimentally under actual spray conditions. It is extremely important to stress that a comparison between two different curves cannot be made. A comparison of points on any particular curve can be made, however.

The data was taken in the following manner. A BH-6 mercury lamp was run steady state in the position of the light source (see Fig. 1). A Wratten 75 filter was placed in front of the condensing lens and the transmitted radiation was condensed into the sample volume. The camera being focused on the sample volume gathers the fluorescent light and, with the aid of an additional lens behind the camera, focuses the fluorescent light onto a 6292 photomultiplier. A Wratten 21 filter was placed before the photomultiplier to pass fluorescent radiation but not reflected radiation.

A manifold system was used with the spray nozzle so that solvents of varying dye concentration could be quickly and successively changed. The fluorescent strength was observed on a high sensitivity a.c. VTVM connected to the photomultiplier. An a.c. instrument was necessary since the BH-6 was a.c. operated.

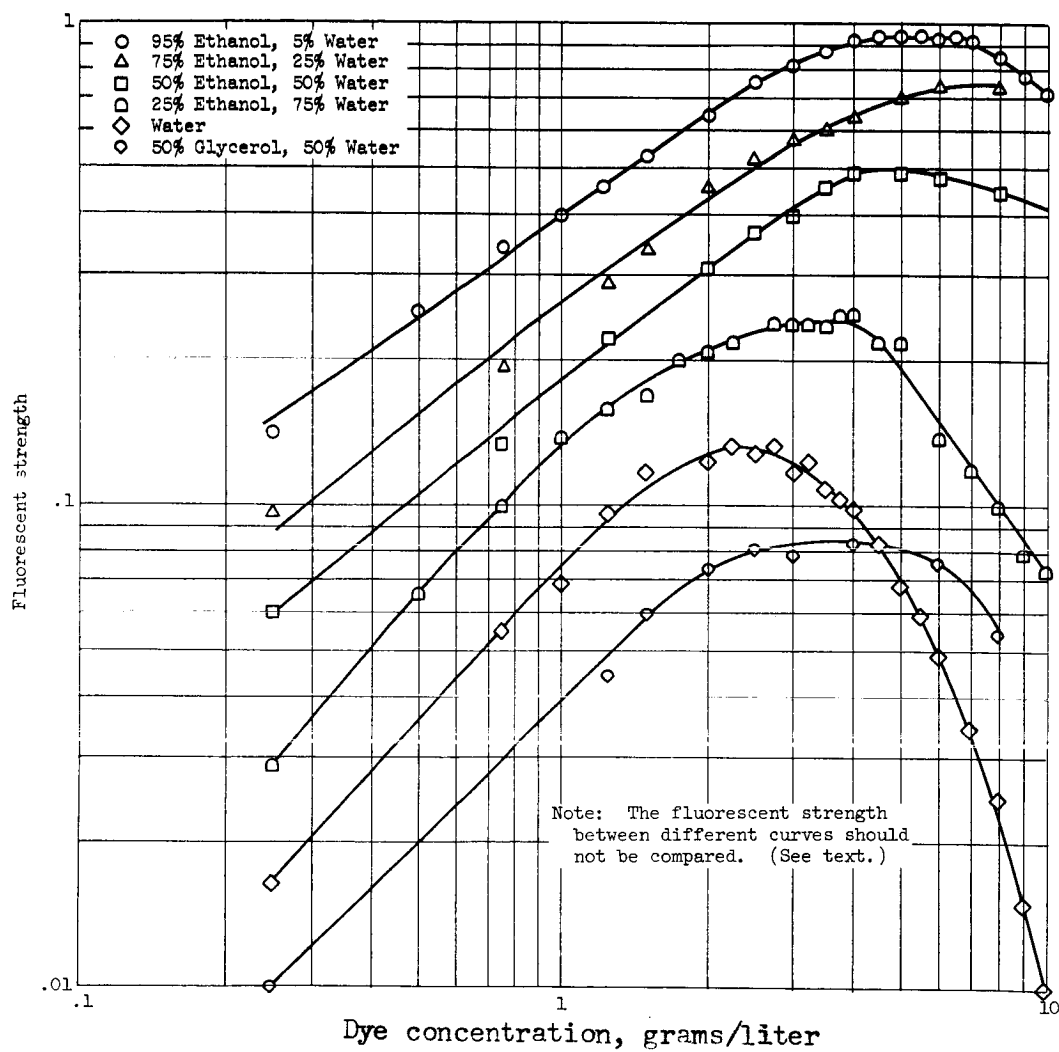


Figure 44. - Relative fluorescent strength of fluorescein as a function of dye concentration in various solvents as determined experimentally.

It can thus be seen that the data for any solvent at varying dye concentrations can be compared since the dye concentration does not affect the fluid properties. As the solvent is changed, however, the spray will change and the number and size of the drops in the field of view of the camera will change. Thus no comparison of fluorescence between different solvents can be obtained nor are they implied.

The curves in Figure 44 have thus been located on the graph by a suitable multiplication of the raw data by a different constant for each solvent. This has been done to keep the data points of each curve from interfering with that of another curve.

The curves for water of Figures 43 and 44 can be seen to agree closely. The optimum dye concentration is 2.25 grams per liter for both curves. The glycerol and ethanol curves do not agree quite as well between the two figures, but the qualitative agreement is certainly evident. As mentioned previously Figure 43 is an approximation with certain assumptions made. The curves of Figure 44 were obtained experimentally under conditions close to those of actual data taking conditions. Where differences occur the curves of Figure 44 are preferred.

A possible reason for the more rapid reduction of fluorescent strength at high concentrations in Figure 44 might be the following. The curves of Figure 43 might be close to those expected from viewing the irradiated area along the same direction as the exciting radiation. The curves of Figure 44 were obtained by viewing the irradiated drops perpendicular to the axis of the exciting radiation. The surfaces

normal to the camera axis can thus be expected to fluoresce less brightly than those surfaces normal to the axis of the exciting light since the exciting light is spread out over a greater area. This should be accentuated at higher concentrations when considerable attenuation of the exciting radiation will be present in the larger drops and the fluorescence will be limited to a thin layer on the surface rather than of the entire drop volume.

Cause of Concentration Quenching in Uranin Solutions

When uranin is present in a solvent at very low concentrations it will exist in the solution in the form of a single molecule or monomer. As the concentration is increased these monomers will associate to form a two molecule group or dimer. The dimers are not fluorescent but will still absorb the exciting radiation. The following three general extinction processes may occur (24):

Type I. - Extinction by induction transfer of one monomer to another.

Type II. - Extinction by transfer of excitation energy to dimers or higher complexes.

Type III. - Extinction by inert absorption, depending on the presence of nonluminescent complexes in the solution. The amount of exciting radiation available to monomers capable of fluorescing is thus reduced.

The first type depends upon the absolute monomer concentration. The second depends upon the absolute dimer concentration and also at low concentrations to the absolute monomer concentration. The third

depends upon the relative absorption of the monomers and dimers (24).

Levshin and Krotova (23) have concluded from a study of concentration quenching of uranin in aqueous and glycerol solutions that the type II (the authors refer to this as "migration of excitation energy to nonluminescing aggregates") extinction is predominant in uranin solutions. The authors found that identical degrees of quenching occurred in aqueous and glycerol solutions when the dimer concentration was the same even though the monomer concentration was radically different. The authors concluded that the low degree of inactive absorption had a comparatively weak effect upon concentration quenching. The dimer concentration for a given uranin concentration is higher for an aqueous solution than a glycerol solution due to difference in the heat of dissociation which are 2.2 and 1.0 kcal/mole, respectively.

The fact that the concentration quenching is dependent upon dimer concentration and that dimer concentration is higher in aqueous than glycerol solutions for the same uranin concentration will explain the more rapid fall-off of fluorescent strength with uranin concentration in the aqueous solution.

Temperature Effect on Quenching in Uranin Solutions

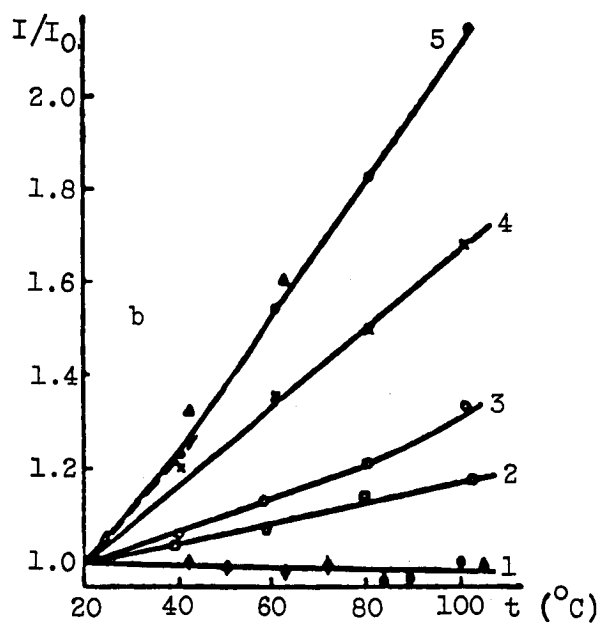
In the previous section the cause of concentration quenching was stated to be due to transfer of energy from the monomers (which are capable of fluorescence) to the dimers (which do not fluoresce). Since this transfer of energy would require an excited monomer to approach a dimer, anything which would increase the frequency of monomer-dimer

collisions would also increase quenching. Increased collision frequency would be obtained from heating the solution, and the resulting increase in fluorescent quenching is termed temperature quenching.

A compensating phenomena occurs, however, in concentrated uranin solutions. The dimer concentration, which appears to be the ultimate cause of quenching in uranin solutions, is reduced with increasing solution temperature. The increased temperature causes the dimers to dissociate and form monomers which are capable of fluorescence (23).

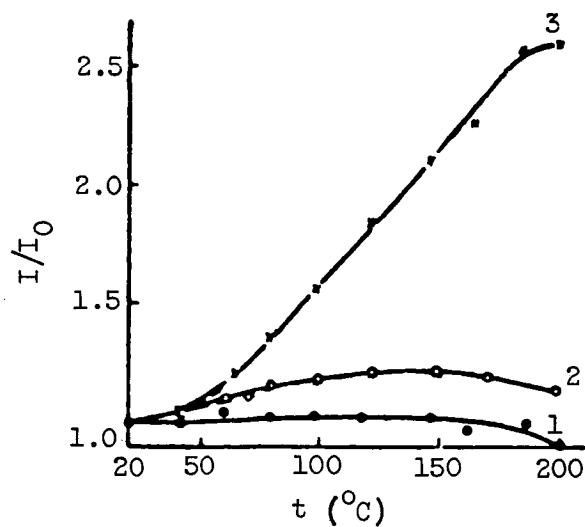
This phenomena is shown in Figure 45(a) for aqueous solutions and in Figure 45(b) for glycerol solutions of uranin. It can be seen that at low concentrations, such as curve 1 for either solvent, true temperature quenching is occurring since dimer concentration is negligible. In an aqueous solution with as low as 1.5 grams per liter uranin concentration (curve 2, Fig. 45(b)) it can be seen that fluorescence is increased with increased temperature. This increase continues out to 100° C so that no effect of temperature quenching will occur in vaporization studied with aqueous solutions even in a heated atmosphere. The peak fluorescent strength of an aqueous solution at 20° C occurs at a concentration of 2.5 grams per liter of uranin (see Fig. 44) so that an effect midway between curves 2 and 3 of Figure 45(a) can be expected.

From the above it can be expected that a shift in the optimum dye concentration for uranin in aqueous solutions will occur toward higher concentrations. Thus if a solution is mixed for optimum concentration at room temperature two compensating effects will occur when studying vaporization. As the temperature of the drop increases,



(a) Aqueous solution.

Curves (in grams per liter) 1- 3.76×10^{-3} ,
2-1.51; 3-3.76; 4-7.53; 5-15.05



(b) Glycerol solution.

Curves (in grams per liter) 1-0.376;
2-15.05; 3-7525

Figure 45. - Effect of temperature on aqueous and glycerol uranin solutions.

and vaporization occurs, the dye concentration will increase. At the same time, however, a shift in the optimum dye concentration towards higher concentrations will occur due to temperature increase of the drop.

It can be seen from Figure 45(b) that the increase in fluorescence with temperature is not as spectacular as in aqueous solutions (curve 2 of Fig. 45(b) has the same dye concentration as curve 5 of Fig. 45(a)). This is as expected since the dimer concentration is lower in glycerol than in aqueous solutions at a given uranin concentration (23).

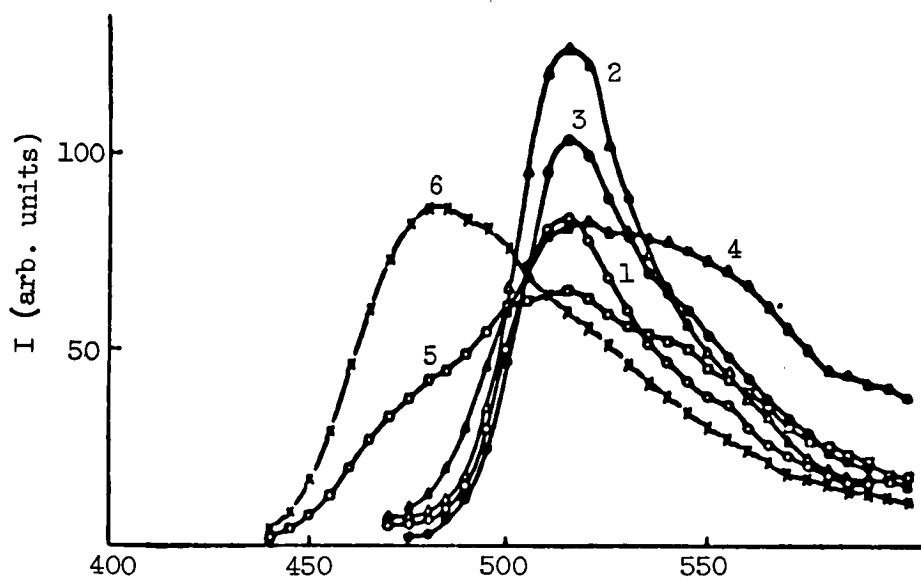
It can thus be seen that temperature quenching should not present any problems in vaporization studies with this technique when concentrated uranin solutions are used.

Effect of Solution pH on Fluorescence

An observed shift in the spectrum of the fluorescence in uranin solutions with varying solution pH has been observed by several workers (25,27). Reference 25 reports fluorescent peaks at 5150, 5500, and 4750 Å, the relative magnitude of each depending upon solution pH.

Figure 46 (27) shows the effect of pH on the fluorescence spectrum of uranin solutions for a very small uranin concentration (0.01 grams/liter). In Reference 27 the fluorescent peaks agree well with those in Reference 25.

The reason for the shift is given as follows (27). The band with a maximum at 4700-4800 Å is associated with the cation or positively



Curve 1 - 0.0001 N KOH (pH = 9.0))
 2 - 1 N KOH (pH = 14.0)
 3 - 0.000001 N HCl (pH = 7.1)
 4 - 0.0001 n HCl (pH = 4.1)
 5 - 2 N H₂ SO₄ (pH 2)
 6 4 N HNO₃

Uranin concentration 0.01 grams per liter

Figure 46. - Effect of solution pH on the fluorescent spectrum of uranin.

charged fluorescein ion. The bands with maxima at 5400-5500 A and 5150 A are associated with singly and doubly charged anions, respectively. In a highly basic solution the doubly charged anion predominates. As the solution pH is reduced the singly charged anion concentration increases and finally for highly acidic solutions the cation predominates.

The importance of the above to this technique can be shown as follows. Uranin, a basic salt, when added to a solvent will increase the solution pH. The pH attained at any uranin concentration depends upon the solvent used. As an example, at a uranin concentration of 5 grams per liter the measured pH of an ethanol solution was 10 while that of a 65% glycerol-35% water solution was only 8.4. If it is assumed, momentarily for illustration, that the curves of Figure 46 hold for concentrated uranin solutions, then the ethanol solution will fluoresce more (see curve 2) than that of the glycerol-water solution (see curve 1).

It must be recalled that Figure 46 was obtained at very low uranin concentrations and may not be valid at the high concentrations used in this technique. At high uranin concentrations the dimer concentration is considerable and shifts in solution pH may increase the dimer concentration and thus encourage quenching. This must be considered in any future tests of the above.

Again assuming Figure 46 applies, it can be seen that addition of NaOH to a glycerol-water solution or even to the ethanol solution would increase the pH and thus increase fluorescence. This is a possibility for future study at high uranin concentrations.

It was generally true that ethanol sprays resulted in better drop pictures than glycerol-water sprays. This would tend to establish that Figure 46 might be at least qualitatively true for concentrated uranin solutions.

Some measurements were made of total fluorescence versus solution pH for ethanol, ethanol-glycerol, glycerol-water, and water solutions with 0.01 grams per liter of uranin. The measurements were made on a Beckman Model DU Spectrophotometer and again only dilute uranin solutions could be studied. The results were judged only qualitatively and it was found that the glycerol-ethanol solutions behaved much like pure ethanol while the glycerol-water solutions behaved like water as could be expected. Since ethanol sprays give better drop pictures and therefore can be assumed to fluoresce more intensely than glycerol-water sprays, and that glycerol-water solutions quench at lower concentrations than ethanol sprays, it is felt that the fluid properties might be varied with ethanol-glycerol solutions to more advantage than with glycerol-water solutions.

A tabulation of fluid properties of ethanol-glycerol solutions could not be found in the literature so a measurement of the properties was made. The results are tabulated in Appendix I.

STATISTICAL CONSIDERATIONS

In the section on "possible errors in sizing particles" several errors were discussed which could be termed systematic errors. An example might be that of setting the Iconumerotor clipping level consistently too high. This would result in a consistent undersizing of the particles. This error is a determinate error, however, since it can be evaluated by an experimental calibration and corrected.

This section deals with random errors which arise inevitably in any sample due to the laws of probability. An example of such an error occurs in the flipping of a coin. If the coin were flipped 10 times the most probable result would be five heads and five tails if the coin were fair. If the results were two heads and eight tails, however, it could not be immediately concluded that the coin was unfair and that the probability of heads is $1/5$. The above results are due to the randomness of a small sample. It is possible to flip a fair coin ten times and not get one head or to get all heads. This occurs less frequently than five heads but is still possible.

If the coin were flipped 10,000 times and only 2000 heads occurred, the intuitive feeling is that something is wrong with the coin. Intuitively the large sample gives more confidence in the results. This intuition can be made more precise by the concept of a confidence interval.

If by some means an interval can be placed around the observed result and the statement can be made that if the experiment were performed many times the result would lie in this interval, then much more can be inferred from the result. An example might be the following. Let a coin be flipped 100 times and 20 heads occur. By some means an interval is set up which includes 10 to 30 heads. If this interval has a confidence of 95%, that is 100 experiments would have the results in this interval 95 times, then it is pretty sure that the coin is unfair.

The second and third parts of this section will deal with the above problem. The possible error due to edge effects will now be considered.

Possible Error Due to Edge Effects on the Film

If a film of a given size is scanned on the Iconumerator there will be some drops on the edge which will be partially masked. The effect of these partially masked drops on the size distribution depends upon which edge they are found. Figure 47 shows several drops of diameter d located in various positions. The shaded portion of each drop represents the residual emerging from the sizer for the largest category in which the drop is counted. Each position will now be discussed.

It can be seen that drop 1 has its center more than $d/2$ from the edge and thus does not have any edge effect. This drop will be sized correctly.

Drop number 2 has its center closer than $d/2$ to the bottom edge,

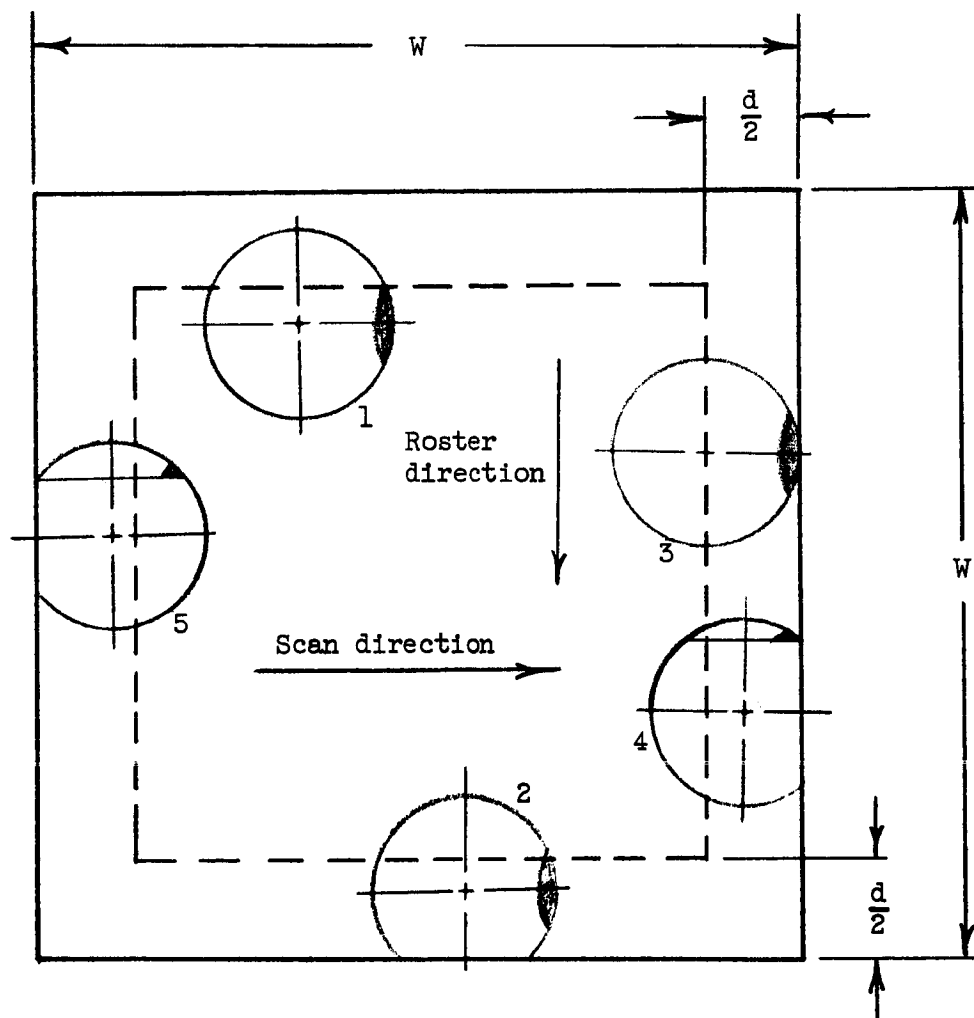


Figure 47. - Diagram of edge effect model.

but its residual is seen to be within the masked area. This drop will thus be sized correctly. If its center is extremely close to the edge, its residual may touch the edge but will still be sized correctly. If its center is within $d/2$ below the bottom edge of the film it will be undersized. If this were along the top edge and the residual touched the mask it would be considered an extension of the mask and would not be counted. This is due to the fact that the Ico-numerator counts only the first intercept of any residual. The drop center would have to be very near the edge at the top for the above to occur. The error due to a drop of type 2 at the top is small and can be neglected.

Drop 3 whose center is exactly $d/2$ from the mask will be sized correctly. An intercept on the upper part of the residual will have a leading and a trailing edge signal and thus give a proper count pulse.

The trouble begins with a drop such as number 4. The last chord and residual countable are shown at the top side of the drop. All intercepts below this chord will lack a trailing edge which causes the count pulse. The drop will be undersized and will be recorded as a drop whose diameter is equal to the last whole chord.

Drop 5 also causes undersizing. The intercepts below the chord drawn will not have a leading edge, i.e., they will be considered part of the mask since a leading and a trailing edge signal are necessary to pass through the anticoincidence circuit. The drop will be recorded as one with a diameter shown by the chord drawn.

No correction is possible for drops of type 4, 5, and for type 2 whose center is below the bottom edge. The only thing possible is to estimate the percentage of drops which will be deleted from the larger categories and placed in smaller categories. The estimation can be made as follows.

From the discussion above it can be seen that the problem can be reduced to that of how many drops of diameter d will be found whose center lies within $d/2$ of the left or right border or below the bottom edge. It can be assumed that a drop will be found anywhere within the square of side W with equal probability since this square represents less than a 2×2 mm. square in the spray. Thus the probability P of finding a drop of diameter d within the three edge areas is:

$$P = \frac{\text{Area of edge sections}}{\text{Entire area}}$$

or

$$P = \frac{3\left(W \times \frac{d}{2}\right)}{W^2 + \frac{Wd}{2}} = \frac{3d/2}{W + \frac{d}{2}}$$

thus

$$P \approx \frac{3d}{2W}$$

when

$$W \gg \frac{d}{2}$$

As would be expected the larger drops have a greater chance of being undersized. With the data reported in this paper, however, only a small percentage of even the largest drops will be undersized.

The largest drops observed are on the order of 200 microns in the spray or 5 mm. on the film. The mask width W is $1\frac{3}{4}$ inches or 44.5 mm. Therefore,

$$P = \frac{3 \times 5 \times 100}{2 - 44.5} = 16.8\%$$

This error is small in comparison to those due to the randomness of the sample in the large size categories which are discussed in the next part of this section. The error becomes even smaller for the smaller drops. The error due to addition of counts in the smaller categories is negligible. A small percentage of a small number of drops added to categories containing a large number of drops already will cause little error in the small categories.

There is, of course, randomness involved in this edge effect. The probability calculated above is just an estimate. On any particular film all or none of the large drops might lie on the mask edge.

A priori Confidence Interval Estimate

It is desirable to have an a priori estimate of the confidence interval about a distribution curve. This would allow the estimate of possible error before the experiment is performed. In this way a better understanding of the sample size necessary will be possible. The following model was proposed in an attempt to satisfy the above.

The counting of each drop was considered as a Bernoulli trial, that is, the sizing of each drop is independent of that of every other drop, the drops are selected randomly, and there are only two possible outcomes, success and failure. When considering each size classifica-

tion separately, a success represents a drop falling in the limits of this size category, and a failure represents the drop falling outside of this size category. These are clearly the only two possibilities. The drop either is or is not in the particular size category.

The probability of success is denoted by p and that of failure by q . Clearly $p + q = 1$. The probability p is determined by the true spray distribution itself. This is clear since the proportion of the drops in the true population that are between the large and small size limits of the category of interest is just the probability p that any randomly chosen drop will fall in that size classification when counted.

The following notation will be used. Let:

Number of drops counted be n

Number of drops in a category be k

Probability of success be p

Probability of failure be q

k is then distributed by the binomial distribution with k as the random variable and p and n as parameters.

$$f(k; p, n) = \binom{n}{k} p^k q^{n-k} \quad \text{where} \quad \binom{n}{k} = \frac{n!}{k!(n-k)!}$$

p is unknown and the best estimate available for p is \hat{p} (26) (the maximum likelihood estimator) where $\hat{p} = k/n$. Therefore the distribution of \hat{p} is:

$$g(\hat{p}; p, n) = \binom{n}{n\hat{p}} p^{n\hat{p}} q^{n-n\hat{p}}$$

If can be shown that the expected value of \hat{p} is p and that the

variance of \hat{p} is pq . Use is made of the Central Limit Theorem which states: If a population has a finite variance σ^2 and mean μ , then the distribution of the sample mean $\hat{\mu}$ approaches the normal distribution with variance σ^2/n and mean μ as the sample size increases (26). Therefore, for large samples, \hat{p} will be approximately normally distributed with mean p and variance pq/n . Thus $\frac{\hat{p} - p}{\sqrt{pq/n}} = \frac{\hat{p} - p}{\sqrt{p(1-p)/n}}$ will be approximately distributed by the unit normal distribution.

A fiducial probability statement can be set up as follows. If the experiment were repeated 100 times, the quantity $\frac{\hat{p} - p}{\sqrt{p(1-p)/n}}$ would lie between $-d\gamma$ and $d\gamma$ 100 γ times where $d\gamma$ and γ are determined from the unit normal distribution by the following:

$$\frac{1}{\sqrt{2\pi}} \int_{-d\gamma}^{d\gamma} e^{-(1/2)t^2} dt = \gamma \quad \text{where } 0 \leq \gamma \leq 1$$

This statement can be written:

$$P\left(-d\gamma < \frac{\hat{p} - p}{\sqrt{p(1-p)/n}} < d\gamma\right) \cong \gamma$$

or the equivalent:

$$P\left(\frac{2n\hat{p} + d\gamma^2 - d\gamma\sqrt{4n\hat{p} + d\gamma^2 - 4n\hat{p}^2}}{2(n + d\gamma^2)} < p < \frac{2n\hat{p} + d\gamma^2 + d\gamma\sqrt{4n\hat{p} + d\gamma^2 - 4n\hat{p}^2}}{2(n + d\gamma^2)}\right) \cong \gamma$$

for a 95% confidence interval $d\gamma = 1.96$; therefore, for even moderately large n , $n \gg d\gamma^2$. For very small \hat{p} , however,

$4n\hat{p} - 4n\hat{p}^2 = 4n\hat{p}(1 - \hat{p})$ may be of the same order as $d\gamma^2$. Therefore, the above reduces to:

$$P\left(\hat{p} - d\gamma\sqrt{\frac{\hat{p}(1 - \hat{p})}{n} + \frac{d\gamma^2}{4n^2}} < p < \hat{p} + d\gamma\sqrt{\frac{\hat{p}(1 - \hat{p})}{n} + \frac{d\gamma^2}{4n^2}}\right) \cong \gamma$$

And for a 95% confidence interval with $d\gamma = 1.96$,

$$P\left(\hat{p} - 1.96\sqrt{\frac{\hat{p}(1 - \hat{p})}{n} + \frac{d\gamma^2}{4n^2}} < p < \hat{p} + 1.96\sqrt{\frac{\hat{p}(1 - \hat{p})}{n} + \frac{d\gamma^2}{4n^2}}\right) = 0.95$$

Figures 48 and 49 are plots of the function $1.96\sqrt{\frac{\hat{p}(1 - \hat{p})}{n} + \frac{d\gamma^2}{4n^2}}$ versus \hat{p} for various sample sizes n . Figure 49 shows the above for small \hat{p} . The dashed line is the above function when $d\gamma^2/4n^2$ is neglected for $n = 500$. It can be seen that the discrepancy is great for small \hat{p} but decreases rapidly with increasing \hat{p} . For $p > 0.1$ the simplified function $1.96\sqrt{[\hat{p}(1 - \hat{p})]/n}$ can be used even for $n = 500$. For larger n the discrepancy will be less for any \hat{p} .

It should be noted that only one-half of the confidence interval is plotted. The entire interval would involve placing the plotted function on both sides of \hat{p} .

An example of the use of Figures 48 and 49 is as follows. Suppose that it is determined that for a size category containing 1% of the total population an error of no more than 20% can be tolerated. This would mean that \hat{p} must be known to within 0.002 or $0.008 < \hat{p} < 0.012$. Figure 49 is entered with $\hat{p} = 0.01$ and $I = 0.002$. It can thus be seen that 10,000 drops must be counted.

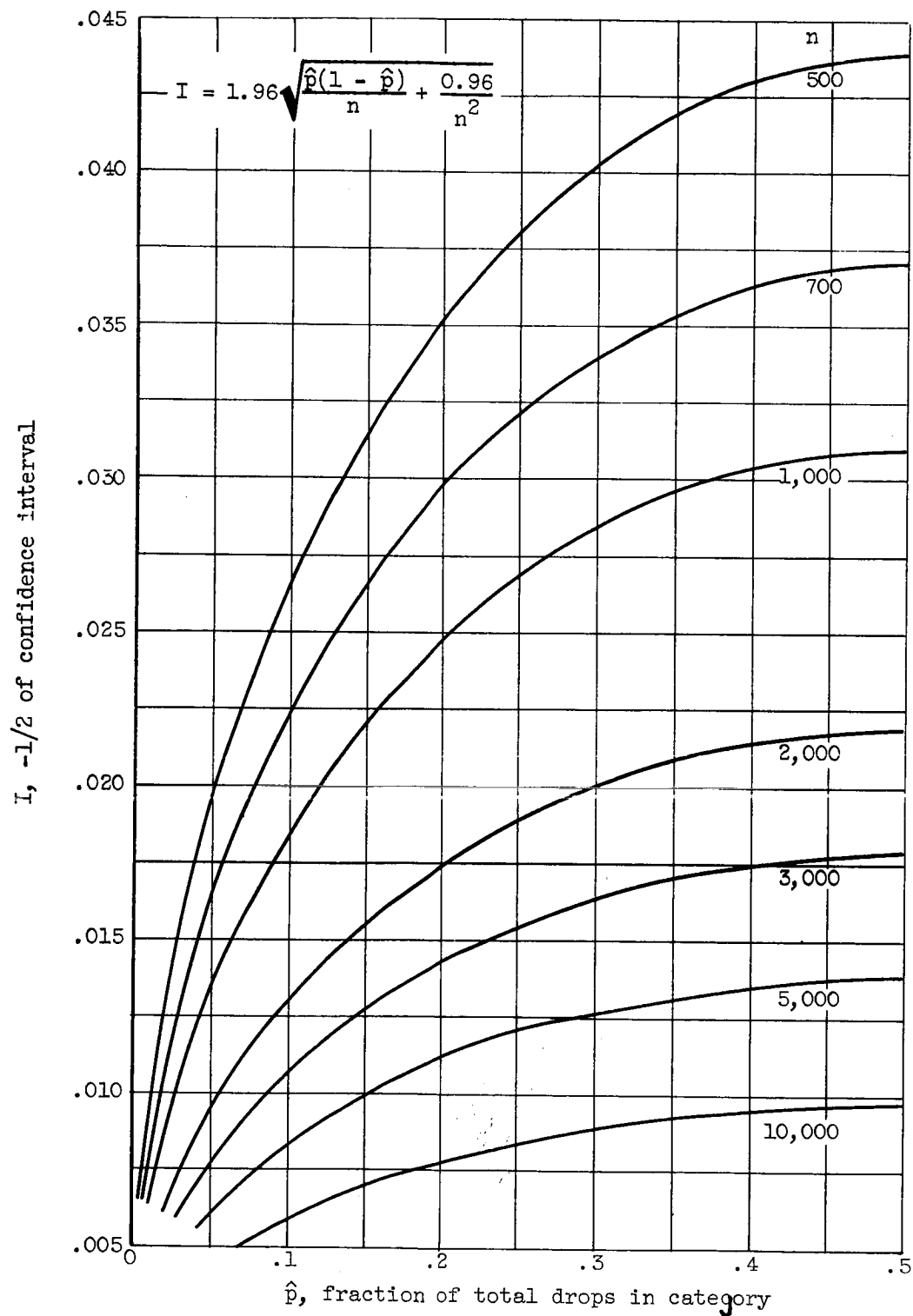


Figure 48.- A priori confidence interval (95%) versus fraction of drops in size category for various sample sizes.

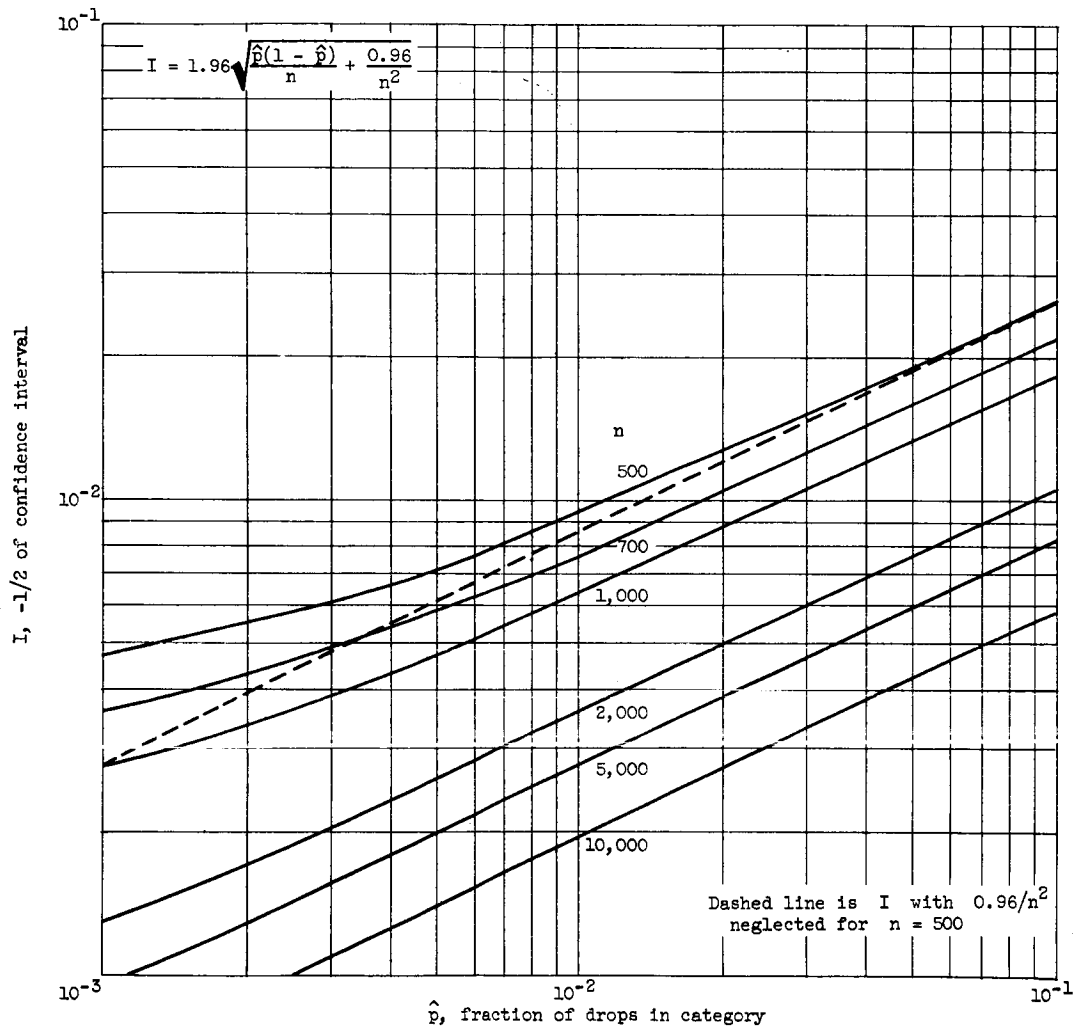


Figure 49. - A priori confidence interval (95%) for small fraction of drops in a size category.

These figures can also be used after the data are taken to get a quick estimation of the possible error involved. Say that 5000 drops have been counted and that the smallest $\hat{p} = 0.01$. Entering Figure 49 with these values I is determined to be 0.0028. Thus it is known with 95% confidence that $0.0072 < \hat{p} < 0.0128$ or if the experiment were repeated 100 times that \hat{p} will fall in this interval 95 times. The above possible error is then $0.0028/0.01 = 28\%$.

The above can, of course, be repeated for each size category and an interval placed around the entire distribution.

After a discussion of the confidence intervals obtained by the t-distribution in the next section, the results of the two methods are compared.

Confidence Interval Using the t-Distribution

A second method which is often used to obtain confidence intervals involves the t-distribution. This was developed by W. S. Gossett who wrote under the pseudonym "Student" (26) and thus the distribution is also called Student's t-Distribution.

The quantity:

$$t = \frac{\bar{x} - \mu}{\sqrt{\frac{\sum_{i=1}^m (x_i - \bar{x})^2}{m(m-1)}}$$

has only one parameter μ and is distributed by the t-distribution with $m - 1$ degrees of freedom.

The above is used here in the following manner. The number of films sized of a particular set of data is designated by m (here

$m = 24$). The number of drops in a particular size category on each of the m films is denoted by x_i ($i = 1, 24$). The average observed number of drops in the particular size category is:

$$\bar{x} = \frac{\sum x_i}{m}$$

The t -distribution is actually derived for estimating the mean of a normal distribution. It is technically only good for a normal distribution, but it is generally used for any distribution. In this case the drop size distribution is certainly not a normal distribution. It is not the drop size distribution, however, to which the t -distribution is being applied. Each x_i may be considered the average density per unit area of film for a particular drop size category. Thus x_i is already an average value which is taken from a considerable number of drops on the film. It can thus be expected, due to the Central Limit Theorem mentioned previously, that x_i will be approximately distributed normally about the true mean μ .

A 95% confidence interval can be set up much like that in the previous section.

$$P(-t_{0.05} < t < t_{0.05}) = \int_{-t_{0.05}}^{t_{0.05}} f(t; m-1) dt = 0.95$$

or

$$P\left(x - t_{0.05} \sqrt{\frac{\sum (x_i - \bar{x})^2}{m(m-1)}} < \mu < \bar{x} + t_{0.05} \sqrt{\frac{\sum (x_i - \bar{x})^2}{m(m-1)}}\right) = 0.95$$

$t_{0.05}$ is that point of the t-distribution such that the area under the extreme ends of the distribution is 0.05 or in each end is 0.025. For $m - 1 = 23$ degrees of freedom, $t_{0.05} = 2.069$.

The above calculation must be repeated for each size category each of which contains 24 x_1 's. It would thus be a very long task to analyze every distribution reported in this paper of which there are 54 spray conditions and locations and 9 overall spray conditions. Thus 6 representative distributions were selected 3 of which are from the larger samples and 3 from the smaller samples. The calculations were performed on a digital computer and the results as well as plots of the results are given in Appendix II.

It can generally be seen from all of these plots that the confidence interval is larger for all sizes for smaller samples. For any distribution the confidence interval is larger in those size categories containing fewer drops.

It should be noted that the above discussion pertained to a 95% confidence interval. A confidence interval is meaningless unless its confidence level is specified. The error can be made to look smaller by employing a 50% confidence interval, as is often done, rather than a 95% confidence interval. The interval width will be reduced by the ratio

$$\frac{t_{0.50}}{t_{0.05}} = \frac{0.685}{2.069} = 0.311$$

Thus the possible spread of the data would appear to be only 1/3 of that reported here. Of course, if the experiment were repeated it could be expected to fall within this interval only half of the time.

For this reason a 95% confidence interval is preferred.

Comparison of A Priori and t-Distribution Confidence Intervals

From the 6 drop size distributions mentioned in the previous discussion, the maximum error possible due to random fluctuations in the sample were calculated using both the a priori and t-distribution confidence intervals. The percent error was calculated by dividing $1/2$ of the confidence interval by \hat{p} or the number of drops observed for the a priori and t-distribution intervals, respectively. The absolute magnitude of this percentage, of course, is not correct since \hat{p} for instance cannot be expected to be precise. Both percentages, however, were obtained in the same manner so they can be compared to each other.

The results are shown in Figure 50. The line drawn on the figure represents the line about which the points would be if the correlation between the two methods were perfect. It can be seen that the correlation is very good. In general, however, the error estimated from the t-distribution confidence interval is slightly larger than for that of the a priori interval. A possible reason for this is as follows. It should be recalled that when using the t-distribution, the variation of each small sample (each film) from that of the overall average in any given size category was considered in the term

$$\sum (x_i - \bar{x})^2. \text{ With the a priori method only the total sample (all}$$

24 films) was considered and pure probability theory was applied to this. Thus no fluctuations in each small sample were considered. If

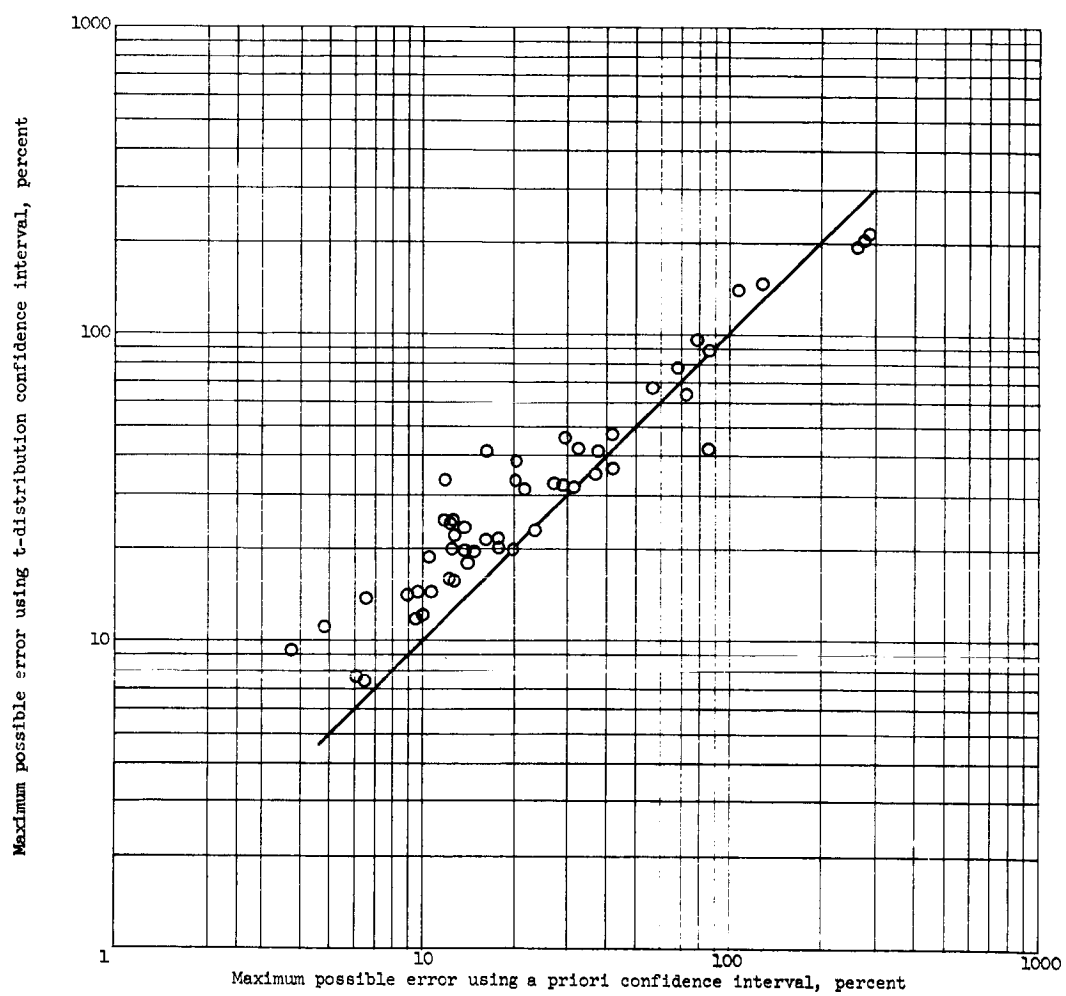


Figure 50. - Comparison of a priori and t-distribution confidence intervals.

there was a fluctuation from one small sample to the next which was greater than that of pure statistical random variations then the t-distribution method would certainly detect this fluctuation.

Such a variation beyond pure random variation can be expected for a small sample in a spray. The spray can be expected to vary slightly with time. This is due to the random disturbances causing sheet and ligament breakup and also random ligament formation itself. This variation is realized and the data sought is the time averaged distribution. The population observed in the sample volume is thus not a constant population but that of a time varying population.

Due to the close agreement between the two methods, it is felt that the time variation of the population is not extremely large. It is very likely then that this time variation has been damped out of the total sample. The only sure way of knowing this, however, would be to perform the above calculations with considerably larger samples. It would be an interesting experiment to use partial samples of say 10 films instead of one and count a total of 200 films instead of 24. This would mean that each x_i was the sum of the drops on 10 films in a particular size category with $i = 1$ to 20. A t-distribution of 19 degrees of freedom would then be used. With the above, the variation in x_i should be closer to pure random variation, and the a priori and t-distribution confidence intervals should agree even more closely.

CENTRIFUGAL PRESSURE-ATOMIZING NOZZLE

The data presented in this paper was obtained from the spray formed by a centrifugal nozzle. The flow of the fluid through this nozzle will now be discussed, and a possible mode of sheet break-up will be presented.

Flow of Liquid Through a Centrifugal Nozzle

Figure 51 shows the construction of a typical centrifugal nozzle. The important dimensions are shown in the side and front views of the nozzle.

The fluid enters around the swirl slot cylinder as shown on the left of Figure 51(a), and flows down the four swirl slots into the swirl chamber. Due to the offset of the swirl slots (s in Fig. 51(b)) from the nozzle center, the fluid is given a tangential velocity component upon delivery into the swirl chamber. If this tangential velocity component is sufficient (sufficient offset s and flow rate) the fluid will be held to the outer walls of the swirl chamber by centrifugal force, and an air core will exist throughout the swirl chamber and orifice. Upon leaving the orifice the annular fluid sheet will expand into a conical sheet due to the sudden removal of the constricting boundary.

The analysis of the flow through the centrifugal nozzle is patterned after that of Novikov (28). Novikov considered purely tan-

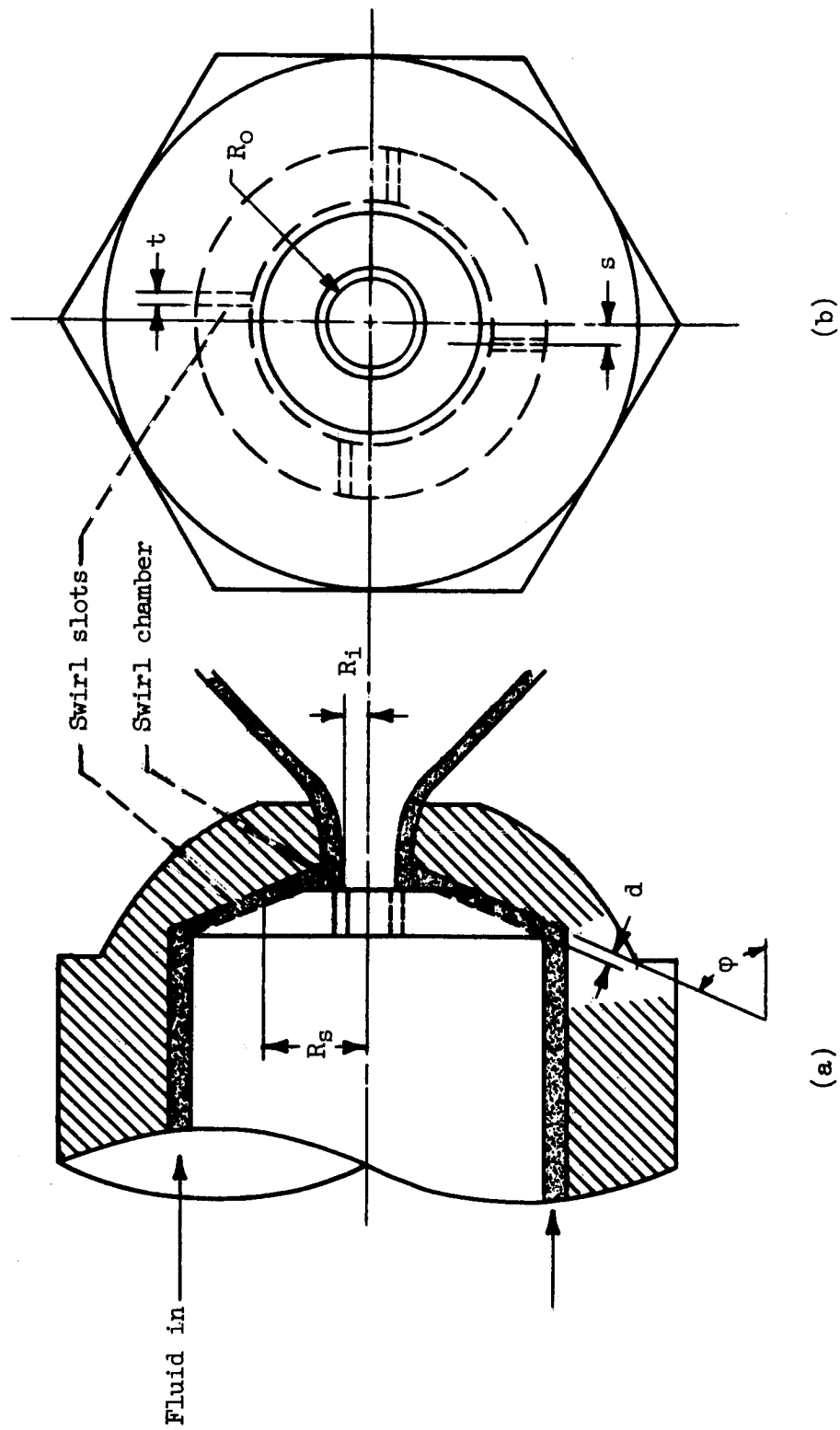


Figure 51. - Centrifugal pressure atomizing nozzle.

gential input with the swirl chamber angle $\phi = 90^\circ$. With tangential input the swirl slot offset s would be equal to the swirl chamber radius. Only slight modifications are necessary to convert Novikov's analysis to the more general case.

An ideal fluid and irrotational flow is assumed. There are thus no frictional losses. This analysis is therefore a good approximation only in the case of a fluid of very low viscosity. The effect of viscosity on the flow pattern will be discussed later.

The following notation is used:

t = swirl slot width

d = swirl slot depth

s = swirl slot offset

R_o = orifice diameter

R_i = air core diameter

ϕ = angle between swirl chamber boundary and nozzle axis

n = number of swirl slots

Q = volume flow rate

m = mass flow rate

M = momentum

r = radial distance from nozzle axis

V = velocity in swirl slot

u = axial velocity in swirl chamber

w = tangential velocity in swirl chamber

The assumption of irrotational flow gives the following form for the free-vortex tangential velocity:

$$w = \frac{\Omega}{r} \quad (1)$$

The velocity V of the fluid emerging from the swirl slots can be transformed into two components, an axial component V_a and a tangential component V_t such that:

$$V_a = V \cos \phi \quad (2)$$

and

$$V_t = V \sin \phi \quad (3)$$

Only V_t contributes to the angular momentum of the fluid emerging from the swirl slots, and this angular momentum is:

$$M_s = mrV \sin \phi = \rho QsV \sin \phi \quad (4)$$

Since the fluid is frictionless there is no external torque on the swirling fluid and angular momentum is preserved. The angular momentum of an incremental annular area in the swirl chamber can be written:

$$\Delta M = \rho \Delta Q r w = \rho 2\pi r \Delta r u \frac{\Omega}{r} \quad (5a)$$

or

$$\Delta M = 2\pi \rho u \Omega r \Delta r \quad (5b)$$

and thus

$$M = 2\pi \rho u \Omega \int_{r_1}^{r_2} r \, dr \quad (6)$$

where r_1 = air core radius and r_2 = swirl chamber radius at the cross-section considered. Therefore,

$$M = \pi \rho u \Omega (r_2^2 - r_1^2) \quad (7)$$

It can be seen that:

$$Q = \omega \pi (r_2^2 - r_1^2) \quad (8)$$

and thus

$$M = \rho Q \Omega \quad (9)$$

By equating (4) and (9) it can be seen that

$$\Omega = sV \sin \varphi \quad (10)$$

The tangential velocity is thus:

$$w = \frac{sV \sin \varphi}{r} \quad (11)$$

In the above the axial velocity u was assumed not to be a function of r . This can be shown to be true by use of the radial pressure gradient equation:

$$\frac{dp}{dr} = \frac{\rho}{g} \frac{w^2}{r} \quad (12)$$

and Bernoulli's equation:

$$\frac{p}{\rho} + \frac{w^2}{2g} + \frac{u^2}{2g} = H \quad (13)$$

which show that:

$$\frac{du}{dr} = 0 \quad (14)$$

or the axial velocity is constant over any cross-section perpendicular to the nozzle axis.

At the orifice and at $r = R_1$ (air core radius) $p = 0$ and equation (13) can be written:

$$u^2 = 2gH - \left(\frac{sV \sin \varphi}{R_1} \right)^2 \quad (15)$$

in which equation (11) was used. The continuity equation is:

$$Q = \pi(R_O^2 - R_I^2)u = nt \, dV \quad (16a)$$

or

$$u^2 = \left[\frac{nt \, dV}{\pi(R_O^2 - R_I^2)} \right]^2 \quad (16b)$$

Equating (15) and (16), solving for V^2 , and using this in (15) to solve for u , and finally inserting u into (16a) yields:

$$Q = \frac{\pi(R_O^2 - R_I^2)nt \, dR_I}{\sqrt{(nt \, dR_I)^2 + [(R_O^2 - R_I^2)s \sin \phi]^2}} \sqrt{2gH} \quad (17)$$

The volume flow rate can also be written:

$$Q = C\pi R_O^2 \sqrt{2gH} \quad (18)$$

where C = the discharge coefficient. Equations (17) and (18) can be solved for C to yield:

$$C = \frac{1 - \frac{R_I^2}{R_O^2} \sqrt{\frac{R_I^2}{R_O^2}}}{\sqrt{\frac{R_I^2}{R_O^2} + \left(\frac{\pi R_O s \sin \phi}{nt \, d} \right)^2 \left(1 - \frac{R_I^2}{R_O^2} \right)^2}} \quad (19)$$

If we define:

$$\alpha = 1 - \frac{R_I^2}{R_O^2} \quad (20)$$

and

$$A = \frac{\pi R_O s \sin \phi}{nt \, d} \quad (21)$$

Equation (19) can be written:

$$C = \frac{\alpha \sqrt{1 - \alpha}}{\sqrt{1 - \alpha + A^2 \alpha^2}} \quad (22)$$

This result is identical to that of Novikov (28) except A has a slightly different form. If a single swirl slot of radius R_x is located at $r = R$ the swirl chamber radius and $\phi = 90^\circ$, then:

$$A = \frac{R_o R}{R_x^2} \quad (23)$$

which is Novikov's definition of A .

It can be seen that α is the ratio of the annular area of fluid to the orifice area. Thus α can have a value of $0 < \alpha < 1$. A can have any positive value depending upon nozzle configuration.

The final step is to maximize the flow with respect to the air core radius. According to Novikov (28) this suggestion was first made by G. M. Abramovich (29). As can be seen from Equation (18), this would mean maximizing C with respect to R_1 . C can be more easily maximized with respect to α which will give the same result since:

$$\frac{\partial C}{\partial R_1} = \frac{\partial C}{\partial \alpha} \frac{\partial \alpha}{\partial R_1} = - \frac{2R_1}{R_o^2} \frac{\partial C}{\partial \alpha} \quad (24)$$

Since $R_1 \neq 0$, by making $\partial C / \partial \alpha = 0$ then $\partial C / \partial R_1 = 0$.

The above results in:

$$1 - 2\alpha + \alpha^2 - \frac{A^2}{2} \alpha^3 = 0 \quad (25)$$

A is known from the nozzle geometry and thus α can be determined.

C is calculated from Equation (22).

Figure 52 shows the solutions of equations (22) and (25) versus A . The nozzle used for the data in this paper has the following dimensions as shown on Figure 51: $R_o = 0.009$ inch, $s = 0.016$ inch, $n = 4$ (number of swirl slots), $t = 0.010$ inch, and $d = 0.005$ inch. Thus $A = 1.22$, $C = 0.393$, and $\alpha = 0.6$.

Discharge coefficients for the Monarch F80, 0.75 gph, 30 degrees solid cone nozzle with fluids of a wide range of viscosity are shown in Figure 53. The Reynolds number used is that calculated from the flow rate assuming the nozzle running full and the nozzle throat diameter as the reference dimension. It can be seen that as Reynolds number becomes large, the discharge coefficient appears to be approaching that of the nonviscous theory. Each fluid appears to lie on a separate line however, and this plot was made inversely proportional to Reynolds number only so that the limiting case of infinite Reynolds number could be shown.

The increase in discharge coefficient is due to the decrease of the air core diameter found in the nozzle throat. At low Reynolds number a boundary layer will form on the nozzle walls (38) and the tangential velocity thus decreased. The centrifugal force necessary to maintain the air core will decrease and the nozzle throat will run fuller. The area increase will thus increase the discharge coefficient. For very low Reynolds number the air core may disappear and the fluid will fill the throat of the nozzle.

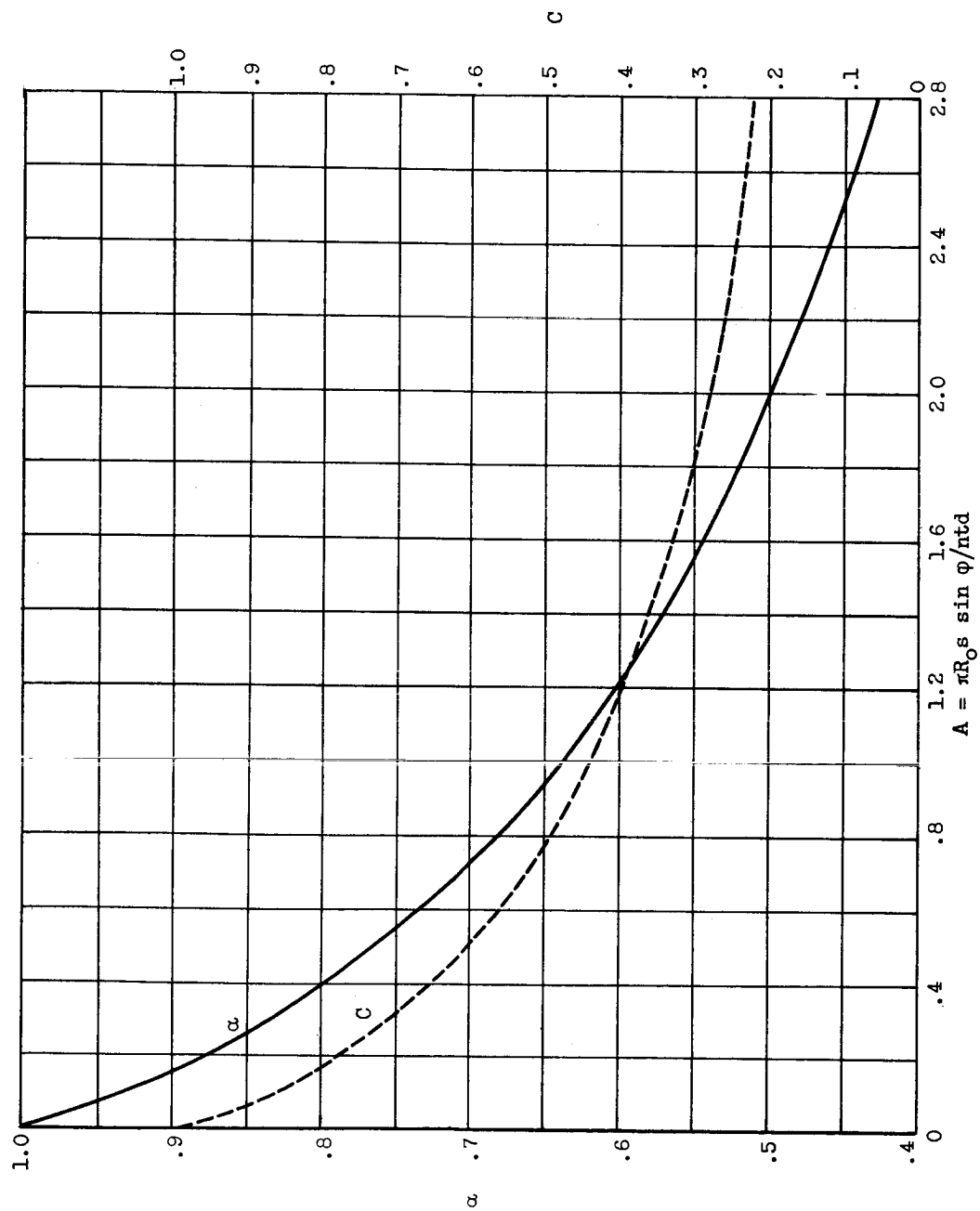


Figure 52. - Discharge coefficient and fraction of orifice filled versus A .

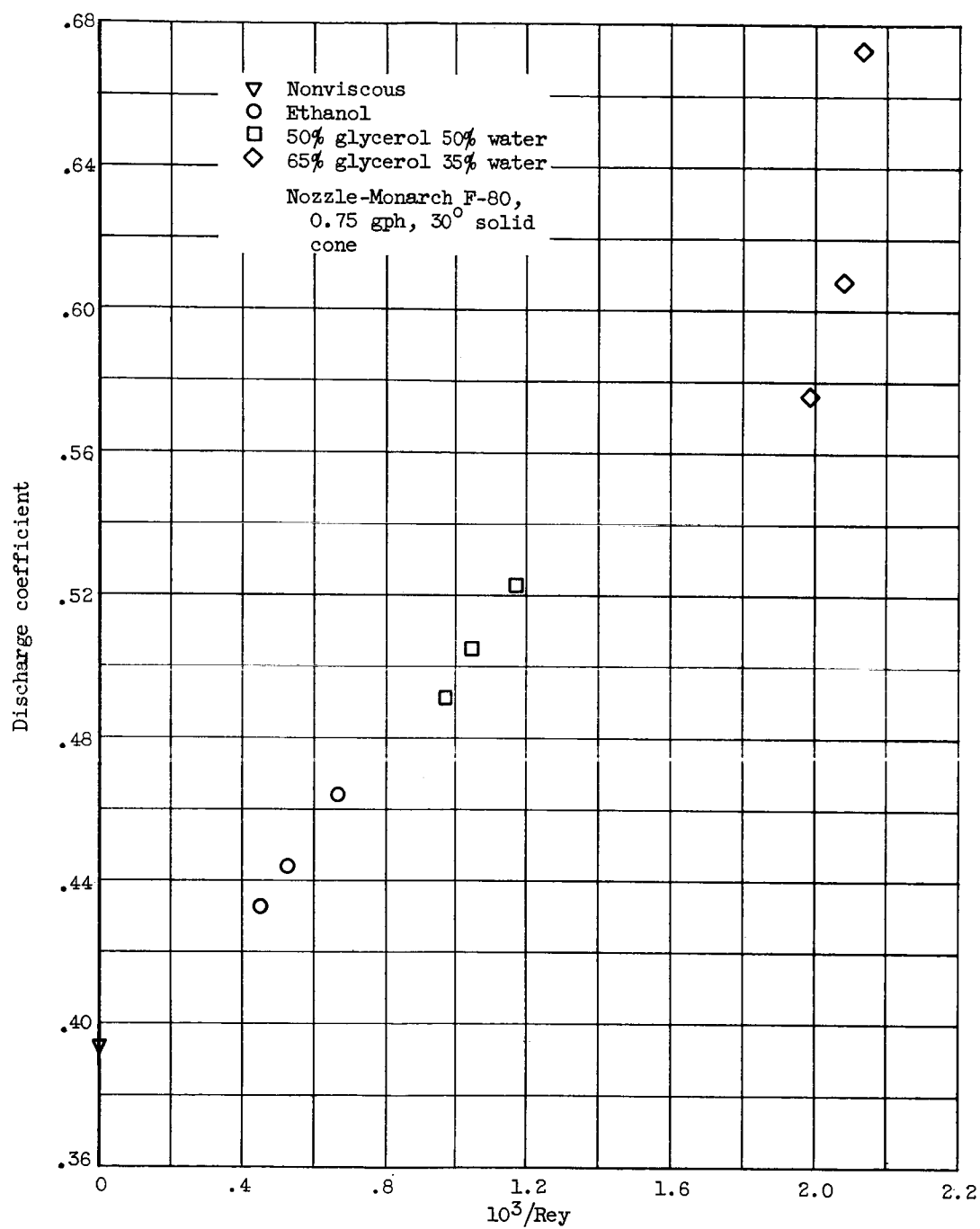


Figure 53. - Discharge coefficients for some real fluids.

A Model for Sheet Break-up

At the exit of a properly operating swirl nozzle the liquid will form a thin expanding conical sheet. Since only the small drag force acts along the surface of the sheet parallel to the motion, the sheet velocity can be assumed constant. The circumference of a circular section cut perpendicular to the axis of the cone increases with increasing distance from the nozzle, and by continuity the sheet thickness must thus decrease.

The stability of a flat sheet moving relative to a gas has been studied by several investigators (39, 40 and 41). Antisymmetric wave growth on the sheet has been emphasized since this has greater instability than a symmetric wave (39).

Once a disturbance has been initiated an unbalanced pressure is exerted on the sheet due to a local decrease in pressure on the crests and an increase in pressure in the valleys of the wave. The surface tension due to the curvature of the surface will oppose the aerodynamic forces and try to restore the sheet to a flat surface. If viscous forces are considered (41) these will tend to limit the growth of the disturbance. If the aerodynamic forces prevail, the amplitude of the disturbance wave (assumed sinusoidal) will grow until the sheet is disintegrated.

The sheet is assumed to rupture at both crests and valleys (41) or else at full wavelengths (40). This separated section of fluid sheet is then assumed to draw up into a circular ring which then breaks up according to Rayleigh's analysis (42) with a disturbance wavelength

of nine times the radius of the ligament-like ring.

The radius of the cylindrical ring is thus (40)

$$r_c = \sqrt{\frac{h\lambda_s}{\pi}} \quad (26)$$

where h is the sheet thickness, λ_s is the disturbance wavelength on the sheet, and it is assumed that the sheet breaks up into full wavelength sections (say at the crests).

The disturbance wavelength on the cylinder will be 9 times that of equation (26), and the drop radius will then be (39)

$$r_d \cong 1.06 \sqrt{h\lambda_s} \quad (27)$$

According to the nonviscous analysis of Squire (39) the wavelength of maximum instability is

$$\lambda_s = \frac{4\pi\sigma}{\rho_g V^2} \quad (28)$$

where σ is the liquid surface tension, ρ_g is the gas density, and V is the relative velocity between the gas and the liquid sheet. If the Weber number is defined as

$$W = \frac{\rho_g V^2 h}{\sigma} \quad (29)$$

then equation (27) becomes

$$r_d \cong 5.32 h W^{-1/2} \quad (30)$$

A single drop size will obviously not occur. It can be expected that a spectrum of ring or ligament sizes will result from the sheet break-up, and that for any given ligament a spectrum of drop sizes will result from the ligament break-up.

The important information to be gained from equation (30) is that some measure of the drop size distribution (perhaps the maximum drop size) may be a function of the sheet thickness and the Weber number.

When viscous forces are added to the analysis (41) the wavelength of the disturbance of maximum instability is increased and the wave growth decreased as compared to the nonviscous case. The longer wavelength will result in larger drops (eq. (27)), but if it is assumed that growth of the wave must reach a certain value (41) before break-up occurs, the sheet thickness will be less at rupture which will favor a smaller drop size. The particular geometry of the fluid sheet must thus be known to evaluate the effect of viscosity.

If the drops formed by the sheet and ligament break-up are above a critical size determined by (42)

$$r_{\text{crit}} = \frac{10 \sigma}{\rho_g V^2} \quad (31)$$

The drop will shatter into smaller drops. This is a result of the dynamic pressure force favoring break-up exceeding the surface tension force which holds the drop in its spherical shape.

DATA PRESENTATION

The data presented in this paper was taken using a Monarch F-80, 0.75 gph, 30° solid cone nozzle. Six stations were located in a plane perpendicular to the nozzle axis and 1.25 inches downstream from the nozzle. Each station represents a sample volume of 4x4x0.2 mm. A schematic of the data stations can be seen in Figure 54. Although the sampling volume did not extend to the very outer edge of the spray, the drop population was so sparse beyond station 6 that a reasonable sized sample would have been difficult to obtain.

Spray photographs were taken at each of the six stations with three fluids at three nozzle pressures. The fluids and pressures used are as follows:

- (1) Ethanol at 40, 70, and 100 psig.
- (2) 50 percent glycerol - 50 percent water at 130, 170, and 210 psig.
- (3) 65 percent glycerol - 35 percent water at 170, 210, and 250 psig.

The above solutions are on a percent weight basis.

120 exposures (10 flashes on each of 12 photographs) were taken at each of the 54 conditions and locations. The drop count data which is number of drops per sample volume is thus 120 times as great as

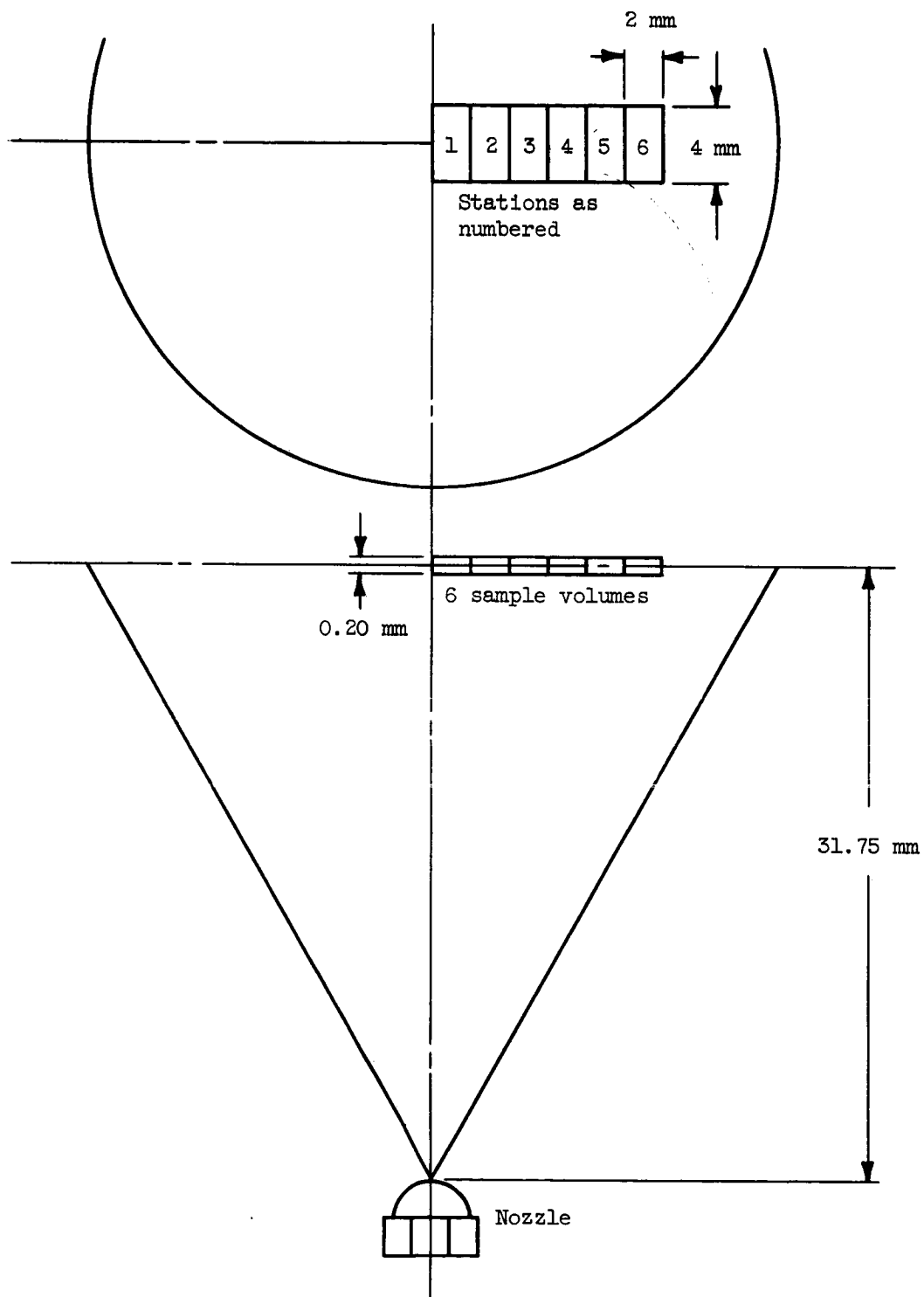
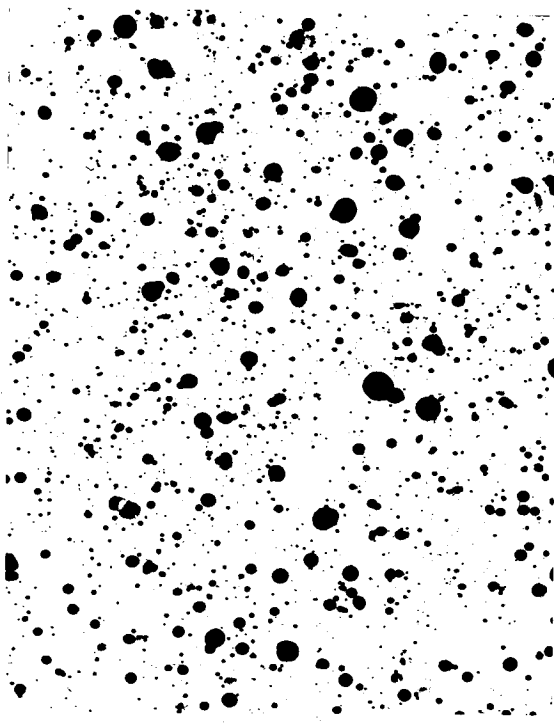


Figure 54. - Location of data sampling stations.

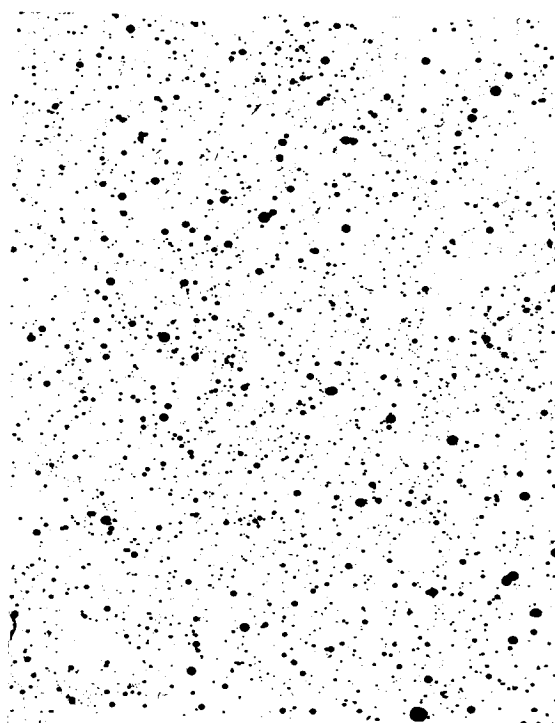
would be expected at any instant of time.

Examples of spray photographs obtained are shown in Figure 55. These photographs were taken at station 1 using ethanol at 25, 40, 70, and 100 psig.

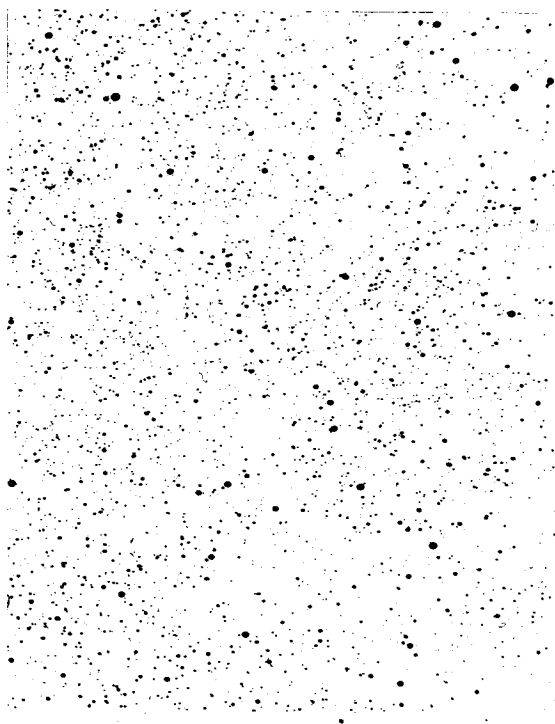
The raw drop count data obtained from the photographs of all 54 conditions and stations and the mean diameters calculated from these counts are given in Appendix III.



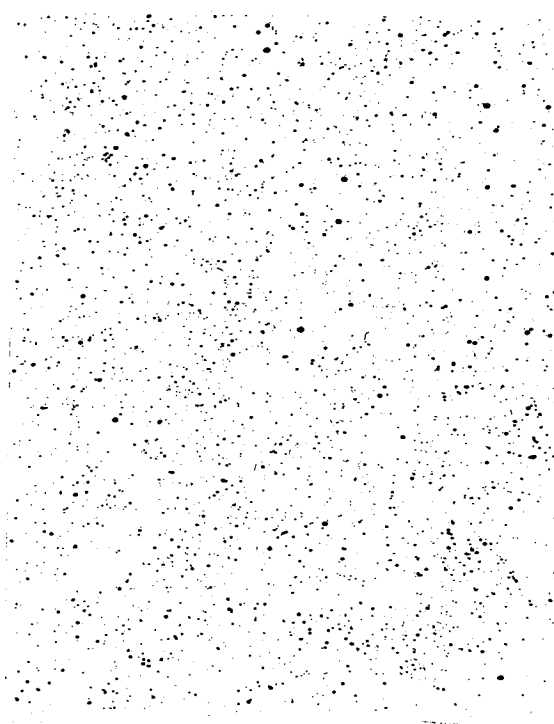
25 psig



40 psig



70 psig



100 psig

Figure 55. - Sample photographs of an Ethanol spray.

DATA REDUCTION AND ANALYSIS

The objective of the data reduction was to fit a distribution to the drop size data and then correlate the parameters of the distribution with the spray variables (pressure, viscosity, surface tension, and density) and position in the spray. The inverse problem could then be solved: knowing the spray variables what is the drop size distribution at a given position in the spray. This has been accomplished and will be outlined in the following sections.

The Drop Size Distribution

If a unification of the data is to be accomplished it must be done with normalized distributions. Normalization requires information over the entire range of drop size from zero to infinity. Nothing is known about the distribution below a drop size of 10 microns, and thus an extrapolation must be made. For the drop size number distribution an extrapolation might involve fifty percent or more of the area under the curve while for the drop size volume distribution it will generally be less than one percent. This results of course from the peak of the number distribution lying around a drop size of 10 microns while the volume distribution peak lies well out into the size range where the data is well defined. For this reason the distribution curve fits were made on the volume distribution.

The drop size categories were selected such that the increments increase in size by multiples of $\sqrt{2}$. This choice provides a constant percent uncertainty of size for all the categories, i.e., the category sizes are small for small drop sizes and large for large sizes. When this category system is plotted on a logarithmic scale the category boundaries are uniformly spaced.

If the cumulative drop volume (percent less than a given size) is plotted on log-probability graph paper and the result is a straight line then the data fits the log-normal distribution* (43) with drop volume density and cumulative volume distributions

$$\frac{dv}{dy} = \frac{\delta}{\sqrt{2\pi}} e^{-\delta^2 y^2 / 2} \quad (1)$$

$$v = \frac{1}{\sqrt{2\pi}} \int_{-\infty}^{\delta y} e^{-u^2 / 2} du \quad (2)$$

where

$$y = \log \frac{x}{\bar{x}} \quad (3)$$

x is drop size, \bar{x} is the volume or mass median, and δ is inversely related to the spread of the distribution.

Figure 56 shows a cumulative volume versus drop size plot (circles and dashed line) for a typical set of data (ethanol, 40 psig, station 1).

It should be noted that these 3 equations differ slightly from those of reference 43. Here the logarithm is to the base 10 and $\delta = \sqrt{2} \delta^ / \log e$ where δ^* is that of reference 43.

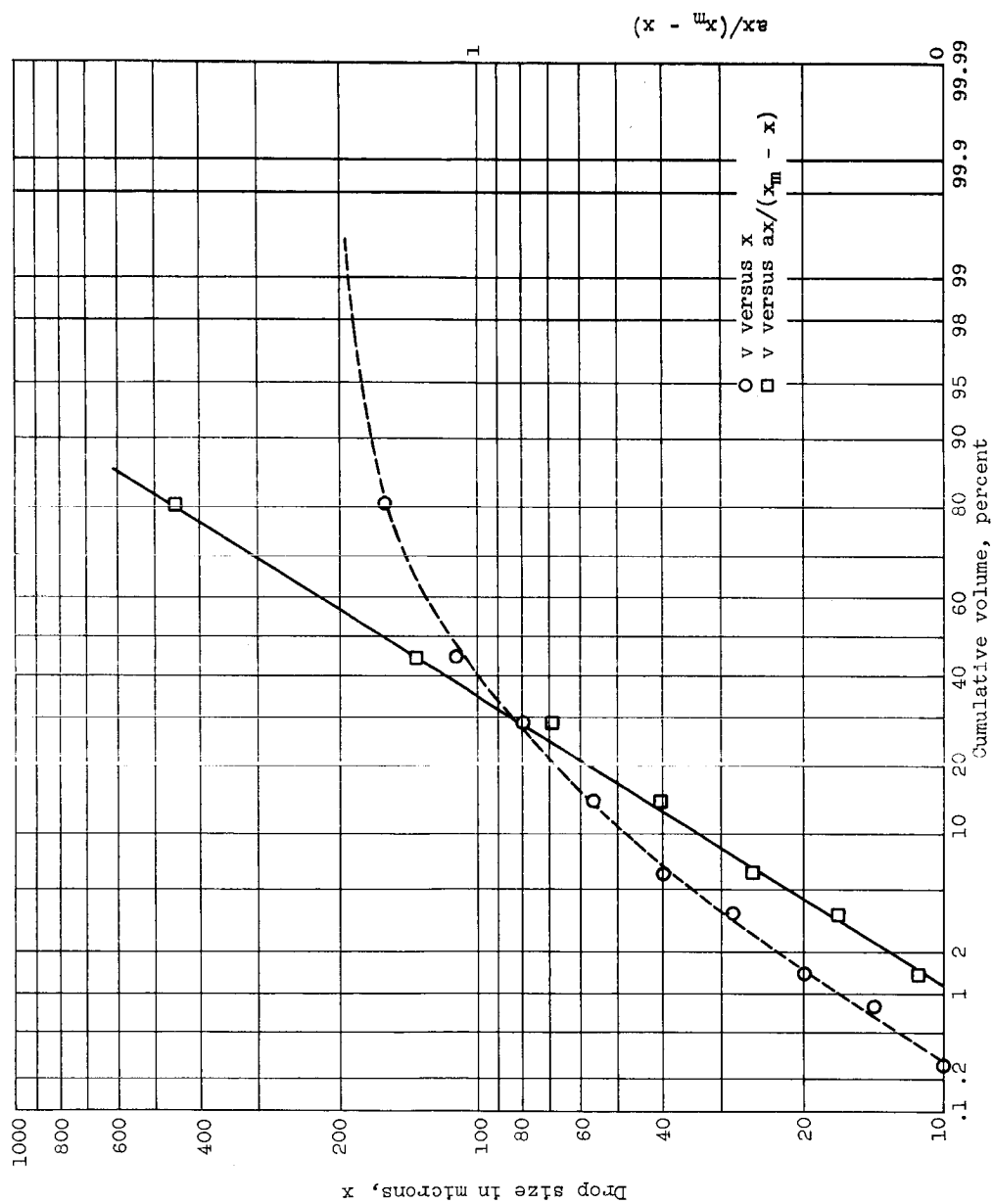


Figure 56. - Cumulative volume distribution for a typical set of data.

It can be seen that a straight line may be a good approximation for small drop sizes but obviously not for large sizes. This falling-off for large sizes is typical of all the data. The log-normal distribution is thus not the proper distribution to fit this data.

A simple transformation of the independent variable is possible which will cause the data to lie on a straight line. This is accomplished by a redefinition of equation (3) resulting in

$$y = \log \frac{ax}{x_m - x} \quad (4)$$

where x_m is a maximum drop size and a is a parameter which determines the mass median

$$x_{50} = \frac{x_m}{a + 1} \quad (5)$$

and thus the skewness of the distribution. Equations (1) and (2) remain the same and along with equation (4) define what is often referred to as the upper-limit function (43). The cumulative volume distribution versus $ax/(x_m - x)$ is shown in Figure 56 (squares and solid line).

The concept of maximum drop size is a desirable property of a distribution since it coincides with the physical reasoning of the break-up process. The fluid sheet and ligament disintegration will result in a maximum drop size (an infinitely large drop is untenable), and this largest drop will be further influenced by drag forces. If the drag forces exceed the surface forces the drop will be unstable and break up into smaller drops (44).

Without further evidence, x_m in equation (4) must be considered just another parameter which enables a straight-line cumulative volume plot to be made.

If, however, x_m can be shown to coincide with the largest observed drop size (as will be the case) then it must be conceded physical significance.

The number density and cumulative number distributions for the upper limit function are

$$\frac{dn}{dy} = (1 + ae^{-y/\log e})^3 \left(\frac{x_{30}}{x_m} \right)^3 \frac{\delta}{\sqrt{2\pi}} e^{-\delta^2 y^2 / 2} \quad (6)$$

and

$$n = \frac{1}{\sqrt{2\pi}} \left(\frac{x_{30}}{x_m} \right)^3 \left[a^3 e^{9/2(\delta \log e)^2} \int_{-\infty}^{\delta y + 3/\delta \log e} e^{-u^2/2} du \right. \\ + 3a^2 e^{2/(\delta \log e)^2} \int_{-\infty}^{\delta y + 2/\delta \log e} e^{-u^2/2} du \\ + 3ae^{1/2(\delta \log e)^2} \int_{-\infty}^{\delta y + 1/\delta \log e} e^{-u^2/2} du \\ \left. + \int_{-\infty}^{\delta y} e^{-u^2/2} du \right] \quad (7)$$

The various mean diameters are determined from (43)

$$\frac{\bar{x}_q}{x_{qp}} - p = \frac{\int_0^{x_m} x^q \frac{dn}{dx} dx}{\int_0^{x_m} x^p \frac{dn}{dx} dx} \quad (8)$$

The simplest calculations are those involving $q = 3$ and are

$$\bar{x}_{32} = \frac{x_m}{1 + ae^{1/2(\delta \log e)^2}} \quad (9)$$

$$\bar{x}_{31} = \frac{x_m}{\left[1 + 2ae^{1/2(\delta \log e)^2} + a^2e^{2/(\delta \log e)^2} \right]^{1/2}}$$

$$\bar{x}_{30} = \frac{x_m}{\left[1 + 3ae^{1/2(\delta \log e)^2} + 3a^2e^{2/(\delta \log e)^2} + a^3e^{9/2(\delta \log e)^2} \right]^{1/3}} \quad (10)$$

The rest of the mean diameters can be calculated from

$$\frac{\bar{x}^{p-c}}{x_{pc}} = \frac{\bar{x}^{q-c}}{x_{qc}} \quad (11)$$

using equations (8), (9), and (10).

Spray Parameters in Dimensionless Groups

If a dimensional analysis is performed assuming that a measure of drop size, say x_m , is a function of orifice diameter, liquid density,

viscosity, and surface tension, nozzle pressure drop, and liquid velocity at the nozzle orifice or

$$x_m = f(D_o, \rho_L, \mu_L, \sigma, P, v) \quad (12)$$

then it is found that

$$\frac{x_m}{D_o} = f\left(\frac{\rho_L v D_o}{\mu_L}, \frac{P D_o}{\sigma}, \frac{\rho_L v^2}{P}\right) \quad (13)$$

The term $\rho_L v^2/P$ will remain essentially constant since it can be shown that

$$\frac{\rho_L v^2}{P} = 2g_c \left(\frac{c}{\alpha}\right)^2 \quad (14)$$

where c is the discharge coefficient and α is the fraction of the nozzle orifice filled with liquid. c/α should remain essentially constant.

The second term on the right of equation (13) can be shown to be

$$\frac{P D_o}{\sigma} = \frac{1}{2g_c} \left(\frac{\alpha}{c}\right)^2 \left(\frac{D_o}{h}\right) \left(\frac{\rho_L}{\rho_g}\right) \left(\frac{\rho_g v^2 h}{\sigma}\right) \quad (15)$$

where ρ_g is the gas density, h is the sheet thickness, and v is the liquid velocity. If the gas is assumed stationary, the last term on the right of equation (15) is the Weber number discussed in connection with sheet break-up. This Weber number would be the best when correlating drop size from sheet break-up, but it is a difficult quantity to evaluate. The determination of sheet thickness and velocity at break-up would require a formidable study in itself.

The dimensionless quantities thus used for the correlations in this paper are,

$$\text{Reynolds number} = \frac{\rho_L v D_o}{\mu_L} \quad (16)$$

and

$$\text{Weber number} = \frac{\rho_L v^2 D_o}{\sigma} \quad (17)$$

The velocity used in equation (16) is that calculated from the nozzle running full.

The spray parameters and dimensionless groups determined for the various flow conditions are given in table III. The abbreviations used under "condition" should be interpreted as E40 meaning ethanol at 40 psig, etc., and 50G130 meaning 50 percent glycerol at 130 psig.

TABLE III - FLUID PROPERTIES AND FLOW PARAMETERS FOR THE DATA

Condition	Density, g/cc	Viscosity, cp	Surface tension, dyn e/cm	Flow rate Q(cm ³ /sec)	Reynolds number	Weber number
E40	0.8084	1.46	23.4	0.486	1500	2694
E70	0.8084	1.46	23.4	0.617	1903	4715
E100	0.8084	1.46	23.4	0.720	2220	6735
50G130	1.1263	6.0	70.0	0.8175	855	2927
50G170	1.1263	6.0	70.0	0.9129	954	3827
50G210	1.1263	6.0	70.0	0.9867	1031	4728
65G170	1.1670	15.2	68.5	1.097	469	3911
65G210	1.1670	15.2	68.5	1.1259	481	4831
65G250	1.1670	15.2	68.5	1.1771	503	5752

Correlation of Drop Size Volume Distribution

The form of equation (1) which was used to fit the experimental drop size volume distribution was

$$\frac{dv}{d \log x} = \frac{\delta x_m}{\sqrt{2\pi} (x_m - x)} e^{-\delta^2 y^2 / 2} \quad (18)$$

where again

$$y = \log \frac{ax}{x_m - x} \quad (4)$$

and x is the drop size in microns, x_m is the upper limit of drop size, a is a skewness parameter, and δ is a parameter inversely proportional to the spread of the distribution. The logarithms are to the base ten in all of the equations presented here. Equation (18) was used since the experimental data is in the form of drop volume Δv_i in a logarithmic increment of drop size ($\log x_{i+1} - \log x_i$) or $\log \sqrt{2}$.

Each of the distributions was fit to equation (18) using a weighted least-squares method. A definite trend of x_m versus position in the spray could be seen, but there seemed to be considerable scatter in the individual values of a and δ . Considerable effort was spent in trying to extract usable information on the a and δ without success.

It was noted, however, that if the curve fits of equation (18) were plotted versus $\log x$ that all of the distributions were very similar in shape but only translated along the x axis. This would imply, at least as a first approximation, that all of the distributions might be represented by equation (18) with the same a and δ but different x_m .

A weighted least-squares fit was then performed simultaneously on all of the data to determine the best value of a and δ while each distribution was allowed its individual value of x_m . The best

value of a was very close to one, thus $a = 1$ was used in the remaining correlations. It can be seen from equation (5) that the mass median diameter is one-half of x_m . This means that the form of volume distribution represented by equation (1) is symmetrical when plotted versus $\log x$.

Since a and δ are constant for all of the distributions, equation (9) shows that \bar{x}_{32} and x_m differ only by a constant. The trend of x_m versus position in the spray was similar to that of \bar{x}_{32} calculated from the raw data which is shown in Figure 57. The raw data mean diameters are calculated from

$$x_{qp}^{q-p} = \left(\sum_{i=1}^n n_i x_i^q \right) / \left(\sum_{i=1}^n n_i x_i^p \right) \quad (19)$$

where n_i is the number of drops in the i^{th} size category.

It can be seen from Figure 57 that \bar{x}_{32} and thus x_m appears to consist of two modes. Mode one centered on the spray axis decreases rapidly with pressure and mode two located off the spray axis decreases more slowly with pressure and is translated away from the spray axis with increasing pressure. These trends are similar with the glycerol-water sprays.

The following correlation for x_m portrays its behavior the most adequately of the several equations tried:

$$\frac{x_m}{D_0} = A_1 e^{-\theta^2/2S_1^2} + A_2 e^{-(\theta-M)^2/2S_2^2} \quad (20)$$

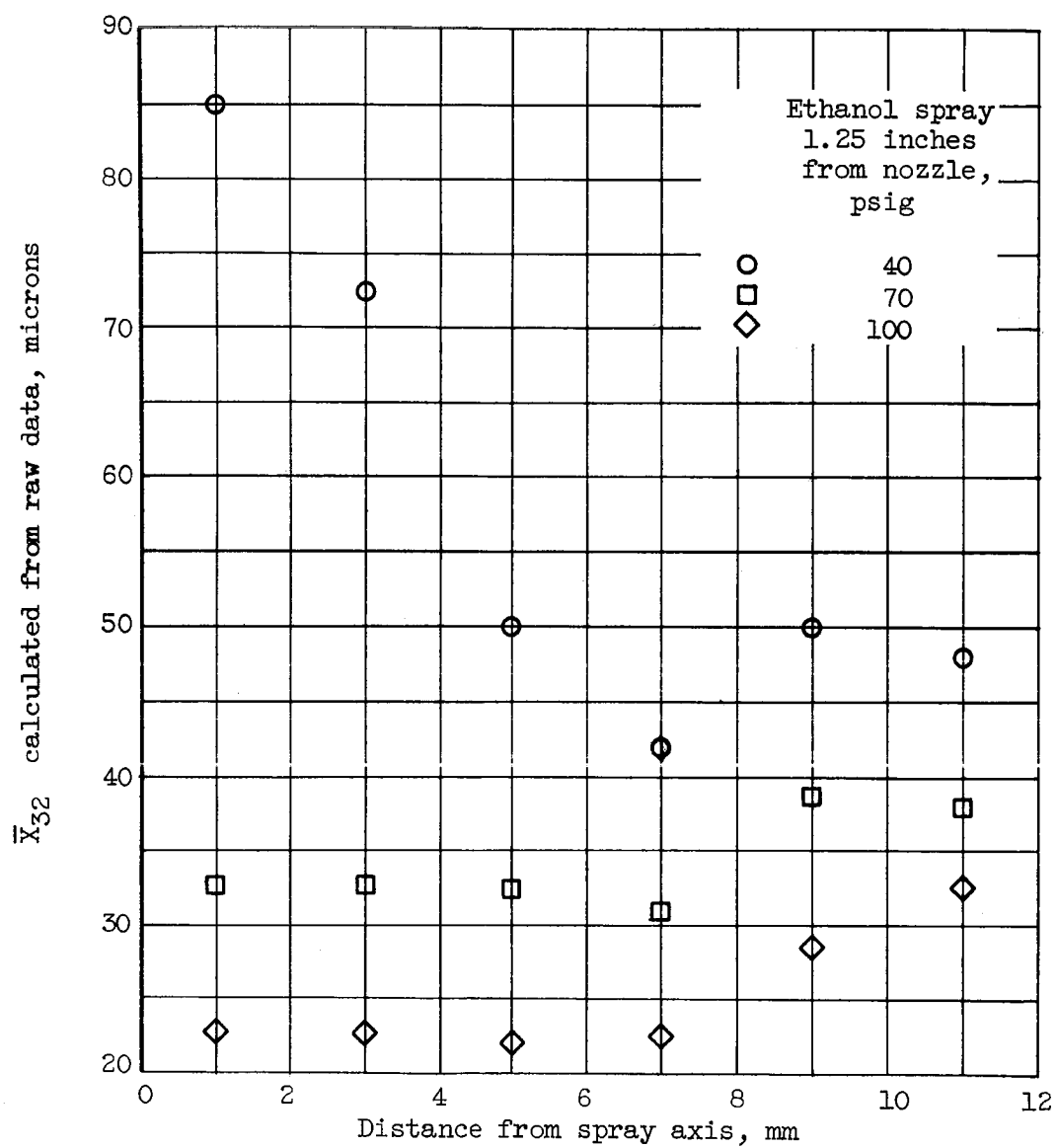


Figure 57. - Sauter mean diameter versus position in the ethanol sprays.

where D_o is the nozzle diameter in microns, θ is the angular displacement from the spray axis in degrees,

$$A_1 = 1.24 e^{-0.1462 R^2 W^{1/2}} \quad (21)$$

$$A_2 = 0.618 W^{-0.1638} \quad (22)$$

$$S_1 = 5.951 \quad (23)$$

$$S_2 = 14.91 R^{1/2} W^{-1/4} \quad (24)$$

$$M = \frac{34 RW}{3.15 + RW} \quad (25)$$

$$R = (\text{Reynolds number}) \times 10^{-3}$$

$$W = (\text{Weber number}) \times 10^{-3}$$

S_1 , S_2 , and M are angular quantities in degrees.

A_1 , and A_2 are dimensionless.

The above maximum drop size correlation was obtained with

$$a = 1.0, \delta = 2.3677. \quad (26)$$

The effect of each term in equation (20) on the maximum drop size can be seen by investigating equations (21) to (25). The term $R^2 W^{1/2}$ in the exponent of A_1 is approximately proportional to the cube of liquid velocity for constant fluid properties. A_1 will thus decrease very rapidly with increasing fluid velocity. This effect can be seen for the ethanol sprays in Figure (58) in which

$$x_{m1} = A_1 D_o e^{-\theta^2 / 2 S_1^2} \quad (27)$$

$$x_{m2} = A_2 D_o e^{-(\theta - M)^2 / 2 S_2^2} \quad (28)$$

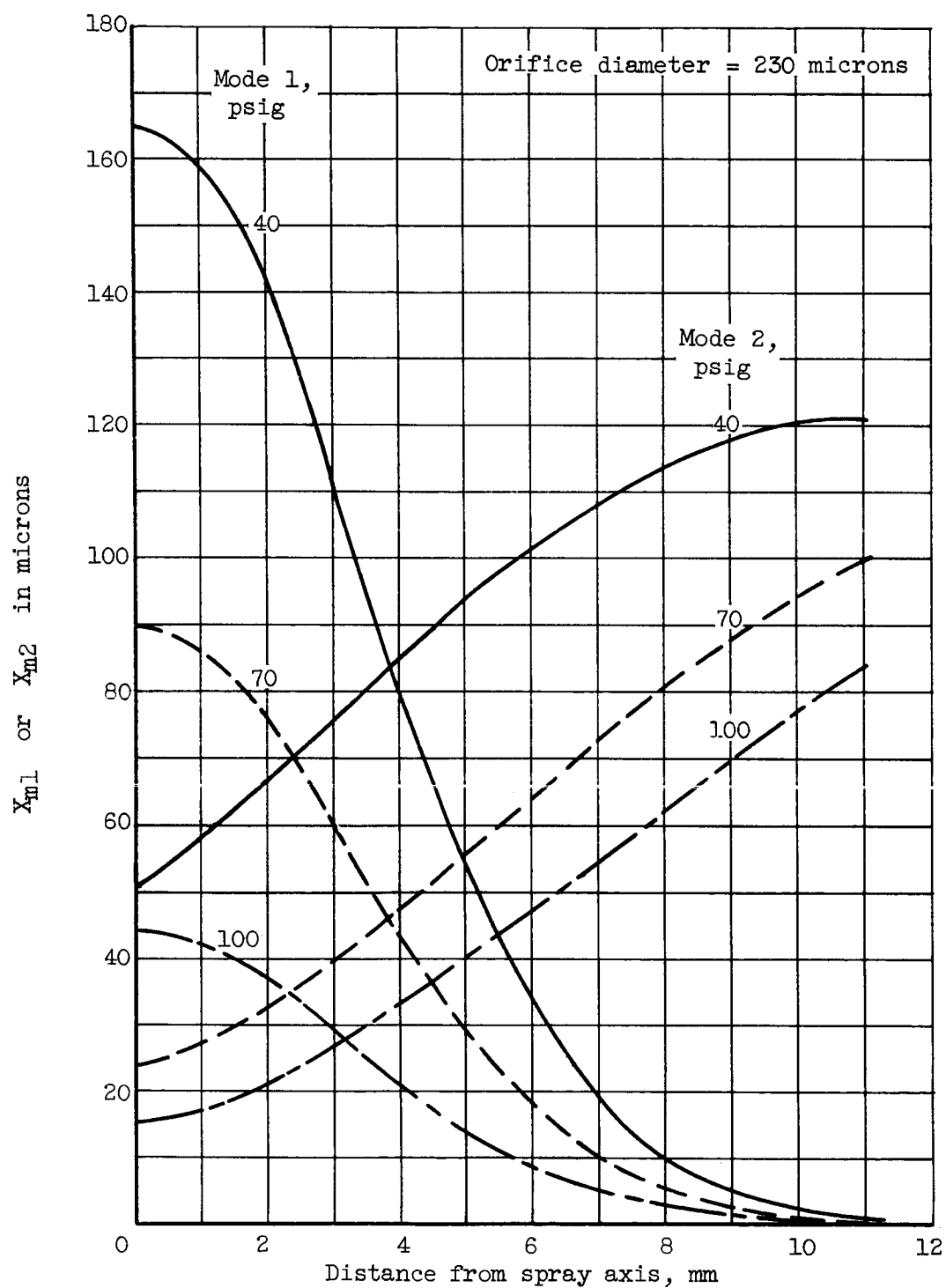


Figure 58. - Pressure effect on bimodal property of X_m for ethanol sprays.

The plots are made with distance from the nozzle axis rather than angle as the abscissa. This is related to angle by

$$d = 31.75 \tan \theta \quad (29)$$

The amplitude of mode 2 (A_2) has a weak dependence on only Weber number. The change in mode 2 evident in Figure 58 is due mainly to a translation of the peak to larger angles. Equation (25) defines the location of this peak. The term RW is a rapidly changing function of fluid velocity since it is approximately proportional to the velocity cubed for constant fluid properties. M can thus be seen to change rapidly for low values of RW but then become asymptotic to $M = 34$ for high values of RW . The spread of mode 2 (S_2) will change very little for a given fluid for which it can be shown to be proportional to the square-root of discharge coefficient. For the ethanol sprays the change in S_2 is less than 4 percent for sprays from 40 to 100 psig.

The effect of viscosity on the two modes can be seen in Figure 59. The Weber number is similar for both sets of data and thus the amplitude of mode 2 is nearly the same. The increased viscosity of the dashed curve has caused a narrowing and shifting toward the spray axis for mode 2.

The discussion of possible reasons for the observed behavior of x_m will be postponed until the mass distribution within the spray is presented.

Figure 60 shows the maximum drop size calculated from equation (20)

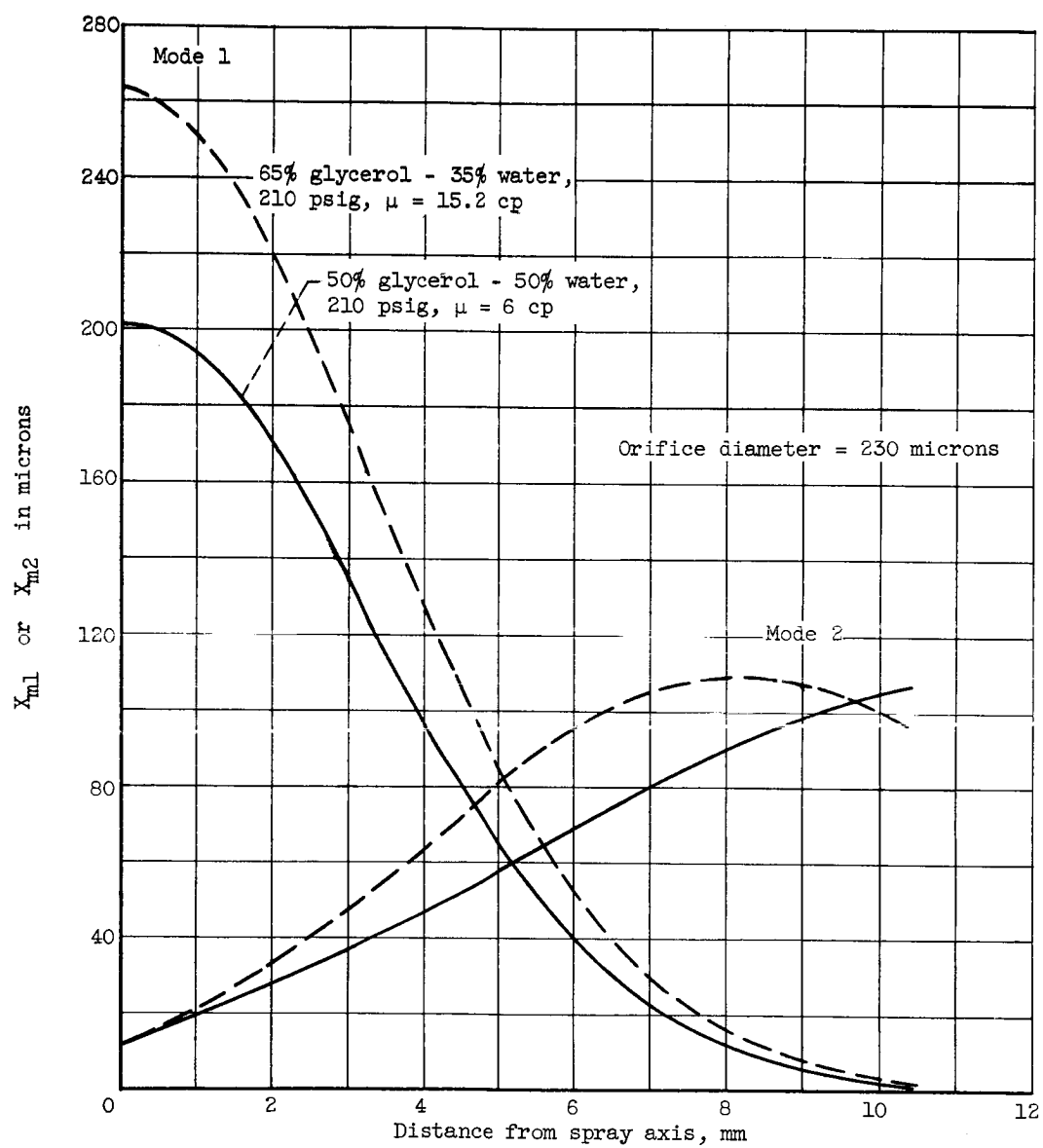


Figure 59. - Viscosity effect on bimodal property of X_m .

versus the largest observed drop size from the raw data. Since the raw data was classified according to categories it is only possible to say that the largest drop is between two limits. If x_m calculated falls between these limits the ordinate and abscissa were plotted as equal. If x_m was smaller than the lower limit of the category or larger than the upper limit of the category, the observed largest size was plotted as the lower or upper limit of the category respectively. It can be seen that x_m calculated in general falls within the boundaries of the category of the largest observed drop size. Thus x_m must be considered to be a parameter with physical significance.

Figure 61 shows the Sauter mean diameter (\bar{x}_{32}) calculated from the correlated values of a , δ , and x_m compared to that calculated from the raw data. It can be seen that the agreement is fairly good but there is some scatter of the points. The raw data \bar{x}_{32} cannot be considered a precise quantity itself since it contains some random variation due to the finite sample size. It must also be recognized that such a simple expression as equation (20) cannot be expected to precisely describe the maximum drop size obtained from such a complex phenomena as sheet and ligament break-up from a centrifugal nozzle.

Examples of the drop size volume distributions are given in Figures 62 and 63. The distributions are plotted versus $100 \ x/x_m$, the percentage of the maximum drop size. All of the distributions are unified into a single curve by plotting in this manner. Figures 64

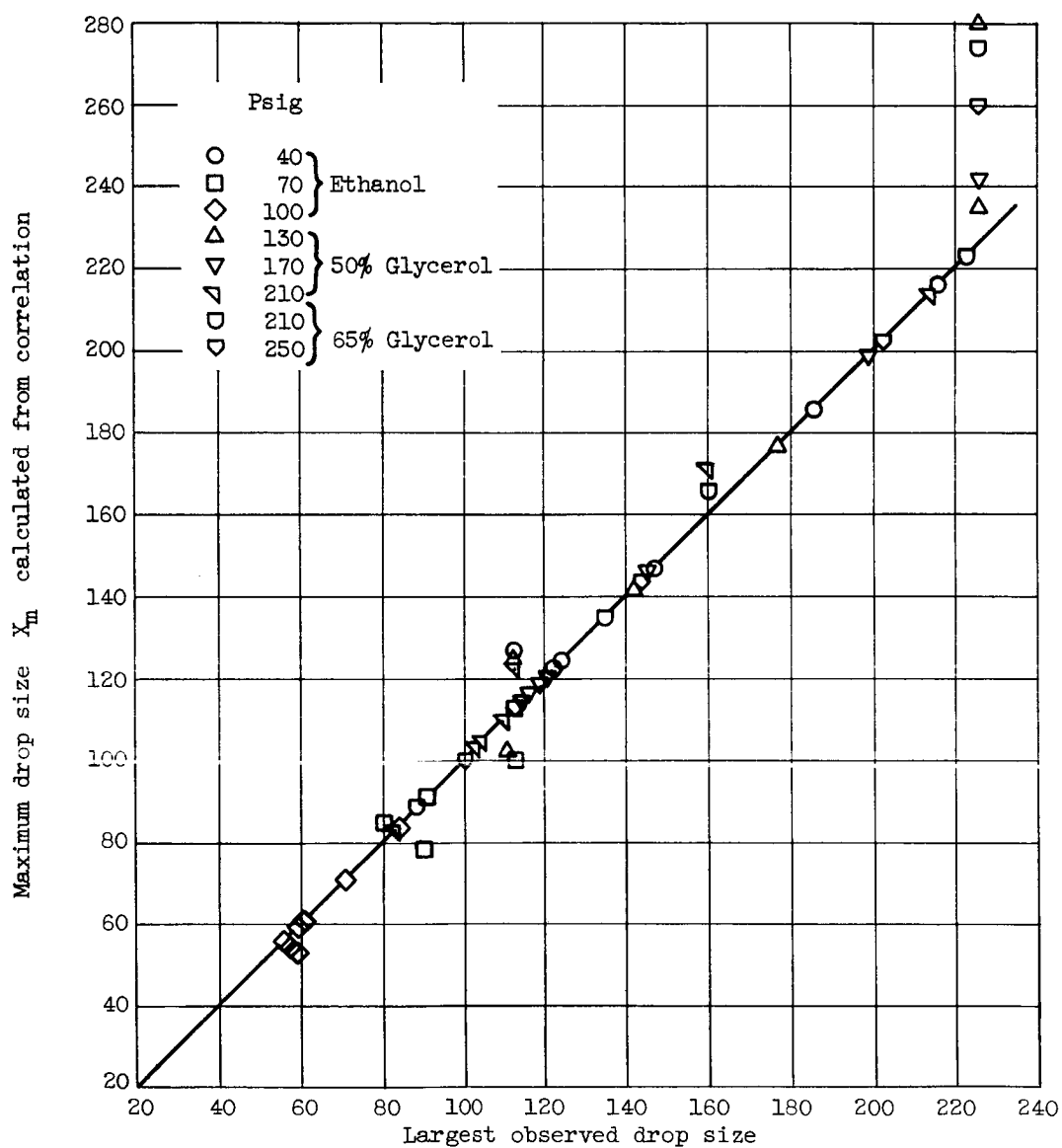


Figure 60. - Calculated maximum drop size compared to largest observed drop size.

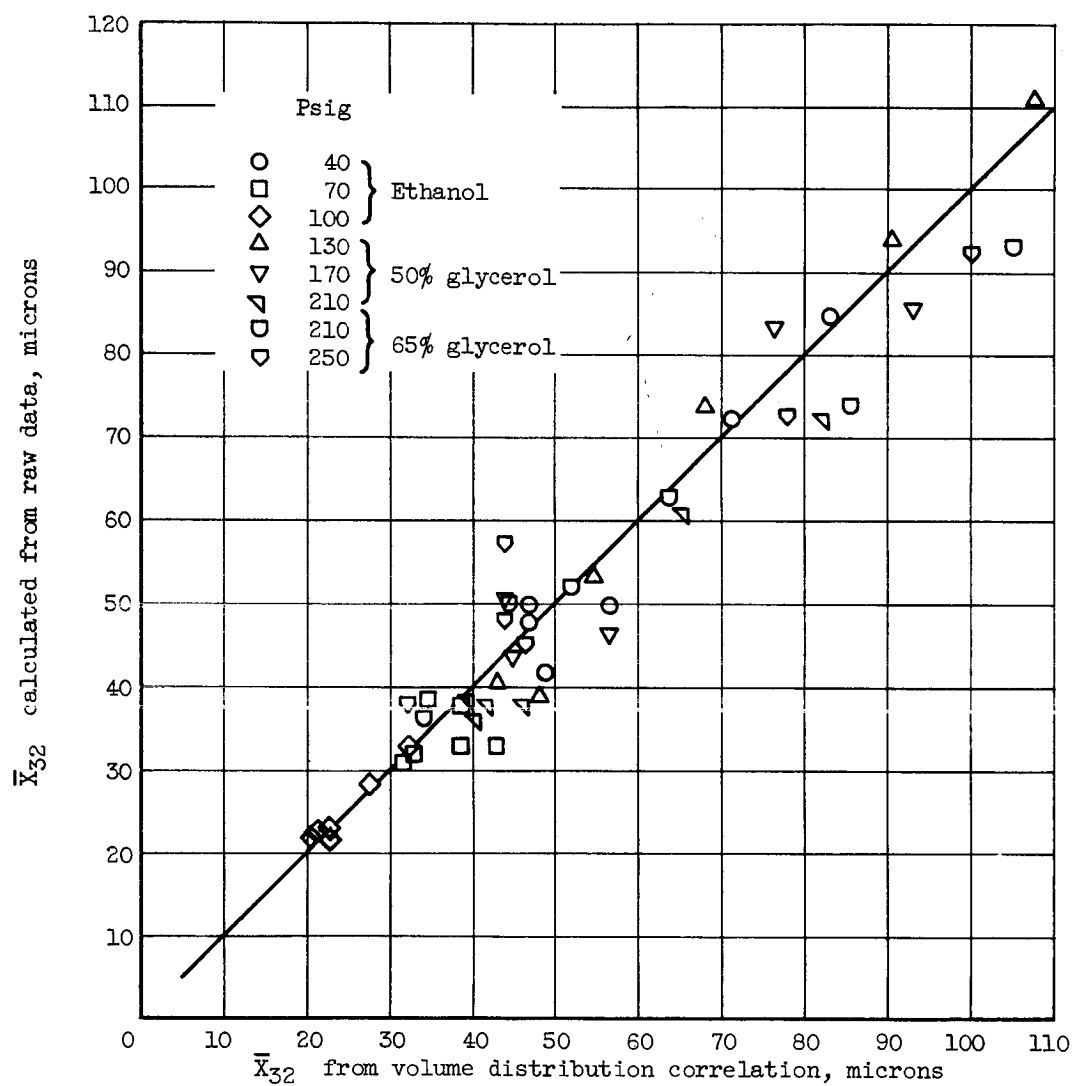


Figure 61. - Comparison of Sauter mean diameters calculated from correlation to that of raw data.

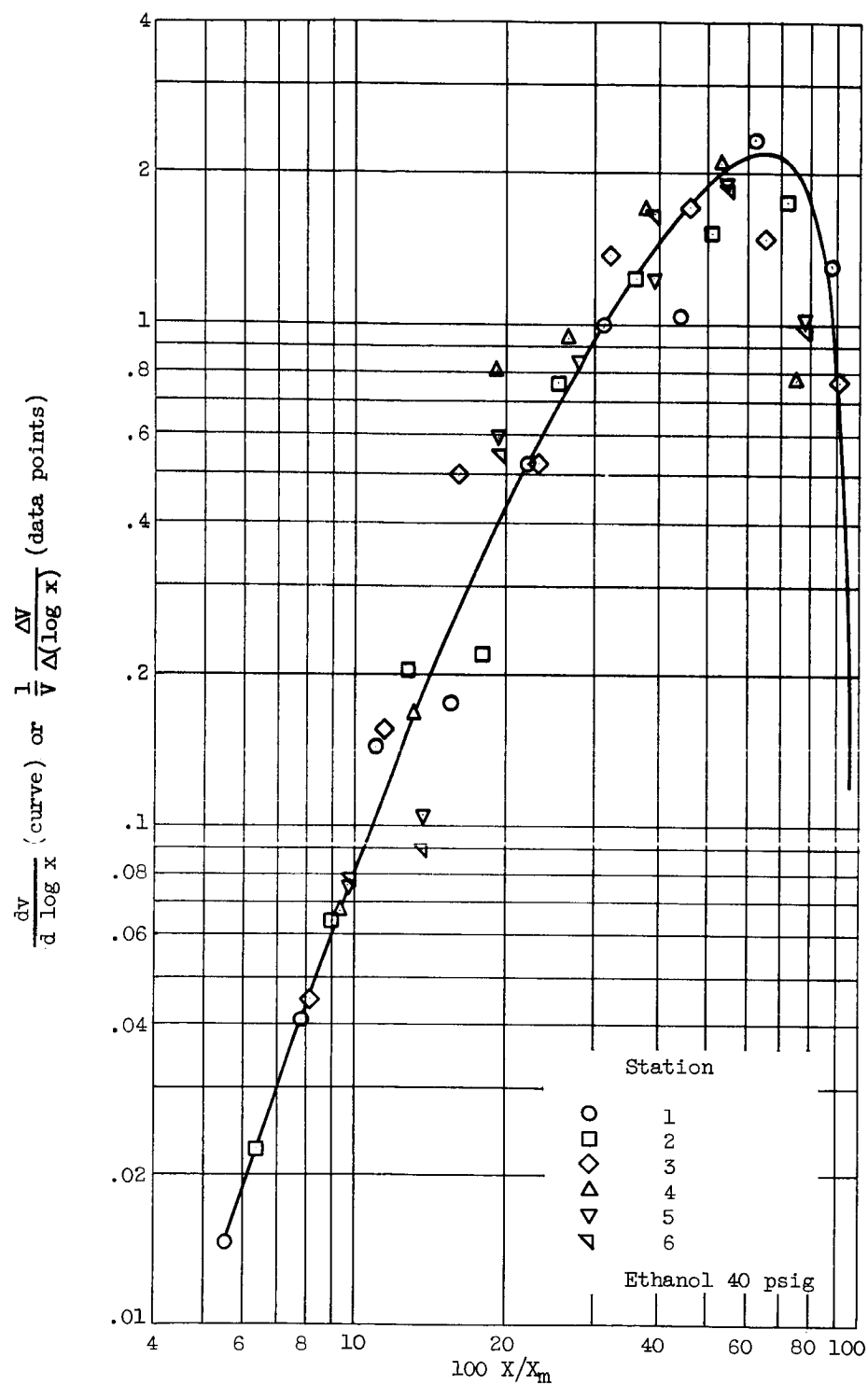


Figure 62. - Volume distribution versus percent maximum drop size for ethanol sprays.

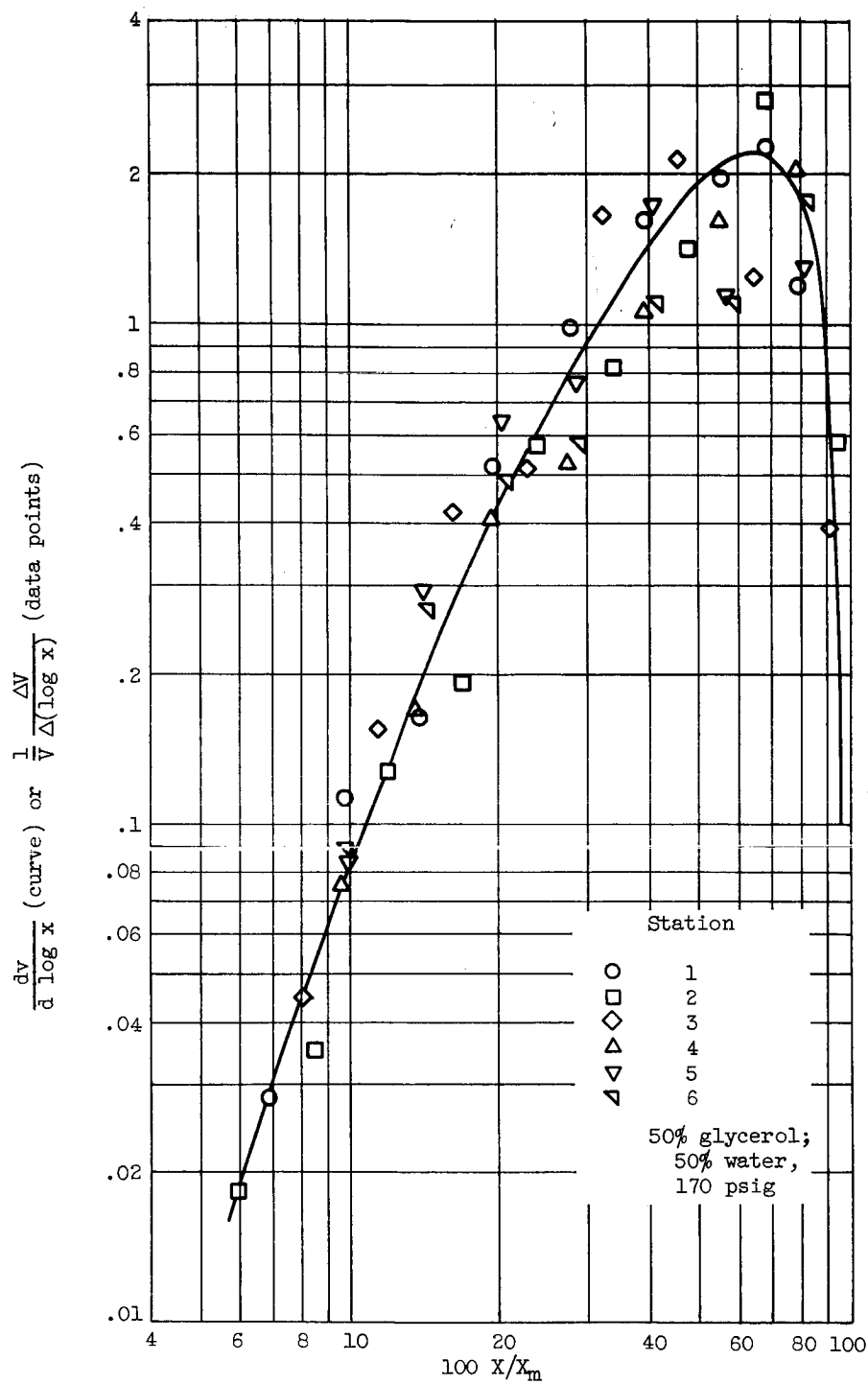


Figure 63. - Volume distribution versus percent maximum drop size for glycerol sprays.

and 65 are examples of the drop size number distributions for which the fitted curve again is the same for all of the data.

It should be noted here that the data correlation was obtained by using all of the data presented in Appendix III except for that of 65 percent glycerol at 170 psig. As can be seen from the raw data this condition represents a spatial spray distribution completely contrary to that of the rest of the data. Virtually no large drops are found at the center of the spray which is opposed to the conclusions which would be obtained from the other data. When this situation was observed this part of the experiment was repeated, but the same results occurred. There is apparently a new mode of break-up occurring for this very viscous fluid at low pressure. It is known that the nozzle orifice is close to running full at this condition.

Due to the above it can be seen that an extrapolation of the correlation (eq. (20)) to that of lower Reynolds number than used in the correlation is extremely dangerous.

Comparison of Results to Other Data

In Figure 66 the cumulative volume versus the transformed independent variable $(x/x_m - x)$ for several sets of data is presented. The open symbols represent all six stations for ethanol at 40 psig. The solid line represents the result of the presently discussed drop size correlation. When plotted as shown, all of the fitted cumulative distributions fall on this line since x_m is the only variable between different positions in the spray or different spray conditions.

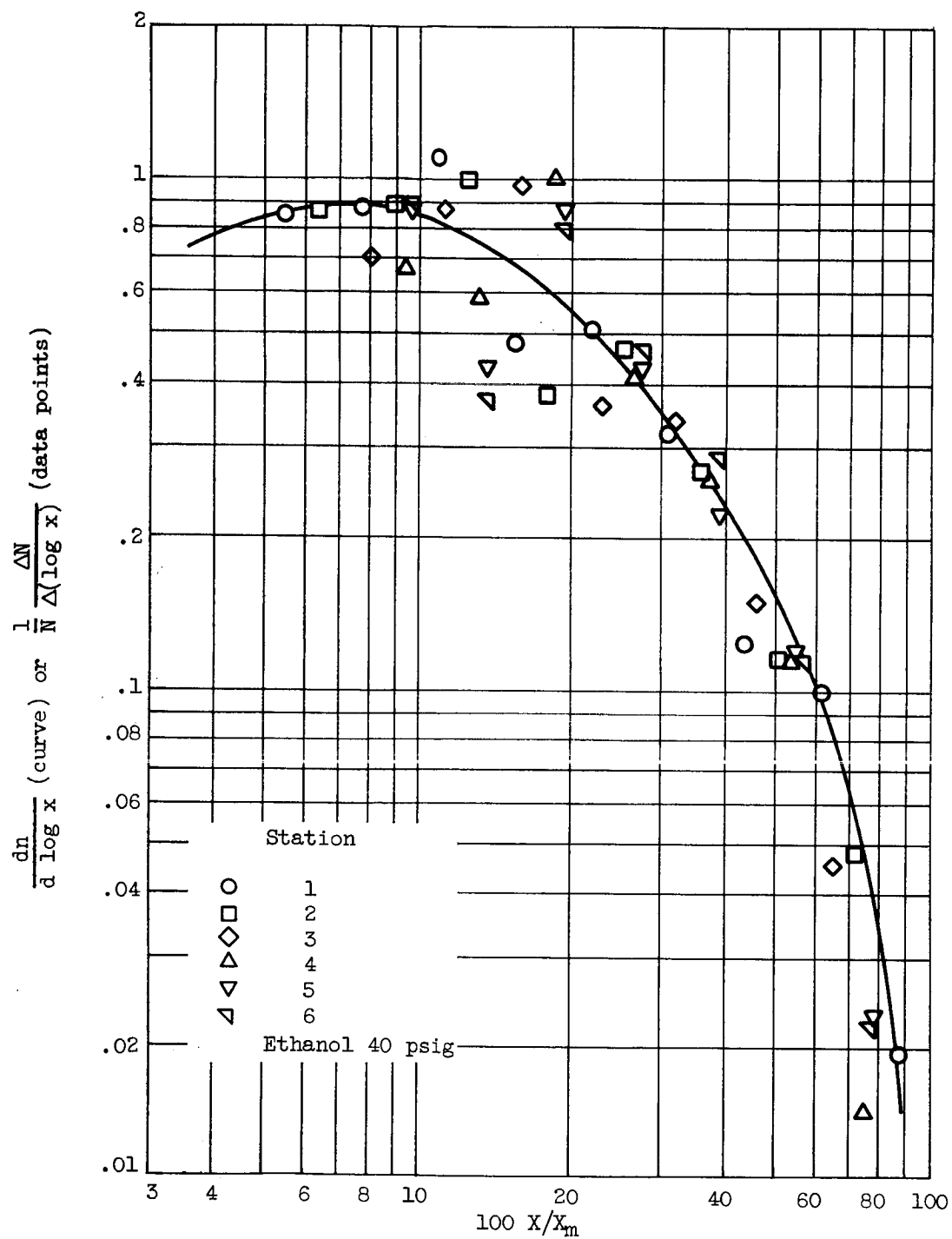


Figure 64. - Number distribution versus percent maximum drop size for ethanol sprays.

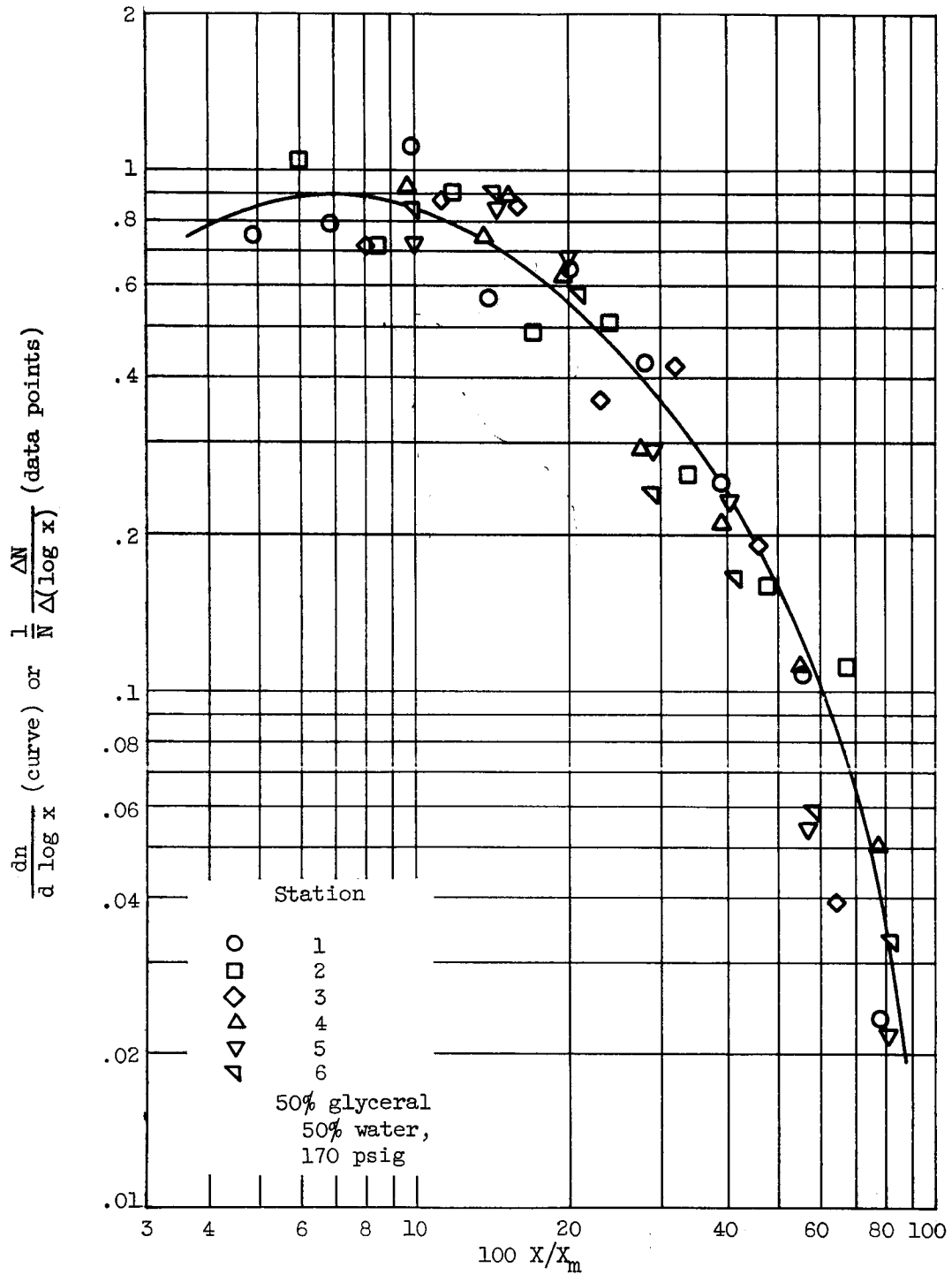


Figure 65. - Number distribution versus percent maximum drop size for glycerol sprays.

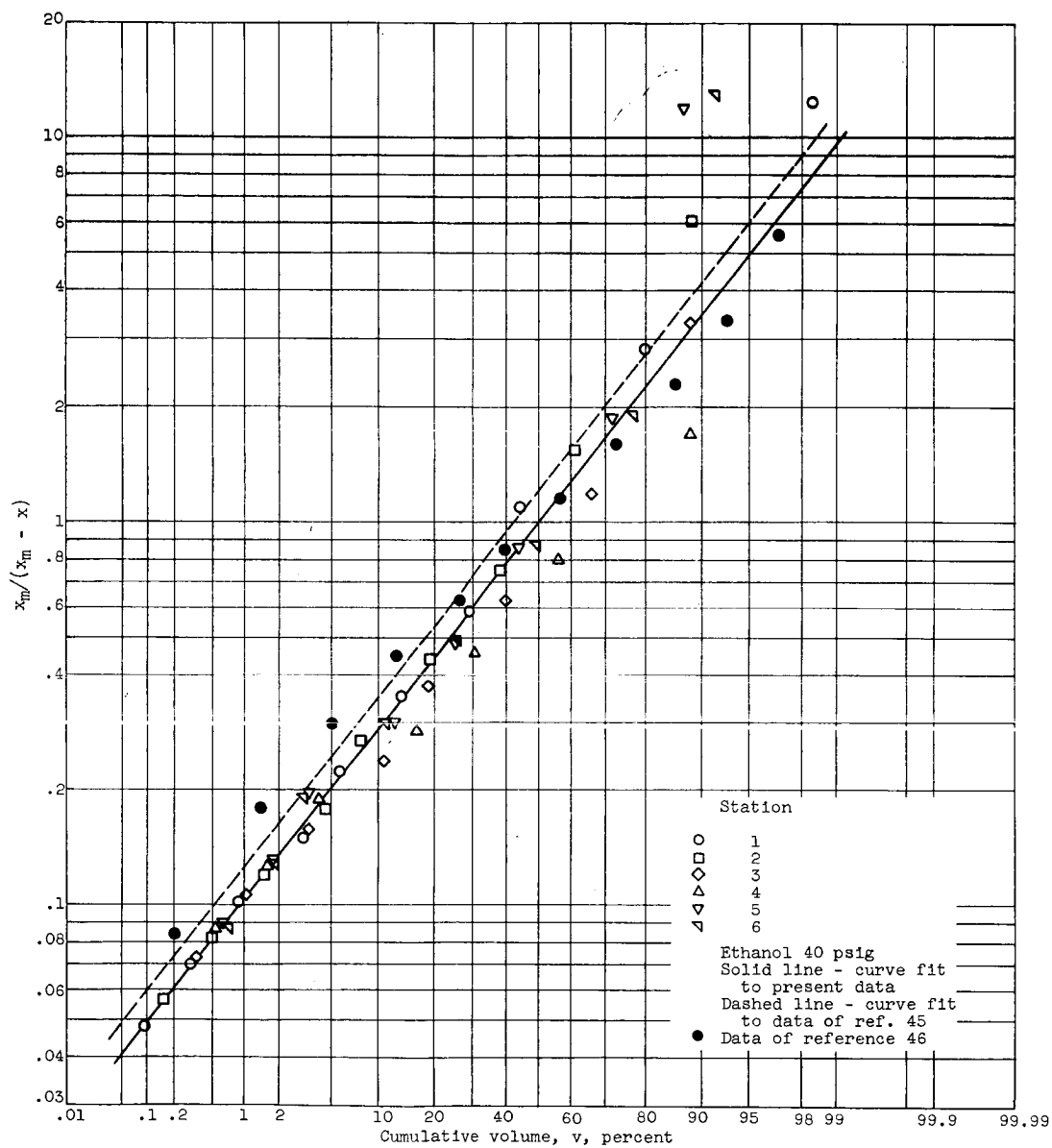


Figure 66. - Comparison of data on upper-limit function cumulative volume basis.

The dashed line represents the results from a similar plot in Reference 45 in which data was compared for impinging jets of heptane with considerable difference in the flow conditions. The jet diameters ranged from 0.029 to 0.089 inch, jet velocities from 30 to 100 fps, and the velocity difference between the jets and surrounding gas from 0 to 235 fps. Despite the radical difference in conditions the data was all consolidated very nearly into a single line. Although the injector was completely different in construction than the presently discussed centrifugal nozzle, it can be seen from Figure 66 that exactly the same slope (thus the same value of δ in the upper limit function) was obtained. Such precise agreement was of course a fortunate coincidence and should not be expected to occur frequently. The value of δ determined from the dashed line is 0.833. The point in common between the break-up process with impinging jets and a centrifugal nozzle is that they both involve the break-up of a liquid sheet.

The solid circles of Figure 66 represents the cumulative volume plot of data from reference 46. This data was obtained with a water spray from a conventional hollow cone simplex swirl nozzle with a cone angle of 80 degrees, a nominal rating of 0.80 gph, and a pressure of 100 psig. The spray was sampled by catching the drops in cells filled with a low density solvent and located 10 inches from the nozzle. The maximum drop size was estimated from this data by an extrapolation of the last four categories of the drop size number distribution.

Since 50 percent of the spray volume is obtained at

$$\frac{x_{50}}{x_m - x_{50}} = \frac{1}{a} = 1 \quad (30)$$

it can be seen that $a = 1$ which agrees with the data of this paper. If the best straight line were drawn through the data points it can be seen that the slope does not agree with the solid line of Figure 66, although the difference is not considerable.

Precise agreement between data obtained by different sampling methods cannot be expected. The present data as well as that of reference 45 were obtained by photographic methods which do not disturb the spray. In reference 46, however, the data can be expected to be warped somewhat due to the collection of the spray in cells filled with a solvent. The very small drops will follow the air flow right around the cells while the large drops may shatter upon impact with the solvent unless their velocity is extremely low. Coagulation may also occur between drops in the solvent to form larger drops.

The present data correlation agrees in a qualitative way with that of Reference 48 in which a 45 gph, 80 degree swirl nozzle was used. Due to the difference of nozzle angle (80° versus 30°) and nozzle size (45 gph versus 0.75 gph) the numbers do not agree, but the trend of drop size versus angle in the spray both show first an increase to a maximum and then a decrease with increasing angle. The agreement is obtained for conditions of high Reynolds number in which the second mode of equation (20) predominates.

The correlation of Reference 48 also shows that drop size depends

on Weber number to the -0.21 power, and no dependence on Reynolds number. In the correlation of this paper it can be seen from equations (20) to (25) that at high Reynolds number x_m (thus drop size) does not depend on Reynolds number but only on Weber number to the -0.164 power.

Figure 67 represents the relationship between mass (or volume) median diameter (x_{50}) and Sauter mean diameter (\bar{x}_{32}) for data of References 46 and 47. Both sets of data were obtained with the solvent filled cell drop collection method. The nozzles were of similar configuration to that of the present paper. In Reference 47 a constant orifice diameter (0.031 in.) was maintained while internal design changes were made to vary the ratio of tangential to axial fluid velocity. In Reference 46 hollow cone nozzles of similar design but different sizes (0.65 to 20 gph), hollow cone with altered swirl slot configurations, and two solid cone nozzles were used.

The noteworthy point of Figure 67 is that in spite of the radical differences in nozzle size and change of swirl slot configuration the ratio of x_{50} to \bar{x}_{32} remains the same. If this is interpreted with regard to the upper-limit function it can be shown by equations (5) and (9) that

$$\frac{x_{50}}{\bar{x}_{32}} = \frac{1 + ae^{1/2(\delta \log e)^2}}{1 + a} \quad (31)$$

is a constant. For this to be true, one of two conditions must be satisfied: (1) for any change in a a definite and compensating

change in δ must occur; and (2) a and δ are both constant. The latter is believed to be the most likely condition.

If a and δ are constant for the data of References 46 and 47 this would indicate that the drop size distribution spread and skewness are not a function of nozzle size or spray angle (determined by ratio of tangential to axial velocity). The possibility of a and δ being a function of Reynolds or Weber number is not excluded by the above.

The ratio of x_{50} to \bar{x}_{32} for the data of Figure 67 is 1.18 while that of the data presented in this paper is 1.30.

The concept of a constant value of δ is substantiated by Mugele (44) who correlated a wide range of spray data from various injector configurations using the upper limit function. He suggested a constant value of δ for a given injector type but the variation for different injectors with similar break-up mechanisms was not substantial. The suggested δ for impinging jets was 3.19 while that for a swirl atomizer was 3.71. These values have been modified to account for the difference in the upper limit function between Reference 44 and the present paper. These values are considerably higher than those determined from Reference 45 and the data of this paper ($\delta = 2.37$).

Mugele (44) also correlated x_m and \bar{x}_{32} with nozzle diameter, Reynolds number, and a dimensionless group which can be shown to be proportional to the ratio of Weber to Reynolds number. If the ratio

of the two correlations for a swirl atomizer are taken, the result is that x_m/\bar{x}_{32} is proportional to Reynolds number to the -0.15 power. Thus for constant δ , a is also a function of $R^{-0.15}$ (see eq. (9)). The standard deviations of the correlations are 26 percent for \bar{x}_{32} and 42 percent for x_m . Since a is a fairly weak function of Reynolds number, it is possible that a is as much a function of the spray sampling technique as it is of the flow conditions.

Spatial Mass Distribution

The spatial mass distribution is the drop mass summed over all sizes which is found in a unit volume of space within the spray. It was observed that the trends were similar to that of maximum drop size and thus the same functional form was used. The equation is presented in its normalized form such that its integral with respect to distance from the spray axis from zero to infinite is nearly one. The normalization is accurate if $M \geq 2S_2$.

The function was fit to the raw data using a weighted least-squares method and the results were

$$Q = \frac{e^{-D^2/2S_1^2} + Ae^{-(D-M)^2/2S_2^2}}{2\pi(S_1^2 + \sqrt{2\pi} AS_2M)} \quad (32)$$

where

$$A = 2.54 \times 10^{-3} R^2 W^3 \quad (33)$$

$$S_1 = 2.57 \quad (34)$$

$$S_2 = 3.05 R \quad (35)$$

$$M = \frac{21.4 R^{1/2} W}{5.30 + R^{1/2} W} \quad (36)$$

and again

$$R = (\text{Reynolds number}) \times 10^{-3}$$

$$W = (\text{Weber number}) \times 10^{-3}$$

and D is the distance from the spray axis in millimeters.

The spatial mass distributions for the ethanol sprays are shown in Figure 68. The ratio of the amplitudes of the second to the first mode (eq. (33)) increases rapidly with spray velocity since $R^2 W^3$ is proportional to the eighth power of velocity for constant fluid properties. As with maximum drop size the first mode disappears and the second mode predominates at high pressures. The spread of the second mode (eq. (35)) can be seen to increase directly with spray velocity. The location of the peak of the second mode (eq. (36)) will move away from the spray axis rapidly with increasing sheet velocity ($\alpha v^{5/2}$) at low Reynolds and Weber numbers but then become asymptotic to 21.4 mm at high velocities.

It should be noted that the position variable for the maximum drop size correlation was angle (θ in eq. (20)) while that of spatial mass distribution was distance from the spray axis (D in eq. (32)). This was done to facilitate normalization of equation (32). θ can be replaced by D by use of equation (29) or, with sufficient accuracy over the range of angle used, by $1.8 D$.

An estimate of the incremental mass flow rate Δw of drops in

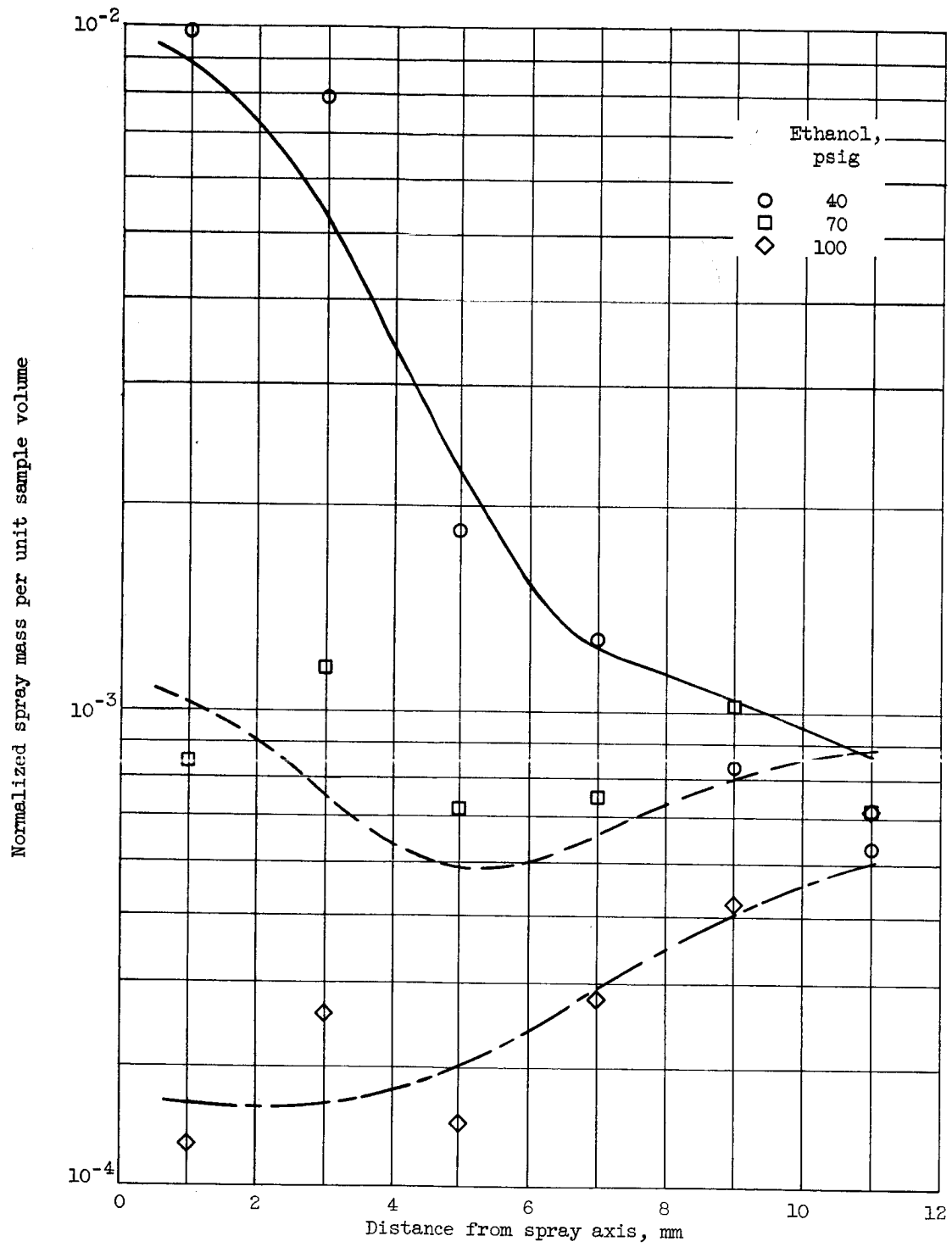


Figure 68. - Spatial mass distribution for ethanol sprays.

the size range x to $x + \Delta x$ flowing through the annulus of radius D to $D + \Delta D$ can be made from

$$\Delta w = 2\pi w \int_D^{D+\Delta D} \int_x^{x+\Delta x} DQ \frac{dv}{dx} dx dD \quad (37)$$

where w is the total mass flow rate, Q is the spatial mass distribution given by equation (32), and

$$\frac{dv}{dx} = \frac{\log e}{x} \frac{dv}{d \log x} \quad (38)$$

where $dv/d \log x$ is given by equation (18). When the Reynolds and Weber numbers have been specified, Q is a function only of D , but dv/dx is a function of x and also of D through x_m of equation (20) (with θ replaced by D). Since the above assumes that drop velocity is not a function of drop size or position in the spray, it must be considered an approximation only. It is the best that can be done, however, until the necessary information on drop velocities is available.

A Possible Explanation for the Observed Mass Distribution and Variation of Maximum Drop Size with Angle in the Spray

If the cone of fluid leaving the orifice of the swirl nozzle is laminar so that sheet break-up does not occur, the inwardly directed surface tension force will overcome the outwardly directed momentum of the fluid until the fluid sheet is turned in toward and finally intersects the spray axis. If the pressure is equal on both sides

of the fluid sheet and gravity is neglected, the distance from the nozzle at which maximum radial displacement of the sheet occurs is (49)

$$z = 0.42 \frac{\rho Q v}{4\pi\sigma} \quad (39)$$

where ρ , v , and σ are the liquid density, velocity, and surface tension, and Q is the liquid flow rate.

If some turbulence is present in the sheet such that a wave-like disturbance grows as the sheet progresses downstream, rings of fluid will form, as previously described, when the sheet ruptures at the peaks and valleys of the waves. If this disintegration occurs at or beyond the value of z given by equation (39), the liquid will have an axial or inwardly directed velocity. This would account for the preponderance of large drops and the bulk of the fluid being found near the axis of the spray.

Concurrent with the above break-up mechanism, a competing mechanism may be operating on the sheet closer to the nozzle. This may involve locally high values of turbulence which eject ligaments of fluid from the sheet or cause local rupture of the sheet which then contracts into ligaments. The ligaments will subsequently break or contract into drops which will no longer be subjected to the inward force of surface tension in the sheet. This would account for the second mode of maximum drop size or mass distribution which is located off the spray axis.

As the sheet velocity and turbulence increase, sheet break-up

will occur closer to the nozzle, inward sheet velocity at break-up will decrease, less mass will be thrown toward the spray axis, and the second mode will move away from the spray axis. The increased velocity will cause the most unstable disturbance wavelength to decrease, and smaller drops will result.

In the limit of very high velocities and turbulence levels, the sheet may be torn into ligaments and then drops immediately upon exit from the nozzle. The bulk of the fluid will have its velocity component directed at the angle in which an intact sheet would have left the nozzle. This angle was measured at 34 degrees from the nozzle axis.

The induced air flow which increases with fluid velocity (50) and fineness of spray break-up, will tend to move the smaller drops toward the center of the spray. Just outside the spray cone the induced air velocity is directed perpendicular to the spray cone and is gradually turned parallel to the spray axis as the axis is approached.

Conclusions Drawn From Data Analysis

The drop size volume distribution of a centrifugal swirl atomizer obtained within a small sample volume in the spray can be adequately described by the upper limit log normal function with only one variable. The upper limit function contains three parameters (a , δ , and x_m), but a and δ can be considered as constants even with varied fluid properties and variable position in the spray. The remaining parameter

(x_m) is a variable which is a function of fluid properties, nozzle size and pressure drop, and position in the spray. The parameter x_m has been correlated with the above dependent variables and shown to correspond to the largest observed drop size.

The parameter a , although a constant when the drop size volume distribution is considered locally, may be a function of fluid properties and nozzle parameters when the spray as a whole is considered. This can be a result of adding together distributions which differ because of the spatial dependence of x_m , and the resultant distribution may have a skewness not apparent on a local basis.

The parameter δ shows indications of being a more fundamental quantity which might be considered a constant for a given fluid break-up mechanism.

FORTRAN IV PROGRAM FOR WEIGHTED LEAST-SQUARES CURVE FIT

The Fortran IV computer program discussed in this paper was written to enable a weighted least-squares fit of an upper-limit log normal distribution function to drop-size volume distribution data. In this equation the parameters appear nonlinearly and the familiar linear least-squares equation fit cannot be used.

The usual methods for handling nonlinear equations, linearizing by a Taylor expansion and gradient or steepest-descent methods, were tried with no success. The steepest-descent method appeared to be converging but at such a slow rate that it was prohibitive to use on the large amount of data to be correlated. The Taylor expansion method, without using a weighting function, approached convergence rapidly but then oscillated when the minimum of the sum of the squared deviations was reached. Judicious control over the size of the parameter corrections cut down on the oscillation, but it appeared that this was a poor over-all strategy since each set of data would require individual scrutiny. When a weighting function was used with the Taylor expansion method, failure of convergence was the rule rather than the exception.

The nonlinear parameter method proposed by Marquardt (51) provides a solution to the problems encountered with the above two

methods. It is basically the linearized Taylor expansion method with a Lagrange multiplier λ added to the diagonal elements of the scaled matrix of the least-square equations. This Lagrange multiplier provides a simple and general method of controlling the convergence of the iterations. If λ is small the iterations will converge rapidly as in the Taylor expansion method, but may have to be increased especially during the latter stages of iteration to prohibit oscillation around the desired least-squares solution.

The Least-Squares Weighting Function

The need for a weighting function in curve fitting a normalized drop size volume distribution can be seen from the following example. A typical set of data may have an ordinate of 10^{-2} for a 10 micron drop size and an ordinate of one for a 100 micron drop size. A deviation from the fitting curve to the 100 micron data point of 0.05 (5 percent) would be acceptable, but this same deviation at the 10 micron data point would represent an error of 500 percent. Yet a least-squares fit without a weighting function would give both of these deviations equal importance. In general a least-squares fit will favor the large ordinates and will give less satisfactory results for the small ordinates.

The proper weighting function for use in a least-squares curve fit is inversely proportional to the square of the probable error (52). Any proportionality constant will cancel out of the least-squares equations and thus,

$$w_i = \frac{1}{E_i^2} \quad (1)$$

where w_i is the weighting function and E_i the error in the i^{th} data point.

Let Y_i be the ordinate and P_i be the percent error of the i^{th} data point. Then equation (1) can be written

$$w_i = \frac{1}{(P_i Y_i)^2} \quad (2)$$

If the error in the data points is unknown, a constant percent error might be used. This will again cancel out of the least-squares equations and thus

$$w_i = \frac{1}{Y_i^2} \quad (3)$$

can be used.

In some instances the error may be known to be constant such as in a meter reading. A weighting function of one must then be used.

A Weighting Function for Frequency Distributions

In the section on apriori confidence interval estimate an expression was developed for the width of the 95 percent confidence interval for the fraction of drops in each category. This confidence interval is used to represent the error in each data point which is necessary to determine the proper weighting function.

Let N be the total number of drops counted in all size categories

and N_i be the number of drops observed in the i^{th} category. The possible error in N_i due to random variation in the sampling process will be

$$\Delta N_i = 1.96 \sqrt{\frac{N_i(N - N_i)}{N}} + 0.96 \quad (4)$$

Unless N_i is very close to N or one the 0.96 term can usually be neglected. If the number distribution is to be used in the curve fit, ΔN_i can be used in equation (1) to determine the weighting function.

If a quantity derived from the frequency distribution is to be fit, then the theory for propagation of error should be used (53). Let V be a function of several variables $X_j (j = 1, n)$, and let $S_V, S_{X_1}, S_{X_2}, \dots, S_{X_n}$ be the probable errors in V and the X respectively. Then

$$S_V^2 = \sqrt{\sum_{j=1}^n \left(\frac{\partial V}{\partial X_j} \right)^2 S_{X_j}^2 + \sum_{j=1}^n \sum_{k \neq j}^n \rho_{X_j X_k} \frac{\partial V}{\partial X_j} \frac{\partial V}{\partial X_k} S_{X_j} S_{X_k}} \quad (5)$$

where $\rho_{X_j X_k}$ = the correlation between X_j and X_k .

An example where equation (5) would be used is when the frequency distribution is a drop-size distribution and it is desired to fit the normalized drop volume distribution

$$V_i = \frac{N_i D_i^3}{\sum_{j=1}^n N_j D_j^3} \quad (6)$$

where D_i is the drop size associated with the i^{th} size category.

If the error is in the N_k and the N_k are uncorrelated,

$$(\Delta V_i^2) = S_{V_i}^2 = \frac{D_i^6(1 - 2V_i)(\Delta N_i)^2 + V_i^2 \sum_{j=1}^n D_j^6(\Delta N_j)^2}{\left(\sum_{j=1}^n N_j D_j^3\right)^2} \quad (7)$$

where the ΔN_k are determined from equation (4), and then

$$w_i = \frac{1}{(\Delta V_i)^2} \quad (8)$$

is the correct weighting function.

Equations (7) and (8) were used to determine the weighting functions used in the Fortran IV Program found in Appendix IV. It should be noted that the terms $N_i D_i^3$ and $\Delta N_i/N_i$ had been computed in previous programs and are read into this program as $ZZ(I,J)$ and $ER(I,J)$ respectively. The I and J indices denote the i^{th} data point of the j^{th} data set.

The Method of Weighted Least Squares with Nonlinear Parameters

If the fitting equation were linear in its parameters the standard method of least squares would be to minimize

$$\varphi = \sum_{i=1}^n w_i (f_i - y_i)^2, \quad i = 1, n \quad (9)$$

with respect to each of the parameters $\beta_1, \beta_2, \dots, \beta_k$, where the y_i are the values of the n data points,

$$f_i = f_i(X_i; \beta_1, \beta_2, \dots, \beta_k) \quad (10)$$

is the value of f evaluated at the i^{th} value of the independent variable X_i , w_i is the weighting function, and n is the number of data points. The minimization procedure yields k linear equations in the k unknown parameters $\beta_1, \beta_2, \dots, \beta_k$. Let the fitting function be

$$f_i = \sum_{s=1}^k h_{is} \beta_s \quad (11)$$

where h_{is} is not a function of the parameters. The system of k equations will be

$$\sum_{i=1}^n w_i h_{it} y_i = \sum_{s=1}^k \left[\sum_{i=1}^n w_i h_{is} h_{it} \right] \beta_s, \quad t = 1, k \quad (12)$$

and the solution for the β_s can be obtained.

When f is nonlinear in the parameters it cannot be written as in equation (11), and the system (eq. (12)) cannot be solved for the β_s . f can be linearized by an approximation using a truncated Taylor series

$$f_i(X_i; \hat{\beta}_s + b_s) = f_i(X_i; \hat{\beta}_s) + \sum_{j=1}^k \left(\frac{\partial f_i}{\partial \beta_j} \right)_{\hat{\beta}_s} b_j, \quad (13)$$

with each term on the right evaluated at some initial or current value of the β_s , say $\hat{\beta}_s$ and the b_j are incremental changes in the β_j , or

$$b_j = \beta_j - \hat{\beta}_j. \quad (14)$$

Equation (13) is then substituted into equation (9) and ϕ is minimized with respect to each of the parameters to yield

$$\sum_{i=1}^n w_i (f_i - y_i) \frac{\partial f_i}{\partial \beta_s} = \sum_{j=1}^k \left[\sum_{i=1}^n w_i \frac{\partial f_i}{\partial \beta_j} \frac{\partial f_i}{\partial \beta_s} \right] b_j, \quad s=1, k \quad (15)$$

The special notation of equation (13) has been dropped for brevity, but it must be noted that f_i , $\partial f_i / \partial \beta_j$, and $\partial f_i / \partial \beta_s$ are evaluated at the particular values of the parameters and are no longer functions of the parameters.

The linear system (eq. (15)) of k equations in the k unknowns b_j can now be solved. An iteration procedure is used with initial values $\hat{\beta}_j$ inserted into equation (15) and the solution for the b_j determined. A new value of β_j is determined from equation (14) and the iteration continued until the minimum ϕ is reached.

Equation (15) can be put into matrix notation

$$AB = G \quad (16)$$

where

$$A^{k \times k} = (a_{sj}) = \left(\sum_{i=1}^n w_i \frac{\partial f_i}{\partial \beta_s} \frac{\partial f_i}{\partial \beta_j} \right)$$

$$B^{k \times 1} = (b_j) \quad (17)$$

$$G^{kxl} = (g_s) = \left(\sum_{i=1}^n w_i (f_i - y_i) \frac{\partial f_i}{\partial \beta_s} \right)$$

$$j = 1, k \text{ and } s = 1, k.$$

The above method is referred to as the Gauss or Gauss-Newton method (51).

The above iteration method was used in the weighted least-square fit of an upper limit log-normal distribution function to normalized drop size volume distributions. This function as used had the form

$$\frac{dv}{d \log X} = \frac{\delta X_m}{\sqrt{2\pi} (X_m - X)} e^{-\delta^2 y^2 / 2} \quad (18)$$

where

$$y = \log \frac{aX}{X_m - X}, \quad (19)$$

X is drop size, v is normalized drop volume in a logarithmic incremental drop-size range, and a , δ , and X_m are the equation parameters. Schemes were tried which limited the parameter correction to a fraction of b_j determined from equation (13), but no uniform method was determined which was successful with all of the sets of data. Control over b_j seemed especially critical as the minimum ϕ was approached. This experience corroborates the statement of Marquardt (51) that failure to converge is not uncommon.

Marquardt's algorithm was thus used with the addition that the A

and G matrices (eq. (17)) contain a weighting function. Equation (16) is first scaled such that

$$A^*B^* = G^* \quad (20)$$

where

$$A^* = (a_{ij}^*) = \left(\frac{a_{ij}}{\sqrt{a_{ii}a_{jj}}} \right)$$

$$G^* = (g_j^*) = \left(\frac{g_j}{\sqrt{a_{jj}}} \right) \quad (21)$$

$$b_j = \frac{b_j^*}{\sqrt{a_{jj}}}$$

and b_j^* are the elements of the solution vector B^* . A Lagrange multiplier λ is then added to the diagonal elements of A^* . In matrix notation the system of k equations to be solved for the b_j^* , $j = 1, k$ is

$$(A^* + \lambda I)B^* = G^* \quad (22)$$

where I is the unit matrix.

It can be seen from equation (22) that as $\lambda \rightarrow 0$ the system of equations will approach equation (20), the Gauss method. This will yield the largest but not necessarily convergent corrections to the parameters. As $\lambda \rightarrow \infty$, $b_j \rightarrow 0$ (ref.51) and thus control of λ will determine the rate of convergence in the iteration.

A satisfactory procedure is to decrease λ by a factor of 10 on each iteration which remains convergent. Convergence is checked by insuring that ϕ (eq. (9)) has been decreased by the iteration. As

the iteration proceeds and approach to the Gauss method results, a divergent correction may occur. λ is then increased to reduce the parameter correction sufficiently.

The Fortran IV Program in Appendix IV uses the above technique to fit the upper-limit log-normal function to normalized drop size volume distribution data. The normalization was achieved by calculating (from the fitting curve) the volume missing from a drop size of zero to ten microns and correcting the raw data by this amount. The program as listed represents the final step in the correlation of maximum drop size with spray conditions and position in the spray. Only the best values of the various coefficients are thus determined since the exponents of the Reynolds and Weber numbers had been fixed from previous runs of the program.

The subroutines SOLVE, ADOTB, and NEG(54) found at the end of the program are used to solve the system of linearized equations for the corrections to the parameters.

The subroutine AJEAN which is not included in Appendix IV is used to obtain the solution to

$$\text{ERF}(X) = \frac{2}{\sqrt{\pi}} \int_0^X e^{-u^2} du \quad (23)$$

which is necessary in calculating the cumulative volume and number distributions.

APPENDIX I. - MEASURED PROPERTIES OF GLYCEROL-

ETHANOL SOLUTIONS AT 20° C

TABLE IV - GLYCEROL-ETHANOL SOLUTION PROPERTIES VRS. PERCENT GLYCEROL

Percent glycerol by weight	Viscosity centipoise	Density, g/cc	Surface tension, dynes/cm
0	1.200	0.7895	22.3
10	1.724	0.8218	22.8
20	2.595	0.8594	23.5
30	4.213	0.8981	24.2
40	7.33	0.9396	24.9
50	13.59	0.9832	25.9
60	27.3	1.0297	26.9
70	60.4	1.0802	29.0
80	153.9	1.1357	32.7
90	422	1.1961	41.8
100	1412	1.2609	63.4

APPENDIX II. - 95 PERCENT CONFIDENCE INTERVALS

USING THE t-DISTRIBUTION

The 95 percent confidence intervals obtained using the t-distribution are given in Table V for six typical drop size number distributions. Only the upper limit of this interval is given since it is symmetrical about the observed number of drops.

Figure 69 shows the percent error calculated for each of the data points assuming the maximum error is one-half of the 95 percent confidence interval.

TABLE V - CONFIDENCE INTERVALS FOR SIX SAMPLE DATA GROUPS

Drop size microns	Number of drops	Upper limit of Con. Int.	Number of drops	Upper limit of Con. Int.	Number of drops	Upper limit of Con. Int.
11.9	1678	1837	1007	1121	602	686
16.8	745	801	356	408	167	200
23.8	834	900	397	454	297	357
33.6	319	366	185	219	179	215
47.6	391	438	193	239	223	276
67.3	226	262	143	195	142	173
95.1	97	117	79	104	91	122
134.5	40	53	53	76	37	53
190.3	6	11	10	17	13	22
226.3			4	10	1	3
Total	4336		2427		1752	
11.9	262	294	195	262	170	198
16.8	204	255	84	117	164	204
23.8	186	228	183	220	102	123
33.6	43	57	109	133	28	38
47.6	45	66	65	80	23	32
67.3	23	34	27	38	9	16
95.1	7	15	6	11	3	7.5
134.5	1	3	1	3		
Total	771		670		499	

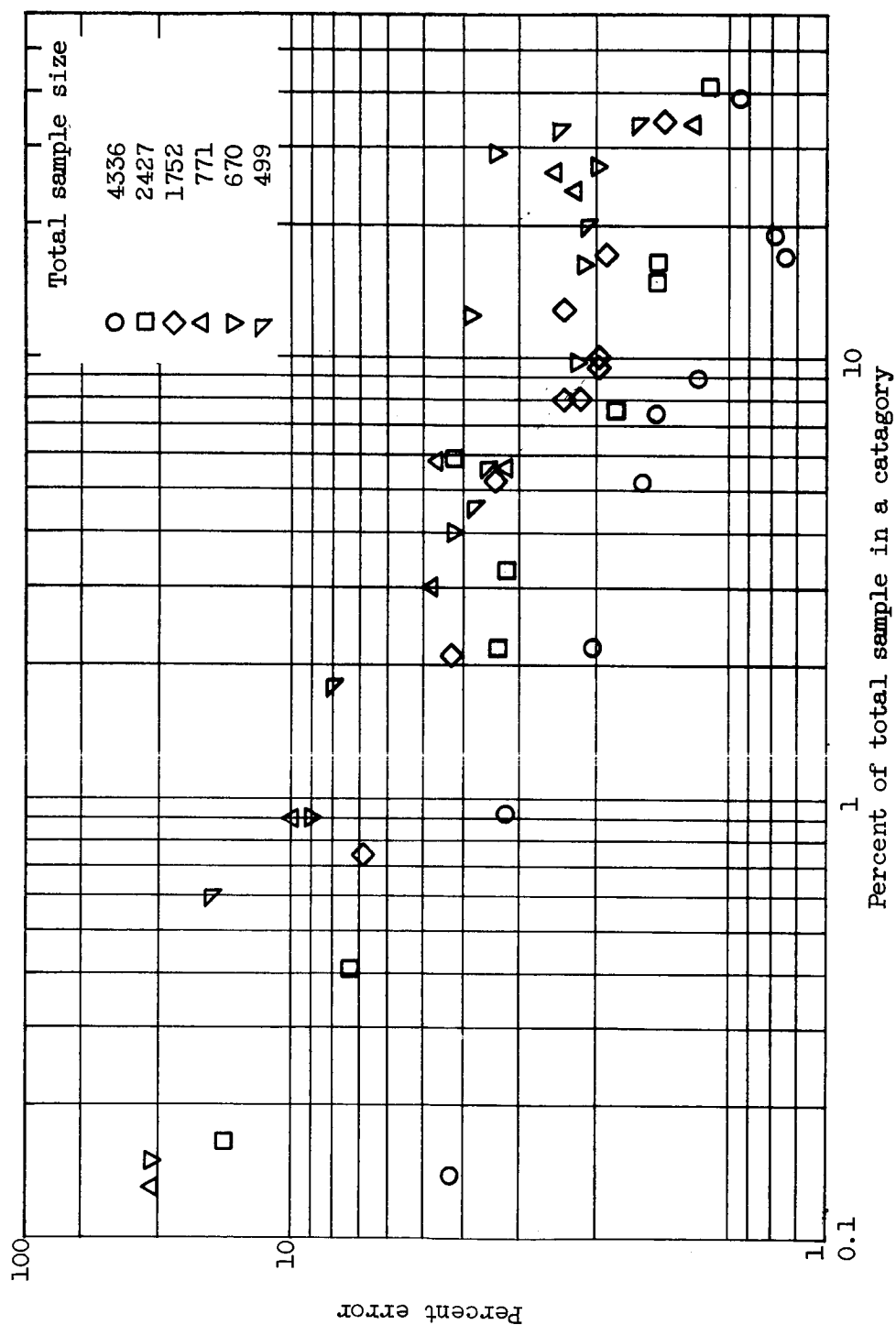


Figure 69. - Percent error versus percent of total sample.

APPENDIX III. - DROP COUNT TABULATIONS

TABLE VI - NUMBER OF DROPS COUNTED AND MEAN DROP SIZES

Spray conditions - Ethanol, 40 psig

Drop size range and log mean diameter, microns	Station number					
	1	2	3	4	5	6
10.00 - 14.14 11.89	1473	1678	1040	686	188	195
14.14 - 20.00 16.82	585	745	421	314	129	84
20.00 - 28.28 23.78	739	834	467	537	262	183
28.28 - 40.00 33.64	319	319	175	219	129	109
40.00 - 56.57 47.57	339	391	164	140	67	65
56.57 - 80.00 67.27	224	226	72	62	36	27
80.00 - 113.14 95.14	83	97	22	8	7	5
113.14 - 160.00 134.50	67	40	4	0	2	1
160.00 - 226.27 190.30	13	6	0	0	0	0
226.27 - 320.00 269.10	0	0	0	0	0	0
\bar{x}_{32}	85.0	72.5	50.1	42.0	49.8	48.0
\bar{x}_{30}	49.1	43.7	33.0	31.1	36.1	35.2
\bar{x}_{10}	27.7	26.0	21.9	23.0	26.2	25.8

TABLE VI. - Continued

Spray conditions - Ethanol, 70 psig

Drop size range and log mean diameter, microns	Station number					
	1	2	3	4	5	6
10.00 - 14.14 11.89	1336	2039	1184	1073	475	99
14.14 - 20.00 16.82	389	632	309	453	326	149
20.00 - 28.28 23.78	393	532	312	435	558	437
28.28 - 40.00 33.64	109	133	116	138	125	109
40.00 - 56.57 47.57	97	107	82	69	76	78
56.57 - 80.00 67.27	21	25	15	11	32	23
80.00 - 113.14 95.14	2	4	2	3	7	1
113.14 - 160.00 134.50	0	1	0	0	0	0
160.00 - 226.27 190.30	0	0	0	0	0	0
226.27 - 320.00 269.10	0	0	0	0	0	0
\bar{x}_{32}	32.8	32.9	32.6	31.1	38.7	37.9
\bar{x}_{30}	23.9	23.3	23.8	23.5	28.9	31.2
\bar{x}_{10}	17.7	17.1	17.7	18.2	21.9	25.8

TABLE VI. - Continued

Spray conditions - Ethanol, 100 psig

Drop size range and log mean diameter, microns	Station number					
	1	2	3	4	5	6
10.00 - 14.14 11.89	1260	1978	1523	1739	744	508
14.14 - 20.00 16.82	303	467	298	628	501	403
20.00 - 28.28 23.78	186	316	207	359	581	670
28.28 - 40.00 33.64	35	72	50	90	116	171
40.00 - 56.57 47.57	25	31	24	26	62	95
56.47 - 80.00 67.27	3	5	2	4	6	17
80.00 - 113.14 95.14	0	0	0	0	1	1
113.14 - 160.00 134.50	0	0	0	0	0	0
160.00 - 226.27 190.30	0	0	0	0	0	0
226.27 - 320.00 269.10	0	0	0	0	0	0
\bar{x}_{32}	23.0	22.7	22.1	22.6	28.6	32.6
\bar{x}_{30}	18.2	18.2	17.8	18.6	23.2	26.5
\bar{x}_{10}	14.9	15.0	14.7	15.6	19.1	21.6

TABLE VI. - Continued

Spray conditions - 50% glycerol, 50% water, 130 psig

Drop size range and log mean diameter, microns	Station number					
	1	2	3	4	5	6
10.00 - 14.14 11.89	806	962	916	846	221	170
14.14 - 20.00 16.82	272	333	281	299	170	170
20.00 - 28.28 23.78	310	376	214	227	125	95
28.28 - 40.00 33.64	180	174	121	85	43	29
40.00 - 56.57 47.57	172	187	109	74	44	23
56.57 - 80.00 67.27	143	137	49	39	15	9
80.00 - 113.14 95.14	105	74	33	18	1	3
113.14 - 160.00 134.50	72	53	20	4	0	0
160.00 - 226.27 190.30	30	12	1	0	0	0
226.27 - 320.00 269.10	0	0	0	0	0	0
\bar{x}_{32}	110.8	94.0	74.1	53.8	39.1	40.5
\bar{x}_{30}	64.0	53.4	41.1	32.4	28.7	28.3
\bar{x}_{10}	33.9	28.8	22.5	19.9	21.2	20.2

TABLE VI. - Continued

Spray conditions - 50% glycerol, 50% water, 170 psig

Drop size range and log mean diameter, microns	Station number					
	1	2	3	4	5	6
10.00 - 14.14 11.89	620	735	936	1080	319	255
14.14 - 20.00 16.82	203	259	202	254	247	246
20.00 - 28.28 23.78	289	332	195	217	188	159
28.28 - 40.00 33.64	148	178	84	99	80	66
40.00 - 56.57 47.57	165	185	97	71	64	45
56.57 - 80.00 67.27	112	96	44	38	15	16
80.00 - 113.14 95.14	65	58	9	17	6	9
113.14 - 160.00 134.50	28	41	1	2	1	2
160.00 - 226.27 190.30	6	3	0	0	0	0
226.27 - 320.00 269.10	0	0	0	0	0	0
\bar{x}_{32}	85.8	83.5	46.4	49.3	44.1	50.8
\bar{x}_{30}	51.9	49.8	30.0	30.1	30.6	33.0
\bar{x}_{10}	30.0	28.5	19.5	18.8	21.6	22.0

TABLE VI. - Continued

Spray conditions - 50% glycerol, 50% water, 210 psig

Drop size range and log mean diameter, microns	Station number					
	1	2	3	4	5	6
10.00 - 14.14 11.89	453	570	572	639	719	577
14.14 - 20.00 16.82	158	194	95	149	529	473
20.00 - 28.28 23.78	167	263	90	133	428	354
28.28 - 40.00 33.64	116	129	55	44	125	138
40.00 - 56.57 47.57	136	140	31	35	99	61
56.57 - 80.00 67.27	66	76	11	11	22	31
80.00 - 113.14 95.14	26	28	3	5	6	6
113.14 - 160.00 134.50	10	7	0	0	0	0
160.00 - 226.27 190.30	2	0	0	0	0	0
226.27 - 320.00 269.10	0	0	0	0	0	0
\bar{x}_{32}	72.3	61.0	38.0	38.6	36.3	37.9
\bar{x}_{30}	45.0	40.0	25.4	25.4	26.7	27.5
\bar{x}_{10}	27.4	25.6	17.4	17.4	20.0	20.3

TABLE VI. - Continued

Spray conditions - 65% glycerol, 35% water, 170 psig

Drop size range and log mean diameter, microns	Station number					
	1	2	3	4	5	6
10.00 - 14.14 11.89	385	610	200	228	282	357
14.14 - 20.00 16.82	93	150	128	173	184	231
20.00 - 28.28 23.78	146	208	169	150	186	174
28.28 - 40.00 33.64	78	103	70	51	43	48
40.00 - 56.57 47.57	66	75	58	40	45	21
56.57 - 80.00 67.27	25	36	32	19	24	5
80.00 - 113.14 95.14	5	5	16	10	6	1
113.14 - 160.00 134.50	0	0	8	4	1	0
160.00 - 226.27 190.30	0	0	4	0	0	0
226.27 - 320.00	0	0	0	0	0	0
\bar{x}_{32}	44.8	42.9	87.1	59.7	47.7	30.2
\bar{x}_{30}	31.5	29.9	49.4	36.8	32.0	23.2
\bar{x}_{10}	22.0	20.8	28.0	23.1	21.8	18.3

TABLE VI. - Continued

Spray conditions - 65% glycerol, 35% water, 210 psig

Drop size range and log mean diameter microns	Station number					
	1	2	3	4	5	6
10.00 - 14.14 11.89	602	712	318	370	322	359
14.14 - 20.00 16.82	167	185	248	234	185	217
20.00 - 28.28 23.78	297	273	211	231	152	168
28.28 - 40.00 33.64	189	176	107	89	57	44
40.00 - 56.57 47.57	153	179	73	59	40	36
56.57 - 80.00 67.27	202	97	56	45	19	13
80.00 - 113.14 95.14	91	45	26	12	7	2
113.14 - 160.00 134.50	37	20	6	2	2	0
160.00 - 226.27 190.30	13	2	0	0	0	0
226.27 - 320.00	0	0	0	0	0	0
\bar{x}_{32}	93.3	74.1	63.1	52.3	50.8	36.4
\bar{x}_{30}	58.4	45.8	40.7	34.7	32.4	26.2
\bar{x}_{10}	34.5	27.5	25.9	23.1	21.2	19.3

TABLE VI. - Continued

Spray conditions - 65% glycerol, 35% water, 250 psig

Drop size range and log mean diameter microns	Station number					
	1	2	3	4	5	6
10.00 - 14.14 11.89	623	814	279	405	509	474
14.14 - 20.00 16.82	152	205	253	266	298	388
20.00 - 28.28 23.78	279	258	164	230	308	353
28.28 - 40.00 33.64	149	105	83	66	84	104
40.00 - 56.57 47.57	159	141	68	62	46	40
56.57 - 80.00 67.27	73	101	52	38	34	12
80.00 - 113.14 95.14	76	22	15	4	12	2
113.14 - 160.00 134.50	43	18	3	1	2	0
160.00 - 226.27 190.30	6	2	0	0	0	0
226.27 - 320.00	0	0	0	0	0	0
\bar{x}_{32}	92.5	73.0	57.5	45.0	48.4	32.0
\bar{x}_{50}	55.2	43.0	38.0	30.9	31.4	24.8
\bar{x}_{10}	30.9	24.7	24.9	21.5	21.0	19.6

APPENDIX IV - NONLINEAR PARAMETER, WEIGHTED LEAST SQUARES FITTING PROGRAM

```

C THIS PROGRAM FITS AN UP. LIM. EQUATION WITH UP-TO 25 PARAMETERS TO A SET OF
C DATA WITH UP-TO 528 POINTS, USING A LEAST SQUARES METHOD WITH A LAGRANGE
C MULTIPLIER.
C
C
C NP = NUMBER OF DATA POINTS, NC = NUMBER OF CONSTANTS IN FITTING EQUATION,
C NR = NUMBER OF DATA RUNS, NCON = NUMBER OF SPRAY CONDITIONS.
C ANG(I) = ANGLE TO CENTER OF SIX STATIONS, GBOUND(I) = DROP SIZE CATEGORY
C LIMITS, GSTORE(I) = LOG-MEAN DROP SIZE, DELN(I,J) AND ZZ(I,J) ARE THE
C NUMBER OF DROPS AND DROP VOLUME FOR THE I-TH SIZE CATEGORY OF THE J-TH RUN.
C B(I) = INITIAL ESTIMATES OR CURRENT VALUES OF THE EQUATION CONSTANTS.
C ER(I,J) = PERCENT ERROR IN THE NUMBER OF DROPS COUNTED
C REY(J) AND WEB(J) ARE THE REYNOLDS AND WEBER NUMBERS
C THE FOLLOWING DIMENSION STATEMENT IS GENERAL FOR ANY EQUATION FIT
  DIMENSION ANF(26,26),B(25),BB(25),BNF(26,26),BSTORE(25),COMFNT(21
    1),DNF(25),DYDB(528,25),EN(26),WTF(528),X(528),Y(528)
C
C THE FOLLOWING DIMENSION STATEMENT IS FOR THIS PARTICULAR PROBLEM****
  DIMENSION G(11),DELN(11,48),ZZ(11,48),ER(11,48),XM(48),DEVXMJ(48)
  1,ANG(6),NAA(48),ERZZSQ(11),SUMZI(48),AC(48),RDV(8),R(4,48),DELI(48
  2),CRFT(48),REY(8),WEB(8),THK(8),FRW(8),FSIGMA(8),FLGRW(8),FLR(8),F
  3LW(8),COMNT2(21),FMOM(8),FWBMOM(8),FREWB(8),GMOM(8),GWBOM(8),GRE
  4WBM(8),FLM(8),CALFSQ(8),XMX32R(48),X32(48),ACDEF(48),GBOUND(11),GS
  5STORE(11),GUSE(528),XX(5),GRW(8),RDW(8),X31(48),X30(48),X20(48),X21
  6(48),X10(48),SUMNI(48),DELNI(48),DELNF(48),XM1(48),XM2(48),XM3(48)
  7,FLRDW(8),XMMAX(8),XNZFR(8),ALFMX(8),STDV1(8),STDV2(8)
C
  DOUBLE PRECISION ANF,DNF,EN,SUMD,D,DD,SUMCOR,SUMDEV,SUMK,SUMJ,SUMY
  1,BNF
  DIMENSION FAC(30),CONT(60)
  B2 = 0.0
  SIGN = 1.
  CALL AJEAN (FAC(1),CONT(1))
  PI = 3.1415927
  SP = SQRT(2.0*PI)
  CC = 6.6439
  PE = 0.434295
  PE2 = PE**2
C READ IN INPUT DATA HERE
  READ(5,100)(COMENT(I),I=1,21)
  READ(5,100)(COMNT2(I),I=1,21)
  READ(5,101) NP
  READ(5,101) NC
  READ(5,101) NR
  READ(5,101) NCON
  READ(5,120)(ANG(I),I=1,6)
  READ(5,166)(GBOUND(I),I=1,11)
  IP = 0
417 READ(5,102)(B(I),I=1,NC)
  DO 5 J=1,NR
    READ(5,103)(R(I,J),I=1,4)
  5 READ(5,104)(GSTORE(I),DELN(I,J),ZZ(I,J),I=1,11)
    DO 1 J=1,NR
      READ(5,103)(R(I,J),I=1,4)
      READ(5,119)(FR(I,J),I=1,11)
    1 CONTINUE
    DO 2 J=1,NCON
      READ(5,121) REY(J),WEB(J)
    2 CONTINUE
C READ IN INPUT DATA COMPLETED.
  DO 333 J=1,NCON

```

```

REY(J) = REY(J)*1.0E-03
WEB(J) = WEB(J)*1.0E-03
FLR(J) = ALOG(REY(J))
FLW(J) = ALOG(WEB(J))
FRW(J) = REY(J)**2*WEB(J)**(0.5)
GRW(J) = REY(J)*WEB(J)
RDW(J) = REY(J)**(-0.50)*WEB(J)**(0.25)
333 CONTINUE
FNUM = NP-1
FN = 11.0
IGAUSS = 1
ITESTD = 1
IMAX = NC+1
IC = 0
DO 15 J=1,NR
SUMZZ = 0.0
SUMNN = 0.0
SUMEZZ = 0.0
DO 16 I=1,11
IF(I.EQ.1) DELN1(J)=DFLN(1,J)
IF(ZZ(I,J).NE.0.0) GO TO 7
II = I-1
DELFN(J) = DELN(II,J)
NAA(J) = II
GO TO 19
7 SUMZZ = SUMZZ + ZZ(I,J)
SUMNN = SUMNN+DELFN(I,J)
ERZZSQ(I) = (ER(I,J)*ZZ(I,J))**2
16 SUMEZZ = SUMEZZ+ERZZSQ(I)
19 SUMZI(J) = SUMZZ
SUMNI(J) = SUMNN
N = NAA(J)
C CALCULATE WEIGHTING FUNCTION WTF(IC) HERE
DO 79 I=1,11
IC = IC+1
IF(I.GT.N) GO TO 83
GUSE(IC) = GSTORE(I)
SZ95SQ = (SUMEZZ*(CC*ZZ(I,J)/SUMZI(J))**2 + CC**2*(1.0-2.0*ZZ(I,J)
1)/SUMZI(J))*ERZZSQ(I))/(SUMZI(J)**2)
WTF(IC) = 1.0/SZ95SQ
II = IC
GO TO 79
83 II = II-1
GUSE(IC) = GBOUND(I)
WTF(IC) = WTF(II)
79 CONTINUE
JC = IC-1
15 CONTINUE
FLAGRG = 0.02
DO 11 J=1,NC
DO 11 I=1,NP
11 DYDB(I,J) = 0.0
C START OF ITERATION LOOP
6 DO 55 M=1,50
IF(M.LE.7) GO TO 380
FLAGRG = FLAGRG*0.5
380 FLAGRG = FLAGRG*0.5
IF(FLAGRG.LT.1.0E-07) FLAGRG=1.0E-07
DD = D
DO 8 I=1,NC
8 BB(I) = B(I)

```

```

9 IC = 0
  IS = 0
  JA = 1
  JB = 10
  JC = 17
  DD 124 J=1,NR
  IS = IS+1
  IF (IS,LE,6) GO TO 10
  JA = JA+1
  JB = JB+1
  JC = JC+1
  IS = 1
10 CONTINUE
  AS = ANG(IS)**2
  AG = ANG(IS)
  IF (IS,NE,1) GO TO 777
  F89 = WFB(JA)**B(R)
  F11 = GRW(JA)
  F1035 = B(6) + F11
  HH = B(1)
  FF = B(5)*RDW(JA)
  CF = B(7)*F89
  B1S = HH**2
  B1C = HH*B1S
  G1 = FRW(JA)
  EX2 = EXP(-B(3)*G1)
  GG = B(2)*EX2
  ANGMX = 34.0*F11/F1035
  XMMAX(JA) = CF
  XMZER(JA) = GG**2
  ALFMX(JA) = ANGMX
  STDV1(JA) = HH
  STDV2(JA) = 0.707/FF
777 CONTINUE
  EX1 = EXP(-0.5*AS/B1S)
  F1 = GG**2*EX1
  BJC2 = FF**2
  AMF = AG-ANGMX
  AMF2 = AMF**2
  EX3 = EXP(-BJC2*AMF2)
  F2 = XMMAX(JA)*EX3
C  DEFINE MAXIMUM DROP SIZE XM(J) HERE
  XM(J) = F1+F2
  XM1(J) = F1
  XM2(J) = F2
  A = 1.0
  DEL = B(4)
  IF (M,NF,1) GO TO 782
  WRITE(6,173) (R(I,J),I=1,4),XM1(J),XM2(J)
  GO TO 780
782 IF (XM(J).LT,0.00) GO TO 748
780 DELI(J) = DEL
  AC(J) = A
  SUMZ = SUMZI(J)
  Y10 = ALNG10(10.0*A/(XM(J)-10.0))
  A10 = DEL*Y10
  H = -A10/1.414214
  ERX = SUB(H,B2,FAC(1),CONT(1),SIGN)
  C = (1.0+ERX)/2.0
  CRFT(J) = C
  F = 6.6439*C/SUMZ

```

```

      DO 125 I=1,11
      IC = IC+1
      G(I) = GUSE(IC)
C   DEFINE NORMALIZED EXPERIMENTAL DATA POINTS X(IC) HERE
      X(IC) = F*ZZ(I,J)
      XMI = XM(J)-G(I)
      IF(XMI.LE.0.0) GO TO 126
      T = ALOG10(A*G(I)/XMI)
C   DEFINE FITTING UPPER LIMIT FUNCTION Y(IC) HERE
      Y(IC) = DEL*XM(J)*EXP(-(DEL*T)**2/2.0)/(XMI*SP)
      IF(I.NE.1) GO TO 128
131  GCUB = GSTORE(I)**3
      NNNN = Y(IC)/(F*CC*GCUB)
      FNNN = NNNN
      SUMNI(J) = SUMNI(J)+FNNN-DELN(I,J)
      ZZZZ = FNNN*CC*GCUB
      DELN(I,J) = FNNN
      SUMZ = SUMZ(I,J)-ZZ(I,J)+ZZZZ
      F = F*SUMZ(I,J)/SUMZ
      SUMZ(I,J) = SUMZ
      ZZ(I,J) = ZZZZ
      X(IC) = F*ZZ(I,J)
      GO TO 128
126  Y(IC) = 0.0
      GO TO 128
228  IF(I.EQ.NAA(J)) GO TO 131
128  IF(ITEMTD.EQ.1) GO TO 125
      IF(XMI.LE.0.0) GO TO 127
C   DEFINE PARTIAL DERIVATIVES OF THE UPPER-LIMIT FUNCTION WITH RESPECT TO EACH
C   CONSTANT DYDB(IC,K) K=1,NC
      QNT = PE*T*DEL**2
      DYDXM = Y(IC)*((XM(J)*QNT-G(I))/(XM(J)*XMI))
      DYDD = (1.0 - (DEL*T)**2)*Y(IC)/DEL
      DYDB(IC,1) = DYDXM*F1*AS/B1C
      DYDB(IC,2) = DYDXM*2.0*GG*EX1*FX2
      DYDB(IC,3) = -DYDB(IC,2)*B(2)*G1
      DYDB(IC,4) = DYDD
      DYDBJC = 2.0*F2*BJC2*AMF*DYDXM
      DYDB(IC,6) = -DYDBJC*ANGMX/F1035
      DYDF = -DYDXM*F2*2.0*FF*AMF2
      DYDB(IC,5) = DYDF*RDW(JA)
      DYDB(IC,7) = DYDXM*F2/R(7)
      DYDB(IC,8) = DYDXM*F2*FLW(JA)
      GO TO 125
127  DO 130 K=1,NC
      DYDB(IC,K) = 0.0
130  CONTINUE
125  CONTINUE
124  CONTINUE
      IF(IGAUSS.EQ.0) GO TO 62
129  IF(ITEMTD.EQ.1) GO TO 46
C   SET UP MATRIX ANF FOR SOLUTION OF WEIGHTED LEAST-SQUARES EQUATIONS.
      DO 14 J=1,NC
      DO 12 K=1,NC
12  ANF(J,K) = 0.0
14  ANF(J,IMAX) = 0.0
      DO 30 J=1,NC
      DO 20 K=1,NC
      DO 18 I=1,NP
      IF(ABS(DYDB(I,J)).LT.1.0E-19) GO TO 18
      IF(ABS(DYDB(I,K)).LT.1.0E-19) GO TO 18

```

```

      ANF(J,K) = ANF(J,K)+WTF(I)*DYDB(I,J)*DYDB(I,K)
18  CONTINUE
20  CONTINUE
      DO 22 I=1,NP
22  ANF(J,IMAX) = ANF(J,IMAX)-WTF(I)*(X(I)-Y(I))*DYDB(I,J)
30  ANF(IMAX,J) = 1.0
      ANF(IMAX,IMAX) = 1.0
      DO 32 I=1,NC
32  DNF(I) = DSQRT(ANF(I,I))
      DO 40 J=1,NC
      DO 35 K=1,NC
      IF(J.EQ.K) GO TO 33
C   SCALE ANF MATRIX
      ANF(J,K) = ANF(J,K)/(DNF(J)*DNF(K))
      GO TO 35
33  ANF(J,J) = 1.0
35  CONTINUE
      ANF(J,IMAX) = ANF(J,IMAX)/DNF(J)
40  CONTINUE
C   STORE ANF IN BNF SINCE ANF DESTROYED BY SOLVE SUBROUTINE
      DO 240 J=1,IMAX
      DO 240 K=1,IMAX
240  BNF(J,K) = ANF(J,K)
41  DO 42 I=1,NC
42  ANF(I,I) = 1.0+FLAGRG
C   SOLVE FOR SCALED CORRECTIONS TO EQUATION CONSTANTS EN(I)
      CALL SOLVE(ANF,IMAX,EN)
      DO 44 I=1,NC
C   CALCULATE NEW VALUES FOR EQUATION CONSTANTS B(I)
44  B(I) = BB(I)+EN(I)/DNF(I)
      WRITE(6,99)
      WRITE(6,113)(B(I),I=1,NC)
45  ITESTD = 1
      GO TO 9
46  SUMD = 0.
      WRITE(6,99)
      WRITE(6,171)(XM(I),I=1,NR)
      WRITE(6,174)(ALFMX(I),I=1,NCON)
      WRITE(6,178)(STDV2(I),I=1,NCON)
      WRITE(6,175)(XMZER(I),I=1,NCON)
      WRITE(6,176)(XMMAX(I),I=1,NCON)
      DO 48 I=1,NP
48  SUMD = SUMD+WTF(I)*(X(I)-Y(I))*2
      D = SUMD
      ITESTD =
      WRITE(6,161) M,FLAGRG,D
      IF(M.EQ.1) GO TO 55
      IF(D.LE.DD) GO TO 50
748  FLAGRG = FLAGRG*3.0
      WRITE(6,169) IC,FLAGRG
      IF(FLAGRG.GT.200.0) GO TO 60
      DO 49 J=1,IMAX
      DO 49 K=1,IMAX
49  ANF(J,K) = BNF(J,K)
      GO TO 41
50  DCHK = (DD-D)/D
      IF(DCHK.LT.0.0001) GO TO 60
      DO 52 I=1,NC
      ABB = ABS((B(I)-BB(I))/B(I))
52  IF(ABB.GT.0.001) GO TO 55
      GO TO 60

```

```

55 CONTINUE
C  END OF ITERATION LOOP
60 CONTINUE
    IGAUSS =
    GO TO 6
62 CONTINUE
C
    DO 510 J=1,NR
        WRITE(6,173)(R(I,J),I=1,4),XM1(J),XM2(J)
510 CONTINUE
        WRITE(6,175)(XMZER(I),I=1,NCON)
        WRITE(6,176)(XMMAX(I),I=1,NCON)
        WRITE(6,174)(ALFMX(I),I=1,NCON)
        WRITE(6,177)(STDV1(I),I=1,NCON)
        WRITE(6,178)(STDV2(I),I=1,NCON)
91  IA = 0
        WRITE(6,98)
        WRITE(6,112)
        WRITE(6,99)
        WRITE(6,113)(B(I),I=1,NC)
C  CALCULATE MEAN DIAMETERS X32(K),X31(K),ETC.
        DO 92 K=1,NR
            F1 = 1.0/(PF*DELI(K))**2
            DEL = DELI(K)
            A = AC(K)
            A2 = A**2
            A3 = A*A2
            EX1 = EXP(0.5*F1)*A
            EX2 = EXP(2.0*F1)*A2
            EX3 = EXP(4.5*F1)*A3
            DEN32 = 1.0+EX1
            DEN31S = 1.0+EX1*2.0+EX2
            DEN31 = SQRT(DEN31S)
            DEN30C = 1.0+EX1*3.0+EX2*3.0+EX3
            DEN30 = DEN30C**(.10/3.0)
            X32(K) = XM(K)/DEN32
            X31(K) = XM(K)/DEN31
            X30(K) = XM(K)/DEN30
            X30C = X30(K)**3
            X31S = X31(K)**2
            XMC = XM(K)**3
            COFN = X30C/XMC
            X20(K) = SQRT(X30C/X32(K))
            X21(K) = X31S/X32(K)
            X10(K) = X30C/X31S
            SUMX1 = 0.0
            SUMY1 = 0.0
            SUMX2 = 0.0
            SUMY2 = 0.0
            SUMXY = 0.0
            SUMDWT = 0.0
            SUMD = 0.
            IS = IA+1
            IF = IA+11
            DO 90 I=IS,IF
                IA = IA+1
                SUMDWT = SUMDWT+WTF(I)*(X(I)-Y(I))**2
                SUMD = SUMD+WTF(I)*(Y(I)-X(I))
                SUMX1 = SUMX1+X(I)
                SUMY1 = SUMY1+Y(I)
                SUMX2 = SUMX2+(X(I))**2

```

```

SUMY2 = SUMY2+(Y(I))**2
SUMXY = SUMXY+X(I)*Y(I)
90 CONTINUE
DENRHO = SQRT((SUMX2-SUMX1**2/FN)*(SUMY2-SUMY1**2/FN))
RHO = (SUMXY-SUMX1*SUMY1/FN)/DENRHO
WRITE(6,97)
WRITE(6,116)(COMENT(I),I=1,21)
WRITE(6,99)
WRITE(6,116)(COMNT2(I),I=1,21)
WRITE(6,99)
WRITE(6,107)(R(I,K),I=1,4),RHO,AC(K),DELI(K),XM(K),CRFT(K)
WRITE(6,108)
V10 = 1.0-CRFT(K)
A = AC(K)
DEL = DELI(K)
SUM7 = 0.
SUMN = 0.
N = 0
F1 = 1.0/(PE*DEL**2)
F2 = 2.0*F1
F3 = 3.0*F1
C * * * * *
C IN THE FOLLOWING CALCULATIONS FNX = EXPERIMENTAL NUMBER DISTRIBUTION,
C FNF = FITTING NUMBER DISTRIBUTION, VX = EXPERIMENTAL CUMMULATIVE VOLUME,
C V = FITTING CUMMULATIVE VOLUME, XNC = EXPERIMENTAL CUMMULATIVE NUMBER,
C FNC = FITTING CUMMULATIVE NUMBER DISTRIBUTION. ALL ARE NORMALIZED.
C * * * * *
DO 93 J=IS,IF
  N = N+1
  D = GBOUND(N)
  XMI = XM(K)-D
  ADX = A*D/XMI
  IF(XMI.LE.0.0) GO TO 660
  T = ALOG10(ADX)
  IF(T.LE.0.0) GO TO 640
  H = DEL*T/1.414214
  ERX=SUB(H,B2,FAC(1),CONT(1),SIGN)
  V = 0.5*(1.0+ERX)
  GO TO 670
640 H = -DEL*T/1.414214
  ERX=SUB(H,B2,FAC(1),CONT(1),SIGN)
  V = 0.5*(1.0-ERX)
  GO TO 670
670 CONTINUE
  H = DEL*(T+F3)/1.414214
  IF(H.LE.0.0) GO TO 641
  ERX=SUB(H,B2,FAC(1),CONT(1),SIGN)
  FN3 = 0.5*(1.0+ERX)
  GO TO 642
641 H = -H
  ERX=SUB(H,B2,FAC(1),CONT(1),SIGN)
  FN3 = 0.5*(1.0-ERX)
642 H = DEL*(T+F2)/1.414214
  IF(H.LE.0.0) GO TO 643
  ERX=SUB(H,B2,FAC(1),CONT(1),SIGN)
  FN2 = 0.5*(1.0+ERX)
  GO TO 647
643 H = -H
  ERX=SUB(H,B2,FAC(1),CONT(1),SIGN)
  FN2 = 0.5*(1.0-ERX)
647 H = DEL*(T+F1)/1.414214

```

```

      IF(H.LE.0.0) GO TO 644
      ERX=SUB(H,B2,FAC(1),CONT(1),SIGN)
      FN1 = 0.5*(1.0+ERX)
      GO TO 645
644 H = -H
      ERX=SUB(H,B2,FAC(1),CONT(1),SIGN)
      FN1 = 0.5*(1.0-ERX)
645 CONTINUE
      FNC = CDFN*(EX3*FN3 + 3.0*EX2*FN2 + 3.0*EX1*FN1 + V)
      IF(N.EQ.1) FN10 = FNC
      GO TO 675
660 V = 1.0
      FNC = 1.0
675 CONTINUE
      IF(N.EQ.1) GO TO 680
      NN = N-1
      SUMZ = SUMZ+ZZ(NN,K)
      VX = V10+CRFT(K)*SUMZ/SUMZI(K)
      SUMN = SUMN+DELN(NN,K)
      XNC = FN10+(1.0-FN10)*SUMN/SUMNI(K)
      GO TO 690
680 VX = V10
      XNC = FN1
690 CONTINUE
      FNX = 6.6439*(1.0-FN10)*DELN(N,K)/SUMNI(K)
      FNF = X30C*Y(J)/GUSE(J)**3
      XDXM = GUSE(J)/XM(K)
      XDXMMX=GUSE(J)/(XM(K)-GUSE(J))*A
      WRITE(6,109) GUSE(J),XDXMMX,XDXM,X(J),Y(J),FNX,FNF,D,ADX,VX,V,XNC,
1FNC
93 CONTINUE
      KK = NAA(K)
      WRITE(6,160) SUMDWT,SUMD,DELN1(K),DELN(1,K),DFLNF(K),DELN(KK,K)
      WRITE(6,172) X32(K),X31(K),X30(K),X21(K),X20(K),X10(K)
C *****
92 CONTINUE
      GO TO 417
97 FORMAT(1H2)
98 FORMAT(1H1)
99 FORMAT(1H0)
100 FORMAT(2X,13A6)
101 FORMAT(I3)
102 FORMAT(1P8E10.2)
103 FORMAT(4A6)
104 FORMAT(2(OPF7.2,F7.0,1PE16.7))
107 FORMAT(8H0 RUN = 4A6,10X,20H CORRELATION INDEX =F9.6,3X,4H A =F7.4
1,3X,6H DEL =F7.4,3X,5H XM =F8.3,2X,3HCF=F8.6)
108 FORMAT(130H0 D AD/(DM-D) D/DM EX.VOL.DS. FIT.VL.DS. EX.NUM.DS.
1 FIT.NUM.DS. D AD/(DM-D) EX.CUM.VOL FIT.CUM.VL EX.CUM.NUM FI
2T.CUM.NUM )
109 FORMAT(OPF7.2,2F7.3,1P4E11.3,OPF11.2,F8.3,1P4E11.3)
112 FORMAT(20H0 COEFFICIENTS )
113 FORMAT(1P12E11.3)
116 FORMAT(2X,21A6)
117 FORMAT(4A6,1P2E16.7)
119 FORMAT(1P6E12.5)
120 FORMAT(6F10.4)
121 FORMAT(2F7.0,F7.3)
160 FORMAT(20H0 SUM( W*(X-Y)**2 )=1PE10.3,17H SUM( W*(Y-X) )=1PE10.3,
113H ORIG.FIN.N=OP4F8.1)
161 FORMAT(5H M = I3,9H FLAGRG =1PE10.3,5H D = 1PE10.3)

```

```

166 FORMAT(11F7.2)
169 FORMAT(7H0 IC = 14,8H FLAG = F10.3)
171 FORMAT(18F7.1)
172 FORMAT(8H0 X32 =F8.3,7H X31 =F8.3,7H X30 =F8.3,7H X21 =F8.3,7H
1 X20 =F8.3,7H X10 =F8.3)
173 FORMAT(4A6,3F12.2)
174 FORMAT(8H0ALFMAX=8F8.2)
175 FORMAT(8H0XMZER =8F8.2)
176 FORMAT(8H0XMMAX =8F8.2)
177 FORMAT(8H0STDV1 =8F8.2)
178 FORMAT(8H0STDV2 =8F8.2)
END
$IBFTC SOLVE DECK
SUBROUTINE SOLVE (ANF,IMAX,A )
DIMENSION ANF(26,26),SUB(26),DEN(26),A(26)
DOUBLE PRECISION ANF,SUB,DEN,A,XK,XK1
CALL ADOTB(ANF(1,1),IMAX,1,1,DEN(1))
DO 3 I=2,IMAX
DO 6 K=1,IMAX
6 SUB(K)=0.
L=I-1
DO 1 J=1,L
CALL ADOTB(ANF(1,1),IMAX,J,I,XK)
XK1=XK/DEN(J)
1 CALL NEG(XK1,ANF(1,1),IMAX,J,SUB(1))
DO 2 J=1,IMAX
2 ANF(I,J)=ANF(I,J)-SUB(J)
CALL ADOTB(ANF(1,1),IMAX,I,I,DEN(I))
3 CONTINUE
DO 4 J=1,IMAX
4 A(J)=ANF(IMAX,J)/ANF(IMAX,IMAX)
RETURN
END
$IBFTC ADOTB DECK
C SUBROUTINE TO FORM THE DOT PRODUCT OF VECTOR A AND B
C DESIGNATING A AND B AS ROWS OF A MATRIX F. IMAX INDICATES
C THE LENGTH OF THE ROW,I1 AND I2 THE ROWS TO BE DOTTED, AND
C XK THE FINAL DOT PRODUCT.
SUBROUTINE ADOTB (F,IMAX,I1,I2,XK)
DIMENSION F(26,26)
DOUBLE PRECISION F,XK
XK=0.0
DO 1 I=1,IMAX
1 XK=XK+F(I1,I)*F(I2,I)
RETURN
END
$IBFTC NEG DECK
C SUBROUTINE TO FORM THE MATRIX CALCULATION,A=A-KC
C
SUBROUTINE NEG(XK1,A,IMAX,I1,SUB)
DIMENSION A(26,26),SUB(26)
DOUBLE PRECISION A,SUB,XK1
DO 1 I=1,IMAX
1 SUB(I)=SUB(I)+XK1*A(I1,I)
RETURN
END

```

BIBLIOGRAPHY

1. Benson, G. M.: Ph.D. Thesis, 1960, Univ. Wis.
2. Pringsheim, P.: Fluorescence and Phosphorescence. Interscience, N.Y., 1949.
3. Neblette, C. B.: Photography, Its Materials and Processes. D. Van Nostrand Co., Inc. Princeton, N.J., 1962.
4. Marshak, I. S.: Soviet Physics Uspekhi, vol. 5, no. 3, Nov.-Dec. 1962, p. 478.
5. Fisher, L. H.: Physical Review, vol. 72, no. 5, 1947, p. 423.
6. Handbook of Chemistry and Physics, 14th Ed.
7. Penning, F. M.: Electrical Discharges in Gases. MacMillan, N.Y., 1957.
8. Mansberg, H. P., Yamagami, Y., and Berkley, C.: Electronics, Dec. 1, 1957.
9. Mansberg, H. P.: Cutler-Hammer, AIL Division, Private Correspondence, April 17, 1962.
10. Hoyt, G. D., and McCormick, W. W.: Jour. Opt. Soc. Am., vol. 40, Oct. 1950, p. 658.
11. Whitlow, L.: Electronic Engineering, Nov. 1961.
12. Vanyukov, M. P., and Mak, A. A.: Sov. Phys. Uspekhi, vol. 1, no. 1, Sept.-Oct. 1958, p. 137.
13. Fischer, H.: Jour. Opt. Soc. America, vol. 47, no. 11, 1957, p. 981.
14. Mak, A. A.: Optics and Spectroscopy, vol. 8, 1960, p. 145.
15. Marshak, I. S.: Applied Optics, vol. 2, no. 8, 1963, p. 793.

16. Vanyukov, M. P., and Mak, A. A.: Soviet Physics Doklady, vol. 3, 1958, p. 1268.
17. Marshak, I. S.: Soviet Physics Uspekhi, vol. 5, no. 3, 1962, p. 478.
18. Mak, A. A.: Dissertation (State Optics Institute), 1960.
19. Vanyukov, M. P., Mak, A. A., and Muratov, V. P.: Optics and Spectroscopy, vol. 8, 1960, p. 233.
20. Schardin, H., and Funfer, E.: Z. angew. Physik, vol. 4, no. 5, 1952, p. 185.
21. Pressman, Z.: SMPTE, 5th Int. Cong. High-Speed Phot. Proc., 1962.
22. Miller, H. A., Henn, R. W., and Crabtree, J. I.: PSA Journal, Nov. 1946, p. 586.
23. Levshin, V. L., and Krotova, L. V.: Opt. and Spect., vol. 13, 1962, p. 457.
24. Levshin, V. L., and Baranova, E. G.: Opt. and Spect., vol. 6, no. 1, 1959, p. 31.
25. Kantardzhyan, L. T.: Bull. Acad. Sci. USSR, Phys. Ser. vol. 23, no. 1-6, 1959, p. 125.
26. Mood, A. M.: Introduction to the Theory of Statistics. McGraw-Hill, New York, 1950.
27. Adamov, V. A., Kantardzhyan, L. T.: Opts. and Spectr., vol. 11, 1961, p. 226.
28. Novikov, I. I.: Zhurnal Tekhnicheskoi Fisiki, vol. 18, 1948, p. 345.

29. Abramovich, G. N.: (Theory of Centrifugal Nozzles) in the collection (Industrial Aerodynamics) published by Central Aero-Hydrodynamical Institute, 1944, p. 18.
30. Pilcher, J. M., and Miesse, C. C.: Injection and Combustion of Liquid Fuels - WADC Tech. Rep. 56-344, ASTIA Document No. AD 118142, 1947, p. 1-1.
31. Pilcher, J. M.: Ibid, p. 4-93.
32. Priem, R. J.: NACA TN 3985, July 1957.
33. Ingebo, R. D.: Chem. Eng. Progress, vol. 58, no. 4, April 1962, p. 74.
34. Anson, D.: Fuel, vol. 32, no. 1, 1953, p. 39.
35. York, J. L., and Stubbs, H. E.: Trans. ASME, vol. 74, no. 7, Oct. 1952, p. 1157.
36. Ingebo, R. D.: NACA TN 3265, Oct. 1954.
37. Pilcher, J. M., Miesse, C. C., and Putnam, A. A.: WADC Tech. Rep. 56-344, ASTIA Doc. No. AD 118142, 1947, p. 4-1.
38. Taylor, G. I.: Quart. J. Mech. Ap. Math., vol. III, part 2, 1950, p. 129.
39. Squire, H. B.: Brit. J. Ap. Phys., vol. 4, June 1953, p. 167.
40. York, J. L., and Stubbs, H. E.: ASME Trans., Oct. 1953.
41. Dombrowski, N., and Johns, W. R.: Chem. Eng. Sci., 1963, vol. 18, p. 203.
42. Hinze, J. O.: App. Sci. Res., vol. A1, 1948, p. 273.
43. Mugele, R. A., and Evans, H. D.: Ind. and Eng. Chem., June 1951, vol. 43, no. 6, p. 1317.

44. Mugele, R. A.: A.I.Ch.E. Journ., vol. 6, no. 1, 1960, p. 3.
45. Foster, H. H., and Heidmann, M. F.: NASA TN D-301, July 1960.
46. Tate, R. W., and Olson, E. O.: ASHRAE Journal, March 1962,
p. 39.
47. Tate, R. W., and Marshall, W. R. Jr.: Chem. Eng. Prog.,
vol. 49, no. 5, May 1953, p. 266.
48. DeCorso, S. M.: ASME Paper No. 61-WA-300. Presented at ASME
Winter Annual Meeting, New York N.Y., 1961.
49. Taylor, G.: Proc. Royal Soc. Ser. A, vol. 253, no. 1274,
Dec. 1956, p. 289.
50. Binark, H., and Ranz, W. E.: Proj. SQUID Tech. Rep. PSU-1-P,
The Pennsylvania State University, University Park,
Pennsylvania.
51. Marquardt, D. W.: J. Soc. Ind. Appl. Math., vol. 11, no. 2,
June 1963, p. 431.
52. Scarborough, J. B.: Numerical Mathematical Analysis, 5th Ed.,
The Johns Hopkins Press, 1962.
53. Beers, Y.: Theory of Error, Addison-Wesley, 1957.
54. Todd, C. A.: Unpublished subroutines, NASA-Lewis Research
Center, Cleveland, Ohio.
55. Dobbins, R. A., Crocco, L., and Glassman, I.: Rev. Sci. Instr.,
vol. 34, no. 2, 1963, p. 162.